Final Report

Autonomous Environmental Sensing

Design Synthesis Exercise

TU Delft

This page is intentionally left blank.

Final Report

Autonomous Environmental Sensing

Students:	Viranca Balsingh	4554000
	Luc Boerboom	4569431
	Jack Cook	4543092
	Vlad Gavra	4663632
	Phillipe Lothaller	4460820
	ChangKyu Park	4646061
	Rolijne Pietersma	4548841
	Max Robertson	4644085
	Natascha Schoenmaker	4667387
	Sebastian Widmann	4656792
Coaches:	Lorenzo Pasqualetto Cassinis	
	Mark Schelbergen	
Supervisors:	Dr. I.C. Dedoussi	
	Dr. ir. M. Snellen	

Date: June 26, 2020

TU Delft

Preface

The Design Synthesis Exercise is the final hurdle within the Aerospace Engineering Bachelor at Delft University of Technology. In light of global events, this year saw a rather different final project, thereby presenting new challenges for the team to overcome. After ten weeks of intensive research and design, this report shows the culmination of the team's efforts.

We were presented with the opportunity to contribute to the examination and monitoring of aviation's environmental impact with a focus on near-airport communities. Our system, CARES (Communities near-Airport Remote Environmental Sensing), is able to measure noise and air quality metrics of aircraft in three dimensional space and time. We hope that CARES will someday help in the reduction of this impact and serve a value and purpose within the scientific community.

We would like to thank our tutors Dr Ir Mirjam Snellen and Dr Irene Dedoussi as well as our coaches Ir Lorenzo Pasqualetto Cassinis and Ir Mark Schelbergen for their academic input, guidance and support throughout the project. Finally, we would like to extend our gratitude to the OSCC and OSSA, specifically Daniel Martini Jimenez, for their time and effort devoted to the Design Synthesis Exercise.

Autonomous Environmental Sensing - Group 08

Contents

Executive Summary

Modern aviation is a key figure in today's society's growing globalisation, providing a fast and reliable means of transportation. With an expected growth of 42% in the number of flights from 2017 to 2040 [13], the aviation sector will provide a consistently growing demand for employment, increasing the regional developments by attracting activities and investments.

Apart from the growing threat of Earth's climate change, sustainability is one of the biggest challenges for the aviation industry in the twenty-first century. Over the next three centuries, the European Union Aviation and Safety Agency (EASA) has identified the six most important aspects, shown in figure 1, which must be tackled to achieve decarbonisation by 2050 and to provide sustainable aviation for future generations.
To understand how aviation impacts the environment, being able to measure aviation's environmental footprint is key in improving the scientific understanding of how the long term effects of aircraft emissions affect human health. While it is known that chemical compounds such as nitrogen oxides NO_x, carbon monoxide CO or particulate matter PM have adverse health effects, the scientific understanding of the long term effects of aircraft emissions is still not perfect.

Figure 1: Sustainability aspects considered to achieve decarbonisation by 2050.

Although ground-level monitoring systems exist and are already in operation, they are unable to quantify the emissions of aircraft types as they cannot distinguish between different sources. Computational models on the other hand currently do not reflect reality in many cases as they primarily rely on assumptions rather than validated data. The predicted results are therefore considered untrustworthy. With the forecast of aviation's development over the next 20 years, airports, local communities and policymakers demand better ways of monitoring the environmental impact of aircraft to enable a constructive discussion on regulatory and other mitigation strategies.

Mission Need Statement

The growing environmental footprint of modern aviation requires improved ways to mitigate the impact of noise and air pollution on near-airport communities.

From the need statement, a more specific project objective can be formulated for the Design Synthesis Exercise 2020, conducted at the Delft University of Technology.

Project Objective Statement

Design an autonomous, mobile, near-real-time monitoring system, able to distinguish emissions between aircraft and external sources using commercial off-the-shelf components within a budget of €25000 with 10 students in 10 weeks.

Conceptual Design Following the concept generation in the baseline report [2], the concepts shown below were investigated in the midterm report [3]. For the comparison, cost of operation, performance, payload application, risk and sustainability were analysed and concept 2, the coaxial octocopter, emerged as the most suitable concept for this mission requirements.

Concept 1: Helium Airship

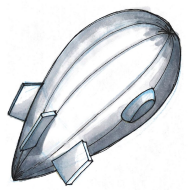

The helium airship is a type of aerostat which generates lift from a lifting gas that is less dense than the surrounding air. Helium was chosen over hydrogen as it has the same lifting capacity while not being flammable. To increase the inherently poor manoeuvrability, four electric-driven propellers are added around the airship.

Concept 2: Coaxial Octocopter

The coaxial octocopter is a type of drone which has outstanding manoeuvrability and high redundancy due to the coaxial propeller configuration. This configuration can maximise the produced thrust for the limited geometrical design space of 2 m, increasing the maximum payload, and offering increased stability performance due to the torque cancellation of the blades.

Concept 3: VTOL Flying Wing

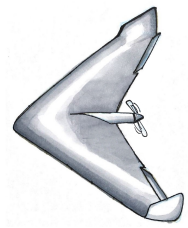

The VTOL flying wing is a hybrid configuration combining a conventional aircraft-style configuration with one tail-propeller for horizontal propulsion and three electric-driven propellers integrated into the frame of the system for vertical propulsion. Since the system can rely on wing-generated lift, the endurance is highly increased and the VTOL capabilities allow for easier operation.

Detailed Design With the final concept chosen, the mission and the associated operations were defined. For each mission, the system will operate in a cylindrical volume with a radius of 5 km and a height of 40 m. The radius of the measurement volume was set based on [43], which examined the environmental costs of aviation near airports and correlated the costs to the exposed noise and air pollution emissions.
During each mission, the system will generate a measurement grid which divides the volume into a rectangular mesh with equidistant nodes of 150 m. Measurement will be taken at each grid node. To maximise the operational time of the system, the autonomous navigation system will perform path planning and geo-caging algorithms to plan the optimal route while staying clear of any active runways and incoming/leaving aircraft. With a measurement duration of 21 days to cover the entire volume, smaller submissions are defined which are executed daily, as shown by the different colours in the figure 2 below.

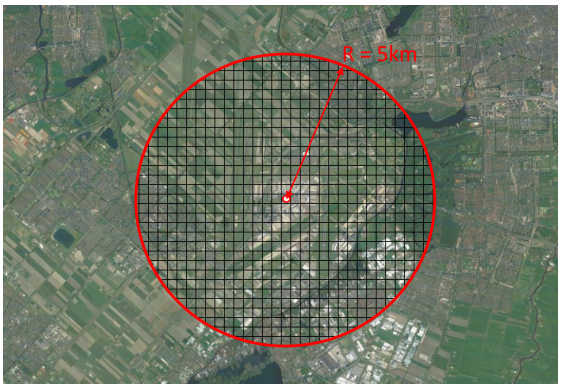

(a) Measurement radius around the centre of Schiphol airport

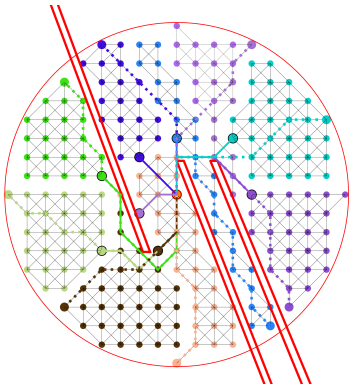

(b) Segregated volume showing the individual submissions and the geo-caging around active runways.

Figure 2: Measurement Volume for Schiphol Airport

To gather the necessary measurement data at each grid node, both air pollution and noise sensors have been selected. The sensors have been selected based on the estimated measurement ranges. These ranges

were derived from the Gaussian plume model for which the emission indices and air quality measurements around Schiphol airport were used. To simply the data-processing of the different signals, electrochemical sensors from Alphasense have been chosen except the ultra-fine particle sensor. Rather than an electrochemical sensor, this sensor is a condensation particle counter which will be provided by Naneos. The electrochemical sensors will be placed in two sensor housings, each box having the same configuration to increase the measurement redundancy of the system.
To measure the different noise levels, MEMS microphones were chosen which can measure frequencies between 6 Hz and 20 kHz. Eight of these microphones will be placed around the sides of the frame, having two microphones on each side.

During operations, the system will generate two levels of data for the client. Next to the raw measurement data which includes the air pollutant concentrations, particulate matter histograms and sound spectrograms, the system will generate emissions metrics. Based on the measured species concentrations and weighted noise values for distinct spatial and temporal measurement points the system will generate four-dimensional emission metrics. To receive information about points of interest which have not been measured, advanced interpolation using radial basis functions will be used.
To generate these metrics efficiently, full autonomy was achieved using a combination radar, GPS-RTK and stereo vision which will be integrated into the Pixhawk autopilot system. Using the radar modules, the system will be able to detect and avoid obstacles while the autonomously landing will be performed using square markers (ArUco markers) which are detected by the stereo vision. Once on the ground, the system will charge autonomously using a battery replacement system inside the ground system. As the drone will also fly close to operating aircraft, an emergency procedure was implemented where the drone will scan the environment and find the closest spot which allows for a safe emergency descend.

For the design of the coaxial octocopter, the structural mass was minimised by selecting the most suitable material based on the expected load cases the UAV will experience during operations. It was found that high modulus carbon fibre with cyanate ester with it's high specific stiffness will offer the best performance for the system by minimising the mass and the aerodynamic impact of the system. With the required hardware and senors selected, the frame of the drone was designed and optimised to both decrease the required volume necessary as well as providing the necessary airflow to the sensors which will measure the air pollutant concentrations. To increase the measurement accuracy of the system, a pipe-like rod was added to the system to feed non-turbulent air into the system rather than being influenced by the turbulence generated by the propellers.

To power the drone, modern lithium-polymer cells were chosen to increase the endurance time of the system while also providing high manoeuvrability from the increased discharge rates. Based on the selected cells, structural and payload mass, the system performance was iterated to determine the minimum structural mass and maximise the endurance time by decreasing the required power during operations. The iterative scheme showed that the propeller diameter must be maximised to decrease the required power. The increased propeller diameter will also decrease the inherent noise pollution as the propellers are operating at a lower rotational speed.
For the power subsystem of the drone, a configuration of ten cells in series and 16 modules in parallel will be used to provide the energy for around 30 min. This power system will be paired with eight 32"-propellers which will be arranged in a coaxial configuration on four arms to provide increased stability properties in the wake of an aircraft during take-off.

Further Development Having finished the design, additional aspects of the system design were taken into account in the last part of this report. As the system will be using either a composite material with carbon fibres or plastics for the battery housing, it was chosen to use filament winding to manufacture the propeller arms and the landing gear. Contrary to hand lay-up, this process is automated and will therefore both decrease the labour costs and manufacturing time for these components. For the battery casing, additive manufacturing methods were selected as the required parts have low-stress concentrations yet an increased complexity with regards to the shape. Therefore, 3D-printing is offering a cheap yet reliable manufacturing method to produce these parts. Additionally, the production and assembly plan for the system will be proposed.

Another important aspect of the project is the sustainability of the system itself during the different produc-

tion stages. Therefore, based on the *Design4Sustainability* concept which was developed by Delft University of Technology together with the United Nations Environment Programme, the following seven aspects were analysed.

Design4Sustainability

- **Low Impact Materials** No harmful impact on the environment during extraction and/or production. Manufactured in closer proximity to the assembly location. Materials can be down-cycled/recycled.
- **Material Use** Decrease system weight and size by using more efficient design to reduce energy consumption during use.
- **Production Techniques** Optimise production techniques by reducing toxic and solid waste and use renewable energy.
- **Distribution System** Optimise transportation strategy to optimise distribution strategy.
- **Impact During Use** Decrease sustainability impact during operations.
- **Initial Lifetime** Improve reliability and durability of the product and minimise maintenance required during operations.
- **End-of-Life System** Reduce the environmental impact of end-of-life disposal.

To guarantee that the system will be profitable when going into operations, a financial analysis will be presented. As the hardware costs were fixed to a maximum of €25000, additional costs such as assembly and production costs and operational costs have been calculated. As there is currently no flying environmental monitoring system which can measure ultra-fine particles, it can be expected that around 15 products can be sold per year which will correspond to a return of investment for one product of 14.7 %. One key aspect in further increasing the profitability of the system is by generating revenue by using a subscription model for the data gathering, transfer and processing through cloud computing.

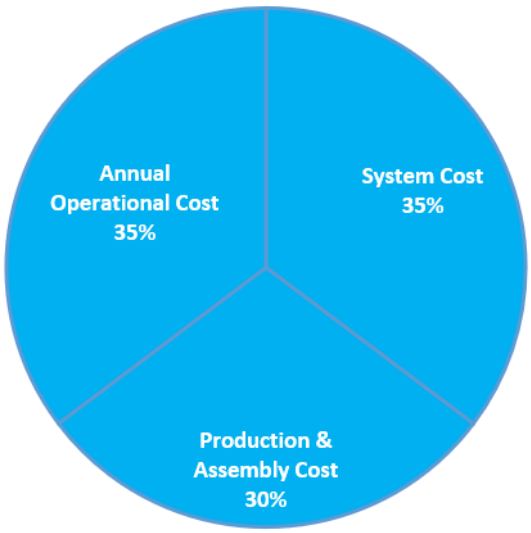

Figure 3: Pie Chart summarising the total annual system costs. Hardware, testing and assembly & production costs are considered one-time investments.

Nomenclature

Acronyms

Symbol	Description	Dimensions	Units
API	Application Programming Interface	-	-
APU	Auxiliary Power Unit	-	-
AQMS	Air Quality Monitoring Station	-	-
ATC	Air Traffic Control	-	-
BMS	Battery Management System	-	-
CAGR	Compound Annual Growth Rate	-	-
CFD	Computational Fluid Dynamics	-	-
CGM	Centre Of Gravity	-	-
CIS	Client Interface Software	-	-
CPC	Condensation Particle Counter	-	-
CPU	Central Processing Unit	-	-
D4S	Design for Sustainability	-	-
DC	Direct Current	-	-
DFT	Discrete Fourier Transform	-	-
DoD	Depth of Discharge	-	%
DOT	Design Option Tree	-	-
EI	Emission Index	-	-
EMPC	Expected Maximum Pollutant Concentration	-	-
ESC	Electronic Speed Controller	-	-
FBD	Free Body Diagram	-	-
FDM	Fused Deposition Modeling	-	-
FMCW	Frequency Modulated Continous Wave	-	-
GPIO	General Purpose Input Output	-	-
GPS	Global Positioning System	-	-
GSE	Ground Service Equipment	-	-
GT	Gradient Threshold	-	-
IDEF0	Icam DEFinition for Function Modelling	-	-

IMU	Inertial Measurement Unit	-	-
LDSA	lung-deposited surface area	-	-
LiPo	Lithium Polymer	-	-
LTI	Linear time-Invariant	-	-
MTBF	Mean Time Between Failures	-	-
OEM	Original Equipment Manufacturer	-	-
OPC	Opticle Particle Counter	-	-
PCB	Printed Circuit Board	-	-
PDE	Partial Differential Equation	-	-
PID	proportional integral differential	-	-
PSD	Power Spectral Density	-	W
RAMS	Reliability, availability, maintainability, and safety	-	-
RBF	Radial Basis Function	-	-
rh	Relative Humidity	-	-
RTK	Real-Time Kinematics	-	-
SAA	Sense and Avoid	-	-
SN	Smoke Number	-	-
SWOT	Strengths, Weaknesses, Opportunities and Threats	-	-
TCAS	Traffic Collision Avoidance System	-	-
TO	Take-Off	-	-
TPM	Technical Performance Parameters	-	-
UAV	Unmanned Aerial Vehicle	-	-
UNEP	United Nations Environmental Programme	-	-

Greek Symbols

Symbol	Description	Dimensions	Units
η	Efficiency	-	-
ϕ	Roll Angle	-	rad
ψ	Yaw Angle	-	rad
τ	Torque	ML^2T^{-2}	N m
θ	Inclination Angle	-	rad
θ	Pitch Angle	-	rad

Roman Symbols

Symbol	Description	Dimensions	Units
FOM	Figure of Merit	-	-
ρ	Density	ML^{-3}	kgm^{-3}
A	Disk Area	L^2	m^2
c_P	Power Coefficient	-	-
c_T	Thrust Coefficient	-	-
C_D	Drag Coefficient	-	-
d	Propeller Diameter	L	m
F	Aircraft LTO Frequency	-	$week^{-1}$
g	Gravitational Acceleration	LT^{-2}	ms^{-2}
J	Advance Ratio	-	-
L_A	Overall A-Weighted Sound Pressure Level	-	dBA
n	Revolutions per Second	T^{-1}	s^{-1}
P	Power	ML^2T^{-2}	W
S	Surface area	L^2	m^2
T	Thrust	MLT^{-2}	N
v	Velocity	LT^{-1}	ms^{-1}
p	Roll rate	-	$rads^{-1}$
PBL	frequency band Level	-	dB
q	Pitch rate	-	$rads^{-1}$
R	Rotation Matrix	-	-
r	Yaw rate	-	$rads^{-1}$
SEL	Sound Exposure Level	-	dBA
SPL	Sound Pressure Level	-	dB
u, v, w	Velocity in Cartesian Coordinates	LT^{-1}	ms^{-1}

Other Symbols

Symbol	Description	Dimensions	Units
CH_4	Methane	-	-
CO	Carbon Monoxide	-	-
NO_x	Nitrogen Oxides	-	-
O_3	Ozone	-	-
SO_2	Sulphur Dioxide	-	-
PM_x	Particles with $\varnothing$x µm	-	-
UFP	Ultra Fine Particles	-	-

Introduction

Modern aviation is a key figure in today's society's growing globalisation, providing a fast and reliable means of transportation. With an expected growth in air traffic of 42% until the end of 2040, the aviation sector will provide a consistently growing demand for employment, increasing the regional developments by attracting activities and investments.

As air traffic will increase, near-airport communities will be increasingly affected by noise and air pollution. To understand how aviation impact the environment, being able to measure aviation's environmental footprint is key for improving the scientific understanding how human health is affected and enable a constructive discussion on regulatory and other mitigation strategies.
Models that simulate the aviation's environmental impact exist but do not reflect reality in many cases as must rely on assumptions. The current standard of measuring noise and air pollution is set by ground-level monitoring systems. These systems can measure noise and air pollution accurately, but they cannot distinguish between different emission sources. Moreover, as both emissions dissipate over time and space, stationary monitoring systems require interpolation to map noise and air pollution to its full extend which inhibits the systems' ability to accurately disclose aviation's environmental impact in all its detail.

Taking Amsterdam Airport Schiphol as an example, current standards regulating the environmental impact of the airport are in place and the compliance is being monitored by the Dutch environmental department. Yet, local communities, policymakers and the management board of the airport are struggling to reach an agreement around the airport's expansion plans as there is not sufficient scientific evidence that the airport complies with the environmental standards.

The objective of this project is to design an autonomous, flying environmental sensing system. The system shall measure both noise and air pollution, distinguish between different emission sources and create aircraft type-specific emission metrics in near-real-time. It must be designed using off-the-shelf components of which at least 70% can be downcycled and have a maximum hardware cost of €25000.

This report will outline the design of this autonomous, flying environmental sensing system. First, the previous phases of the project will be presented to the reader. Within part I, the general stakeholder / system requirements will be presented followed by the risk assessment and sustainable development strategies will be presented which were meticulously applied during all project phases to guarantee a successful project outcome.

In part II of the report, the detailed design will be presented. First, an outline will be given on how the system will perform it's desired mission at the European airports and within the near-airport communities. As the design primarily revolves around the design of the scientific payload, chapter 6 and 7 will present the sensors which are required to perform the mission and what considerations must be taken into account to provide accurate and reliable measurement results. Chapter 8 will then explain how the emission metrics will be generated based on advanced interpolation and optimisation methods to increase the usability of the measured data. The remaining chapters in part II will then outline the subsystem design of the hardware, including the autonomous, structural, power and propulsion system.

In the last part of the report, part III, further developments will be presented to the reader. This includes the manufacturing, production and assembly procedure which was worked out for the system as well as the risk and sustainability assessment of the system. As the financial aspect of the system is crucial to have an economically feasible project, the financial breakdown will be presented in chapter 20. The report will close with a forecast of the future steps which must be taken to prepare this system for the actual operations and a future vision will be presented on how the system can be further improved to increase the market share through innovative and sustainable product evolution.

The Python and MATLAB ® scripts and tools used during the project design are available under the following repository: `https://github.com/VladGavra98/DSE_ARS`

I

Conceptual Design

1
Market Analysis

The purpose of the market analysis is to asses the market the system would be part of and to estimate the competitive cost and volume of the system. A previous market analysis was carried out in the baseline report [2] and focused mainly on identifying comparable stationary and mobile measurement systems. First, a market overview is given in section 1.1 and secondly a SWOT analysis in section 1.2. Where necessary a the conversion rate from dollar to euro of 0.89 was applied from Google Finance.

1.1. Market Overview and Forecast

Monitoring Industry Evaluation It was found that the global air quality monitoring system market size is expected to reach €5.7 billion by 2025, rising at a market growth of 7 % compound annual growth rate (CAGR) during the forecast period[1]. The global noise monitoring market was valued at €624 million in 2019 and has an expected CAGR of 4.21 % from 2020 to 2027[2]. The combined air pollution and noise monitoring market can thus be calculated by summing the two market values, which results in a market size of €6.32 billion. This value will be used to calculate the market share in chapter 20.

Airport Sustainability Industry Evaluation Heathrow airport invested over €6.6 million in electric vehicle infrastructure to lower air pollution caused by the airport[3]. For this reason it is expected that a monitoring system will also be invested in. It does not directly lower the amount of air and noise pollution, but mapping it very carefully can help the airport in finding solutions to decreasing air and noise pollution. In addition, schiphol airport wants to become climate neutral by 2040 and is giving €336000 to local near-airport communities initiatives [4].

Comparable stationary measurement systems The Aeroqual AQS 1 Urban Air Quality Monitor [5] and The AQMest [6] are two such examples. Both systems can detect and measure particulate matter up to $1\mu m$, ozone and NO_x and noise in real time. The AQS 1 is larger and heavier. These systems are, however, not for use around airports. London Heathrow airport studied air pollution and noise with the use of a network of 40 low-cost sensors around the whole facility that measured NO_x, CO_2, and CO. Comparing these measurements to a reference system already present at Heathrow, indicated that the sensors showed constructive use due to the found square error of $R^2 > 0.93$. This system had multiple sensors, enabling it to distinguish non-local emission from emissions related to aircraft taking off. However, this was not done in real-time and the system only measured air pollution and not noise[31]. Another system is the Noise Measuring System (NOMOS) used at Schiphol. Masts with calibrated microphones on them have been placed in areas surrounding Schiphol. NOMOS combines the results of the measurements with the flight schedules to conclude how much noise a certain aircraft created. The data is transmitted real time and available for the public [2] [7].

Comparable mobile systems are the Scentroid DR1000 FLYING LAB and the SNiffer 4D. The Scentroid

[1] https://www.businesswire.com/news/home/20200204005473/en/Global-Air-Quality-Monitoring-System-Market-Expected [cited June 15, 2020]
[2] https://www.verifiedmarketresearch.com/product/noise-monitoring-market/ [cited June 15, 2020]
[3] https://www.heathrow.com/content/dam/heathrow/web/common/documents/company/heathrow-2-0-sustainability/futher-reading/heathrow-sustainability-report-2018-report.pdf [cited June 26, 2020]
[4] https://www.internationalairportreview.com/article/80597/royal-schiphol-group/ [cited June 15 2020]
[5] https://www.aeroqual.com/product/aqs-urban-air-quality-monitor [cited Mar 3, 2020]
[6] https://www.aqmesh.com/product/aqmesh/ [cited Mar 3, 2020]
[7] https://noiselab.casper.aero/ams/ [cited Mar 3, 2020]

DR1000 is valued at €14114,79 and can detect and measure a variety of molecules[8]. The SNiffer 4D measures CO, NO_2, O_x, SO_2, PM_1, $PM_{2.5}$, PM_{10}, C_xH_y (hydrocarbons), the cost is 12310 USD = €10820.20 Analysis of these two potential competitors and similar systems is useful when deciding on a competitive market price for the system, which is done in section 1.1. It can be concluded is that there are mobile systems, but they measure only air pollution and no Ultra Fine Particles (UFP) or noise. Besides this, they are not autonomous systems and thus require significant human contribution to gather data.

System Price and Market Volume Estimation There is no other environmental monitoring system yet that measures UFP, thereby proving a significant gap in the market. It could be argued that a system that can combine monitoring UFP, noise and other relevant air pollutants will be very competitive as there is no competitor that can do all three and is also autonomous, making it approximately 4 times more valuable (assuming equal value for additional features) than the Scentroid DR 1000 and the Sniffer 4D. Roughly speaking it can then be 4 times more expensive, while still being competitive. However, UFP monitoring devices are expensive and alter the system's price significantly. For the financial cost model that is applied in chapter 20, a monthly system price is required to estimate the cash flow and return on investment. To obtain this, the Scentroid and Sniffer 4D are assumed to give value for 2 years, because by then their performances and payload will have deteriorated to a futile extent, which results in a monthly operational cost of €625 by dividing their system price of approximately €15000 by 24 (months). As the system described in this report is 4 times more valuable, a competitive monthly system price is set at €2500. This does not include the operational cost, but the operational cost of comparable systems is assumed to be very similar to the operational cost of the system described in this report because all systems require sensor replacement of parts, maintenance and insurance. This will be further elaborated upon in section 20.1.2. The sole difference in cost between the system described in the project and comparable systems thus comes down to the difference in system cost, which is the sum of hardware, production & assembly and testing cost of the system.
According to [8], all major airports in the UK already perform air monitoring and with over 100 major airports in Europe, there will definitely be enough demand, especially from airports who want to expand. The only real restriction is posed by how many of these systems can be made in a year, Which is estimated to lie around 15. This is the market volume.

1.2. SWOT Analysis

The SWOT analysis analyses the strength, weaknesses, opportunities and threats of the system and a summarised graphical overview of the SWOT matrix is shown in Figure 1.1. The design's strength and opportunity is the integration of an integrated noise and air pollution measurement system in combination with an autonomous flying design concept. These unique features have the potential to outperform current implemented market solutions discussed in section 1.1. It also provides a wider variety of use cases such as autonomous noise and air pollution monitoring during rush-hour periods and measurement of toxic gases during large-scale forest fires. The global pandemic on one hand poses a threat to this project as there is a potential recession going on in the aviation industry. On the other hand, the reduction in air traffic provides an opportunity to look at emission levels when there is no air traffic, which might enable building a clearer picture of the impact of aviation. Furthermore, another threat is posed by the increased market attractiveness, shown by the market's high CAGRs that can result in an increasingly growing field of competitors and a swift development within the industry and cutting-edge technologies.

Figure 1.1: SWOT matrix originating from the matrix showing the identified strength, weaknesses, opportunities and threats.[2]

[8] https://scentroid.com/products/analyzers/dr1000-flying-lab/ [cited Apr 28, 2020]

2
General System Requirements

In the following section, the system and stakeholder requirements for the autonomous environmental monitoring system will be presented. These requirements were either directly derived from constraints posed onto the system or from the customer's wishes and demands and play an import role in the design of the UAV. . Their sources are indicated in squared brackets behind the requirement which, depending on the case, consists of a risk identifier, FFD block identifier, sustainability requirement or the customer needs. To indicate driving or key requirements, the identifiers are highlighted with color boxes(driving* , key). The complete derivation process for these requirements can be found in [2] and [3].

System Requirements

Stakeholder	
AEMS-SH-PERF-01	The system shall have a maximum setup time of one hour before it is ready to take-off
AEMS-SH-PERF-02	The system shall be able to operate in wind conditions up to and including Beaufort-4
AEMS-SH-PERF-03	The system shall be able to operate in dry weather conditions
AEMS-SH-DIMS-01*	The system shall have a maximum overall dimension of two meters when transported
AEMS-SYS-PERF-07	The system shall have a rechargeable power source
AEMS-SH-DIMS-02	The system shall be transportable by (at largest) a van
AEMS-SH-DATA-01	The system shall produce individual aviation emissions metrics
AEMS-SH-DATA-02	The system shall produce individual aviation noise metrics
AEMS-SH-DATA-03	The system shall produce a combined aviation's environmental impact metric
AEMS-SH-DATA-04	The system shall display background noise levels
AEMS-SH-DATA-05	The system shall display background air pollution levels
AEMS-SH-DATA-06	The system shall be able to store or send one day's (8h) worth of measurements
AEMS-SH-SUST-01	The monitoring system shall be at least 70% recyclable or re-usable
AEMS-SH-FNCE-01	The hardware cost of the system shall not exceed €25000, excluding VAT
AEMS-SH-SYS-01	The system shall use off-the-shelf components
General System	
AEMS-SYS-02	The system shall be transported by a van registered under the N2 European Category for road vehicles [[15], SH-DIMS-02]
AEMS-SYS-03	The system shall have a minimum lifetime of 1 working year [SH-DATA-01,02]
AEMS-SYS-05*	The system shall provide at least one back-up measuring instrument for both noise and air pollution [Risk PL1]

3
Risk Strategy

This chapter focuses on the technical risk analysis inherent in the system design. The approach taken for the risk assessment is to first identify and present all of the risks associated with the technical aspect of the design and organise them by the effected subsystem by assigning a unique identifier to the risk. The risks will then be assessed on the likelihood of the risk occurring and the severity of the consequences if it does. Throughout the design process, prevention and mitigation strategies will then be applied to the risks in order to lower both the probability and impact of the risk to an acceptable level. Chapter 18 will present the preventative measures and mitigation strategies.The probability of the risks will be assessed using the metric shown in 3.1. The impact of the risk will be assessed using the impact metric in table 3.1, where the scores are explained in terms of the severity to the mission success.

Table 3.1: Impact and Probability Key

	Key	**Impact**	**Explanation**
Impact	1	Negligible	Risk has almost no impact on system functioning.
	2	Marginal	System should meet majority of requirements.
	3	Moderate	System should meet most of requirements but performance is suboptimal.
	4	Severe	System will not meet majority of requirements and mission success is unsure.
	5	Catastrophic	System will not meet all or almost requirements and mission will be a failure.
	Key	**Likelihood**	**Explanation**
Probability	R	Rare	Almost no chance of occurrence.
	U	Unlikely	Incredibly low chance of occurrence.
	P	Possible	Possibility of occurrence but slim.
	L	Likely	Expected to occur.
	H	Highly likely	Almost certain to occur.

Each risk has first been identified by liaising with all departments within the design team and from the market analysis into similar systems. Financial as well as logistical and scheduling risks were not included in the assessment as they are present in every subsystem within the design and this assessment will only deal with technical risks. The risks are organised into categories based on their relevance. The ID (identification) numbers are a reflection of the subsystem in which the risk is associated, a breakdown of how the first two letters of the ID relate to the category of risk is listed below:

- Manufacturing risks (MF)
- Structural risks (ST)
- Power risks (PW)
- Propulsion risks(PR)
- Payload risks (PL)
- Maintenance Risks (MN)
- Data handling risks (DH)
- Navigation risks (NV)
- Operational risks (OP)
- Maintenance risks (MT)
- Communication risks (CM)
- Control and stability risks (CS)

Probability and impact are denoted by P and I respectively. The scores are assigned both before and after the prevention and mitigation scores are applied, the scores before the strategies are applied are shown below. Section 18 will deal with the risks after prevention and mitigation methods are applied.

PW1-Power system degrades over life time and becomes unusable Probability: H, Impact: 4. This is risk is driven by the inherent nature of batteries to degrade over their operational life. The likelihood of this

happening is high as it is inevitable with all batteries. If this risk is left unchecked the performance of the drone can be severely effected over time and its ability to perform the mission severely compromised.

PW2-Failure of the power system Probability: U, Impact: 5. The drivers of this risk are that the team is inexperienced, exposure to the environment and a complex power system integration, these factors all mean the power system performance is exposed to risk and could fail. The probability of this happening is unlikely as the system will use off-the-shelf components in the power system. The impact this would have on the mission is catastrophic as the mission would not be able to be performed if the power system has failed.

ST1-Failure due to exceeding of design loads Probability: P, Impact: 5. The driver for this risk is that the drone can experience loads on its structure that it was not designed for, this can happen by way of collision or high aerodynamic loading. The probability of this occurring is possible as there are situations the team could overlook or that will be different in reality to the theory. The impact is catastrophic, as the mission will fail if the drone cannot support loads it needs to fly.

MF1-Unable to manufacture Probability: U, Impact: 5.The driver behind this risk is having a complex design or unique material choices that mean manufacturing of the structure or components is too difficult to be done to an acceptable quality. The likelihood of this happening is low because the drone design is common and the need for complex structures is low. The impact this risk would have on the success of the mission is great. If the drone cannot be manufactured it cannot be used to fly the mission at all.

PR1-Failure to provide enough thrust to the drone Probability: U, Impact: 5. This risk is driven by either poor design of the propulsion system or high thrust demands. The probability of this happening is unlikely as the motors and propellers will be chosen by from available components that have been verified and validated and the drone will not be performing high thrust manoeuvres. The impact is catastrophic because it will cause either the drone to be incapable of flying or to be uncontrollable which both will mean the mission cannot be completed.

DH1-Fails to distinguish between aircraft and background metrics Probability: P, Impact: 5. Requirements *AEMS-SH-DATA-01/2/4/5* mean there must be a distinction made between background and aircraft data measured, these are the drivers for this risk. The probability is increased due to the need for computations to extract the aircraft data and the high volume and variation in background data. The impact of this risk is catastrophic as it will mean the recorded data is unusable. To mitigate it, one can set a number of minimum measurements per aircraft type to increase the data pool or provide local re-meshing to a denser grid to extract more information.

DH2-Modelling unable to process data Probability: P, Impact 4. Requirements *AEMS-SH-DATA-01/02/03* present the need to be able to make use of the data for the customer. Before analysis it is expected that the occurrence of this risk is low due to the available resources, however, the impact is severe as the mission success is in question due to the violation of a stakeholder requirement. It is not catastrophic because some requirements are still able to be fulfilled.

CM1-Unable to download data from drone Probability: P, Impact: 3. The need to access the data from the drone would provide near-real-time data for requirement *AEMS-SH-DATA-03*. This would jeopardise few requirements, however, the overall mission is unlikely to fail.

CM2-Data is lost before/during data transfer Probability: U, Impact: 5. With no data available, the mission would be considered a failure as most of the stakeholder requirements would not be met. Modern technology means that it is unlikely but still has to be considered.

PL1-Sensors fail to measure any accurate data Probability: P, Impact: 5. The requirements *AEMS-SH-DATA-03* and *AEMS-F-AUT-04* mean the data from the emission sensors must be accurate enough for a metric to be made for the environmental impact of aircraft (this cannot be done without accurate data) and the navigation and sense and avoid sensors must be accurate enough to avoid collision or entering restricted spaces. This is possible due to the complexity involved in accurately measuring the correct data. The impact is catastrophic due to both no accurate emission data and autonomy data will mean mission failure.

PL2-Sensors damaged during operation, transportation or storage Probability: P, Impact 4. The sensors are required to gather data as well as navigate the drone. Reduced functionality would hinder either or both of these functions. Assuming not all are damaged at once, the probability is possible and impact severe as the mission success is left in question.

NV1-Global location of the drone is unknown Probability: U, Impact: 4. The driver behind this risk is the need to have a global location marker with the emission data and requirement *AEMS-F-AUT-04*. Without a global location, restricted airspace cannot be avoided and the emission data will have no reference locations, this makes the impact high. The probability will be low as GPS-receivers are commonly used and reliable.

NV2-The drone is unable to avoid impact with the local environment or restricted area Probability: P, Impact: 5. This risk is driven by requirement *AEMS-F-AUT-04*. The probability is possible as without a thoroughly investigated path planning and avoidance techniques collisions are possible, The impact is catastrophic as impact will cause damage to the drone and/or the environment and entering restricted space is both illegal and dangerous.

NV3-Unable to determine route pre-arranged destinations Probability: L, Impact 4. The expected large number of destinations means determining a route could present significant difficulties. Not being able to determine a route means little or no measurements, thereby violating requirements *AEMS-SH-DATA-01/02/03/04/05*, thus impacting mission success.

CS1-Drone is uncontrollable Probability: U, Impact: 5. The coaxial octocopter is a commonly used design and has been proved to be controllable, also the drone will not be performing highly difficult and demanding manoeuvres. The impact is of course catastrophic as the drone will inevitably crash and be unable to perform the mission.

CS2-Drone is unstable Probability: L, Impact: 5. The drone design is inherently unstable and must be kept stable through constant complex control algorithms, therefore a small mistake in calibration could cause instability. The impact is catastrophic as a crash would be inevitable.

CS3-No sufficient reaction to necessary sensory inputs (DAA/SAA) Probability: P, Impact: 5. The drone must respond quickly to sensory inputs to avoid them as the drone will be moving with reasonable velocity and may face oncoming obstacles such as birds, this means the likelihood of reacting before a collision is possible. The delay in reaction may cause the drone to collide with obstacles, opposing requirement *AEMS-F-AUT-04*.

OP1-Adverse weather conditions damage/reduce the drone functionality Probability: H, Impact 4. Adverse weather conditions will present inherent risks from wind, temperature, humidity and precipitation. These will hinder the drone's ability to function e.g. manoeuvre with little path deviation in the event of strong wind that is not designed for. The impact depends on the extent of the weather, however, in most cases the mission is not expected to fail.

OP2-Drone becomes a noise nuisance to people and animals Probability: P, Impact: 3. Driven by European UAV regulations (EU:UAV.SPEC.050 1.a.v related to requirement *AEMS-SYS-SUST-06*), this risk must be taken into account. It is possible that this may occur, however, the mission could still be completed successfully and minor changes likely needed to be taken into account.

OP3-Drone causes damage to humans, animals or ground property Probability: P, Impact 4. It is always desired for no human or animal to be in danger from the drone. This concerns the ability to receive certification as well as general safety. Before prevention and mitigation, this risk is seen as possible and would likely result in re-certification issues, therefore possibly failing the entire mission.

MN1-Unable to inspect parts/sections of the drone Probability: U, Impact 3. The need to be able to inspect parts of the drone is critical to maintenance, thereby ensuring the safety of the drone. Due to the use of modular off-the-shelf components, this is seen as unlikely and medium impact score.

Risk Map Now that the risks for the system have been identified a risk map has been made to visualise them, this is shown in figure 3.1. The risks that are located nearer the top right of the risk map are those that

pose the greatest threat to the mission success and will need the most attention during the detailed design. The aim throughout the detailed design is to move the risks toward the bottom left of the risk map by way of prevention strategies, thereby lowering the probability score, and mitigation, to lower the impact score.

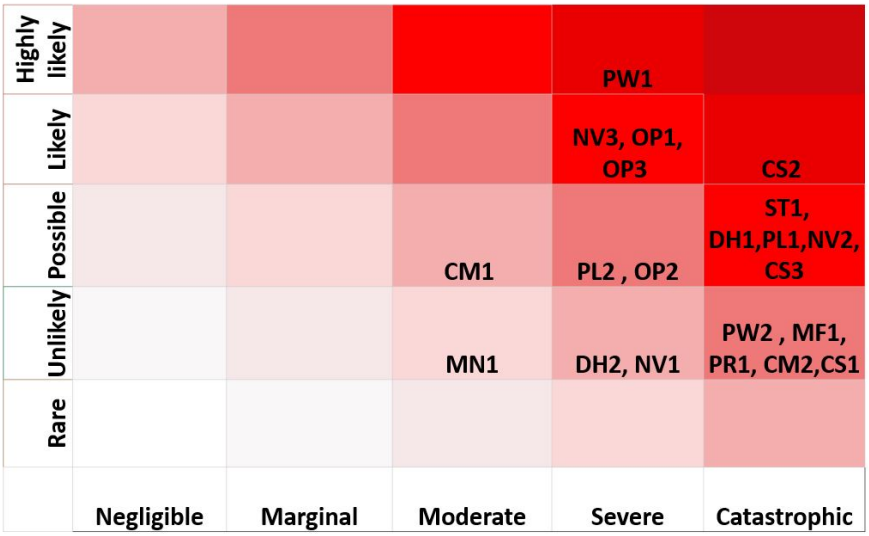

Figure 3.1: Risk map

4
Sustainable Development Strategy

A sustainable development strategy assures that during the design process the three key concepts of sustainability (Environmental, Social and Economical) are taken into account. This chapter addresses the process to warrant the successful implementation of a sustainable development strategy. First the project sustainability

4.1. Project Sustainability

The purpose of the system is to help address the impact the aircraft industry has on the surrounding environment of airports. The aviation industry adds harmful long and short-lived emission species such as NO_x, CO_2, soot, particulate matter, ultra-fine particles and much more to the environment. These species harmfully impact both climate and human health. Furthermore, noise expelled can lead to not only physical but also monetary damage. Aircraft noise was first regulated in 1971, and although further regulations have been implemented, it remains one of the greatest concerns for near-airport communities [43]. The low cost of the system compared to the traditional stationary system makes it an economically viable alternate solution that can be used to supplement the data retrieved by the stationary measurement stations and enhance the accuracy of current models. The data retrieved by the system can be used by policymakers, airport management and aircraft manufacturers to combat the raising impact the aerospace industry has on the environment and health of individuals living in near-airport communities.

4.2. Designing for Sustainability

The Design for Sustainability (D4S) concept uses several different strategies to assure the engineers create a sustainable design. The concept was developed by the Technical University of Delft in collaboration with the United Nations Environmental Programme (UNEP) . The seven different strategies (retrieved from [10]) that should be considered during the design of a product are :

1. Selection of low-impact Materials/Components
2. Optimisation of Material/Component use
3. Optimisation of Production Techniques
4. Optimisation of Distribution/Transportation
5. Reduction of Impact During Use
6. Optimisation of Initial Lifetime System
7. Optimisation of End-of-Life System

A design can be rated according to how it affects each of them. The ratings range from - - to + +. A + + rating is seen as very feasible to implement while a - - score indicates a very negative score and the option is completely infeasible to implement. These ratings in between correspond to an almost feasible option, a neutral option and feasible option respectively [10] [2]. The seven design strategies are discussed in detail below. Thereafter the definitions of how the final ratings for each strategy is achieved are tabulated.

Selection of low-impact Materials/Components Materials are considered low-impact if they can be recycled/reused and do not harm the environment during extraction or production. Components or materials that need to be transported from companies located far away are also not considered to be a low impact due to the increased emission expulsion during transportation. The ratings corresponding to the different strategy attributes are given in table 4.1 [2].

Optimisation of Material/Component use Materials and components should be selected in such a way that they minimise the impact on the environment during operation. Components with decreased weight

and size lead to more efficient designs. As such, the design team should select components that will help to minimise the sustainability impact of the component during use. Table 4.2 defines the corresponding ratings for the different attributes used for optimising materials/components [2].

Optimisation of Production Techniques
During the production of the final product, all aspects of sustainability are affected (environmental, social and economical). An optimised production technique will ensure that less solid and toxic waste is created. Furthermore, the power consumption during production should be minimised, and where possible, renewable energy should be used. The production of the final components/products should also not harm the workers. Table 4.3 shows the ratings that correspond to the different attributes of this strategy [2].

Optimisation of Distribution/Transportation This strategy has been adapted from the definition presented by the D4S manual, to assess how efficiently the design can be transported between different operations locations. The attributes considered in determining a minimum rating are given in table 4.4 [2].

Reduction of Impact During Use This design strategy is used to create a design that will reduce the impact it has on sustainability during operation. The final product should have an overall positive impact on sustainability, this includes eliminating or at the very least minimising the effect the final product has on sustainability during operation. As an example, it is known that the noise produced by the product might not be eliminated, but every effort should be made to minimise this impact to end up with an overall positive added social value. The ratings corresponding to the different attributes used to evaluate minimum requirements is shown in table 4.5 [2].

Optimisation of Initial Lifetime System The optimisation of the initial lifetime of the system is a strategy that is to be used to create a design that is reliable and durable. This strategy also considers the type of maintenance that will be required during operation. The ratings and the corresponding attributes for the strategy can be found in table 4.6 [2].

Optimisation of End-of-Life System This strategy is to be used to create a design that minimises the impact of the product once it has been decommissioned. This includes how much energy would be required to disassemble the product and whether the materials are recyclable. Attributes used to decide on a required minimum rating can be found in table 4.7 [2].

Table 4.1: Selection of low-impact Materials/Components Rating Table [2]

Rating	Attributes
+ +	Transported small distance, low production energy consumption, recycled/recyclable
+	Transported medium distance, low use production energy, mostly recycled/recyclable
o	Transported medium distance, medium use production energy, partially recycled/recyclable
-	Transported medium distance, large use production energy, mostly non-recycled/recyclable
- -	Transported large distance, large use production energy, non-recycled/recyclable

Table 4.2: Optimisation of Material/Component use Rating Table [2]

Rating	Attributes
+ +	Low weight, small volume, compactable
+	Low weight, small volume, not compactable
o	Medium weight, medium volume, compactable
-	Medium weight, medium volume, not compactable
- -	Large weight, large volume, not compactable

4.3. Minimum Objectives

A set of minimum requirements is decided upon by the sustainability manager, the team manager and the system engineers. The selection of the minimum objectives is based on the provided stakeholder requirements and engineering judgement. Sustainable design is considered important for both the stakeholders

Table 4.3: Optimisation of Production Techniques Rating Table [2]

Rating	Attributes
+ +	Few steps, low waste amounts, low non-renewable energy use, excellent safety
+	Many steps, low waste amounts, low non-renewable energy use, excellent safety
o	Many steps, medium waste amounts, medium non-renewable energy use, good safety
-	Many steps, medium waste amounts, medium non-renewable energy use, poor safety
- -	Many steps, large waste amounts, large non-renewable energy use, poor safety

Table 4.4: Optimisation of Distribution/Transportation Rating Table [2]

Rating	Attributes
+ +	Energy efficient transport, efficient logistical movements, overall small distances
+	Energy efficient transport, efficient logistical movements, overall medium distances
o	Partially energy efficient transport, partially efficient logistical movements, medium distances
-	Energy inefficient transport, inefficient logistical movements, overall small distances
- -	Energy inefficient transport, inefficient logistical movements, overall large distances

Table 4.5: Reduction of Impact During Use Rating Table [2]

Rating	Attributes
+ +	No toxic emissions, low energy use, reduced noise,positive social value
+	Few toxic emissions, low energy use, reduced noise,positive social value
o	Medium toxic emissions, medium energy use, normal level of noise, no social value
-	Medium toxic emissions, medium energy use, noise generated,negative social value
- -	Large toxic emissions, large energy use, noise generated, negative social value

Table 4.6: Optimisation of Initial Lifetime System Rating Table [2]

Rating	Attributes
+ +	Extremely reliable and durable product, highly modular design, very easy maintenance
+	Highly reliable and durable product, highly modular design, easy maintenance
o	Reliable and durable product, some modular design, maintenance is not to complex
-	Reasonably reliable and durable product, some modular design, maintenance is difficult
- -	Product is not reliable or durable, no modular design, maintenance is expensive and complex

Table 4.7: Optimisation of End-of-Life System Rating Table [2]

Rating	Attributes
+ +	All components recyclable/reusable, low energy use, no toxic emissions during disassembly
+	Most components recyclable/reusable, low energy use, few toxic emissions during disassembly
o	Most components recyclable/reusable, medium energy use, few toxic emissions during disassembly
-	Few amount components recyclable/reusable, high energy use, toxic emissions product disassembly
- -	Little to no components recyclable/reusable, high energy use, toxic emission during disassembly

and the design team, and as such, a strict set minimum objective has been selected. The minimum ratings for each strategy are presented in a radar diagram known as a strategy wheel. The strategy wheel is presented in figure 4.1. A more in-depth analysis of the selection for the minimum objectives is provided in the baseline report[3] and [2]. As it is evident from the minimum objectives and the strategy wheel, to be able to meet the minimum requirements, the design team should take special consideration of the design strategies related to material selection and the impact during use design strategy. This entails that the team

especially considers these strategies when starting the detailed design phase for the different subsystems.

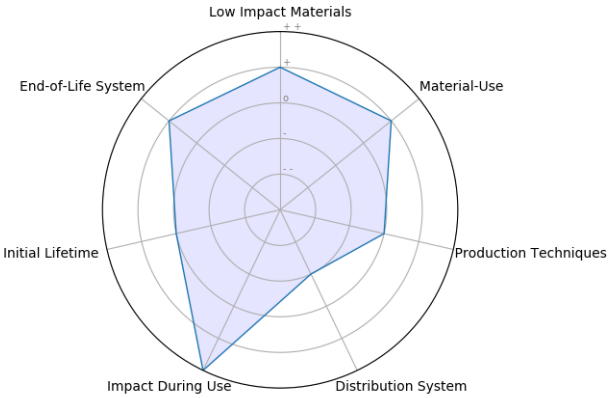

Figure 4.1: Radar diagram visualising minimum sustainability objectives for the design process [2].

To implement these minimum objective, system requirements are generated to aid in the design process. They are listed below in the following coloured box:

Sustainability Requirements

AEMS-SYS-SUST-03*	The amount of harmful gases during operation shall be kept at zero [D4S]
AEMS-SYS-SUST-05	The system shall incorporate changeable consumables [D4S]
AEMS-SYS-SUST-06	The noise produced by the system shall not be invasive to the nearest airport communities, people and animals [D4S, DroneReg [14]]
AEMS-SYS-SUST-07	The system shall be able to determine the amount of gas emissions it is producing [D4S]
AEMS-SYS-SUST-08	The system shall be able to determine the amount of noise emissions it is producing [D4S]
AEMS-SYS-SUST-09	The system shall not carry or use any potentially explosive substances or compounds [D4S]

4.4. Material Evaluation

Materials considered for the design will be assessed on the following material properties (properties which are closely related to sustainability), which are extracted from the software tool CES EduPack 2019 [17] [3]:

1. CO_2 footprint during production
2. Embodied energy during production
3. Processing energy consumption for different production techniques applied
4. Recyclability of the material

The CO_2 footprint during production material property represents the amount (in kg) of the CO_2-equivalent mass of greenhouse gasses that are released as a consequence of producing 1 kg of the material [17]. The embodied energy of a material represents the amount of energy needed to produce 1 kg of the material from the initial feedstocks or ores. Figure 4.2 plots the values of these properties for different material types found in different material families. As is evident in the figure, the two properties correlate. The more energy required to produce a material from the initial feedstock, means higher $C0_2$ emissions are produced

during production. This stems from the fact the a material with a higher embodied energy, undergoes more processes, these increased number of processes in turn increase the $C0_2$ footprint. Popular engineering materials were labelled in figure 4.2 to give insight to the reader about what magnitudes are to be expected.

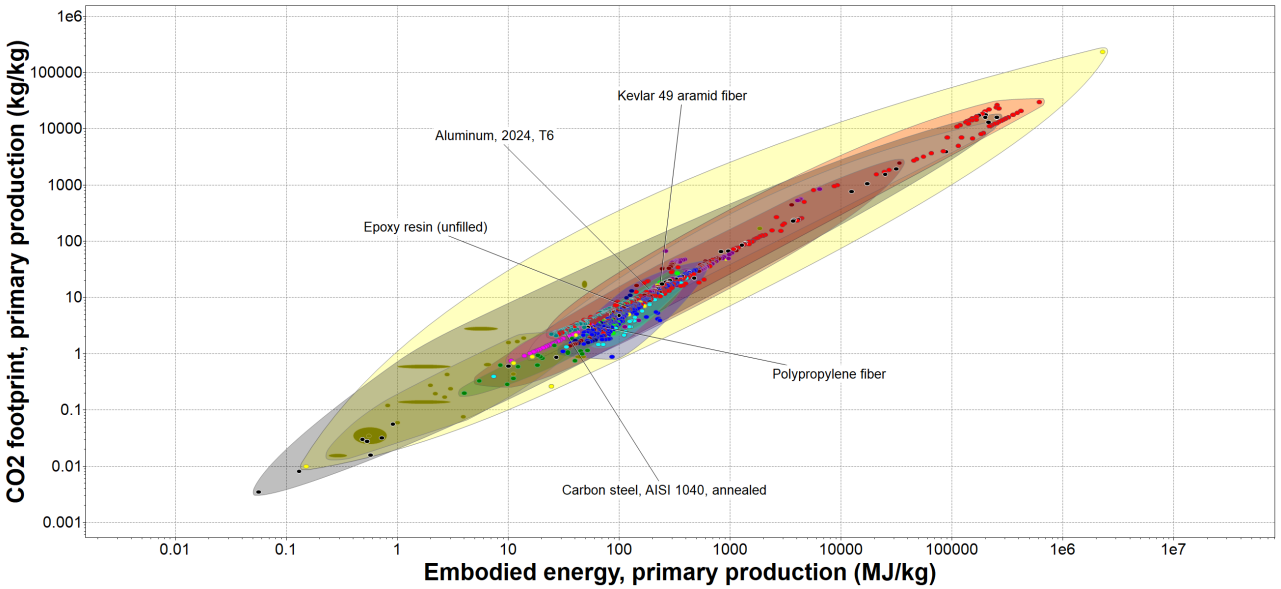

Figure 4.2: Embodied energy during primary production vs. CO2 footprint during primary production for various materials[17]

The different end-of-life options for materials are presented in table 4.8. The design team should aim to make use of materials that at the very least can be downcycled. This decision was made since only very few materials can be truly recycled and reprocessed into the primary supply chain.

Table 4.8: End of Life options for materials [17]

End of Life option	**Description**	**Environmental burden**
Reuse	Extension of product life	Lowest
Re-engineer	Incorporation of re-engineered part into new product	⇓
Recycle	Reprocessing of material into primary supply chain	
Downcycle	Reprocessing into a lower grade material	
Combustion	Recovery of the calorific content of the material	
Landfill	Disposal of material	Highest

II

Detailed Design

5
Measuring Mission

This section will outline the constituents of the mission of the system with a focus on the measuring system. This part of the mission is imperative to the selection and installation of the sensors as well as the processing of their data. It is kept separate from general operations due to its importance and need during detailed design. A general top-down approach is implemented to ensure a clear overview. Therefore, this will be discussed in detail before chapters 6 and 7 which deal with the air quality and noise subsystems. Thereafter, in chapter 8, all of the aforementioned items will be assembled to present a clear picture of the data turned into information and the process there-behind. First, a measuring mission overview in section 5.1 is given in order to present a clear outline of the system's measuring mission. Thereafter the dimensional aspects of the mission will be presented in section 5.2. Verification, validation and further use of the measurement mission and tools are therefore explained in section 5.4.

The appropriate system requirement is presented in the table below.

Measuring Mission Requirements	
AEMS-F-MMI-01	The system shall be able to produce metrics on aircraft types arriving at minimum once per week [AEMS-SH-DATA-01/02]

5.1. Measuring Mission Overview

The selected concept must provide near real-time information on the impact of the aviation industry on near-airport communities. To fulfil this (requirement *AEMS-SH-DATA-03*), the measurement system is to build up a database of information for points within the measuring volume with a ground station located at or near the centre. These points will be referred to as nodes. Over time these nodes will become more populated and information on measured parameters may be presented. Figure 5.1 presents the flow of the mission with respect to the measuring systems in order to achieve this goal.

While the drone is on the ground (left half of figure), the set measuring volume and airport information are loaded into the drone's RAM via an external computer. This software process block is elaborated upon in section 9.2.2. Before launching of the drone, three checks are made: battery level sufficiency, ATC clearance obtained (requirement *AEMS-SYS-REG-08*) and that the weather is favourable (minimum requirement *AEMS-SH-PERF-02*). The latter ensures the prevention of risk *OP1*. Only then may it take off and travel to the first node. Once it has arrived, the system performs the first set of measurements. A further note can be made on the measurements. This includes measuring for all air pollution species defined in chapter 6 as well as noise levels. Further details can be found in section 6 and 7 respectively. The drone then re-positions to the next node to perform the same set of measurements, assuming that the battery level is sufficient still and the wind speeds are again less than 8 $\mathrm{m\,s^{-1}}$, thereby again aiming to prevent risk *OP1*. Once all measurements are complete, such that the drone can still return to the ground station with the remaining battery level, the drone returns. If, however, any of the conditions are not satisfied, the drone must return earlier.

5.2. Measuring Volume

The system must have a defined volume within which it is to operate. The volume will be discretised into a cylindrical 3D grid consisting of four layers and a radius of 5 km. The cylinder is chosen for its optimal ability to reduce the distance the drone needs to fly between measuring nodes and the ground station. An

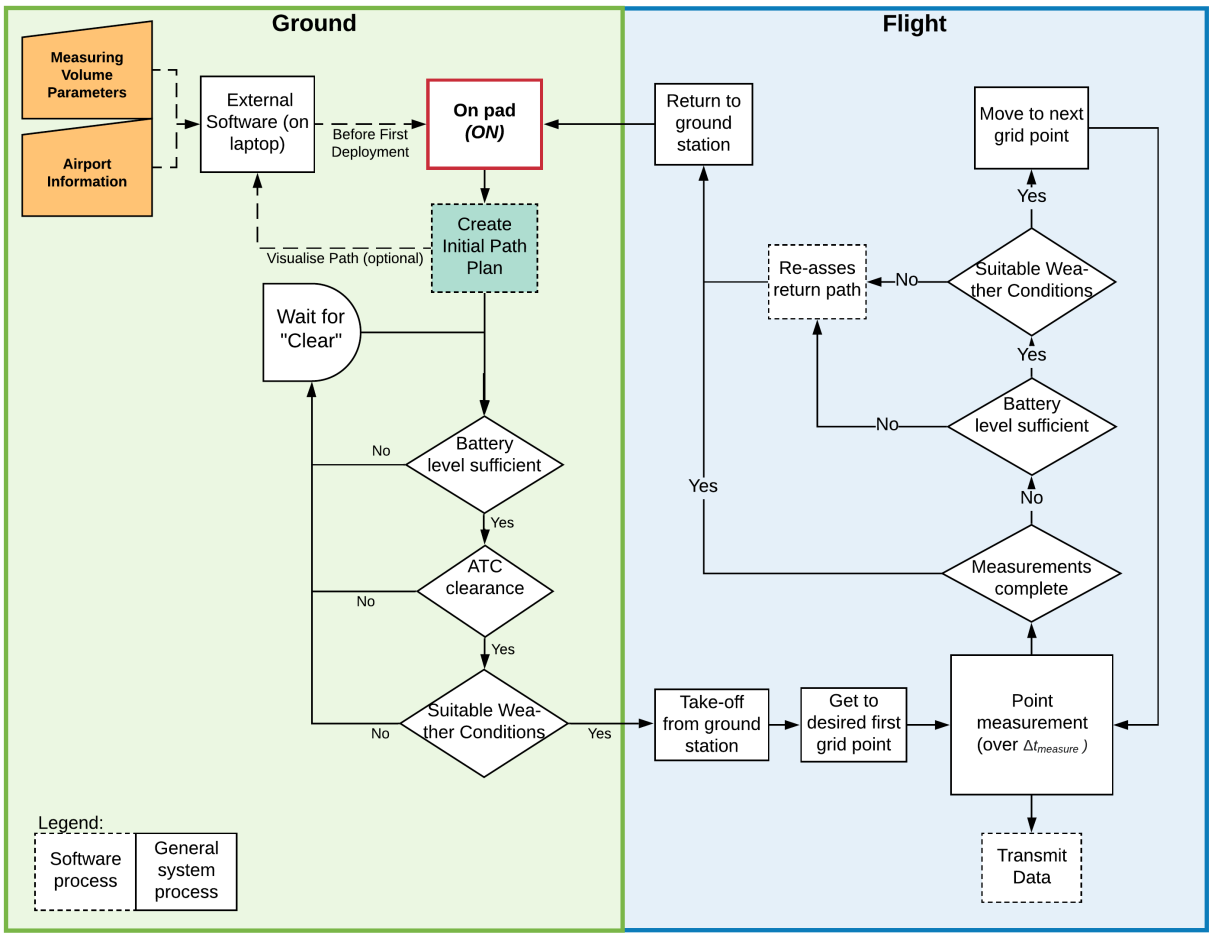

Figure 5.1: Measurement Mission Overview

even number of vertical layers is optimal so the system can measure while returning back to the base. Thus, four layers are opted for because it provides enough vertical resolution even without interpolation, in comparison to two which is not deemed sufficient. Finally, 5 km is selected to include near-airport communities whilst maintaining the smallest region to measure to keep costs, operating time and unwanted data to a minimum. A 5 km distance stems from [43], a report in which an examination of environmental costs near-airports of varying sizes was performed. Whilst these are costs, they deal directly with air quality and noise, explaining that by 5 km, these costs are around 5% of the zero distance estimates [43]. Whilst the author mentions that there are associated errors with the 5 km estimate, a compromise is found, namely, that a measurement volume with 5 km radius is to be designed for with the option of adding more measurement areas at the customer's choice. This could be opted for where certain areas are to be examined for example lack of previous data for a new community or where the airport's perimeter extends beyond 5 km, such as at Schiphol. Figures 5.2 and 5.3 present this approach with Schiphol as a basis airport.

A rectangular mesh is used as it provides an appropriate initial base layer of information with equally spaced distances. It is entirely possible that, before deployment, at many airports, there is little to no information available which means an optimised grid shape can not be found. A note should be made that, after initial deployment, certain areas within these volumes may become of more interest, for example, an area of high air pollution concentrations or high noise levels. Therefore the drone will be able to return to these areas to obtain more data points. The metric details on this are elaborated upon in section 8 and the navigation aspect in 9.2.2.

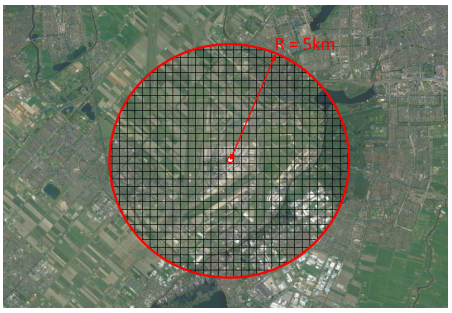

Figure 5.2: Schiphol Measuring Volume - Top View

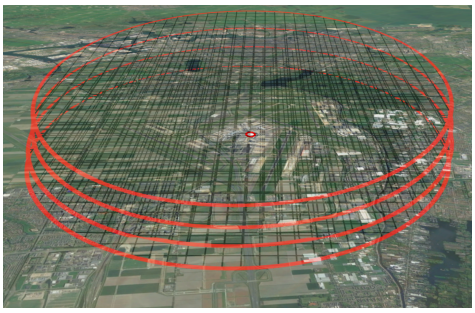

Figure 5.3: Schiphol Measuring Volume - Side View

5.3. Measurement Grid

The grid parameters for the measurement volume are examined in section 5.3.1. Thereafter, the grid variables are evaluated in section 5.3.2. These will be used to determine the final measuring volume.

5.3.1. Grid Parameters

While the mission outline has now been explained, the measurement grid must still be defined in order to determine the number of nodes for the system to cover. The spacing between nodes is required for other subsystems such as for power, performance and aerodynamic aspects (sections 11 and 12) to correctly perform design and sizing. Table 5.1 presents the overview of the parameters needed for the mission definition. Important parameters thereof are elaborated on in more detail below for the limiting case.

Table 5.1: Mission Parameters - set 1

Parameter	Symbol	Value	Unit	Explanation
Minimum Required Data Points	n_{data}	7	-	Number of constants in 3D Guassian plume model distribution in time
Measuring Time	$T_{measure}$	5	s	Balanced time [19]
LTO time length	t_{LTO}	50	s	Limiting case in Europe
Re-fly Number	-	3	-	Worst-case scenario, failed measurement plus complete re-meshing
Drone Cruise Speed	v_{cruise}	10	$m\,s^{-1}$	Average speed from performance [3]
Hovering Time	t_{hover}	7	s	Measuring time +1 second either side for starting and stopping
Total Flight Time	t_{tot}	1800	s	Preliminary estimate from [3]
Number of Layers	-	4	-	Optimum even number for enough resolution (section 5.2)
Radius of Measurement Cylinder	R	5	km	Balance between operational and air and noise aspects (section 5.2)
Operational Time per Day	$t_{op/day}$	18	hrs	Schiphol as a base example with night curfew taken into account + 1h for background

Minimum Required Data Points Determining the measurement grid first involves investigating how long the mission would need to be operative to gather sufficient data (n_{data}) on one aircraft type. Sufficient data is defined as seven node values, which is determined by the number of constants needed for the limiting species or noise equation, namely the Gaussian plume distribution model. More detail can be found on this in section 8. This means for the limiting aircraft type, seven measurements must be taken at different locations to be able to construct useful information. Any number lower is not considered sufficiently accurate. It is also assumed that no data points are recorded at the same location during the operation.

Measuring Time The measuring time ($\Delta t_{measure}$) is set to five seconds. This is based on [19] which presents a set of air quality measurements performed by a quadcopter and then compared to the local sta-

tionary values. The authors observe that the minimum deviation from the local measurements is achieved for measuring while hovering time of around 5 s. Anything less might not be sufficient for all the sensors to converge their output and a longer interval may not result in a value significant for the current node since the environment might have already changed. According to experiment described in [19] the balance is obtained for $\Delta t_{measure} = 5s$.

LTO time length The landing and take-off (t_{LTO}) time length determines how often an aircraft takes-off or lands, which determines the frequency of measurements for each aircraft taking-off or landing. In June 2019, Cirium data shows that there were around 40000 flights to and from London Heathrow, the most congested airport in Europe[1]. This means that within Heathrow's operating hours[2], on average there is an LTO event every 50 seconds. For comparison, Schiphol has about a 10 second longer value.

5.3.2. Measurement Grid Variables

With all fixed parameters defined, this section will present the procedures for calculation of variables and important relations.

Fraction of Active Measuring Time The fraction of active measuring time (f_{AMT}) determines how much time is spent performing measurements gathering data as a fraction of the total operational time of the drone (t_{op}). This corresponds equivalently to equation 5.1, where n_t is the number of nodes traversed, i is the number of each individual flight, ξ is the total number of individual flights, V is the cruise speed and d_f and d_l are the distances between the ground station and the first and last node respectively. The denominator within the fraction corresponds to the summed hovering time, time between nodes and time to and from the set of nodes of each flight respectively. A constant speed is assumed for this analysis to reduce unnecessary complexity. More details can be found in section 12. It should be noted that the higher the spacing, the longer the time between measurements, meaning fewer measurements can be made in the same time.

$$f_{AMT} = \frac{n_t \Delta t_{measure}}{t_{op}} = \sum_{i=1}^{\xi} \frac{n_{t_i} \Delta t_{measure}}{n_{t_i}(\Delta t_{measure} + 2) + \frac{d}{v_{cruise}}(n_{t_i} - 1) + \frac{d_{f_i} + d_{l_i}}{v_{cruise}}} \tag{5.1}$$

Limiting Aircraft Type Frequency All relevant parameters have now been defined. They can be related to each other by means of equation 5.2 where N represents the number of appearances of that limiting aircraft type. The limiting aircraft frequency (F_{lim}) can then be found through division of the total time since the start of operation (T) (equation 5.3).

$$n_{data} = \frac{t_{LTO} f_{AMT}}{\Delta t_{measure}} N \tag{5.2}$$

$$F_{lim} = \frac{N}{T} = \frac{n_{data} \Delta t_{measure}}{t_{LTO} f_{AMT} T} \tag{5.3}$$

5.3.3. Measurement Grid Output

Through the process of iteration as displayed in figure 5.4, the limiting frequency could be found to which a grid spacing and total operational time are associated.

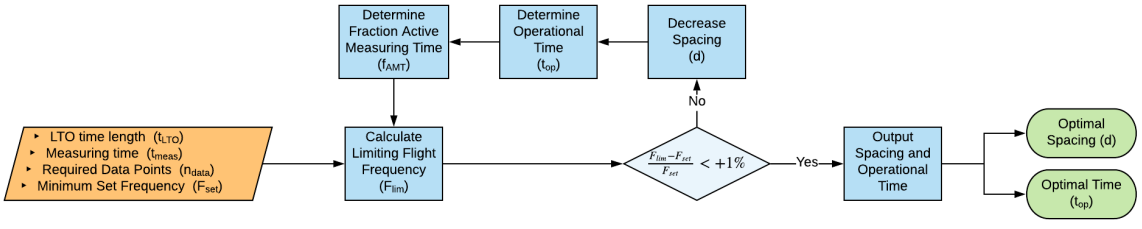

Figure 5.4: Mission Grid Iteration

[1] `https://dashboard.cirium.com/app/profiles/#/airport/airlines/-13001` [cited June 21, 2020]
[2] `https://www.heathrow.com/company/local-community/noise/operations/night-flights` [cited June 10, 2020]

The iteration program makes use of a preliminary navigation planner which performs a simple circular sector outline for its path, such that the drone will make it back to the ground station before the battery levels reach zero. This method is not expected to deviate more than 10% from an optimised path planner which will be described in section 9.2.2. At a later stage, this 10% contingency will be evaluated.

The minimum frequency for relevant aircraft was set to once per week based on requirement *AEMS-F-MMI-01*. Any lower than this would require the customer to work in cooperation for future versions of the product (see chapter 22). This is consistent with airports such as Schiphol's least flown routes. Schiphol currently has 6 currently operating destinations with four scheduled flights per month[3]. This corresponds to about one per week. As each event is being considered an LTO, F_{set} must be set to 2 as the aircraft will fly arrive and then depart again. Table 5.2 presents the new parameters.

Table 5.2: Mission Parameters - set 2

Parameter	Symbol	Value	Unit	Reason
Limiting A/C Frequency	F_{set}	2	1/week	Limiting case at major hubs with reasonable time of operation (*AEMS-F-MMI-01*)
Navigation Contingency	-	90	%	To take optimal path planning into account

This resulted in figures 5.5 and 5.6, where the dashed vertical line corresponds to F_{set}. This corresponds to a total operational time of 23 days. It can be seen that a mesh spacing value of around 150 m is required to reach the limiting frequency. One must stay below the curve in figure 5.6 as the curve is the upper limiting case. Additionally, it was found that f_{AMT} was 31%.

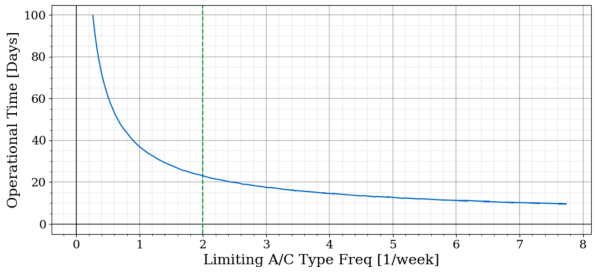

Figure 5.5: Operational Time against Limiting A/C Frequency

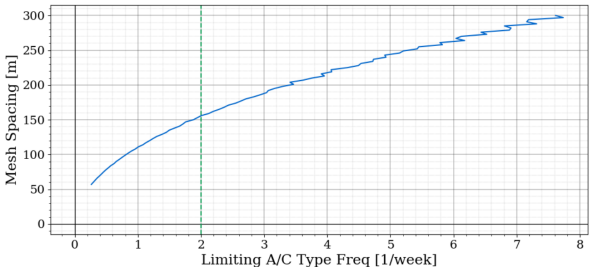

Figure 5.6: Mesh Spacing against Limiting A/C Frequency

A note to be made is that for higher spacing, the results fluctuate more. This is due to the use of a rectangular grid within a circular area, as seen from above. Through increasing of the mesh spacing, eventually some nodes will fall outside the area and therefore not counted. Once the spacing has increased enough, a significant amount of nodes fall away. This repeats frequently in the courser meshes as can be seen in figure 5.6. Finally, it should be noted that with a spacing of $h = 150$ m, there are 13200 nodes. This means that the probability of two data points at the same node during at most three run-throughs would be incredibly small for seven measurement points.

5.4. Verification and Further Use

This section made use of a script able to output operational time and limiting aircraft type frequency. First a rough calculation is made by hand to examine the feasibility of the result. With an intermediate distance to the set of nodes of 2.5 km, the number of nodes that may be measured at is 59, assuming a 150 m spacing. This would require 672 flights resulting in 19 days of operation. This is four hours less than the calculated value in section 5.3.3 which would appear reasonable due to the simplifications used such as the constant use of half of the 5 km radius. Additionally, many unit tests were performed involving the expected trend of results. Examples of these involved checking the output values throughout the node coverage. It could be checked that each flight resulted in a flight time less than t_{tot}. This test was always passed as can be seen in figure 5.7. Secondly, when the drone reaches nodes closer to the ground station, the number of measurable nodes is expected to increase because the distance between the ground station and set of nodes is decreased, thus enabling more time for measurements. This test was also passed with a strong negative

[3] `https://dashboard.cirium.com/app/profiles/#/airport/airlines/-18331` [cited June 21, 2020]

correlation between distance to the set of nodes and the number of nodes measurable. This is shown in figure 5.8. The shapes of both graphs appear from the time limitation per flight which allows for a certain number of nodes to be traversed. Their similarity in patterns confirms this. The lower left data point appears from the last flight where fewer nodes remain traversed than the drone could cover. This results in a shorter flight.

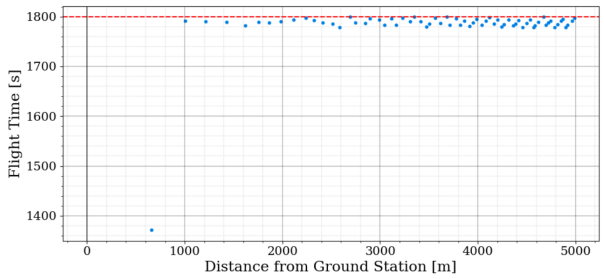

Figure 5.7: Individual Flight Times

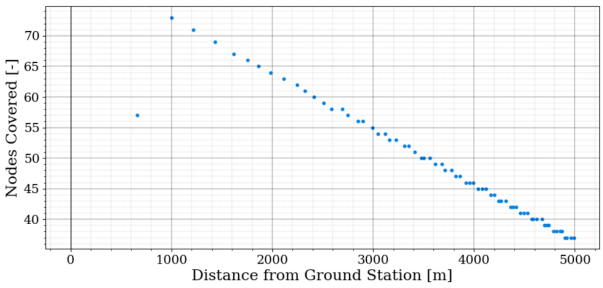

Figure 5.8: Nodes per Individual Flight

Finally, important variables were altered to determine their effect on the optimal spacing and the resulting operational time. This had multiple benefits. It investigated if the equations were logical and input correctly as well as providing useful information for later design or future design iterations as to what changes would affect the measuring volume in what way. The results are presented in table 5.3.

Table 5.3: Parameter Variation Results

Doubled Parameter	**Symbol**	**Operational Days**	**Mesh Spacing**
Data Points	n_{data}	50%	-25%
LTO time	t_{LTO}	-35%	38%
Measuring Time	$t_{measure}$	50%	-25%
Limiting A/C Frequency	F_{set}	-35%	38%
Total flight time	t_{tot}	-25%	negl.

A few notes can be made regarding this outcome. n_{data} has no effect on any variables except F_{lim} which increases as a higher frequency of the aircraft type is required to obtain more data points, thereby increasing F_{lim} for the same mesh spacing (h). The same applies to the measuring time ($\Delta t_{measure}$) and the inverse to LTO time length (t_{LTO}). Increasing F_{set} has the expected outcome of a shift in the dashed horizontal lines in figures 5.5 and 5.6. Importantly all increases in operational time result in a decrease in spacing and vice versa. This is expected from these values (i.e. within equation 5.3) because a finer mesh will require significantly more time to traverse all nodes. Finally, total flight time per individual flight is evaluated to explain that the effect on spacing is negligible so the spacing value may be further used without issues. The operational time does change due to the use of t_{tot} within the time calculations, unlike the previous four terms.

5.5. Compliance of Requirements

The compliance matrix, indicating whether requirements have been met, is presented below.

Measuring Mission Compliance Matrix

Requirement ID.	✓ / o / x	Comment
AEMS-F-MMI-01	✓	Taken into account in section 5.3.3 resulting in spacing and operational time
AEMS-SH-DATA-03	✓	System is to build database as explained in section 5.1
AEMS-SH-PERF-02	✓	Checks on weather conditions are completed (section 5.1)
AEMS-F-REG-08	✓	ATC Clearance must be obtained before launch (section 5.1)

6
Air Pollution Sensing Subsystem

This chapter concerns the air pollution sensing ability of the system (block 3.3.4 in the Functional Flow Diagram which can be found in appendix A). Air pollution sensing is done through commercially available sensors. After the analysis of the requirements for the subsystem in section 6.1, the sensor selection is elucidated in section 6.2. Subsequently, the sensors' operating principles, integration into the system, signal and data processing and calibration are expounded in sections 6.3, 6.4, 6.5 and 6.6, consecutively. Finally, the subsystem's verification and validation and compliance with its requirements are set out in sections 6.7 and 6.8.

6.1. Requirement Analysis

The air pollution sensing subsystem must comply with a number of requirements to ensure expedient functionality of the subsystem within the UAV and the overarching mission. Hereafter, in section 6.1.1, the species to be monitored by the system are listed. Section 6.1.2 explains the accuracy requirements in place for the air pollution measurements. Lastly, the analysis of the expected maximum pollutant concentrations during the mission is elucidated in section 6.1.3. These maximum concentrations define the required measurement range of each air pollution sensor.

6.1.1. Species to Monitor

Whereas the combustion products of aircraft engines mainly consist of CO_2 (72%) and H_2O (27.6%) [28], the residual 0.4% are the species this project addresses. This residual 0.4% of an aircraft engine's exhaust consists of, amongst others, pollutants. As specified in [3], the pollutants to be monitored by the system are methane (CH_4), carbon monoxide (CO), nitrogen monoxide (NO), nitrogen dioxide (NO_2), ozone (O_3), sulphur dioxide (SO_2) and particulate matter. Furthermore, [3] mentioned that the possibility to amend the system with an ultra fine particles (UFP) sensing capability was still being considered. This since the interest in measuring ultra fine particulate matter concentrations is growing as more and more research is conducted into the health hazards of UFP, but no commercially available sole UFP detectors were identified yet. As a commercially available original equipment manufacturer (OEM) for a UFP sensor which fits within the budget for this project is now identified, the drone is amended with a UFP sensing capability. In subsequent sections of this report, NOx (Oxides of Nitrogen) refers to NO and NO_2 as these are the main oxides of nitrogen exhausted by aircraft engines [28]. Furthermore, the number indicated after 'PM' refers to the aerodynamic diameter of the particles in µm, whereas the aerodynamic diameter of a particle is equal to the diameter of a spherical particle, with a density of $1\,g\,cm^{-3}$, which has identical inertial properties in air as the particle of interest [22]. UFP is particulate matter with an aerodynamic diameter less than 0.1 µm. Finally, primary species are the compounds which emerge in a combustion process. Secondary species are the compounds which form through chemical reactions of primary species in ambient air (a process referred to as 'atmospheric chemistry').

6.1.2. Accuracy

The system aims at providing air pollution measurements in compliance with the European Air Quality Directive or EAQD (directive 2008/50/EC of the European Parliament [1]). This directive provides legislation on monitoring and assessment of air quality within the European Union. Annex 1 of this directive indicates data quality objectives for ambient air quality assessment. Objectives are specified for fixed and indicative

[1] https://eur-lex.europa.eu/legal-content/EN/TXT/PDF/?uri=CELEX:02008L0050-20150918&from=EN [cited June 19, 2020]

air quality measurements and air quality assessment through modelling. As this project's system is not a stationary system, the aim is to comply with the data quality objectives for indicative air quality measurements, those being the most limiting objectives applicable. The measurements' corresponding maximum uncertainty values (which differ amongst the species monitored) are indicated in the air pollution sensing subsystem requirements list, secerned by the origin identifier EAQD.

Regarding NOx, two maximum uncertainty values are specified, one corresponding to primary NOx and the other corresponding to secondary NOx. The data quality objectives for primary NOx measurements are more stringent than those for secondary NOx measurement. Therefore, as the drone will encounter both primary and secondary NOx during its mission, the system is to comply with data quality objectives for primary NOx measurements.

Strictly speaking, the data quality objectives for particulate matter measurements apply merely to $PM_{2.5}$ and PM_{10}. However, here, these objectives are applied to measurements of the entire realm of particulate matter, including ultra fine particulate matter.

Finally, no data quality objectives are specified for CH_4 measurements. The chemically most similar species for which objectives are specified in annex 1 of the European Air Quality Directive is benzene. Therefore, the data quality objectives for this species are assumed for CH_4 measurements.

6.1.3. Measurement Range

Electrochemical gas sensors have a measurement range (see section 6.3 for more information on the operating principles of air pollution sensors). The expected maximum air pollutant concentrations the sensors will encounter during the mission should not exceed the sensors' measurement range to ensure optimal functioning of the sensors. Also digital sensors have a maximum pollutant concentration they can handle. Therefore, the expected maximum air pollutant concentrations the sensors will encounter during the mission are approximated to define the (sub)system's required measurement range for each monitored species. In subsequent calculations, exhaust plumes from aircraft engines are considered as main pollution source on airports. This is a conventional assumption according to [28].

Regarding CH_4, CO, NO, NO_2, SO_2 and PM, the expected maximum concentrations are determined through retrieving the maximum emission index (EI) for each species belonging to an aircraft engine which is still operated by an airline which operates the airports identified as the environmental monitoring system's target customers (hereafter referred to as relevant aircraft engine). Emission indices denote the total mass of a species (in g) exhausted by an engine per kg fuel burnt. With these emission indices and the fuel mass flow of the associated engines in the LTO phase corresponding to the one for which the maximum emission index is observed, the emission rate Q in $g s^{-1}$ is calculated for each species (by multiplying the maximum emission indices with the associated fuel mass flow). Subsequently, the emission rates are used in the Gaussian plume model (explained in more detail hereafter) to determine the expected maximum air pollutant concentrations encountered during the mission.

Gaussian Plume Model

According to [11], there are multiple ways to model a plume emitted by a polluting source such as an aircraft engine, a runway or an airport as a whole. These models range from Gaussian plume estimation, Lagrangian stochastic particle simulations, Eulerian advection and dispersion to computational fluid dynamics (CFD) based approaches.

Here, the Gaussian plume model is applied for two reasons. Firstly, it takes into account the following phenomena present in the atmosphere: wind speed, atmospheric stability, the occurrence of temperature inversion, plume temperature, plume initial and exit speed [11]. Secondly, it is a model that can be straightforwardly implemented.

The model's assumptions are listed below together with an explanation of their possible implications for the calculated estimates of pollutant concentrations the sensors will encounter during the mission.

- The emission source is a mathematical point source. This assumption is safe to make considering the dimensions involved in this problem. Those dimensions being an average aircraft engine exit diameter (assumed to be a point source) and a distance of 80 m between the engine and the location at interest for determining the local pollutant concentrations. The 80 m is the closest the drone will

get to an aircraft's engine as explained in section 9.2.1.

- The pollution generation rate is constant. This assumption results in an overestimation or underestimation of the expected pollutant concentrations encountered during the mission depending on whether the species is emitted in higher quantities at high or low thrust settings. This misjudgement occurs as pilots are free to employ lower thrust setting during LTO operations than the thrust settings specified by regulations [28].
- Wind direction and speed are constant in space-time. This does not apply to aircraft in LTO. However, in subsequent calculations the wind is assumed to blow air pollutants directly at the UAV, resulting in a conservative estimation of encountered air pollution concentrations.
- Atmospheric turbulence is constant in space and time. The impact of this assumption is accounted for in the choice of dispersion coefficients which will be expounded later on in this section.

Considering the above assumptions results in the Gaussian plume model (equation 6.1):

$$C_{species} = \frac{Q}{2\pi u \sigma_y \sigma_z} \exp\left(-\frac{1}{2}\frac{y^2}{\sigma_y^2}\right) \exp\left[-\frac{1}{2}\frac{(z-h)^2}{\sigma_z^2}\right] \tag{6.1}$$

With $C_{species}$ the species concentration at a given point in space, Q the point-source emission rate, u the local wind speed, σ_z and σ_y the vertical and lateral dispersion coefficients (consecutively), x the longitudinal coordinate to the plume's axis (which is incorporated in the dispersion coefficients), y the lateral coordinate to the plume's axis, z the height above ground-level and h the height of the emission source above ground-level.

According to [4], a wind speed of $12\,\mathrm{m\,s^{-1}}$ gives rise to the furthest reaching (and slimmest) plume with approximately constant pollutant concentrations whereas a wind speeds above $12\,\mathrm{m\,s^{-1}}$ only increase dilution. Therefore, in subsequent calculations, a local wind speed u of $12\,\mathrm{m\,s^{-1}}$ is used.

The dispersion coefficients can be defined by introducing stability classes which, according to [11], depend on the local environment and the weather. In [11], multiple semi-empirical formulae are collected to estimate the dispersion coefficients. Here, the following Briggs parameterisations are used for the dispersion parameters σ_y (equation 6.2) and σ_z (equation 6.3), corresponding to atmospheric stability classification D (a neutral atmosphere) which applies to conditions in which the wind speed is higher than $6\,\mathrm{m\,s^{-1}}$ at days other than 'clear summer days with the sun higher than 60° above the horizon' [11]:

$$\sigma_y = 0.08x(1+0.0001x)^{-0.5} \tag{6.2}$$

$$\sigma_z = 0.06x(1+0.0015x)^{-0.5} \tag{6.3}$$

As mentioned before, the longitudinal distance x is set to 80 m. y, z and h are set to 0. Setting these parameters as such results in the highest pollutants concentrations to be expected during the mission. This is desirable as the sensor selection is based on these calculations. As Alphasense's sensors that measure the same species optimally within different concentration ranges have approximately the same mass, volume and cost, preferably, an overestimate of expected pollutant concentrations is assumed such that the selected sensors function in any condition encountered during the mission, including lower pollutant concentrations, thereby further preventing risk *PL2* and *PL1*.

Determination of Emission Rates

To retrieve the emission rate of CO, aircraft engine data in EASA's ICAO Aircraft Emissions Databank[2] is used. For the emission rate of CH_4, the maximum EI (belonging to a relevant aircraft engine) and associated fuel mass flow for hydrocarbons in EASA's ICAO Aircraft Emissions Databank is utilised. This as CH_4 is to be labelled as the primary species belonging to the hydrocarbons present in combustion engine exhausts according to [1].

In EASA's ICAO Aircraft Emissions Databank, an EI is only stated for NOx, not for NO and NO_2 separately. However, using the results from [44] separate emission rates for NO and NO_2 can be retrieved. The authors

[2] `https://www.easa.europa.eu/domains/environment/icao-aircraft-engine-emissions-databank` [cited June 22, 2020]

of [44] found a NO_2/NOx ratio of 80% for modern aircraft engines at idle operation. This ratio is found to be 7% when engines operate at their highest power setting (observed during take-off). Thus, the maximum emission rate Q for NOx at idle thrust settings ($Q_{\text{NOx, max, idle}}$) and the maximum emission rate for NOx at take-off thrust settings ($Q_{\text{NOx, max, TO}}$) are determined from EASA's ICAO Aircraft Engine Emissions Databank (belonging to a relevant aircraft engine). Subsequently, $0.80 \cdot Q_{\text{NOx, max, idle}}$ and $0.07 \cdot Q_{\text{NOx, max, TO}}$ are compared and the highest value is used in the Gaussian plume model to estimate encountered NO_2 during the mission. Then, $0.20 \cdot Q_{\text{NOx, max, idle}}$ (100% - 80% = 20%) and $0.93 \cdot Q_{\text{NOx, max, TO}}$ (100% - 7% = 93%) are compared and the highest value is used in the Gaussian plume model to estimate encountered NO during the mission.

Furthermore, no emission indices are stated for PM in EASA's ICAO Aircraft Emissions Databank. However, according to [25], the EI for $PM_{2.5}$ can be approximated as 60% of the smoke number (SN) which is tabulated in EASA's ICAO Aircraft Emissions Databank. Therefore, the emission rates of $PM_{2.5}$ and PM_{10} are found by applying 60% and 40%, subsequently, to the maximum SN (belonging to a relevant aircraft) times the associated fuel mass flow. The maximum emission rate of SO_2 is taken from [28] ($1.3\,\text{g}\,\text{s}^{-1}$).

Maximum Concentration Estimates O_3 and UFP

Then, for O_3 and UFP, no emission rates are available. In case of O_3 since it is a secondary species, in case of UFP since no certification requirements are yet in place regarding an engine's UFP emissions. Therefore, the maximum O_3 and UFP concentrations to be expected during the mission are taken from reference Air Quality Monitoring Stations near Amsterdam Airport Schiphol (reference AQMSs, where 'reference' refers to the classification set by the European Air Quality Directive). Through the Luchtmeetnet 2020 OpenAPI system[3] hourly pollutant measurements are collected from the three AQMSs closest to Schiphol dating from January 1, 2014 to December 31, 2019 (as the measurements taken in 2020 are not yet validated). These three AQMSs are Hoofddorp-Hoofdweg, Badhoevedorp-Sloterweg and Oude Meer-Aalsmeerderdijk. They measure CO, NO, NO_2, O_3 (till July 23, 2017 only), $PM_{2.5}$, PM_{10} and UFP (between July 2017 and March 2018 only), whereas CO and $PM_{2.5}$ are only monitored by station Badhoevedorp-Sloterweg and O_3 is only monitored by station Hoofddorp-Hoofdweg. The data is analysed (ouliers are removed by applying a z-score of 4) and plotted in box plots, see figure 6.1 for an example. The maximum O_3 and UFP concentration found in the resulting data set are selected as expected maximum O_3 and UFP concentration encountered during the mission.

Safety Margin

Finally, as the calculations above do not consider plume mixing (from multiple aircraft engines), atmospheric chemistry and added pollutant concentrations from other on-airport pollution sources, e.g. auxiliary power units (APUs) and airport ground service equipment (GSE), a safety margin of 100% is applied to the expected maximum pollutant concentrations calculated before. The resulting maximum pollutant concentrations are indicated in the air pollution sensing subsystem requirements list, secerned by the origin identifier EMPC (expected maximum pollutant concentration).

Air Pollution Sensing Subsystem Requirements

AEMS-F-SENS-AIR-01	The air pollution sensors shall have a response time (t_{90}) of less than 40 s in any mission condition [AEMS-F-DPR-01]
AEMS-F-SENS-AIR-02	The system shall be able to measure background air pollution levels [AEMS-SH-DATA-05]
AEMS-F-SENS-AIR-17	The system shall measure CH_4 concentrations with a maximum uncertainty of 30% [EAQD]
AEMS-F-SENS-AIR-14	The system shall measure CH_4 concentrations within the range 0 to 34 ppm [EMPC]
AEMS-F-SENS-AIR-18	The system shall measure CO concentrations with a maximum uncertainty of 25% [EAQD]

[3] `https://api-docs.luchtmeetnet.nl/?version=latest` [cited June 22, 2020]

AEMS-F-SENS-AIR-04	The system shall measure CO concentrations within the range 0 to 22 ppm [EMPC]
AEMS-F-SENS-AIR-19	The system shall measure NO concentrations with a maximum uncertainty of 25% [EAQD]
AEMS-F-SENS-AIR-09	The system shall measure NO concentrations within the range 0 to 156 ppm [EMPC]
AEMS-F-SENS-AIR-20	The system shall measure NO_2 concentrations with a maximum uncertainty of 25% [EAQD]
AEMS-F-SENS-AIR-07	The system shall measure NO_2 concentrations within the range 0 to 8 ppm [EMPC]
AEMS-F-SENS-AIR-21	The system shall measure O_3 concentrations with a maximum uncertainty of 30% [EAQD]
AEMS-F-SENS-AIR-10	The system shall measure O_3 concentrations within the range of 0 to 1 ppm [EMPC]
AEMS-F-SENS-AIR-22	The system shall measure SO_2 concentrations with a maximum uncertainty of 25% [EAQD]
AEMS-F-SENS-AIR-12	The system shall measure SO_2 concentrations within the range 0 to 1 ppm [EMPC]
AEMS-F-SENS-AIR-23	The system shall measure particulate matter with an aerodynamic diameter of 10 µm [6.1.1]
AEMS-F-SENS-AIR-24	The system shall measure PM_{10} concentrations with a maximum uncertainty of 50% [EAQD]
AEMS-F-SENS-AIR-25	The system shall measure PM_{10} concentrations within the range 0 to 0.000 684 $g\,m^{-3}$ [EMPC]
AEMS-F-SENS-AIR-26	The system shall measure particulate matter with an aerodynamic diameter of 2.5 µm [6.1.1]
AEMS-F-SENS-AIR-27	The system shall measure $PM_{2.5}$ concentrations with a maximum uncertainty of 50% [EAQD]
AEMS-F-SENS-AIR-28	The system shall measure $PM_{2.5}$ concentrations within the range 0 to 0.000 342 $g\,m^{-3}$ [EMPC]
AEMS-F-SENS-AIR-29	The system shall measure particulate matter with an aerodynamic diameter of 0.1 µm [6.1.1]
AEMS-F-SENS-AIR-30	The system shall measure UFP concentrations with a maximum uncertainty of 50% [EAQD]
AEMS-F-SENS-AIR-31	The system shall measure UFP concentrations within the range 0 to 0.6735 particles m^{-3} [EMPC]
AEMS-F-SENS-AIR-32	The system shall have at least one back-up measuring instrument for each monitored air pollutant [AEMS-SYS-05, Risk PL1]
AEMS-F-SENS-AIR-33	The system shall incorporate changeable air pollution sensors [AEMS-SYS-SUST-05]
AEMS-F-SENS-AIR-34	The air pollution sensing subsystem shall not incorporate potentially explosive substances or compounds [AEMS-SYS-SUST-09]

Regarding AEMS-F-SENS-AIR-01, this requirements has been articulated to limit the system's delay in observing a pollutant's concentration after it occurred. Although the encountered gradient in pollutant concentrations will likely be close to 0 during the majority of the mission, in extreme conditions (when air pollutant concentrations change substantially and rapidly) the encountered concentration gradient may deviate substantially from 0. In these instances, the electrochemical air pollution sensors (measuring CH_4,

CO, NO, NO_2, O_3 and SO_2) may need tens of seconds to come to a stable response. By specifying a sensor's maximum response time (the time the sensor requires to reach 90% of a stable response when the pollutant's concentration changes near-instantly from 0 ppm to a certain positive concentration), a limit is set to the time the system has to hover in one location for the air pollution sensor to output a stable response may the UAV find itself in a rapidly (and substantially) changing pollutant concentration.

6.2. Sensor Selection

With all requirements in place, commercially available air pollution sensors can be selected that fit the system's needs. The company Alphasense[4] is chosen to be the supplier of air pollution sensors as Alphasense provides its clientele with a high degree of customisation of air pollution sensing technologies when requested. Moreover, using sensors from one manufacturer only is expected to ease system integration. Finally, Alphasense is located relatively close to the headquarters of this project, Alphasense being located in Essex, the United Kingdom whereas this project's team is located in Delft, the Netherlands. This relative positioning is expected to influence shipping operations favourably, both from a continuity of the system's operations and sustainability viewpoint.

Regarding Alphasense's sensors measuring CO, NO, NO_2, O_3 and SO_2, the eventually selected sensors comply with the requirements specifying the system's required measurement range for each species, requirement AEMS-F-SENS-AIR-01 (The air pollution sensors shall have a response time (t_{90}) of less than 40 s in any mission condition), and has a measurement uncertainty closest to 0 in case multiple sensors comply with the requirements mentioned before. In case of Alphasense's CO sensors, six sensors comply with requirements AEMS-F-SENS-AIR-04 (The system shall measure CO concentrations within the range 0 to 22 ppm and AEMS-F-SENS-AIR-01 and have an equal measurement uncertainty. Here, the sensor with the highest filter capacity is selected to avoid cross-sensitivity issues, a phenomenon explained in more detail in section 6.6 (Alphasense's CO sensors are cross-sensitive to H_2S, NO, NO_2 and SO_2).

Regarding Alphasense's CH_4 sensors, a pellistor (see section 6.3) is chosen over an infrared sensor as infrared sensors require a ±30 minutes warm-up time after each interruption of power supply. This would complicate the system's operations substantially. The two pellistors Alphasense retails, CH-D3 and CH-A3, perform equally. However, the D-series is lighter giving rise to the choice of CH-D3 over CH-A3.

Then, the OPC-N3 has been selected to provide the system with a PM sensing capability as this sensor is Alphasense's most advanced particulate matter sensor. It detects particles with an aerodynamic diameter of 0.35 to 40 µm. Finally, the Naneos Advanced Partector will provide the system with a UFP sensing capability as this is the only identified commercially available OEM which fits within the budget for this project. It detects particles with an aerodynamic diameter of 0.02 to 0.2 µm.

An overview of the specifications of the selected air pollution sensors for use on the UAV can be found in table 6.1. No response time is tabulated for the OPC-N3 and Naneos AP (measuring PM and UFP, respectively) as these sensors are digital sensors. Thus, they do not have a response time. However, they do have a time resolution of up to 1 s. Other open entries in table 6.1 are not specified by the corresponding sensor manufacturer. To conform to requirement AEMS-F-SENS-AIR-32, the drone will employ a duplicate of every selected air pollution sensor apart from the Naneos AP. This as the budget for the system's hardware does not allow for the inclusion of a second UFP sensor. As can be concluded from table 6.1, the selected air pollution sensors pose a very lenient requirement on the minimum humidity (15% rh) in which the system can operate. This can be seen as compliant with requirement *AEMS-SH-PERF-03*.

6.3. Operating Principles Selected Sensors

The CH-D3, CO-CX, NO-B1, NO2-D4, O3-B4 and SO2-A4 are electrochemical sensors. This means that, through a chemical reaction within the sensor, these sensors transform concentrations of the monitored gas to a current proportional to the concentration of the gas. Electrochemical sensors encompass two to four electrodes. A sensing and a counter electrode are always employed. The sensing electrode catalyses a reaction specific to the monitored gas, which results in a potential within the sensor. The counter electrode revokes the resulting potential within the sensor and thus forms the origin of current flow to a signal analysis device (here, the UAV's main processor which is elucidated in more detail in chapter 13).

[4] `http://www.alphasense.com/` [cited June 21, 2020]

By drawing current from an external source, an electrochemical sensor can restore the compounds required for the reaction at the sensing electrode to take place. However, when a sensor finds itself in a concentration exceeding its overload, these required compounds are used up before the current from the battery can reestablish them and the sensor may get irreversibly damaged. Generally, a sensor's overload is at least an order of magnitude higher than the sensor's measurement range, whereas the sensor's measurement range corresponds to the range of concentrations to which the sensor responds with a linearity above a certain threshold. Thus, exceeding a sensor's measurement range does not permanently damage the sensor. Nonetheless, it does result in faulty readings and extended recovery times.[5]

A third electrode, the reference electrode, may be introduced to augment the sensor's measurement range by eliminating the polarisation effect of the counter electrode[6]. Alphasense employs even a fourth electrode, the auxiliary electrode. This electrode allows a sensor to maintain its accuracy in accuracy-comprising conditions such as occurrences of temperature, pressure and humidity changes or a compound to which the sensor is cross-sensitive (a phenomenon which will be explained in more detail in section 6.6).

The CH-D3 is a pellistor which is a flammable gas sensor. It operates slightly different from the other electrochemical gas sensors. A pellistor comprises a Wheatstone bridge circuit, and thus includes two beads. The active bead is treated with a catalyst, which lowers the ignition temperature of the monitored gas. The combustion of the flammable gas (here, CH_4) warms up the bead which alters the bead's resistance. The difference in resistance between the active and the reference bead is then observed and a gas concentration is associated with it as the difference in resistance is linearly proportional to the concentration of the monitored gas.

Regarding pellistors, an important performance impairment may occur due to incomplete combustion. As pellistors require flameproof and certified housing for safe use of the sensor, conditions may be created within the sensor in which complete combustion is inhibited. Incomplete combustion results in a layer of soot covering the the active bead. This reduces the bead's ability to ignite the flammable gas.[7]

The OPC-N3 is an optical particle counter (OPC) which determines the number of particles passing through its detection chamber based on the scattering of light (from an internal light source) the particles cause. The scattering is assessed through collecting the scattered photons with a photo detector. The particle numbers are subsequently tabulated into counting bins which represent antecedently defined aerodynamic diameter ranges. [8]

The Naneos AP is a condensation particle counter (CPC) which essentially extents the technology from an optical particle counter. In a CPC, particles pass through a chamber in which the air is saturated with a condensable working fluid. Either n-butyl alcohol or water can be employed as working fluid, whereas the Naneos AP employs water. Subsequently, the particles and saturated air enter a condensing chamber in which the supersaturated vapour condenses on the surface of the particles. Through this process the particles grow in size such that they can be detected by a regular particulate matter counter, e.g. an OPC [42].

The electromechanical sensors contain chemical components that are used for the chemical reaction at the sensing electrode to happen. According to [38], these might be harmful to the environment once the sensors are disposed. The degradation rate of all Alphasense sensors is similar, so, to comply to sustainability strategy D4S, another sensor cannot simply be selected. However, the sensors' adverse environmental impact (and thus the sensors' sustainability) can be mitigated by shielding the sensors from the environment. This is realised as the sensors are placed within the payload box of the UAV. See chapter 10 for the structural design of the UAV.

[5] https://www.environics.fi/wp-content/uploads/2014/06/ap-109-getting-the-most-from-toxic-gas-sensors-2014-02-05.pdf [cited June 21, 2020]

[6] https://www.citytech.com/en-gb/loader/frame_loader.asp?page=https://www.citytech.com/en-gb/technology/toxic-sensors.asp [cited June 21, 2020]

[7] http://www.nenvitech.com/catalytic-sensor/ [cited June 21, 2020]

[8] http://www.alphasense.com/WEB1213/wp-content/uploads/2019/03/OPC-N3.pdf [cited June 20, 2020]

6.4. System Integration

As the sensor selection is completed, the next step to take is integrating them. Firstly, the supporting electronics are described in section 6.4.1. Subsequently, other supporting hardware is addressed in sections 6.4.2 and 6.4.3.

6.4.1. Supporting Electronics

Apart from the OPC-N3 and Naneos AP, all selected sensors output an analogue signal and must therefore be connected via specific analogue inputs on the processor board. The OPC-N3 and Naneos AP can more straightforwardly be connected via the common digital inputs on the processor board. The processor board is described in more detail in chapter 13.

To ensure stability of the main processor, the pins from the sensors will be connected to a separate logical board. This board will convert the analogue signals to a discretised digital signal. For this, a lightweight off-the-shelf logical board is chosen, namely the Arduino Micro. The Arduino Micro connects to the main processor through a single USB cable.

6.4.2. Supporting Hardware

All selected sensors are required to be placed in flowing air, albeit flowing air at different flow rates for certain air pollution sensors. Seven fans ensure the required airflow rate to the sensors, whereas the OPC-N3 sensors have build-in fans and thus provide the required airflow themselves. The chosen off-the-shelf fan is the 514 F DC axial compact fan of ebm-papst [9]. Six of the seven fans comprise the bottom of the two gas sensor boxes and the placing of the seventh fan will be explained in 10.1.1.

The gas sensor boxes mentioned above protect the CH_4, CO, NO, NO_2, O_3 and SO_2 sensors against mechanical impacts. Furthermore, they aid in providing the gas sensors the appropriate flow. This as the CO-CX (sensor measuring CO concentrations) filters H_2S, NO_2, NO and SO_2 from the ambient air. Since the system monitors NO_2, NO and SO_2 as well, flow that is filtered by the CO-CX sensor should not flow past the NO_2, NO and SO_2 sensors to avoid faulty measurements, thereby further preventing risk *PL1*. For this reason, a division wall is installed between the CO-CX and the other sensors in the gas sensor box, see figure 6.2.

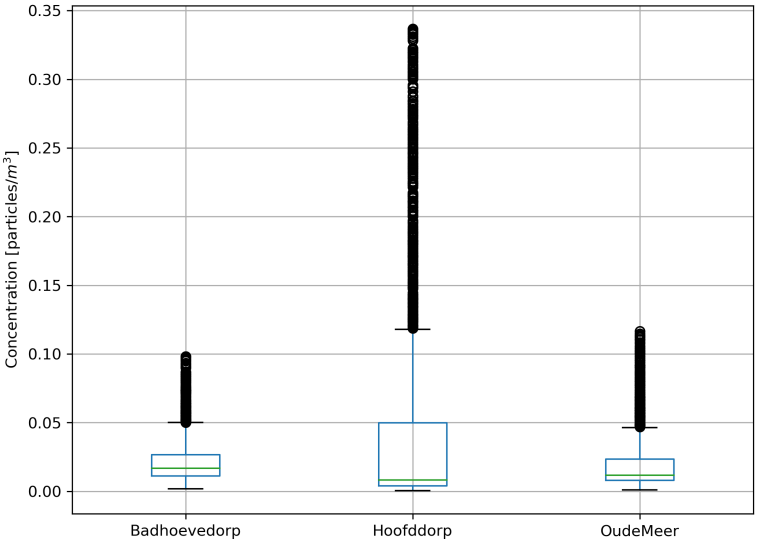

Figure 6.1: Ultra fine particle concentrations shown for the three reference AQMSs near Schiphol

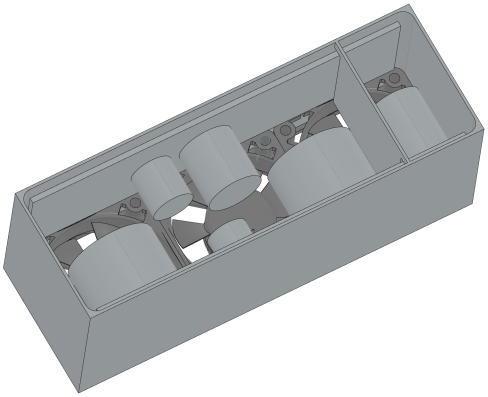

Figure 6.2: Layout Gas Sensor Box. From left to right: NO-B1, CH-D3, NO2-D4, SO2-A4, O3-B4, CO-CX

The sensors in figure 6.2 are attached to a PCB which can be taken out of the sensor box to ease maintenance operations. The placing of the Naneos AP and the two OPC-N3s within the UAV will be clarified in 10.1.1.

[9] `https://www.ebmpapst.com/en/products/compact-fans/axial-compact-fans/axial_compact_fans_detail.php?pID=53763` [cited June 18, 2020]

6.4.3. Boom Design

Finally, as the flow around the drone will be affected by the rotating propellers, lower pollutant concentrations will be recorded when measuring in the disturbed flow compared to concentrations measured outside the local air disturbance [41]. To account for this effect, a boom will be employed on the drone which essentially shifts the sensors' inlet outside the local air disturbance. As a CFD investigation to simulate the local air disturbance would be too resource-intensive to implement, the conclusions reached by [41] are used to size the boom.

According to [41], accurate measurements are obtained when the air is sampled at a vertical distance larger than 0.8 m above the drone (or from the side, at least 1.2 m from the centre of the UAV. Accordingly, a boom structure is implemented on the drone which leads undisturbed air from 0.8 m above the UAV into the payload box. The boom is removable from the structure to ease transportation operations.

6.5. Signal and Data Processing

As explained in section 6.3, the electrochemical sensors generate an analogue signal. These signals are transmitted to the GPIO (general purpose input-output) pins of the Arduino Micro. Subsequently, the Arduino Micro samples the signal to get a concentration array in time $C_{species}(t)$ and thereby converts the analogue signal to a digital signal. To reduce the signal noise, the signal is converted to the frequency domain, a low-pass filter is applied, and subsequently, the filtered signal is converted back to the time domain. This is done using a standard python library such as SciPy.

The unfiltered concentration array is saved in the on-board storage of the UAV (as Python dictionary or a similar data structure). This data is uploaded to the cloud and can be accessed through a software interface upon approval of the operator. More information on this can be found in chapter 13.

For use in the metric which will be explained in further detail in chapter 8, the maximum value recorded during $\delta t_{measure}$ in the filtered concentration array is stored. Since identical sensors record a maximum each, the main on-board processor collects the two values, compares them and calculates their average (if both sensors are still functional and thus two values are available). Then, a label corresponding to the grid location is added to the average (or single available value) and the concentration value is included into the metric list. If the two values are different by more than the sensors' maximum uncertainty (set by the European Air Quality Directive), an exception flag is also reported. This process is applied to the signals corresponding all species measured through analogue sensors (CH_4, CO, NO, NO_2, O_3 and SO_2).

Onto the digital particulate matter sensors, at each grid location, the OPC-N3 reports a concentration histogram (in particles s^{-1}) for 24 particle diameter ranges. The first range being 0.35 to 1 µm, the second 1 to 2 µm, the third 2 to 3 µm, the fourth 3 to 4 µm, the fifth 4 to 5.8 µm after which each subsequent range encompasses 1.8 µm. At each grid point, the microprocessor will save the histogram to the on-board storage together with the associated particle size range (as Python dictionary or a similar data structure). This data is uploaded to the cloud and can again be accessed through a software interface upon approval of the operator.

To ensure a standardised output of the system which is easily interpretable by any user, the stored PM concentrations are integrated over the particle sizes and two values are stored per (functional) OPC-N3 sensor, those being a $PM_{2.5}$ concentration (PM0.35 to PM3) and a PM_{10} concentration (PM3 to PM40). The values from both OPC-N3 sensors are compared and the average values are calculated (if both sensors are still functional). May the two values be available and they differ by more than 50% (the sensors' maximum uncertainty set by the European Air Quality Directive) an exception flag is reported as well. Again, a label corresponding to the grid location is added to the averages (or single available values) and the concentration values are included into the metric list.

The Naneos AP outputs a Python dictionary (or similar data structure) with the particle count (in particles s^{-1}), the average particle diameter (in nm) and the lung-deposited surface area (LDSA) at each grid location. Again, the microprocessor will save this data to the on-board storage. It is uploaded to the cloud and can be accessed through a software interface upon approval of the operator. From the dictionary (or similar data structure), the particle count is selected, a label corresponding to the grid location is added to it and the value is subsequently sent to the metric (see chapter 8). The aforementioned steps are visually represented in figure 6.3, whereas the signals from the OPC-N3s and Naneos AP skip block 2 and 3 as they output a

filtered digital signal right away.

May multiple flags occur in a certain time frame, this is an indication the sensors are failing to report accurate data. The drone's software is programmed such that the drone warns the operator in these instances and returns to base for inspection, thereby further preventing risk *PL1*. May the processor more than once not receive a value from any of the sensors, the operator is warned as well and the drone returns to base for maintenance, thereby further mitigating risk *PL2*. More detail on the system's services can be found in chapter 17.

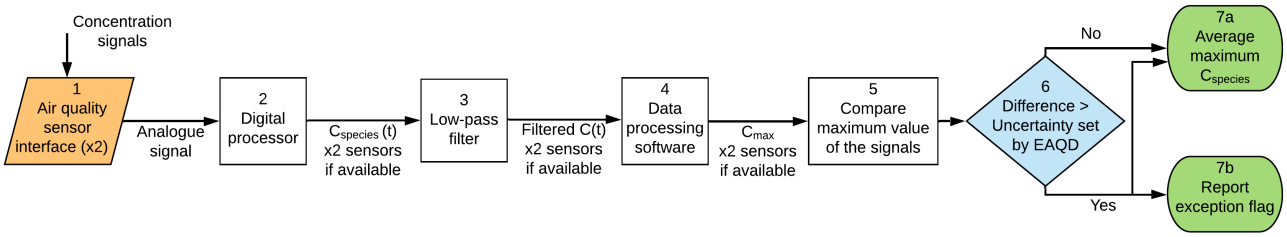

Figure 6.3: Software diagram for air pollution data processing

6.6. Calibration

Whereas all sensors are calibrated by their manufacturer, their measurement uncertainty is comprised during operation as well. This through, for example, temperature changes, pressure changes, humidity changes and, in case of the electrochemical sensors, being sensitive to other species other than the species intended to be measured by the sensor (a phenomenon called cross-sensitivity). Also other phenomena such as zero-drift and sensitivity drift comprise the sensors' measurement uncertainty. Therefore, the signals from all air pollution sensors are calibrated continuously, thereby further preventing risk *PL1*. The calibration is done digitally by the main on-board processor, using the specifications provided by the sensors' manufacturers. For this, measurements will be used taken by the OPC-N3's on-board humidity and pressure sensor, the Pixhawk's pressure sensor (barometer) as well as measurements taken by other sensors than the sensor of which the cross-sensitivity is being corrected.

6.7. Verification and Validation

To verify the code implementation of the Gaussian plume model, unit tests are conducted by calculating the expected concentrations based on a given set of parameters and comparing them to hand calculations. Further unit tests include the implementation of the box model to simulate the dispersion of air pollutants. The box model does not account for turbulence of the air, whereas the Gaussian plume model does. Thus, the box model should render higher expected maximum pollutant concentrations during the mission compared to the Gaussian plume model. If this is not the case, concluded can be that the Gaussian plume model is implemented incorrectly. This verification check is applied and the code is found to pass the check.

The logic behind the calculations estimating the maximum pollutant concentrations encountered during the mission is validated by comparing the estimates with the maximum concentrations measured by one of the three reference Air Quality Monitoring Stations near Schiphol. The logic here refers to the assumption that pollutant concentrations are highest closest to an aircraft engine. However, atmospheric chemistry and the presence of other pollution sources on airports may give rise to the invalidity of this assumption. For all species monitored by the reference AQMSs and estimated through the Gaussian plume model (CO, NO, NO_2, $PM_{2.5}$ and PM_{10}) the measured maximum concentration (after filtering the outliers from the data by applying a z-score of 4) is found to be lower than the estimated maximum concentrations encountered during the mission. Therefore, the logic behind the calculations estimating the maximum pollutant concentrations encountered during the mission is deemed valid.

The system's measurements of ambient air pollutants are validated by operating the system at the location of reference Air Quality Monitoring Station Badhoevedorp-Sloterweg and comparing the system's measurements against the measurements of the AQMS available in real-time through the station's API. As this station does not (or in case of UFP, no longer) measure CH_4, O_3, SO_2 and UFP, the system's measurements with regards to these species must be compared to measurements taken by a reference AQMS that does monitor

these species.

6.8. Compliance of Requirements

As requirements were presented at the beginning of this chapter, the following compliance matrix summarises the now designed subsystem's compliance with the given requirements.

Air Quality Measuring Subsystem Compliance Matrix

Requirement ID.	✓ / o / x	Comment
AEMS-F-SENS-AIR-01	✓	See table 6.1
AEMS-F-SENS-AIR-02	✓	All sensors have a measurement range starting from 0 (see table 6.1).
AEMS-F-SENS-AIR-17	✓	See table 6.1
AEMS-F-SENS-AIR-14	✓	See table 6.1
AEMS-F-SENS-AIR-18	✓	See table 6.1
AEMS-F-SENS-AIR-04	✓	See table 6.1
AEMS-F-SENS-AIR-19	✓	See table 6.1
AEMS-F-SENS-AIR-09	✓	See table 6.1
AEMS-F-SENS-AIR-20	✓	See table 6.1
AEMS-F-SENS-AIR-07	✓	See table 6.1
AEMS-F-SENS-AIR-21	✓	See table 6.1
AEMS-F-SENS-AIR-10	✓	See table 6.1
AEMS-F-SENS-AIR-22	✓	See table 6.1
AEMS-F-SENS-AIR-12	✓	See table 6.1
AEMS-F-SENS-AIR-23	✓	See section 6.2
AEMS-F-SENS-AIR-24	✓	See table 6.1
AEMS-F-SENS-AIR-25	✓	See table 6.1
AEMS-F-SENS-AIR-26	✓	See section 6.2
AEMS-F-SENS-AIR-27	✓	See table 6.1
AEMS-F-SENS-AIR-28	✓	See table 6.1
AEMS-F-SENS-AIR-29	✓	See section 6.2
AEMS-F-SENS-AIR-30	✓	See table 6.1
AEMS-F-SENS-AIR-31	✓	See table 6.1
AEMS-F-SENS-AIR-32	o	Not feasible for the Naneos AP (UFP sensor) due to its price. Met with regards to all other air pollution sensors (see section 6.2).
AEMS-F-SENS-AIR-33	✓	See section 6.4.2
AEMS-F-SENS-AIR-34	o	The CH-D3 (methane sensor) does incorporate potentially explosive compounds but is IECEx certified by Sira [a].
AEMS-SH-PERF-03	✓	Table 6.1 shows a minimum rh of 15%.

[i] https://www.csagroupuk.org/about/sira-certification-our-recent-rebrand/ [cited June 22, 2020]

Table 6.1: Specifications Selected Air Pollution Sensors

Model	Pollutant	Measurement Range [ppm]	Initial Uncertainty [%]	Response Time t_{90} [s]	Max. Power Usage [mW]	Mass [g]	Dimensions [mm] (width ×length ×height)	Minimum Operation Temperature [°C]	Maximum Operation Temperature [°C]	Minimum Operation Pressure [kPa]	Maximum Operation Pressure [kPa]	Minimum Humidity [% rh continuous]	Maximum Humidity [% rh continuous]	Operating Life [months]	Warranty [months]	Price [€2020]
CH-D3[10]	CH_4	50 000	5	< 12	190	10	⌀15.3 ×15.7	-40	50	-	-	-	-	24	24	110
CO-CX[11]	CO	2 000	2	< 40	1.25	8	⌀20.2 ×27.5	-30	50	80	120	15	90	24	24	180
NO-B1[12]	NO	250	10	< 30	0.806	13	⌀32.3 ×19.9	-30	50	80	120	15	90	24	24	150
NO2-D4[13]	NO_2	20	3	< 35	0.047	2	⌀14.5 ×12.3	-20	50	80	120	15	90	24	24	150
O3-B4[14]	O_3	5	4	< 15	0.024	13	⌀32.3 ×19.9	-20	50	80	120	15	85	18	12	225
SO2-A4[15]	SO_2	50	0.01	< 20	0.138	6	⌀20.2 ×20.8	-30	50	80	120	15	90	36	24	170
OPC-N3[16]	PM	$2000\,\mu g\,m^{-3}$	0	-	900	105	75 ×60 ×63.5	-10	50	-	-	0	95	-	24	700
Naneos AP[17]	UFP	5×10^8 particles/m^3	50	-	2 500	530	174 ×88 ×33	0	50	-	-	10	90	-	-	8224

[10] http://www.alphasense.com/WEB1213/wp-content/uploads/2013/07/CHD3.pdf [cited June 20, 2020]
[11] http://www.alphasense.com/WEB1213/wp-content/uploads/2015/01/COCX.pdf [cited June 20, 2020]
[12] http://www.alphasense.com/WEB1213/wp-content/uploads/2013/07/NOB1.pdf [cited June 20, 2020]
[13] http://www.alphasense.com/WEB1213/wp-content/uploads/2013/07/NO2D4.pdf [cited June 20, 2020]
[14] http://www.gassensor.ru/data/files/ozone/O3B4.pdf [cited June 20, 2020]
[15] http://www.alphasense.com/WEB1213/wp-content/uploads/2019/09/SO2-A4.pdf [cited June 20, 2020]
[16] http://www.alphasense.com/WEB1213/wp-content/uploads/2019/03/OPC-N3.pdf [cited June 20, 2020]
[17] https://www.naneos.ch/pdf/naneos_AP_flyer_2018.pdf [cited June 20, 2020]

7
Noise Measuring Subsystem

This section will dive into designing the noise measuring subsystem. As described in the midterm report, the MEMS microphones show very promising specifications [3]. Moreover, it was determined that some signal processing has to be performed to infer useful information from the raw signal.

The subsystem will be performing measurements both during a fly-over and when there is no fly-over. This has a direct impact on the requirements for the lower boundary of the intensity that can be measured, see AEMS-F-SENS-NOIS-04. For the upper intensity, it makes more sense to look at what the system is likely to experience at most during operations. For this, Schiphol Airport is considered as a reference. According to NOMOS, the official Schiphol Noise Monitoring System, the highest sound level encountered is 96 dBA over the year 2019 [1]. Based on this and as a follow-up from the preliminary design phase [3], the subsystem requirements are listed below in the coloured box below.

Noise Sensing Requirements

AEMS-F-SENS-NOIS-04	The system shall be able to measure noise with an intensity of at least 40 dB [MA]
AEMS-F-SENS-NOIS-05	The system shall be able to detect and measure noise up to a minimum achievable intensity of 120 dB [MA]
AEMS-F-SENS-NOIS-06	The system shall be able to measure noise at any frequency within the range 10 Hz to 20 kHz [MA]
AEMS-F-SENS-NOIS-07	The system shall be able to measure low-frequency noise at frequencies within the range 6 Hz to 100 Hz [MA]
AEMS-F-SENS-NOIS-08*	The system shall be able to detect and measure sound levels with an accuracy equal to or better than 1 dB [SH-DATA-04]
AEMS-F-SENS-NOIS-09	The system shall be able to detect and measure sound levels coming from all directions.

Background Theory The well known decibel metric is based on the effective sound pressure emitted per unit time of a source. This is shown in equation 7.1, with P_e the effective sound pressure of a source in N/m^2 and P_{e0} a constant reference effective pressure. In a sound signal, it is possible to determine this intensity for all frequencies individually. As is shown later, these intensities are often curved to take into account the perceptiveness to the various frequencies of the human ear. This is called A-weighting, and the unit of intensity is referred to as dBA after this [37].

$$\text{SPL} = 10\log\left(\frac{p_e^2}{p_{e0}^2}\right) \tag{7.1}$$

7.1. Hardware Selection

Based on the functional analysis and requirements, a microphone model is selected. Namely the InvenSense ICS-40300 MEMS-microphone. This microphone has the weight and size advantages MEMS are known for,

[1] `https://noiselab.casper.aero/ams/report.php#page=report/id=1/period_from=2019-01-01/period_upto=2020-01-01/tod=/nmt=40/rwy=/dir=` [cited June 4, 2020]

while still offering a large frequency range because of its special design. This section will further elaborate on its specifications and usage.

InvenSense ICS-40300 First of all, an important parameter that led to the selection of this sensor is the extended dynamic range. This sensor is specifically build to reach frequencies as low as 6 Hz up to 20 kHz, which is not common for MEMS microphones due to their small exterior. The dimensions of the selected microphone are shown in figure 7.1 Moreover, this is achieved at a mass of only 10 g.Furthermore, other specifications are shown in table 7.1. These will be used for calibrating the sensors as well as for post-processing purposes.

This particular format has the sensor and an amplifier in a small scale chip, which has several benefits. First of all, the signal to noise ratio is very workable at a level of 63 dBA, this means that it is easier to isolate the acoustic signal from the incoming signal which inevitably includes white noise. In turn, this means that there are no analogue components required to adjust the captured signal. Moreover, the captured signal is converted into a digital one with a just a 6 µs latency. Therefore, the sensors can more easily be applied in arrays. This is something that might be considered for future iterations of the system.

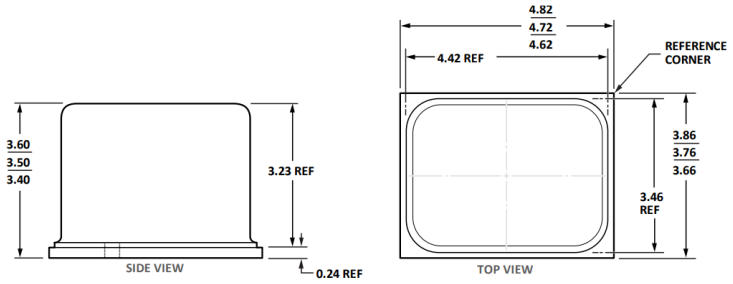

Figure 7.1: InvenSense MEMS-Microphone Dimensions [mm] [2]

Table 7.1: Microphone Specifications

Specification	**Unit**	InvenSense ICS-40300 MEMS
Dynamic Range	dB	30-130
Frequency Range	Hz	6 - 20000
Temperature Range	°C	-40 to +85
Sensitivity	dBV	-45
Signal to Noise	dBA	63
Accuracy	dB	0.5

7.2. Sensor Layout

Now that the pressure level sensor is defined, the next step is to think about how it will be placed on the system. For this, it is important to consider that it must be possible to measure pressure levels on all sides of the drone, such that requirement *AEMS-F-SENS-NOIS-09* is met. Moreover, redundancy of the sensors is something that should be accounted for. From this, and from looking ahead at how the structure of the system will look, it is determined that two of the aforementioned microphone chips will be placed on each side of the drone's structure. This will ensure full surround coverage, as well as a way of cross-referencing incoming signals.

7.3. Calibration

The sensitivity of the sensors is dependant on several environmental conditions. Specifically, the temperature, humidity and the static pressure are of importance. The manufacturer's documentation shows graphs for the relevant influence coefficients for these factors. To calibrate the sensing system accordingly, these factors have to first be measured. This is done using rudimentary sensors. Infineon offers microsensors

[2] `https://invensense.tdk.com/wp-content/uploads/2019/02/DS-ICS-40300-00-v1.3.pdf`

for both pressure and temperature. Similar manufacturers offer microsensors for humidity, e.g. Farnell [3]. These are inexpensive and small sensors which therefore do not require a trade-off.

7.4. Signal Processing

This section describes how the signal coming from the microphones is used to compute useful metrics. Moreover, information is given on the filtering of sound originating from the drone's propellers. Finally, a description is given on how the metrics are turned into readable plots which are later interpolated. The current process is shown visually in figure 7.2.

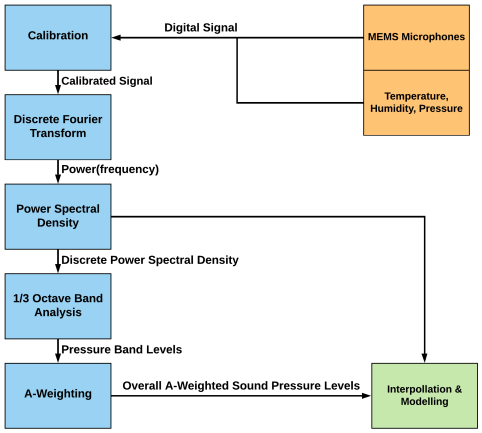

Figure 7.2: Noise processing overview

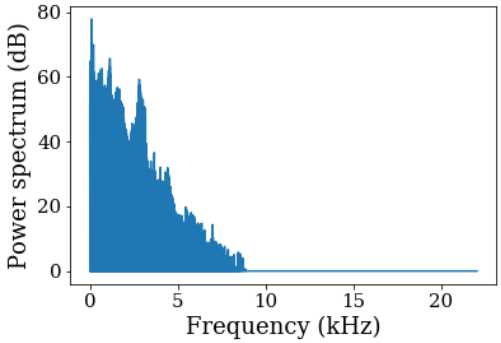

Figure 7.3: Frequency spectrum Boeing-747

Digital processing Now that a digital signal has reached the processor, it is both stored and transmitted to the cloud database. From here it is downloaded and analysed by the data processing software, the raw measurement could also be inspected by the user. Now, some calculations can be done. First of all the signal is a function of time, this is transformed into the frequency domain using a discrete Fourier transform (DFT) , of which the general form is shown in equation 7.2. Then, the discrete power spectral density (PSD) is found using equation 7.3. Which describes the distribution of power over the frequency range. Now, a 1/3-octave band analysis is performed. For this, the frequency range is divided into 1/3-octave ranges and the power level is integrated over these frequency bands. This results in the frequency band levels (PBL) also referred to as sound pressure levels (SPL) in dB, conforming to equation 7.4. At this stage, an intensity is known for each frequency band. Now, the A-weighting can be applied. This is the most commonly used curve to adjust the measured intensities with the goal to account for human ear perceptiveness. This is done by shifting the pressure levels using the curve defined by equation 7.5. Finally, the overall A-weighted sound pressure level L_A is determined. This is done using equation 7.6 [37], where SPL indicates the frequency band levels and $\Delta L_{\mathrm{A}}(i)$ the effect of A-weighting [37]. Adittionally, a tool is build to perform these computations, figure 7.3 shows a PSD from this tool for a Boeing-747 fly-over.

$$X_m = \Delta t \sum_{k=0}^{N-1} x_k e^{-2\pi i k m/N} \tag{7.2}$$

$$P_m = \frac{|X_m|^2 (\Delta t)^2}{T} = \frac{|X_m|^2 \Delta t}{N} \tag{7.3}$$

$$\mathrm{PBL} = 10\log\left[\frac{P(f)\Delta f}{p_{e0}^2}\right] = \mathrm{PSL} + 10\log\Delta f \tag{7.4}$$

$$\Delta L_{\mathrm{A}} = -145.528 + 98.262\log f - 19.509(\log f)^2 + 0.975(\log f)^3 \tag{7.5}$$

$$L_{\mathrm{A}} = 10\log\sum_i 10^{\frac{\mathrm{SPL}(i)+\Delta L_{\mathrm{A}}(i)}{10}} \tag{7.6}$$

[3] http://www.farnell.com/datasheets/1355480.pdf

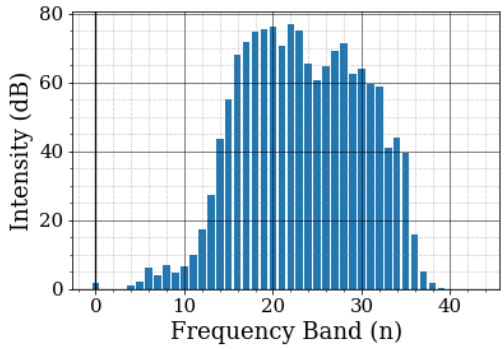

Figure 7.4: frequency band Levels Boeing-747

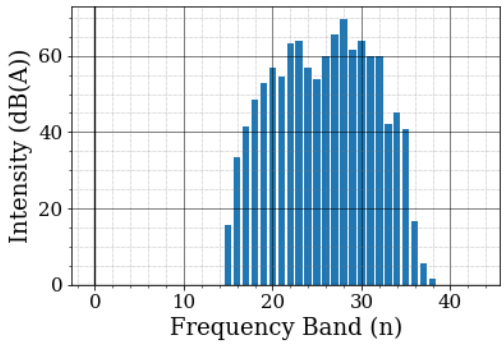

Figure 7.5: A-Weighted frequency band Levels Boeing-747

Filtration of Propeller Noise In the signal processing, it is important to account for the noise made by the drone's own propellers. Due to the various contributing factors such as propeller diameter, pitch, material and shape, it is analytically not feasible to calculate the exact features and characteristics of the noise produced. Thus, the intensity in each frequency band of the propellers is determined through experiments. This is to be done for all thrust settings that are possible to occur during the pre-defined measuring mission, such that based on the thrust settings, the produced intensity and frequency can be determined.

This can then be accounted for in post-processing, by shifting the measured intensity in these frequency bands according to the self produced intensity and frequencies derived from the apparent thrust settings during the measurements. By doing so, the noise of the drone is able to be filtered out from the measurement data to a certain extent. Although the retrieved data is expected to be imperfect, fair measurement data between various aircraft can be achieved with a similar degree of error thus being able to be utilised.

Data Visualisation Now that the signal processing is finished, more detail is given on the methods for visualising the acquired data. First of all, it is important to note that the data at this point is constrained by the grid points. Meaning, the PSD and $L_{\mathrm{A}}(i)$ are only known at these points. Secondly, this data is only known at specific timestamps within the take-off or landing time-period. To attain a complete data frame in all these dimensions, interpolation and modelling is performed, which is described in more detail in chapter 8.

Once the interpolation is performed, there will be approximate frequency band levels for all points in space. From that, it is possible to construct a more fluent contour plot, at a desired altitude. Showing the overall A-weighted intensity L_A in a plane (over the airport map for example), an example is shown in figure 7.6. Furthermore, interpolation also takes places along the time dimension. This makes it possible to show a more fluent spectrogram at a single location, an example that was produced for the Boeing-747 as used before, is shown in figure 13.3. The interpolation here acts as a way of connecting the power spectral densities of various samples (taken at different times). The spectrogram offers the spectral densities over a longer time period, e.g. a full day. It is possible to create this for a single aircraft or for the overall noise at an airport.

All in all, this procedure renders a complete data set in four dimensions (x, y, z, t) with a grid sizing as specified in section 5.3. Important to note is that with this dataset it is possible to compute any metric based on the datapoints. An example is the sound exposure level (SEL) , which is computed using equation 7.7. For this, the L_A values are taken from the database at one location for one aircraft. T represents the domain of the integration, which would generally be taken as the sample length, which is five seconds. However, since the data points in the time dimension will also be dense after interpolation, this domain could be chosen much smaller too. It is important to realise that the data set allows for including a wide variety of metrics that are dependent on the frequency band intensities at any location/distance at any time/period.

$$L_{\mathrm{AE}} = 10 \log \left[\frac{1}{T} \int_0^T 10^{\frac{L_A(t)}{10}} \, dt \right] \tag{7.7}$$

Moreover, an easy distinction can be made between measured data points and interpolated data points. In turn, as with any new data set, this leads to many new research opportunities which are further elaborated upon in chapter 22.

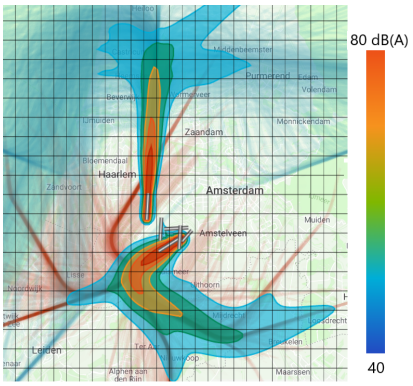

Figure 7.6: Airport L_A Intensity Contour[4]

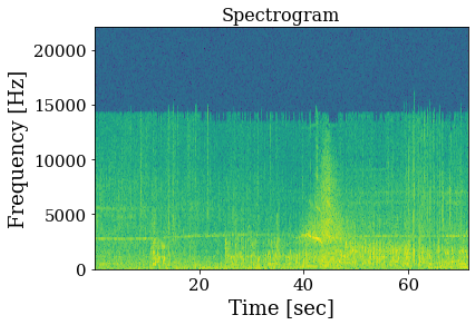

Figure 7.7: Spectrogram Boeing-747

7.5. Verification and Validation

This section identifies the methods used to verify and validate both the signal processing/plotting tool as well as the subsystem as a whole. Moreover, future experiments are proposed when appropriate.

Verification To verify the signal processing tool, several tests are performed. First of all, a singularity test is performed by taking a flat zero signal as input. This results in a L_A value of zero, and a uniform blue spectrogram. Another similar test is done, but using a known input, a 1 kHz signal. This indeed shows a spike at 1 kHz in the frequency band level diagrams and a line at 1 kHz in the spectrogram.
To verify the subsystem, a look is first taken at similar systems. Each component is compared to the relevant component in these systems. Both in terms of technical specifications and hardware integration. This confirmed that the system should work as proposed. Furthermore, each component is double-checked against all the constraints posed by the requirements and by the other subsystems.

Validation To validate the signal processing tool, several tests are performed. First of all, a signal was inputted of which the spectrogram and frequency band levels were determined by existing systems. This rendered equal results.

to validate the subsystem, the results could first of all be compared to the existing stationary measurement systems. This could even be an experiment where the mobile system measures at the same location as the stationary system. Second of all, the subsystem, and eventually the whole system, can easily be tested in a controlled environment. Meaning that a noise source is introduced of which the frequency band levels are known.

7.6. Compliance of Requirements

As requirements were presented at the beginning of the chapter, the following compliance matrix summarises how the design implemented the given requirements.

Noise Measuring Subsystem Compliance Matrix

Requirement ID.	✓ / o / x	Comment
AEMS-F-SENS-NOIS-04	✓	As indicated in table 7.1 this is covered by the range.
AEMS-F-SENS-NOIS-05	✓	As indicated in table 7.1 this is covered by the range.
AEMS-F-SENS-NOIS-06	✓	As indicated in table 7.1 this is covered by the range.
AEMS-F-SENS-NOIS-07	✓	As indicated in table 7.1 this is covered by the range.
AEMS-F-SENS-NOIS-08	✓	As indicated in table 7.1 this is met
AEMS-F-SENS-NOIS-09	✓	This is met due to the layout as described in section 7.2)

[4] https://noiselab.casper.aero/ams/#page=actual

8

Data Processing Subsystem

The current section presents how the outputs delivered by the air quality and noise transducers are processed and used to deliver a meaning full result to the user. It concerns itself with detailing how the data values will be incorporated in a metric (in section 8.2), interpolated (described in section 8.3) and analysed for the system to learn how to more accurately perform the measurements. A section on software verification and validation process will also follow in 8.4

To illustrate how the different subsystems that fall under the function of performing the measuring mission interact, an IDEF0 (Icam DEFinition for Function Modelling with ICAM an acronym for Integrated Computer-Aided Manufacturing) diagram is used. The diagram from figure 8.1 is meant to help visualise the functions, inputs and outputs governing the interface inside the measuring mission subsystems.

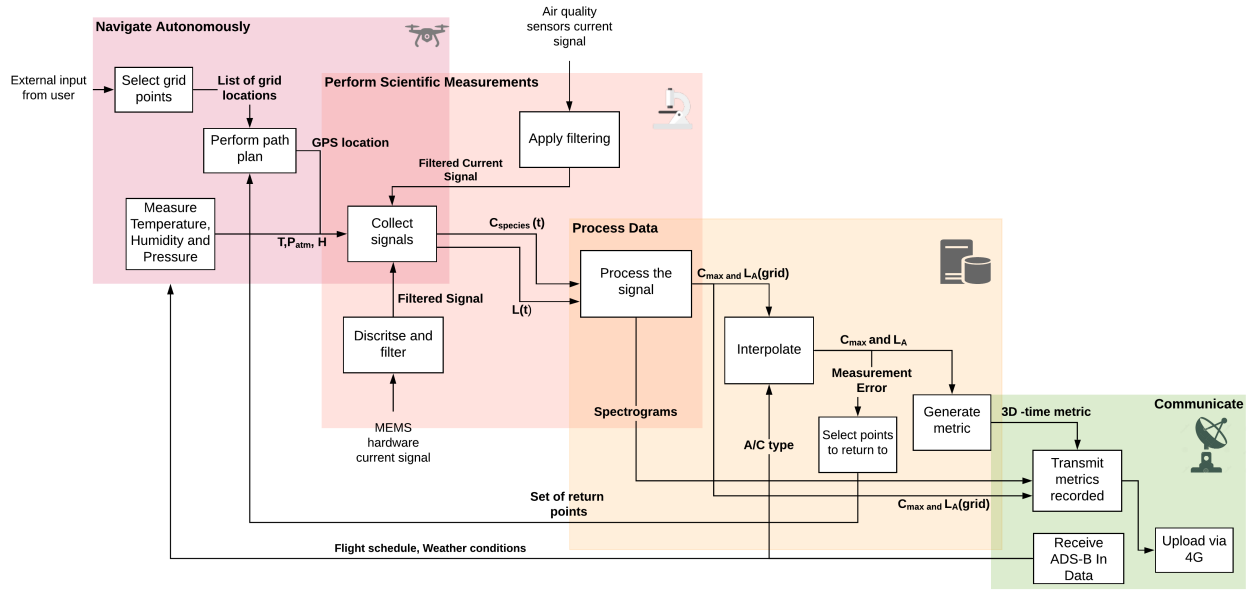

Figure 8.1: IDEF0 containing the Autonomous Navigation, Measuring, Data Processing and Communication subsystem interface

The stakeholder needs, functional analysis and risk prevention strategies result in the next requirements, shown in the coloured box below. They are all valid, as already presented in [2] and [3], the highlighted one being a key subsystem requirement.

Data Analysis Subsystem Requirements

AEMS-SH-DATA-01	The system shall produce individual aviation emissions metrics
AEMS-SH-DATA-02	The system shall produce individual aviation noise metrics
AEMS-SH-DATA-03	The system shall produce a combined aviation's environmental impact metric
AEMS-SH-DATA-04	The system shall display background noise levels
AEMS-SH-DATA-05	The system shall display background emission levels
AEMS-F-DPR-02	The system shall distinguish between different aircraft types [SH-DATA-03]

AEMS-F-DPR-MOD-01	The model shall interpolate between data points scattered in space and/or in time [Risk DH2]
AEMS-F-DPR-MOD-02	The model shall enable for re-meshing [Risk DH1]

8.1. Theoretical Models

To better understand the sensor selection from chapters 7 and 6 and the interpolation problem, some theoretical aspects of noise and air pollution emission and propagation are presented. This section serves as a mere overview. The models presented here are used both as a basis for interpolation and as a means of validation of the measuring subsystems.

Noise spatial distribution is described by the formal solution given in equation 8.1 from [37]. Theoretically, it is a representation of the solution of the inhomogeneous wave equation, a partial differential equation (PDE) . The function returns the sound-wave pressure $p(\vec{r},t)$ as the integration result over a volume that includes all sources of acoustic energy described by the source term q, located in space-time at $\vec{r}_S$.

$$p(\vec{r},t) = \iiint_V \frac{1}{4\pi \|\vec{r}-\vec{r}_S\|} q\left(\vec{r}_S, t - \frac{\|\vec{r}-\vec{r}_S\|}{c}\right) d\vec{r}_S \tag{8.1}$$

From the pressure level, the noise intensity is calculated using the formula from equation 8.2.

The sound pressure level (SPL) depends directly on the power of the source (PWL), the directionality (θ), the distance from the source r and, last but not least, on the characteristics of the media that the spherical sound wave is propagating through. These are summarised in the following equation (from [37]):

$$I := \frac{p_e^2}{\rho_\infty c} \quad \text{and} \quad \mathrm{SPL}(r,\theta) = \mathrm{PWL} - 10.8 - 20\log(r) + \mathrm{DI}(\theta) - \alpha r \tag{8.2}$$

The above functions show, in a limited manner, properties of the sound generation and propagation. The sound intensity I is the highest at the source, where it theoretically approaches infinity, and it decrease with the distance squared (spherical distribution). The integral would return a more accurate pressure level if the source function is known. Reversely, one can trace back the function $q(\vec{r},t)$ if both $p(t)$ and distance $\vec{r}$ to the source are available.

An airport is more realistically seen a multi-source dynamic environment. Despite being possible, identifying those sources and their influence is a resource-intensive task that requires advanced modelling techniques for the PDEs involved. To trace back the source functions from the provided acoustic measurements remains a step to be taken in the future and a valuable application for the data gathered by the user using the current system. For now, the interpolation software aims to generate useful data while limiting the distortion cause on the physics behind it.

Air pollution theoretical model

As mention in 6.1.3, there are multiple ways to describe a plume emitted by a polluting source such as an aircraft, a runway or an airport as a whole. Here, the Gaussian plume model is used. Next to estimating maximum pollutant concentrations encountered during the mission, this model is used as a starting point for interpolation and aircraft identification as well (see section 8.2). The latter two aspects will be treated separately and in more details in sections 8.2 and 8.3, respectively.

As set out in [11] and [4], the Gaussian plume model has limited accuracy. Despite this, it can be used to perform preliminary calculations and it does show, in a simplified way, how physics behind air pollution dispersion works. For this reason, the Gaussian plume model is incorporated both as a tool to determine expected maximum pollutant concentrations during the mission (as described in chapter 6) and as a basis for interpolation. The latter is detailed in section 8.3.

8.2. Metric definition

According to the customer requirements AEMS-SH-DATA-01,-02,-03 the system shall communicate a comprehensive metric of the noise and air pollution around the investigated airport. This translates into two levels of information: raw data and ψ metric.

Raw data The system reports the concentrations, the PM histograms and the sound spectrograms. This information would become useful for scientific studies that would process and model the data themselves. The amount of data generated in this case is significant.

Ψ definition
For a generic user, such as the local authorities or airport board, a more summarised output is desirable. The pollution species concentrations (in ppm and particles/s for PM and UFP values) and the weighted noise value (for a specified pressure band) can be saved together in one list with the given name ψ. At each grid location, the data collected by air quality and noise measuring subsystems is stored in a ψ list which is, in turn, a scalar function of $\vec{x} = [x, y, z, t]$.

$$\psi(\vec{x}) := [\psi_k] = [C_{NO}, C_{NO_2}, C_{CO}, C_{O_3} C_{CH_4}, C_{SO_2}, C_{PM_{2.5}}, C_{PM_{10}}, C_{UFP}, L_A] \quad \text{with k=noise/species} \tag{8.3}$$

This ψ list corresponds to a summarised way of reporting to the user a general noise and air pollution metric. The values can correspond to the background around the airport or they can be labelled as belonging to a specific aircraft type. The labelling process can be seen in figure 8.2, using as inputs the ADS-B (in) data and signal concentrations. For example, if the analogue noise values become higher than the background plus a threshold of 10% and an "A320" aircraft type is the closest (according to ADS-B) and it is taking-off (as part of LTO) then the data at that grid point will be labelled under "A320". If the LTO event passes while the systems is flying to the next grid point the label expires. At each grid point, these checks are performed in real-time by the board processor.

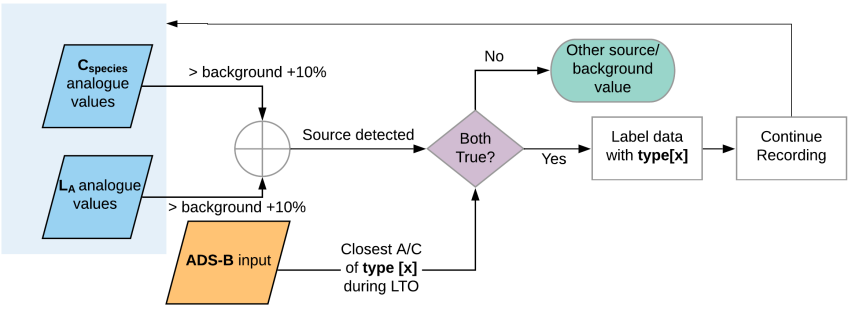

Figure 8.2: Function flow showing how data corresponding to an aircraft (A/C) during LTO is labelled

The data labelled under a particular aircraft can then be used more extensively. For example, the ADS-B receiver provides the relative distance to the aircraft and this can be used to infer the sound level as a function of the distance to the source. The data needed to replicate this dependency will also be communicated to the user.

To increase the resolution, the values retrieved from each grid point are interpolated based on the intrinsic physics. The next section will present the exact procedure. The customer then can use the concentrations to calculate other metrics such as the Air Quality Index (AQI) to measure air pollution or the day-night average for noise values.

The system will communicate to the user the interpolation result under the form of a three-dimensional heat-map. For visualisation purposes, figure 8.3 shows how the result will be visible once the system collected the data. The metric map was generated based on made-up values and hence is by no means representative for real measurements. Last but not least, as already mentioned above, this metric map can be generated both for the environment around the airport or for a specific aircraft type (provided that ADS-B data is accessible in that condition). The user can choose either of them and also which emission species they want to visualise.

8.3. Interpolation and Optimisation

When the drone flies to each measurement location, it uses energy and produces a certain degree of noise. Even if reduced, its environmental impact while flying cannot be zero. As stated by the 5th sustainability

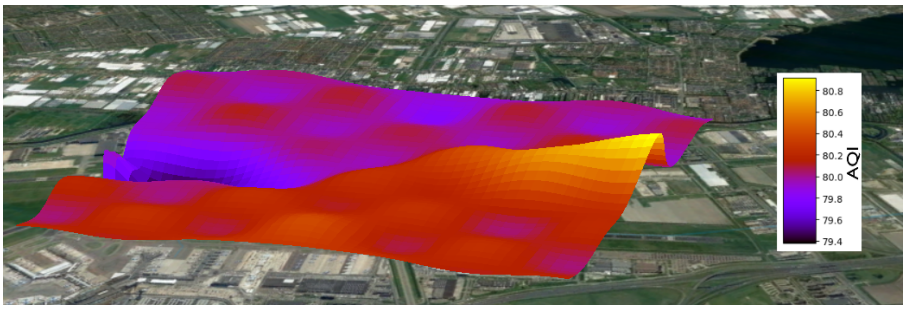

Figure 8.3: Heat-map showing general emission metric over a rectangular part of the domain, based on made-up data (background or aircraft).

criterion (listed in chapter 4), this impact should be minimised. To aid in doing so, *interpolation* is used to gather more resolution before reporting the data.

To interpolate, the above theoretical equations should be mathematically transferred into a generic model (type of interpolation). Multiple modelling options are available and most of them proved to be useful depending on different aspects of the problem: data shape, grid size and distribution (i.e. regular or scattered data points), accuracy, computational cost etc. From the available literature such as [19], [48], [23], the following Design Option Tree (DOT) was generated with all the main classes, it can be seen in figure 8.4.

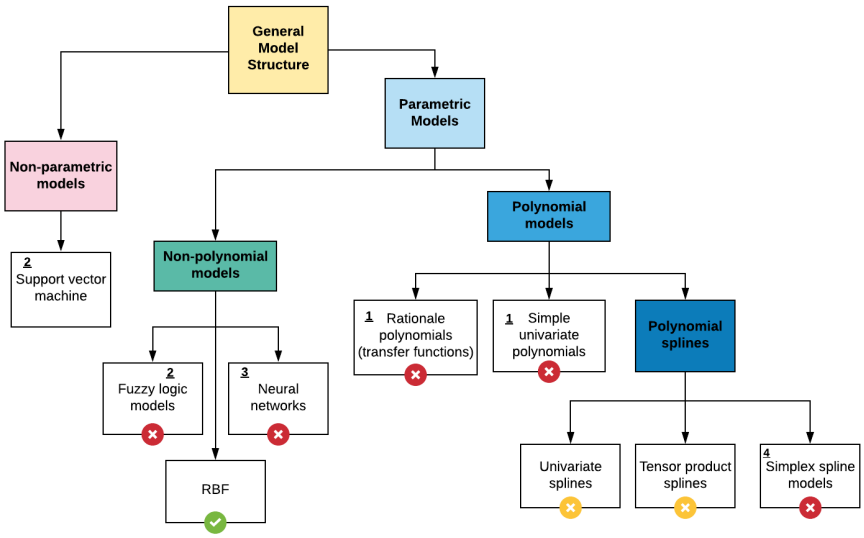

Figure 8.4: Design option tree for interpolation function, removed items are marked by 'X' and the reason is indicated the top-left corner

To select the optimum interpolator, each interpolation model was further inspected for its strengths and weaknesses. The models crossed are not considered later due to one of the following reasons:

1. Model is not efficient when it comes to replicating the features of the physical equations from above. Global univariate polynomials diverge towards the boundary of the domain and rational functions are usually applied for linear time-invariant (LTI) systems (as transfer functions).

2. Support vector machine and fuzzy models either use large amounts of labelled data or categorical variables to classify the remaining points. Neither of these approaches is considered suitable for the current problem.

3. Neural networks are 'black box' models. Since a degree of control is needed over the parameters involved in the interpolation, these models are rejected. Also, they require a large time to develop and train which poses as a weakness for the current project.

4. Multivariate simplex splines, for example B-splines, models are able to achieve the goal. Their weakness lays in the extra complexity needed to define simplex over the scattered domain and time needed to fully implement them. Hence, they are not selected now but are left as possible future applications (see 22).

The last three classes left concern univariate splines, tensor spline and radial basis functions (RBF) . The first two categories were prototyped by using cubic splines and, even though possible, their complexity increases quickly when moving to higher dimensionality in the data. Moreover, they provide a strong dependency on the grid shape and demand a regular grid. To pass the requirement *AEMS-F-DPR-MOD-01*, and therefore prevent risk *DH2*, the model structure (i.e. spline number and list of polynomial coefficients) might have to rebuild itself each time a new data point is added. Since this solution is computationally inefficient, it makes local refinement hard to implement and hence, for this approach only the global grid refinement is acceptable.

To overcome these issues, the RBF model was selected. They are based, according to [23], on a *linear superposition of translates of a single radially symmetric basis function* (or kernel). A function $\phi : \mathbb{R}^4 \rightarrow \mathbb{R}$ is called radial symmetric if it exists an univariate function $\varphi : [0,\infty) \rightarrow$ R such that $\Phi(\mathbf{x}) = \varphi(r)$ with $r = \|\mathbf{x}\|$. The operator $\|\cdot\|$ denotes a norm on $\mathbb{R}^4$. Here, an extension to four dimension of the Euclidean norm is selected and implemented on normalised vectors (to remove the physical units) for its simplicity and generality:

$$\|\mathbf{x}\| = \sqrt{\left(\frac{x}{x_{max}}\right)^2 + \left(\frac{y}{y_{max}}\right)^2 + \left(\frac{z}{z_{max}}\right)^2 + \left(\frac{t}{t_{max}}\right)^2} \tag{8.4}$$

Now, to obtain the estimation $\hat{\psi}$, the RBF interpolant can be defined on a generic grid $\{\mathbf{x}_j : j = 1,\ldots,n\}$ (n distinct nodes) with data values $\{\psi_j : j = 1,\ldots,n\}$. Each grid point $\mathbf{x}_j$ will have its *own basis function*. The general class of kernels Φ is selected for the entire model and it can also be parameterised Φ_ϵ.

$$\hat{\psi}(\mathbf{x}_i) = \sum_{j=1}^{n} w_j \Phi_{(\epsilon)}\left(\left\|\mathbf{x}_i - \mathbf{x}_j\right\|\right) \quad \text{with the point conditions set as} \quad \hat{\psi}(\mathbf{x}_i) = \psi_i \tag{8.5}$$

To train the model, the linear system of n equations from above needs to be solved for the basis weights w_j.

The RBF model is seen as a robust tool for interpolating multi-dimensional scattered data [27]. Moreover, it is simple to implement (Python provides packages that enable it) and versatile since both the basis function and its parameters (ϵ) can be specified. The biggest downside of this approach comes from its computationally expensive evaluation since the coefficient matrix is very dense [23]. Despite this, the CPU and memory resources needed are considered to be sufficient given the current design.

Since the RBF represents a class of functions, the basis can be selected based on the problem at hand from a standard catalogue of kernels such the one shown in [27]. It was decided to try and retain the properties of the intrinsic physics governing the phenomena by implementing basis functions that are also contained in the modelling equations. Hence, two kernels $\Phi_{(\epsilon)}$ are used to interpolate the ψ data while returning its properties. They are shown below in equations 8.6 :

$$f_\epsilon(r) := e^{-r^2/\epsilon^2} \quad \text{and} \quad g_\epsilon(r) := log\left(\frac{1}{\sqrt{\epsilon + r^2}}\right) \tag{8.6}$$

The left basis f_ϵ will be used for the air pollution concentrations since it reassembles a Gaussian Distribution with the mean at zero and the standard deviation equal to ϵ. The second basis, g_ϵ, will be used for interpolating the L_A noise values. The kernel resemblances the inverse squared dependency from equation 8.2 but a correction is needed to limit the kernel from diverging when the distance approaches zero. For this purpose, the ϵ parameter is added to the denominator of g_ϵ. The system will optimise for the best ϵ value as it will be discussed later in section 8.3.2.
According to [23], these kernels provide a converged global solution to the interpolation problem but this statement will be tested during verification in section 8.4.

The interpolation is used to estimate values between measured data points. Thus, it can achieve a much finer resolution inside the same domain. The ratio between the number of estimated points and the sampled grid points is defined as N_{refine}. This factor can be increased by the user if higher resolution is desired.

8.3.1. Gradient Threshold and Cost Map

The complex phenomena that generate noise and pollution concern both transient and steady-state variations of the measured values. To better capture these complex dynamics, local refinements are implemented. As discussed in section 5, the system can perform local grid refinement by visiting points of high interest. A way to select this set of points is by building a cost function that takes as input the gradient of each ψ component. The assumption here states that a higher gradient (in absolute value) would indicate a possible polluting source that raises the levels above the background or an aircraft LTO event. Given that the ψ data is interpolated at any desired moment, the estimation of the partial derivative and also space-time gradient of each list component becomes trivial. The NumPy [1] package from Python provides robust tools that can be incorporated to solve it.

The authors of both [18] and [19] present methods to assess an optimised, finer, path for measurements. On one hand, in [18] the sampling points are selected based on measuring the on-ground distribution and gradients. On the other hand, [19] defines a selective monitoring strategy based on previously recorded values at the grid locations and revisits those points. Since the ground levels of pollution and noise are not recorded with enough spatial distribution by the stationary stations (described in section 1) the second method is selected as the starting point for the current local refinement. One should keep in mind that both articles deal with (highly) polluted urban spaces and their measurements only concern air pollution species. Thus, their findings are used just as concepts for the preliminary design of the current measuring approach.

Based on the discussion from [19], the gradient at each point for all ψ list components, is normalised and then compared to the following two gradient thresholds (GTs) : GT_h and GT_l. If any of the species gradients are higher than GT_h, then the point is expected to correspond to a polluting event or a local pollution source. If the GT is approaching zero, by being lower than the arbitrarily low GT_l, then one can expect a local extremum. In both cases, the location of the point is included in the set $\mathscr{I}$ of 'interesting' points. The GT definition for gradient of species k at one point is given below in equation 8.7 and it is followed by the definition of the set I in equation 8.8:

$$GT_k = \frac{\left|\nabla\hat{\psi}_k\right| - \left|\nabla\hat{\psi}_k\right|_{min}}{\left|\nabla\hat{\psi}_k\right|_{max} - \left|\nabla\hat{\psi}_k\right|_{min}} \tag{8.7}$$

$$\mathscr{I} = \left\{\vec{x}_i \,|\, \left(GT_{i_k} \geq GT_h\right) \cap \left(GT_{i_k} \leq GT_l\right)\right\} \forall\, k \tag{8.8}$$

The exact values of the two thresholds can be specified by the user but both are required to be in the interval (0,1) for the problem to be mathematically solvable. A set of preliminary values that the user of the system can implement: GT_l machine-ϵ for high precision is ideal and GT_h 0.4 - 0.5 as indicated by [19].

Selecting the best GTs becomes a trade-off between desired accuracy and time (or energy) needed to complete the mission. This trade-off is entirely depending on the data at hand and on the events that are investigated. This approach is considered to minimise the required time for local refinement while still improving the accuracy of the model. Also, it reduces the chance of interfering with other airport systems or with the local community environment. Hence, from a sustainability point of view, it is considered in line with the D4S criteria defined in chapter 4.

To summarise, the procedure of measuring the data, calculating the error and then performing a gradient-based refinement is shown by figure 8.5. The first row (top) of the figure describes the normal sampling of the grid. Each point is measured, that interpolation between grid locations is then performed, the GT is calculated and points are added to set $\mathscr{I}$. In the second row (bottom), the UAV flies back to those points and the new measurements are used to estimate the error $|\psi - \hat{\psi}|$.

[1] `https://numpy.org/doc/stable/reference/generated/numpy.gradient.html` [cited June 10, 2020]

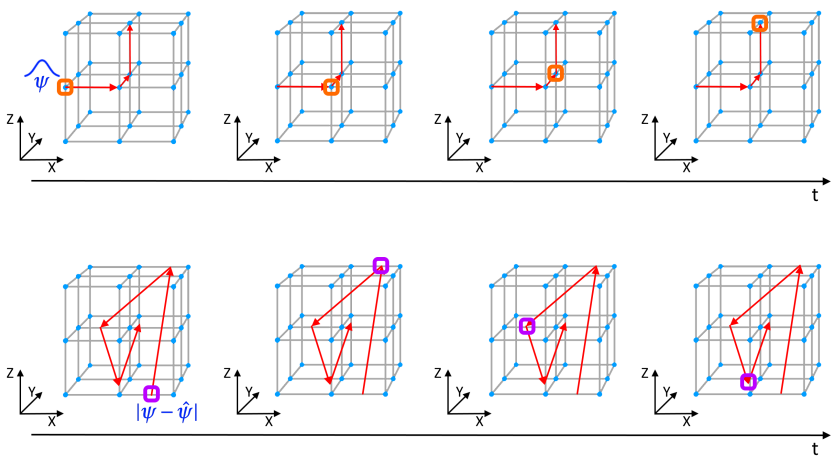

Figure 8.5: Interpolation, error calculation and refinement procedure shown on a generic grid (adapted from [19])

8.3.2. Parameter Optimisation

Looking back the kernels define by equations 8.6, the parameter ϵ can be used to tune the model to better interpolate the data by retaining more its properties. For example, by looking at both equation 6.1 and the kernel f_ϵ, one can see that ϵ can mirror the spatial dissipation σ_y (or σ_z). This coefficients depend on the distance to the plume source according to [11]. In the current scenario, an optimum ϵ will also be dependent on a particular grid distribution and distance between nodes. These dependencies will be detailed more in the next paragraphs.

This parameter can be found during post-processing by solving an optimisation problem. The search for optimum will be performed in the cloud since it is more computationally intensive by using a higher number of data points. For the top-level overview, refer to figure 8.6.

$$\text{MSE} = \frac{1}{n}\sum_{i=1}^{n}\left(\psi_i - \hat{\psi}_i\right)^2 \quad \text{with} \quad n = \text{total number of visited points} \tag{8.9}$$

For the optimisation to converge, the error needs to be able to reach a global minimum with respect to a varying ϵ. This global property depends on three things: (1) the grid size and distribution, (2) the chosen error metric and (3) the ψ data values. (1) is fixed from an operational perspective as already explained in section 17.2.3 so the software takes it as an input. (3) depends entirely on the measurements performed during the mission and hence it does not fall under the direct control of the designer. Despite this, the values from real data measured by the stationary stations around Schiphol will be used to validate the software in 8.4. The second aspect is the only one that can be changed. The error metric shall be a convex function of the variable ϵ. Figure 8.7 from 8.4 shows that this is indeed the case.

The optimisation problem is univariate so the *Golden search* algorithm is proposed. This search method optimises for a reduced number of function calls [23]. Since the interpolation is computationally expensive, this algorithm would provide an efficient choice. Following from simulation, as a rule-of-thumb, the values for ϵ_{min} and ϵ_{max} should be taken symmetrically with respect to the grid spacing (in the current mission the spacing is $d = 150m$).

All the above-mentioned software components are summarised in the software diagram from figure 8.6 corresponding to the modelling and interpolation subsystem. The flowchart comes as an aid for visualisation and description of the measuring part and it is included, with less details, in the general software diagram in figure 13.7.

8.4. Software Verification

For verifying the interpolation code, unit tests were first performed. First, the RBF interpolation was checked against a set of simplified inputs. They are listed below in table 8.1, the execution time is also shown to ensure that the interpolation will not overtake all processing power for a long time. The time and output of each was deemed sufficient.

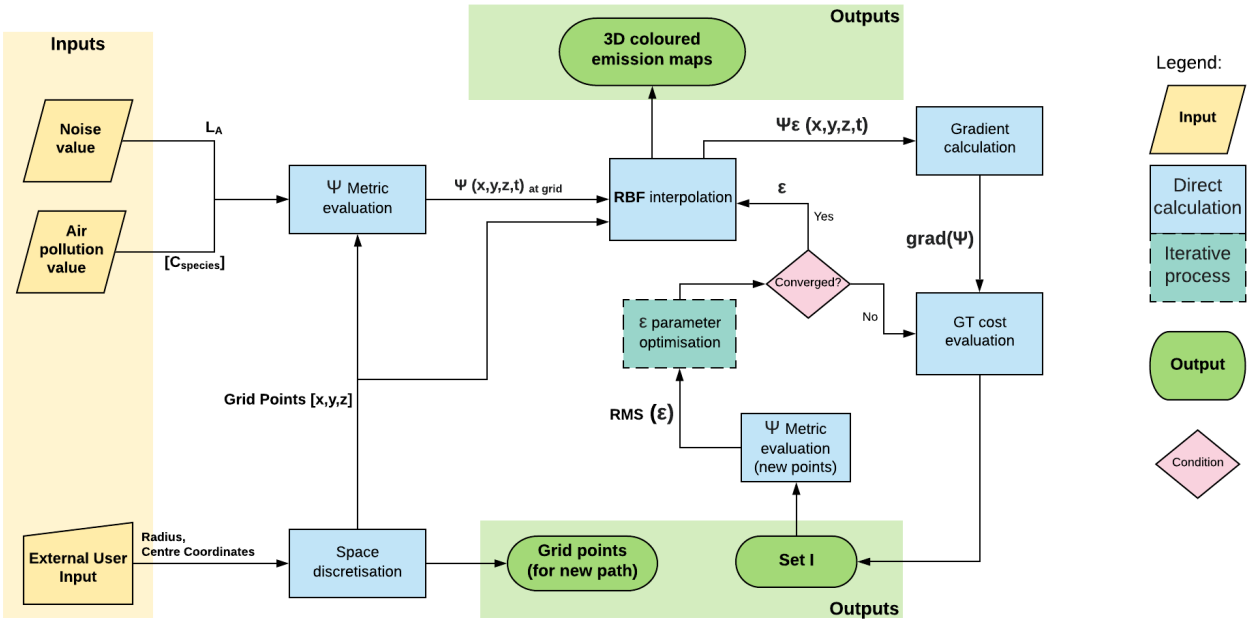

Figure 8.6: Measurement interpolation and model tuning software diagram

Table 8.1: Unit and module tests compliance table, the standard grid corresponds to the measuring mission described in 5

Test	**Input**	**Output**	**Execution Time [s/point]**	**Remark/ Warning**
Unit	Constant data values over domain	Same value	$O(e^{-10})$	**Passed**
Unit	Single point interpolation	Single value	$O(e^{-10})$	**Passed**
Unit	Outside domain, single point	Single value	$O(e^{-10})$	**Passed**
Module	Refined domain ($N_{refine} = 5$), standard grid	MSE <0.5	$O(e^{-11})$	**Passed**
Module	Optimum ϵ search, standard grid	Converged to optimum	$O(e^{-11})$	**Passed**

To test the performance of the entire system, an alteration of the method of *manufactured solutions* is implemented. The ψ data is taken as from a general distribution, a linear combinations of fundamental functions such as: sin(x), cos(x), e^x etc. Such a combination is assumed general enough to capture any phenomena. Then, a sparse grid is defined according to the mission requirements, the shape of the grid array being $\psi = f([x, y, z, t])$. This grid has a spacing of $d = 150\,\text{m}$ and time resolution of $\Delta t = 30\,\text{s}$. These are considered realistic values for a standard measuring mission as already presented in chapter 5. The interpolant is generated and its error is measured by sampling the distribution again, at a much finer rate (given by N_{refine}).

The plot from figure 8.7 shows the outputs of the system test for the parameter estimation procedure. As it can be seen the error does show a convex behaviour with respect to ϵ and hence there is an ϵ value, found by the search algorithm, such that the accuracy of the modelling based interpolation is maximised.

For the given grid spacing and manufactured solution, the search algorithm converged to an $\epsilon = 137$ which is comparable to the grid spacing $d = 150\,\text{m}$. Thus, aspect (2) from section 8.3.2 is successfully verified.

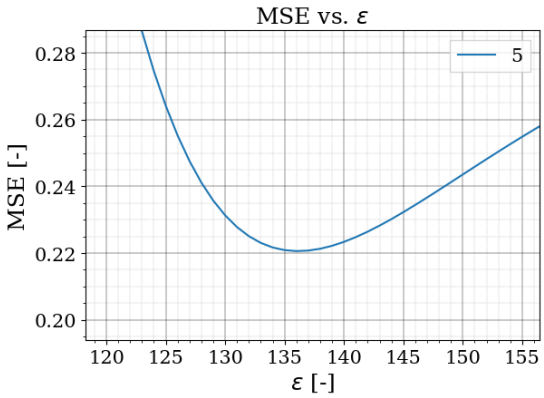

Figure 8.7: Mean squared error against ϵ for and $N_{refine} = 5$.

8.5. Validation and Compliance

For interpolating the real-life data, the O_3 pollution concentrations measured in time were taken from three stations around Schiphol: Badhoevedorp, Hoofddorp and OudeMeer. Following from the previous chapter, these concentrations are less affected by the atmospheric chemical processes [1]. The stations' coordinates (longitude and latitude) were obtained and thus a data array with form $C_{O3} = \psi([x, y, 0, t])$. A similar procedure was followed for noise interpolation. The A-weighted L_A in time is retrieved and processed from a NOMOS station, resulting in $L_A(t) = \psi([0, 0, 0, t])$.

To assess the software performance against real-data, *cross-validation* was implemented. Namely, some grid nodes are taken out, and they are not used for interpolation but the $\hat{\psi}$ is compared at those points with their real value. The count of removed points is half of the total, which corresponds to an equivalent $N_{factor} = 2$ considered realistic for a real mission. Since the elimination is stochastic, the code is run a large number of times and the results error results are averaged. Then, the parameter ϵ that minimises the MSE is found via the optimisation algorithm. The results are visible in figures 8.8 and 8.9. As it can be seen in the plots, the interpolant can converges and finds an optimum parameter even for a sparse grid.

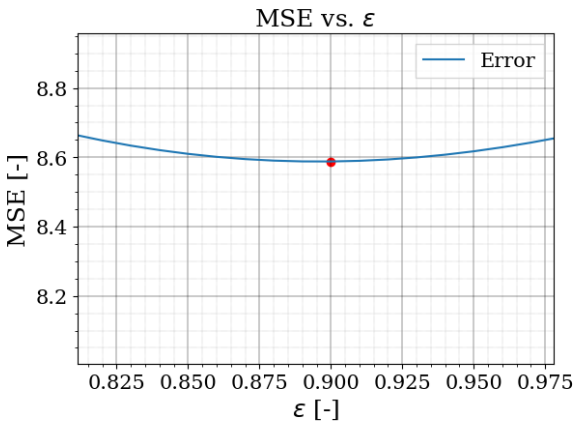

Figure 8.8: Mean squared error against ϵ for $C_{O3} = \psi([x, y, 0, t])$.

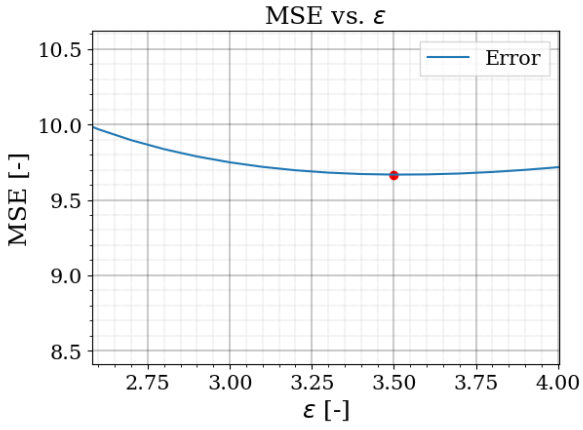

Figure 8.9: Mean squared error against ϵ for $L_A(t) = \psi([0, 0, 0, t])$.

The MSE error achieved is in both cases under 10. Both kernels used to interpolate noise and air pollution converged to an optimum. These minima are presented in the figures by the red markers. The error comes from different sources such as: model errors (the airport is a dynamic, multi-sourced environment, the RBF kernels are not able to capture the physics), inherent noise in the measurement data, numerical errors (the Python interpreter might lose decimal-point precision while inverting the coefficient matrix). Also, the stochastic effect of wind speed and its direction might be present in the data. Despite this, they are not

corrected by the interpolation. For modelling purposes, assessing their influence is an important future step but this goes beyond the extent of the current project.

The above-mentioned validation technique shows that the system can interpolate the given data and it is able to converge to an optimised form based on its parameters. To validate the interpolation model by itself would require a comparison with another type of modelling, such as regression. For example, the air quality data generated by the three stations is a sequence in time. It can be analysed by fitting a smoother curve and then computing the relative error between the new fit and the interpolation.

As future steps, the interpolation model can be greatly improved by using a multi-layer network of augmented RBFs (some information is presented by [27]). Generally speaking, to not only retain the physics behind them measurements, but also to predict it, the focus should move from the model particular solution to governing partial differential equations.

Moreover, the models from which the kernels were inspired from, have their assumptions and limitations. The data generated by the system can be used to improve them.
To conclude the chapter, as requirements were presented at the beginning, the following compliance matrix summarises how the design implemented them:

Data Processing Compliance Matrix

Requirement ID.	✓ / o / x	Comment
AEMS-SH-DATA-01	✓	Presented by section 8.2
AEMS-SH-DATA-02	✓	Presented by section 8.2.
AEMS-SH-DATA-03	✓	Taken into account in section 8.2, the ψ list
AEMS-SH-DATA-04	✓	Taken into account in section 8.2, based on chapter 7.
AEMS-SH-DATA-05	✓	Taken into account in section 8.2, based on the work from chapter 6.
AEMS-F-DPR-01	✓	Taken into account by section 6.5 by using two sensor arrays.
AEMS-F-DPR-02	✓	Taken into account in section 8.2 that describes the metric reported for one aircraft.
AEMS-F-DPR-MOD-01	✓	Completed by section 8.3 via the RBF selection.
AEMS-F-DPR-MOD-02	✓	Explained in section 8.3 and 8.3.2 via the local re-meshing and parameter optimisation.

9
Autonomy and Control Subsystem

This section will cover how the drone will autonomously perform the operations it will undertake. This subsystem will introduce methods for navigating the drone through the airport and nearby communities through the use of hardware (section 9.1) and software (section 9.2). The decisions and strategies for the control of the drone will be laid out in section 9.3. Finally, the verification and validation of these subsystems will be presented in section 9.5.

Following from the stake-holder requirements from chapter 2, the subssytem requirements are listed below:

Autonomy & Control Subsystem Requirements	
AEMS-SYS-AUT-02	The system perform path planning without external control by pilots during the flying session [FFD-3.2.1]
AEMS-F-AUT-04	The system shall autonomously avoid external harmful objects and restricted areas [FFD-3.5.1]
AEMS-F-AUT-06*	The system shall be able to fly continuously for multiple sessions during a working day of minimally 8 hours [FFD-3.4]
AEMS-F-AUT-07	The system shall be able to measure or estimate state parameters while flying [FFD-3.1.5,3.2]
AEMS-F-AUT-08	The UAV shall return to its docking station at the end of the mission without external control by operators [FFD-3.2.1,3.5]
AEMS-F-AUT-09	The system shall begin execution of external commands within 3 s from when the signal was received [FFD-3.1.1]
AEMS-F-AUT-10	The system shall detect objects with a size of at least 1000 mm^2 at a distance between 1-20 m [FFD-3.1.3]
AEMS-F-AUT-11	The system shall be able to fly during night time [SH-DATA-06]
AEMS-F-AUT-12	The UAV shall not tip over during landing [risk CS2]
AEMS-F-AUT-13	The UAV shall terminate operation in the event of an emergency [risk OP3]
AEMS-F-AUT-14	The camera's field-of-view shall not be obstructed by any other subsystems.

9.1. Hardware Selection

During the midterm report [3] several hardware components were decided upon to ensure the drone is able to complete operations autonomously, in this section more depth will be given into the hardware components and manufacturers and models will be chosen and along with the reasons for these choices and their specifications.

Autopilot The autopilot system is responsible for determining and controlling the drones attitude, altitude and guidance based on information on its current state. This information is in the form of inputs from the global navigation system, disturbances to the system, the ADS-B, emission data, range sensors, altitude sensors and internal feedback from the IMU . The autopilot then adjusts the power output to the individual propeller motors based on the desired trajectory of the drone.

A widely used autopilot system on the market currently is the Holybro Pixhawk 4®[1], making it ideal in the prevention of risk *CS1* due to the large amount of verification and validation this system has been through. The advantage of this product is that many sensors and sub-components are compatible with it, as well as the benefit of including its own software, for programming the autonomous mission of the drone and implementing the specific dimensions and details of the drone being designed. This reduces the complexity of the integration and reduces any costs that may be involved in integrating the many components that make up the autonomous system. The specifications of this product are found in table 9.1. This autopilot also comes with a kill switch in which the drone can be safely turned off manually, this is useful for when the drone is in maintenance, being inspected, in transport or in an emergency.

Table 9.1: Holybro Pixhawk 4® specifications[2]

Property	**Holybro Pixhawk 4**	**Unit**
Price	192.20	€
Dimensions	44 x 84 x 12	mm^3
Weight	15.8	g
On-board sensors	Accelerometer, Gyroscope, Magnetometer, Barometer	
Power module output	4.9 - 5.5	V
USB Power Input	4.75 - 5.25	V

Another big advantage of using the Holybro Pixhawk 4® is that the software used to program the autopilot includes features that apply specifically for this mission, for example, geo-caging, navigation to waypoints and it comes with the co-axial octocopter as an airframe option. The sofware used is called QGroundControl® and an example is shown in figure 9.1.

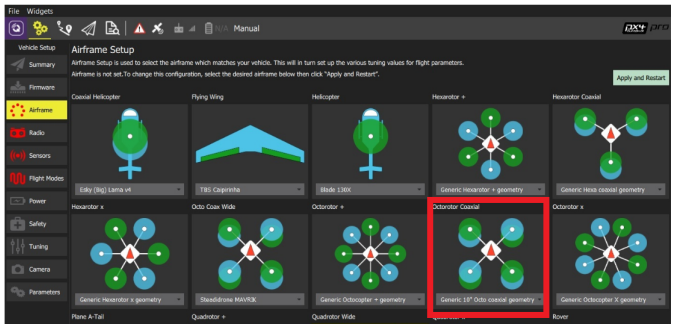

Figure 9.1: Coaxial octocopter airframe feature in QGroundControl®

Radar Sensors Radar is a time-of-flight sensor that uses radar waves to detect an objects location and speed. The radar sensor that will be used for the on-board Sense and Avoid (SAA) system. The unmanned aerial vehicle (UAV) will make use of four Texas Instrument AWR1642BOOST-ODS frequency modulated continous wave (FMCW) radar sensor which are equipped with its own evaluation module. The AWR1642BOOST-ODS is a single-chip 76 GHz to 81 GHz automotive radar sensor[3]. The specifications for the sensor can be found in table 9.2. The chosen radar sensor complies with requirement *AEMS-F-AUT-10*.

Figure 9.2 shows how the field-of-view of the radar sensors can be used to ensure that four radar sensors cover the dimensions of the drone in order to sense obstacles that may approach the drone from any direction within the azimuth plane. The drone will have a maximum total width and length of 2 m, if one assumes that the arms of the drone are placed at a 45° angle from the body and that therefore the maximum horizontal and vertical distance from the centre of the drone is 1 m. Assuming, as an extreme case, that the radar sensors are placed in the centre of the drone, the total width the radar sensor will cover is 5.5 m. This is more than enough to cover the entire drone on that particular side and will mean that the radar sensors will

[1] `https://docs.px4.io/v1.9.0/en/flight_controller/pixhawk4.html` [cited June 03, 2020]
[2] `https://shop.holybro.com/pixhawk-4_p1089.html` [cited June 03, 2020]
[3] `https://www.ti.com/tool/AWR1642BOOST-ODS`[cited June 03, 2020]

Table 9.2: AWR1642BOOST-ODS radar specifications[3]

Property	**AWR1642BOOST-ODS**	**Unit**
Price	266.62	€
Dimensions	66 x 85 x 2	mm^3
Weight	40	g
Max. Velocity	10	$m\,s^{-1}$
Range	20[4]	m
Resolution	4	cm
Field-of-View - Azimuth	±70	°
Field-of-View - Elevation	±40	°
On-board memory	1.5	MB
Processor	Arm® Cortex® R4F	-

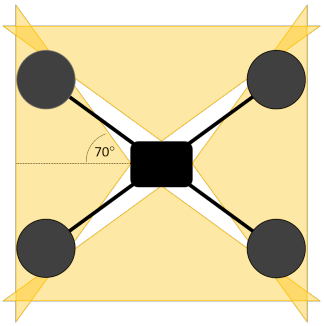

Figure 9.2: Radar field-of-view in Azimuth plane

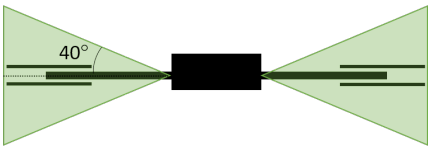

Figure 9.3: Radar field-of-view in the elevation plane

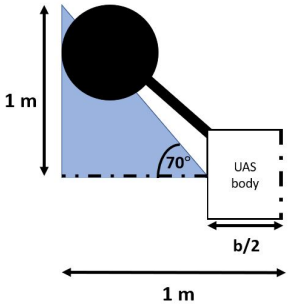

Figure 9.4: Body dimensions based on radar field-of-view

indeed detect potential obstacles to all parts of the drone. It should be noted that at this stage it is assumed that the drone body dimensions are small compared to that of the arms, however there is enough contingency to account for the size of the body. In fact in order for the radar sensors to cover the whole drone the dimensions of the body must be less than or equal to 1.272 m in width and length, assuming the radar sensors are placed in the middle of each edge. Figure 9.4 shows how this is calculated along with equation 9.1, where b is the width/length of the body.

$$\frac{b}{2} = 1 - \frac{1}{\tan 70} \tag{9.1}$$

Figure 9.3 shows the side view of the drone with the radar sensors attached and the field-of-view. In order to ensure that the radar sensors provide enough coverage for the drone against any obstacles approaching from the sides, the radar must cover the maximum height of the drone. By taking the most critical case, where the body is of the maximum size, as calculated above, the height of the field of view at extremities of the drone can be calculated. Using the same procedure as done previously for the azimuth plane the height of the field of view at the outer perimeter of the drone (i.e. at the propellers) is 0.611 m.

Camera A camera will be used to assist the drone in the vision based autonomous landing procedure. This procedure is based on pattern recognition. Furthermore, the camera will be used in emergency situations where the drone needs to perform an immediate decent. The safe completion of an emergency descent requires an accurate evaluation of the surrounding terrain, including the undulations in the terrain and any obstacles. This procedure requires the camera to have the capability to return information about the distance to either the ground. Due to the need for the camera to perform tasks that involve depth perception, a stereo-vision camera is opted

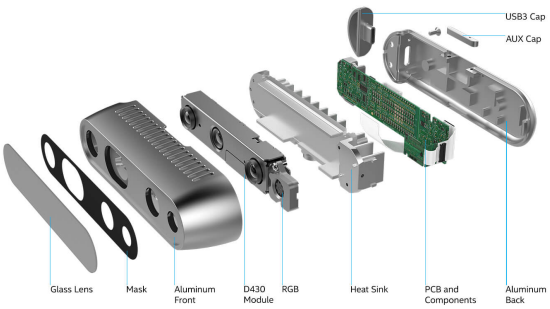

Figure 9.5: Intel® RealSense™ Depth Camera D435 [5]

for. The Intel® RealSense™ Depth Camera D435, is a stereo vision camera that can calculate depth with the already built-in vision processor, even in low-light conditions [5]. An exploded view of the device featuring all its components can be found in 9.5. Further specifications of the stereo camera are given in table 9.3.

Table 9.3: Intel® RealSense™ Depth Camera D435 specifications[5]

Property	**Intel® RealSense™ Depth Camera D435**	**Unit**
Price	158.95	€
Dimensions	90 x 25 x 25	mm^3
Weight	72	g
Maximum range	10	m
Minimum range	0.1	m
Output frame rate [FPS]	90	FPS
Field-of-View (Horizontal x Vertical x Diagonal)	87±3 x 58±1 x 95±3	°

GPS module The type of global navigation chosen for the FAEMS is Global Positioning System (GPS) . The GPS data will be handled by the autopilot system and used to implement path planning methods to navigate to locations of interest for emission and noise measurements as well as being used to avoid areas that the drone is not permitted to enter, this is known as geo-caging. The GPS data is also used to give location stamps to measurements that are taken, thereby giving relevance to the data in terms of the near-airport community. The decision was made to use GPS receivers with RTK (Real-Time Kinematics) capabilities. The reason for this came from requirements AEMS-SYS-REG-04 and AEMS-F-OPR-07 . This is because that GPS alone has typical accuracy of 4.9 mm [6], which is deemed to be too inaccurate. However with the addition of RTK, the global location of the UAV is accurate to within centimetres.

The strategy used for RTK is to place a GPS receiver at both the ground station and the drone, the information received by the ground station is then transmitted to the drone and used to correct the errors in the information received at the drone.

The GPS-RTK unit chosen for the drone is the Here+® V2 RTK GNSS (M8P) as it is the small, light and energy efficient, it is also the cheapest of the GPS-RTK packages that are compatible with the chosen autopilot system that comes ready to be used. The package includes one receiver that is configured to be used at the ground station and one configured for use on the drone [7]. The GPS receiver should be mounted on top of the drone away from components that effect the GPS signal, this will help prevent risk *NV1*, if this were to happen the risk can be mitigated by using the IMU for global positioning for brief periods of GPS loss or making an emergency landing if the signal does not return. Section 17.2.4 presents further details on emergency procedures.

Table 9.4: Here+® V2 RTK GNSS (M8P) specifications[7]

Property	**Here+® V2 RTK GNSS (M8P)**	**Unit**
Price	532.35	€
Dimensions	67 x 17 (ø x h)	mm^3
Weight	50	g
Power consumption	0.24	W

Telemetry Telemetry data will be crucial for the maintenance and inspection of the drone, in particular the autonomy system. Telemetry data will be logged by the autopilot system and sent via 4G in order for a user to view the data in QGroundControl to determine how the drone is performing and whether any components may need replacing and/or re-calibrating. As explained in section 13.

[5] `https://store.intelrealsense.com/buy-intel-realsense-depth-camera-d435.html` [cited June 04, 2020]
[6] `https://www.gps.gov/systems/gps/performance/accuracy/` [cited May 19, 2020]
[7] `http://www.proficnc.com/gps/77-gps-module.html` [cited June 04, 2020]

Power Module The Holybro Pixhawk 4® comes with a power management board included. The function of this board is to provide regulated power to autopilot and ESCs. It also transmits data about the battery's voltage and current supplied to the flight controller and the motors to the autopilot. The specifications of this unit are shown in table 9.5.

Table 9.5: Specifications for pingRX and Pixhawk 4 power management board [8][9]

Property	Pixhawk 4 power management board	pingRX	Unit
Dimensions	68 × 50 × 8	34 × 19 × 8	mm
Weight	36	5	g
Input voltage	7-51 (2-12s LiPo)	4-6	V
Range	-	160	km
Cost	-	221.23	€

ADS-B Aircraft can broadcast their location and course information in real-time using ADS-B. This will make it a critical component in operating in and near the airport, in order to avoid any collisions or interruptions to airport operations, to prevent risk *NV2*. The ADS-B receiver used needs to be compatible with the chosen autopilot, receive data from all aircraft within the area, real-time and be small and lightweight. The*pingRX* fulfils all of these requirements, the technical specifications can be seen in table 9.5. The ADS-B receivers output data includes the location and heading of the aircraft as well as the flight ID[10], the location and heading will be used for geo-caging during path planning and the flight ID can be used as a stamp during noise and emission measurements to identify responsible aircraft. This hardware component therefore aids in the drone comply with requirement *AEMS-F-AUT-04*.

9.2. Navigation

This section will deal with safe navigation of the drone through the airport and near-airport environment. Section 9.2.1 will present methods to restrict the drone's operational area and section 9.2.2 will explain methods for path planning through the operational environment. Section 9.2.3 will concern itself with the drones ability to avoid obstacles, whilst section 9.2.4 and 9.2.5 will present the landing and emergency landing protocols.

9.2.1. Geo-caging

One of the most important aspects of navigation with respect to safety is geo-caging. Geo-caging ensures that the drone does not enter a restricted volume by use of a pre-defined 3D volume as a no-entry zone, thereby complying with requirement *AEMS-F-AUT-04*. This ensures no disturbance to regular airport operations as defined by *AEMS-SYS-REG-04*. This section will make use of Schiphol as a base example.

Active Runways present the greatest danger risk. This is a contributing factor to risk *NV2*. Therefore, these runways will be geo-caged with extreme caution. The worst case scenario for the danger zone from the centre of the runway would be a landing at the edge of the runway surface. This can occur in situations of high crosswinds or misjudged pilot approaches. With the limiting case of the largest aircraft in the world, namely the AN225, landing towards the outer edge of the runway, equation 9.2 may be formulated, where SF represents a safety factor. Runway width (W_{rwy}), distance from aircraft's longitudinal axis to the outer landing gear (y_{ldg}) and wingspan (b) are presented in figure 9.6. The aircraft figure is adapted from the AN225 Brochure[11].

$$W_{gc} = SF\left(\frac{W_{rwy}}{2} - y_{ldg} + \frac{b}{2}\right) \tag{9.2}$$

[8] https://cdn.sparkfun.com/assets/9/b/1/8/6/PM07-Quick-Start-Guide.pdf [cited June 05, 2020]

[9] https://uavionix.com/products/pingrx/ [cited June 14, 2020]

[10] http://www.aeroshop.eu/media/upload/dokumentacija/Garrecht/Garrecht_TRX-1090_dataport_manual.pdf [cited 25 June 2020]

[11] https://www.antonov-airlines.com/wp-content/uploads/2019/07/Antonov-Airlines-brochure.pdf [cited June 12, 2020]

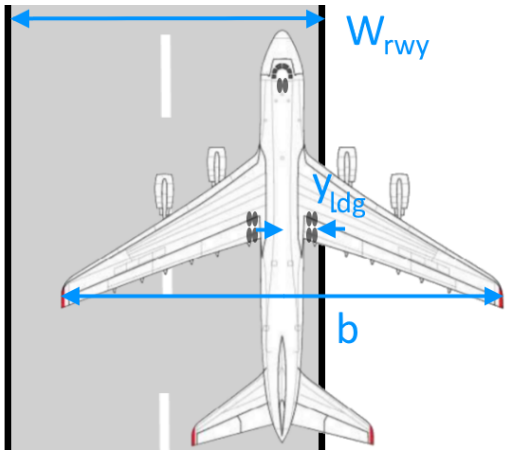

Figure 9.6: Runway Geo-caging Parameters

y_{ldg} and b may use the extreme values from the AN225 which are approximately 4 m and 89 m respectively . The safety factor is preliminarily set to 1.5, however, it is stressed that this variable is kept open to greater values should issues arise within the certification and ATC permission procedures (see chapter 17). With Schiphol as an example, making use of the greatest runway width of 60 m[12], this results in a geo-caging width of 106 m from the centre of the runway. This information has been obtained by airport charts of Schiphol from the Dutch ATC administrative body LVNL (Luchtverkeersleiding Nederland).

A five kilometre extension from the end of the runway is added to the geo-cage to allow for a measurement ground station located at or near the end of an active runway, whilst still providing full geo-caging abilities. However, during departure and arrival aircraft must use the SID (Standard Instrument Departure Routes) and STAR (Standard Arrival Routes) respectively unless otherwise instructed by ATC. For example, according to LVNL charts for Schiphol, one can see that for 4.0 nautical miles from the base of runway 36L that the departure must be flown in a straight line (see example figure 9.7), whereas for runway 24, a left turn may be completed 1.2 nautical miles after the end of the runway (see example figure 9.8). Since the use of runways 36L and 24 are almost always the only active runways at Schiphol, these will be further used for the base example.

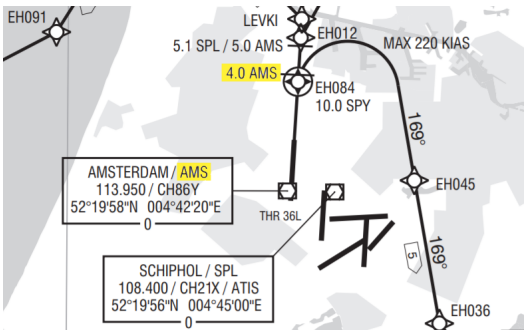

Figure 9.7: Schiphol Runway 36L Departure Routes

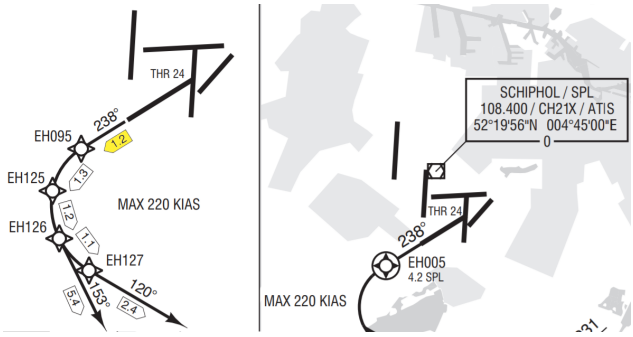

Figure 9.8: Schiphol Runway 24 Departure Routes

This must be evaluated in order to determine the safe geo-caged area. For runway 36L, no changes are required, however, for runway 24 a further volume must be added to account for different departures (e.g. figure 9.8). It should be noted that in certain occasions, often for smaller aircraft, non standard departures are given to shorten flight time. This adjustment is purely preferable for the pilot, however, every aircraft (and pilot flying) operating within a commercial airport is required to be able to use standard departures (SIDs). During operation of the drone, these must be avoided to prevent any collision risk outside the geo-caged volume.

Finally, a height of 500 m is used as the base runway geo-caged altitude. The drone is unlikely to ever need

[12] `https://www.antonov-airlines.com/wp-content/uploads/2019/07/Antonov-Airlines-brochure.pdf` [cited June 12, 2020]

to reach that height but it is chosen such that if a failure would occur above an active runway, it would take around 10 s to fall to the ground, enabling the implementation of redundancies. An example thereof is that the pilot is alerted through his or her cockpit instruments (through TCAS and is therefore able to abort the take-off in time. If the aircraft passes its no-return speed, so-called “V1", it should be at at least a 100 m altitude after 10 s, assuming a nominal climb speed. This is generally sufficiently high to avoid obstacles. Beyond the runway, the geo-caged volume altitude increases linearly to 1400 m altitude by use of a 10° climb, which is rather extreme. This will cover all flights in and out of the airport. Around 50 departing and 50 arriving flights were randomly selected for the active runways. The geo-cage around runways 36L and 24 can be seen in figure 9.9 and figure 9.10 respectively. The departing flights are displayed in blue and arriving flights in green. It can be seen that all flights fit comfortably within the geo-cage.

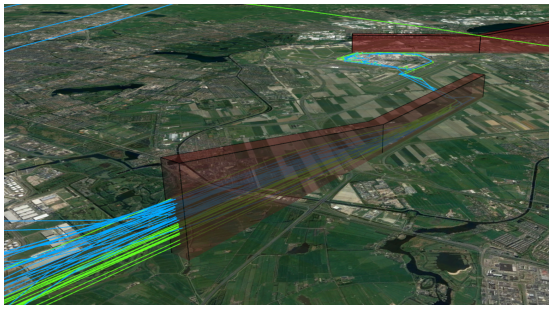

Figure 9.9: Schiphol Runway 36L Arrivals and Departures with Geo-cage

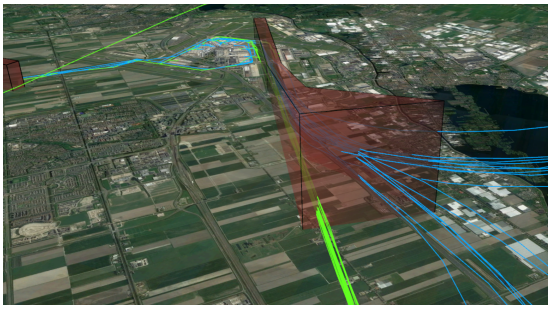

Figure 9.10: Schiphol Runway 24 Arrivals and Departures with Geo-cage

A few concluding notes should be made. The reason for this section’s importance and detailed explanation lies within the certification, an important factor in requirement *AEMS-SYS-REG-09*. In order for the SORA process to be completed successfully, it has to be demonstrated that the system may be operated in a safe and reliable way. This section aims to contribute to this mentality. Should the aircraft breach these geo-caging volumes, the consequences could be disastrous. The procedures for these navigational issues can be found in section 17.2.4. The path planning will take these volumes to be avoided into account in section 9.2.2. Finally, the implementation of these geo-caged areas can be completed with QGroundControl® as previously discussed.

9.2.2. Path Planning

The path planning aspect of the mission is crucial to the efficiency of the operation but also, importantly, contributing to the safety of the mission. Requirements *AEMS-SYS-AUT-02* and *AEMS-F-AUT-06/08/09* are of critical importance to this section. A brief overview has been presented in chapter 5, highlighting the mesh to be used. The restricted volumes are presented in subsection 9.2.1. This addition of these no-entry zones requires an in-depth analysis of the most efficient routes to take and significantly increases the complexity of the problem. It is therefore, that the preliminary navigation planner in section 5.3.3 is to be re-evaluated.

Grid Node Coverage The issue presented, is the lack of constraints to be able to optimise the problem. The drone must cover all of the nodes while returning to base to recharge (requirements *AEMS-F-AUT-06/08)*. If it returns with a still high battery level, measuring time is wasted, if it is returning with a critical battery level, the risk of emergency shutdown increases. It is aimed to find this balance. Each layer will be evaluated individually and for now assumed that the drone will fly around the runway rather than over. This is favourable for certification. Additionally, this simplifies the problem and also provides a more energy efficient approach due to the increased power required when ascending. First, two general methods are examined: “all-round" method and “segmented" method. The “all-round" method plans one path around all node without planning for returns to base. This means that the route it takes is optimal but the returns reduce efficiency. The drone would continuously determine whether it should return to the ground station or measure the next point along the one path. Figures 9.11 and 9.12 present two examples of this approach, a more systematically square path and a more systematically circular path respectively.

Significant issues arise with this method. Firstly, it would be very computationally expensive to determine a route from such a large node set. Such a path also has difficulties with the irregularity around the geo-caged

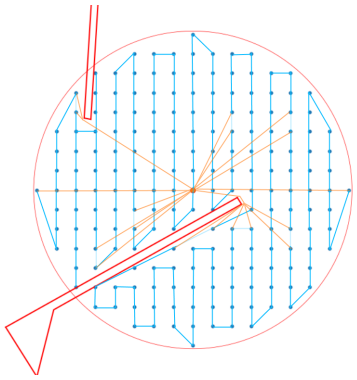

Figure 9.11: “All-Round" Squared Path Planning Approach

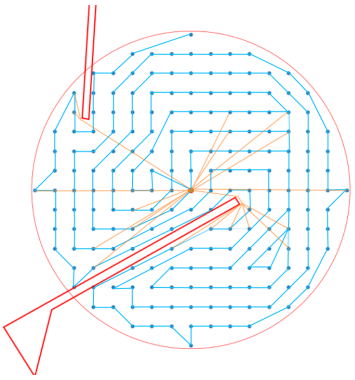

Figure 9.12: “All-Round" Circular Path Planning Approach

areas. This means that paths often need to be retraced, thereby reducing the efficiency of the operation. Finally, with the implementation of the “all-round" method, it can be seen (especially with figure 9.12) that enclosed areas will form which require significant extra time and distance to be covered. Implementing a path planner to take this into account, as well as minimising the distances for returning to base and minimising computational cost is beyond an achievable level within the set time frame. This is an aspect that could be further investigated after the DSE. Chapter 22 presents this in more detail.

The “segmented" method has the advantage of smaller data sets to work with, thereby reducing the computational cost. This would also ease the complexity of the operation meaning that changes can be implemented quickly, for example, in the event of an emergency or early return to the ground station, thereby required a re-evaluation of the set paths again. The “all-round" method would simply not allow for this flexibility and additionally, due to the aforementioned limitations, the “segmented" method has been opted for. Additionally, this contributes to prevention of risk *NV3*.

Algorithm Evaluation With the segmented approach opted for, the appropriate algorithm(s) needed to be chosen. Four widely used algorithm categories are considered and presented in figure 9.13.

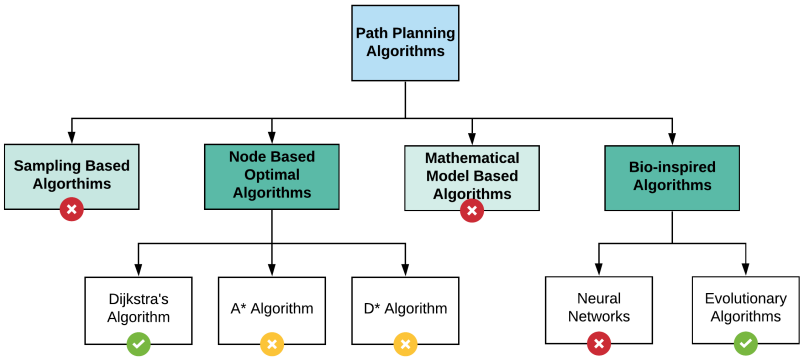

Figure 9.13: Path Planning Algorithms

Sampling based algorithms are immediately discarded. This is because the mission has been defined as to measure all nodes within the measurement volume, and not random locations within (see chapter 5). Importantly, some of these algorithms are non-optimal as well as non-converging under certain conditions [47]. Mathematical model based algorithms are also discarded. This because they examine the kinematics of a moving system and optimise the path based on constraints set in that aspect. For this mission, however, the importance lies behind traversing all the nodes. This also means many constraints must be set to even find a solution, often which restrict the problem in question significantly [47].

Bio-inspired algorithms were further examined as a node or cell based map is required for implementation, thereby enabling the traversing of nodes. However, neural networks, which aim to follow similar processes to how neurons process information, are not able to form standard rules which means that the time con-

sumption and reliability of the algorithm are not guaranteed [47]. This variation in path forming time would not be suitable for the mission due to the aforementioned need for flexibility of path changes (requirement *AEMS-F-AUT-09*). On the other hand, evolutionary algorithms, aiming to imitate natural biological evolution and social behaviour, can be seen as beneficial for a smaller set of nodes due to its fast convergence rate and higher reliability [47]. The process determines the 'fittest' node paths iteratively to find the 'strongest' solution [47].

The three main node based algorithms are Dijkstra, A* and D*, each which is a variation of the former. Dijktra's algorithm finds the shortest route between two points using specified coordinates. A*, on the other hand, does not have to traverse. Finally, D* is similar to A* with the exception of a dynamic environment. Whilst this in theory may be implemented, there is no benefit with the extra computational cost as any issue with dynamic movement within the measuring volume is dealt with in section 9.2.3.

Overall, two different algorithms will be implemented: Dijkstra's algorithm and an evolutionary algorithm. Dijkstra's algorithm will be used to reach and return from segments. This is because during the path planning, for finding routes to many nodes, Dijkstra is better than A* due to its reliability and ability to use the same information for path routing for closely located nodes [47]. This means a database is already existent for each node's fastest route to and from the ground station. Therefore, in emergency situations, The drone will know exactly how to get back without wasting time calculating the optimal route. This is paramount to the execution of the task within 3 s as defined by requirement *AEMS-F-AUT-09*. Additionally, this mitigates the risk *OP1* . Finally, the evolutionary algorithm will be implemented to traverse all the nodes within a segment with the shortest distance.

Algorithm Implementation The process works back from the node with the greatest path distance from the ground station. By working its way towards the base station in segments, as many as possible furthest located nodes by path distance are covered in one flight. This has the positive effect of reducing travelling time between outer nodes. It should be noted that travel between nodes is limited by geo-caging constraints and measuring volume boundaries (see chapter 5).

The chess-like figures 9.15, 9.16 and 9.14 present three examples of allowable movements where no restrictions are imposed, boundary restrictions are imposed and geo-caging restrictions are imposed respectively.

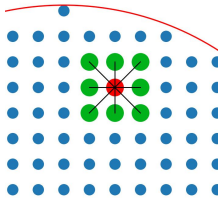

Figure 9.14: No Node Restrictions

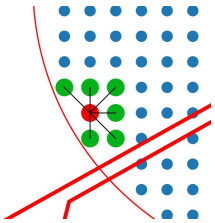

Figure 9.15: Boundary Restriction

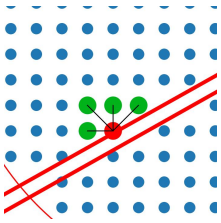

Figure 9.16: Geo-cageing Restriction

The process of determining segments and paths is presented in figure 9.17. All relevant node and constraint data is input, then thereby allowing automatic path planning (requirement *AEMS-SYS-AUT-02*). This is followed by the listing of all allowable neighbour nodes as previously mentioned. Once the node with the greatest distance from the ground station has been identified, the number of points that can be measured before not having a sufficient battery level to return can be calculated. This is achieved through energy-limiting calculations as explained in 12.7.6. Next, the node within the defined segment with the shortest distance to the ground station is identified. This is the path which will be taken to reach the segment. Both the furthest and closest nodes for the segments are calculated using Dijkstra's algorithm, denoted by the circled *Dj* in the top right corner of the process box. Dijkstra's algorithm is implemented with the use of open-source code from *rosettacode*, an online chrestomathy community [13]. The evolutionary algorithm, implemented with use of a python module called *mlrose* by Genevieve Hayes[14], is then able to determine the best route within the segment. More specifically, a genetic algorithm type is used. This is denoted by a circled *Ev*. Both of these modules have been verified by extensive testing of random scenarios. The databases are used to

[13] `https://rosettacode.org/wiki/Dijkstra%27s_algorithm#Python` [cited June 17, 2020]
[14] `https://readthedocs.org/projects/mlrose/downloads/pdf/stable/` [cited June 17, 2020]

prevent unnecessary recalculations of longest or shortest paths, thereby reducing calculation time.

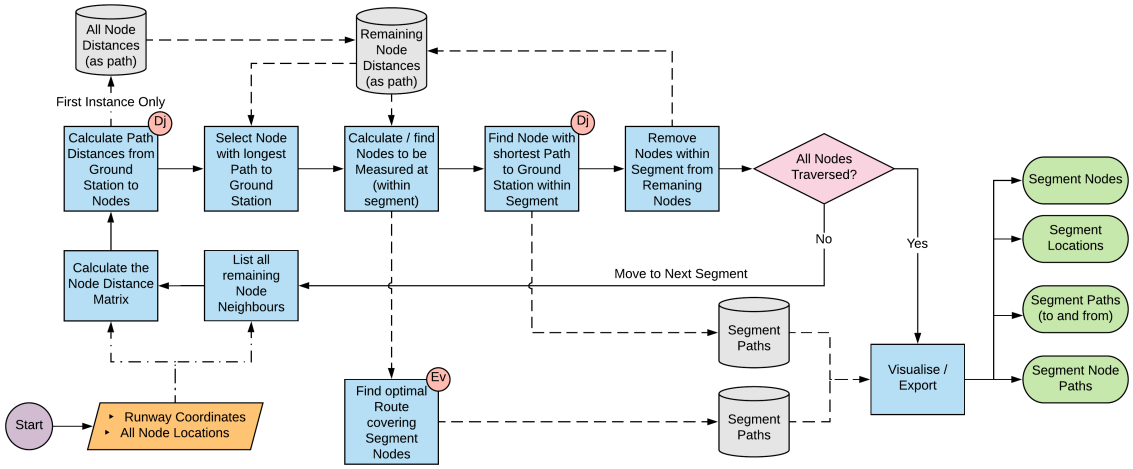

Figure 9.17: Path Planning Flowchart

Path Planning Scenarios With Schiphol again as a base example, and a sparser grid for enhanced visual interpretive ability, figure 9.18 presents the path planning result. The individual segment traversing can be seen in an example in figure 9.19. The ground station is located at the centre of the measuring volume. The node with the furthest path per segment is indicated by a larger node and its route dashed. The node within the segment with the shortest route is represented by a larger node with a black outline and its route a solid line. The thin lines between nodes are representative of the paths within the segments. It can be seen that the segments work their way towards the ground station, thereby minimising wasted travelling time to and from the segment. This helps prevent risk *OP2*.Additionally it was found that the time for covering one layer was more than 10% smaller than the preliminarily calculated values in section 5.3.3. This is expected as the preliminary path planner lacked optimised routes.

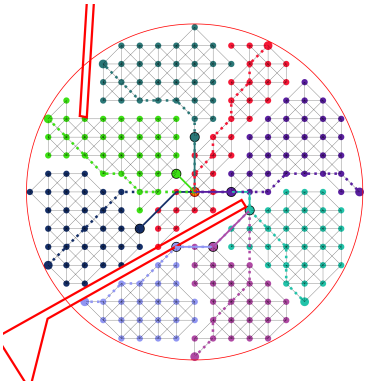

Figure 9.18: Segmented Path Plan

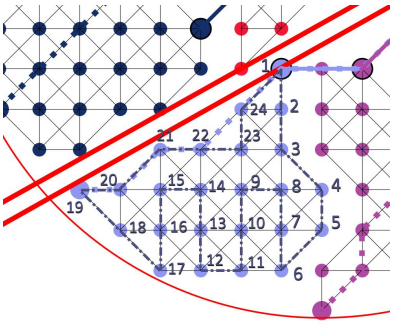

Figure 9.19: Segment Path Plan

This system is designed to operate at not just one airport (requirement *AEMS-F-OPR-11*). Figures 9.20 and 9.21 present different runway configurations. If one runway is being used for take-offs and landings, the drone would need to fly over the geo-caged runway volume (less preferred) or create two measuring volumes, on either side of the runway. This would be dependent on the airport's preference. If no routes can be found at all by the system, the customer and customer service will be notified for detection of the issue, assuming the software is unable to process the error. This mitigates risk *NV3* and more details can be found in chapter 17.

Finally, in the event the ground station has to be placed in a location with significant distance from the centre of the measuring volume, figures 9.22 and 9.23 show the path planning result with the ground station circled for clarity.

Local Re-meshing Coverage Chapter 8 mentions that local refinement is solved by the means of the GTs-

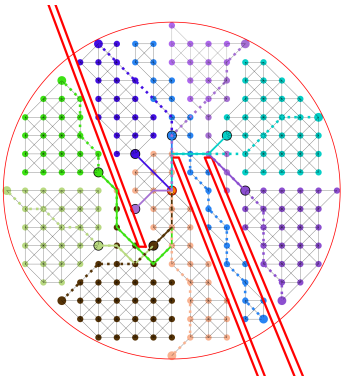

Figure 9.20: Airport Variation - 1 runway

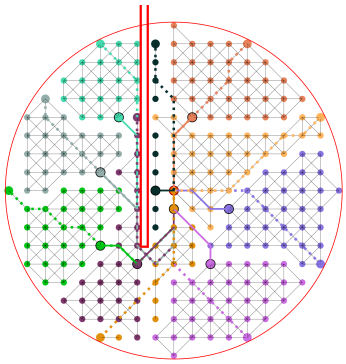

Figure 9.21: Airport Variation - 3 runways

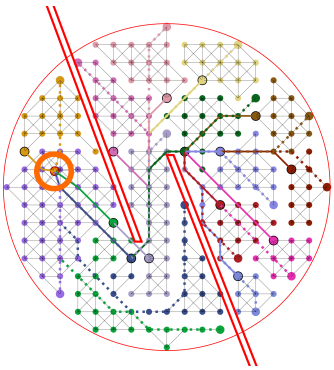

Figure 9.22: Non-centred Ground Station - Parallel Runways

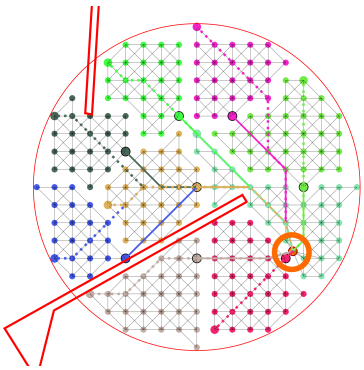

Figure 9.23: Non-centred Ground Station - Schiphol Runway Configuration

based cost assessment. The put corresponds to a list of points **I**. Since these points are not constrained to be grid nodes, a new path plan needs to be generated. This can be achieved the by same approach as detailed above.

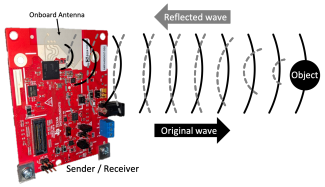

(a) Radar theory

(b) Radar setup to determine response from wall

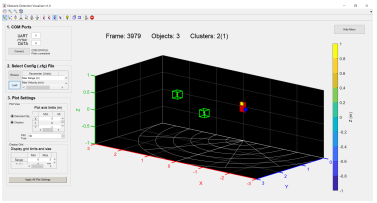

(c) Radar Setup and corresponding radar detection's

Figure 9.24: Radar theory and tests

9.2.3. Obstacle Detection and Avoidance Module

Unmanned, autonomous aerial vehicles require a on-board sense and avoid system that allows for the vehicle to detect and avoid obstacles in its path, the prevention of risk NV2 and to meet requirement *AEMS-F-AUT-04*. Radar sensors can operate in adverse weather conditions as well as provide direct range, angle and velocity measurements. A disadvantage of Radar is the interpretation of data due to the scatter present in a radar reading. Radar modules consist of a transmitter and a receiver. The transmitter uses an oscillating electronic circuit at a specific frequency to emit a signal through an antenna, this signal is in the radio-wave range of the electromagnetic spectrum. The transmitted impulse is sent as pulses in a beam such as shown in figures 9.24a. The receiver detects the signal as it is echoed off of objects in its path. Because the pulses

travel at the speed of light, which is a constant, the distance to an object can be calculated based on the time taken for the pulse to return.

The procedure followed by the drone to to detect obstacles in the path while manoeuvring from one way point to another is shown in figure 9.25. During operation, the radar is continuously sending and receiving radar waves. Once an object has been detected, the drone will begin to manoeuvre out of the way. The drone will start moving in the opposing direction of where the most detections where made. Figure 9.24c, shows output detection in the presence of a wall at a distance of 2 m. As can be seen in figure 9.24b, the radar detects two objects (both objects are the same wall), indicated by the green boxes. The output created by the setup in figure 9.24c, the radar has detected more objects on the right, and as such will begin to manoeuvre the left. This algorithm is able to avoid both stationary and moving obstacles.

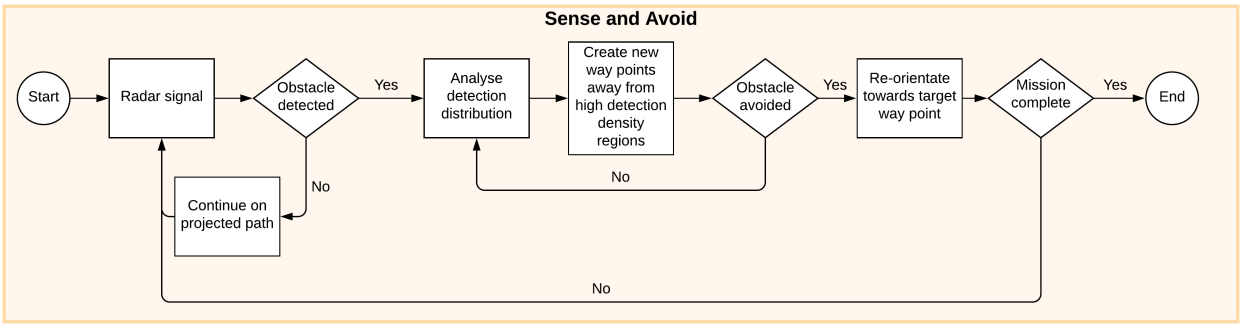

Figure 9.25: Flow chart indicating how the drone implements the Sense and Avoid module

9.2.4. Landing Module

The landing module is used to safely land the drone at the ground station. Previous methods for autonomous landing are based on location data provided by the GPS and inertial navigation system. This method can be very inaccurate and cause deviations of up to 3m [45]. As the drone will have to land on a charging platform, more accurate solution is required. More accurate navigation methods during the landing procedure can be achieved using pattern recognition. Using square planar markers one can accurately estimate the vehicles pose [35]. An example of a square planar marker is the ArUco marker which is shown in figure 9.26. The OpenCV library contains a ArUco module which can be used to locate a marker within a picture. The same library can be used to determine the location of the marker, which can be used to navigate the drone more accurately to the charging platform. The flow chart for the landing procedure can be found in figure 9.27. The pseudocode for the landing procedure algorithm is shown below in algorithm 1.

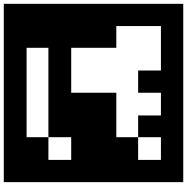

Figure 9.26: Example of ArUco marker

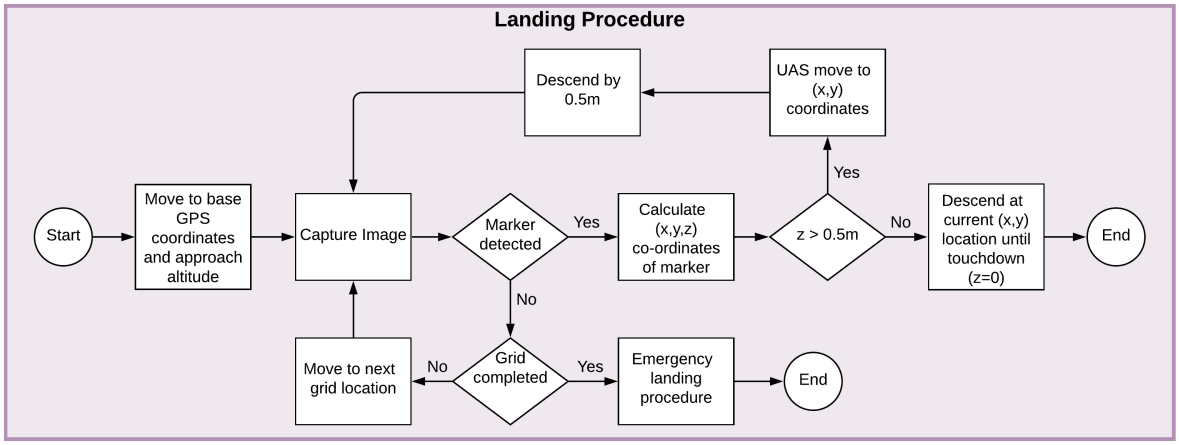

Figure 9.27: Flow chart indicating the landing procedure of the UAV

Algorithm 1: Landing algorithm

```
landed ← False;
x, y ← GetCoordinates();
z ← 4;
grids ← GridLocationArray(1-9);
while landed = False do
    for grid in grids do
        image ← ImageCapture();
        detection← MarkerLocate();
        if detection = TRUE then
            x_travel, y_travel ← GetMarkerDistance();
            Move(x_travel, y_travel);
            z -= 0.5;
            if z ≤ 0.5 then
                landed ← TRUE
            end
        end
    end
end
```

Should the marker not fall within the cameras field of view during the initial image capture, the drone will have to traverse the surrounding area to try locate the marker. The drone will scan a further eight areas, to see if it can identify the marker. The movement of the drone and the different areas to be scanned can be visualised in figure 9.28. Should the marker still not be detected, the drone will engage the emergency landing procedure. In order to comply with requirement *AEMS-F-AUT-11* the drone must be able to fly during the night, this will mean the camera will need to make use of a light, this is easy to implement and the chosen light was the ARC high intensity strobe light, this is because it can be easily connected to the autopilot through a micro-USB cable, it is cheap, lightweight and is FAA approved for use on drones, it has both a strobe setting for when the drone is flying and a fixed setting for use in landing, the cost of this light is €33.10 and it's mass is 4.5 g [15].

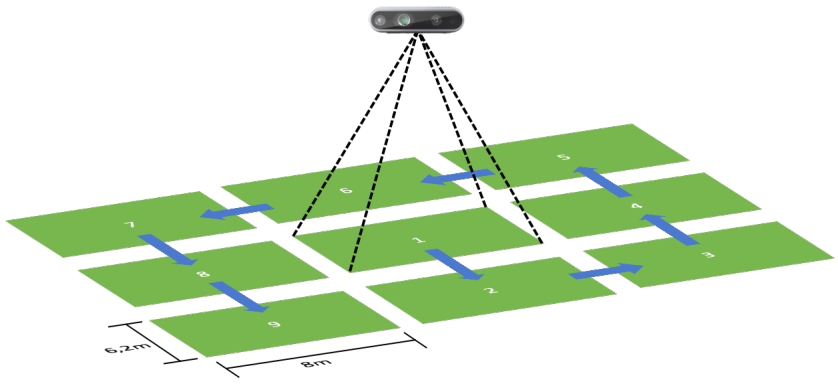

Figure 9.28: Drone movement if marker is not detected in scanned area

ArUco marker detection Python and OpenCV2 have a built in ArUco marker library. Integrating different elements from the library allows for the algorithm to not only detect the marker within a image frame, but it can also be used to determine the distance from the centre of the image frame to the centre of the AruCo marker. The detection algorithm is limited to images that contain the full marker. The results of processed images can be found in 9.29. The red arrows in sub-figures 9.29a and 9.29b indicate the trajectory, given in metres, required for a precise landing. Sub-figure 9.29c, the algorithm was not able to detect the full marker, and as such was not able to calculate the distance to the markers centre.

[15] `https://www.amazon.com/Firehouse-Technology-Approved-Flights-Quadcopter/dp/B073PMGLXR` [cited 21 June 2020]

Algorithm 2: Marker detection algorithm

```
edge length ← length of marker edge;
height, width ← image.size;
image_centre ← width/2, height/2 # Image origin (x,y = 0,0) found in top left corner;
if detection = TRUE then
    corner1, corner2, corner3, corner4 = CornerDetection() # [px_x, px_y];
    marker_centre = mean value of corner differences # [px_x, px_y];
    side_length = Average distance between corners # [px];
    distance_per_pixel = edge_length / side_length # [m/px];
    distance_to_marker = marker_centre - image_centre # [px];
    drone_travel_distance = distance_to_marker * distance_per_pixel # [m];
end
```

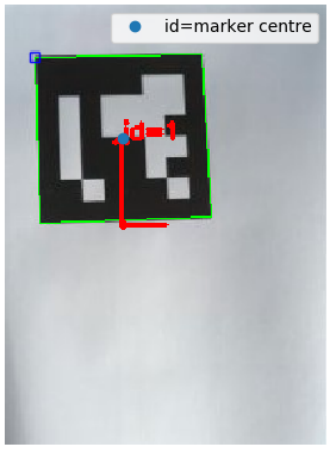

(a) Nearby marker found and trajectory needed for landing calculated

(b) Distant marker found and trajectory needed for landing calculated

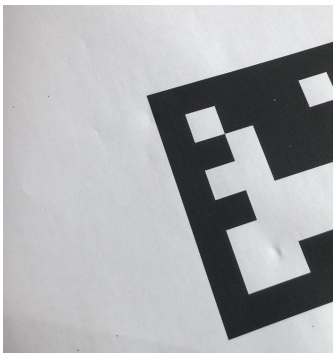

(c) Marker not identified nor processed

Figure 9.29: Aruco marker identification tests

9.2.5. Emergency Landing

A procedure needs to be implemented that can perform a safe landing of the drone in case of an emergency situation, this will be the mitigation strategy for risks *NV1*, *NV2*, *CS1*, *CS2* and *CS3*. This procedure needs to take place without the assistance of pattern recognition as explained in the regular landing module. A stereo vision camera is used to assess the angulation present in the terrain and whether any larger obstacles are in the way that may hinder the from executing a safe landing. The stereo vision camera outputs the different depth levels, represented as different colours on the image. The different colours from pixel to pixel can be used to find the difference in depth levels from one pixel to another. Large variations in colour from one pixel to the other indicate the presence of large varying depth value. These variations create a unsuitable landing location for the drone. An area suitable for landing will be seen in the image as an large area with very little to no variation in colour (as this indicates the area is rather flat).

Once the drone has received a signal to perform an emergency landing, the drone will descend to a height of 4 m and use the stereo vision camera to scan the ground. The scanned area, at a height of 4 m, will cover an area of 6.2 m by 8 m.The area within the captured image is analysed using an algorithm that determines areas, which have a minimum size of 2 m by 2 m, with little to no angulation. With a suitable area determined, the drone will manoeuvre to the desired location, and perform its descent. Due to this procedure only being implemented during emergencies, the drone will not be programmed to search for different areas to scan. If no suitable area is located, the drone will descend at the location it is currently hovering at. This procedure therefore enables the system to comply with requirement *AEMS-F-AUT-13*, the procedure can be implemented by programming it into the autopilots firmware in the safety protocols [16].

[16] `https://docs.px4.io/v1.9.0/en/config/safety.html` [cited 20 June 2020]

Algorithm 3: Emergency Landing algorithm

```
FOV_width ← 8 #m FOV_height ← 6.2 #m image ← ImageCapture();
height, width ← image.size();
gray_image ← RGBtoGray(image);
laplace ← LaplacianTransform(gray_image);
landing_size_height ← 2;
landing_size_width ← 2;
grid_width ← width*landing_size_width/FOV_width;
grid_height ← height*landing_size_height/FOV_height;
for i in range(0,height - grid_height) do
    for j in range(0,width - grid_width) do
        if region_scan() = TRUE then
            # region scan searches the image for large enough landing regions;
            x_landingpos, y_landingpos ← i,j
        end
    end
end
```

The pseudocode for the algorithm used to search for a suitable landing location during a emergency procedure is given in algorithm 3. The code recieves a stereo image as an input (see figure 9.30a). The image provides information about the different depth levels of the area where the picture is taken. The image is then converted to grayscale (figure 9.30b) so it can be further processed and a Laplacian operator is applied to the grayscale image (figure 9.30c). The laplace transformed image indicates the edges present in the image. Areas between edges are suitable for landing, and need only be further evaluated if they meet the minimum area size requirements. An example of a suitable are for the dummy image is indicated by the black rectangle in figure 9.30d.

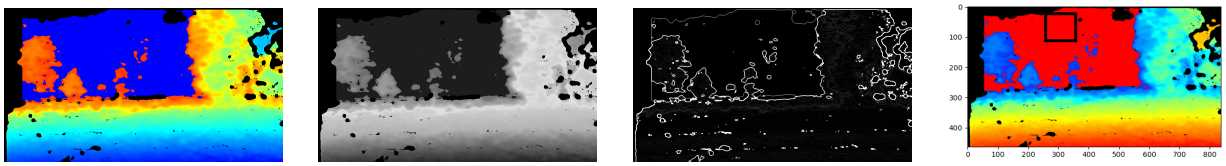

(a) Original Image [30] (b) Grayscale Image (c) Laplace transformed Image (d) Landing area overlayed on Image

Figure 9.30: Image processing used to determine landing area during emergency situations

9.3. Control

The control system of the drone will adjust the angular velocities of the propellers based on inputs from the various different sensors used during all phases of operation. The autopilot will be responsible for controlling how much power will be directed to each individual propeller motor through the ESC. The propellers of the drone will move in the directions shown in figure 9.32, the green arrow displaying the flight direction. In order for the drone to remain stable and not cause constant yawing the propellers that lie diagonally across from one another will turn in the same direction, and in an opposite direction to the ones neighbouring them, the propellers that lie directly above or below will also turn in the opposing direction. This is due to the moments caused by the propellers rotation.

Both the orientation and trajectory of the drone will be manoeuvred with regards to a body reference frame. The control system will take Euler angles, velocities, accelerations and sensory data as inputs and compute the changes in the motor velocities and accelerations needed to achieve a new, desired position or trajectory. The reference frames used are shown in figure 9.31 , with the X_b-axis being the longitudinal axis pointing ahead, the Y_b-axis the lateral axis, pointing in the direction such that the frame is right-handed and the Z_b-axis being the vertical axis pointing downwards, this frame is fixed to the drone body. This is all relative to the body of the drone. u,v and w are the velocities in the X, Y and Z directions (the inertial reference frame) respectively and ϕ, θ and ψ are respectively the angles around the axis' in the directions shown in the figure.

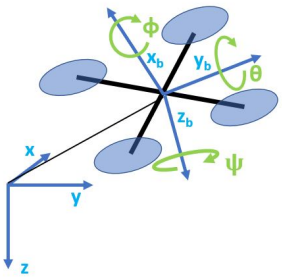

Figure 9.31: Reference frame

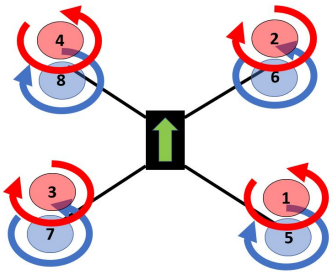

Figure 9.32: Coaxial octocopter propeller directions

An example of how the differing thrust levels produced by the drone can orientate it are shown in figure 9.33. By controlling the velocities of the different propellers, the trajectory of the drone can be controlled. It should be noted that both the drag and weight forces have been excluded from figure 9.33 as it is simply to show the relationship between the thrust settings, orientation and velocity of the drone. Figure 9.33d is the least intuitive relationship, it follows directly from figure 9.32 as the yaw is produced due to a reactionary moment produced by the larger torques from propellers 1, 4, 6 and 7.

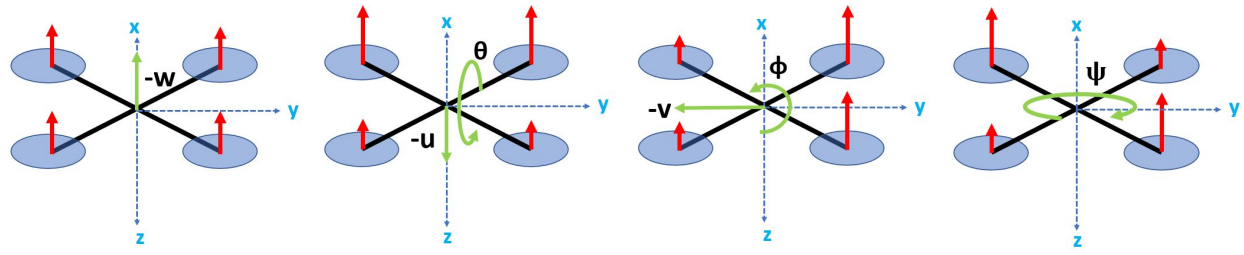

(a) Ascending (Control Input U_1)

(b) Positive pitch and negative velocity in the x axis (Control Input U_2)

(c) Positive roll and negative velocity in the y-axis (Control Input U_3)

(d) Positive yaw (Control Input U_4)

Figure 9.33: The relationships between the thrust levels, Euler angles and velocities

The control architecture of the drone is shown in figure 9.34. The figure shows how the inputs and outputs of each of the given components and subsystems are used as indicators or references for the drone to act upon or for another subsystem to use, these are the state parameters, this therefore fulfils requirement *AEMS-F-AUT-07*. The control inputs U_i are the inputs needed to perform different manoeuvres, as can be seen in figures 9.33, these are all functions of the angular velocities of the different propellers, Ω_i. The symbols p, q and r represent the roll rate, pitch rate and yaw rate respectively. $\dot{u}$, $\dot{v}$ and $\dot{w}$ are the time derivatives of u, v and w, the linear accelerations. $\dot{p}$, $\dot{q}$ and $\dot{r}$ are the angular accelerations in their respective directions and are the time derivatives of p, q and r. It should be noted that the X, Y and Z locations produced by the GPS-RTK system are those in the inertial reference frame, in order to be useful to control the trajectory and navigation of the drone they must be transformed into coordinates based on the body reference frame of the drone, this transformation is shown graphically in figure 9.31. The relationship between the inertial reference frame and body reference frame is shown in equation 9.3, where the letters s and c in the rotation matrix (R) stand for sin and cos respectively and the subscripts representing the Euler angles, for example $s_\phi = \sin\phi$. The system is under-actuated, this means there are more degrees of freedom than control inputs, therefore equation 9.3 shows how Euler angles are used for the transformation between reference frame, even for translation.

$$\underbrace{\begin{bmatrix} c_\psi c_\theta & -s_\psi c_\phi + c_\psi s_\theta s_\phi & s_\psi s_\phi + c_\psi c_\phi s_\theta \\ s_\psi c_\theta & c_\psi c_\phi + s_\psi s_\theta s_\phi & -c_\psi s_\phi + s_\psi c_\phi s_\theta \\ -s_\theta & c_\theta s_\phi & c_\theta c_\phi \end{bmatrix}}_{R} \begin{bmatrix} x_b \\ y_b \\ z_b \end{bmatrix} = \begin{bmatrix} x \\ y \\ z \end{bmatrix} \tag{9.3}$$

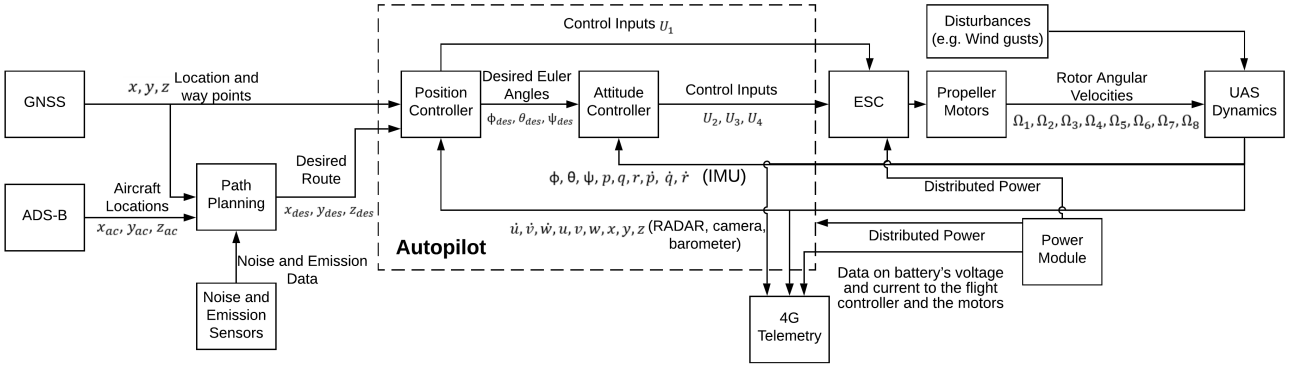

Figure 9.34: Control architecture

9.3.1. Stability

Centre of gravity range The coaxial octocopter design is inherently unstable, the stabilisation of the drone in flight must be done by controller inputs at all times. This does not mean however that an optimal centre of gravity (c.g.) range cannot be used for the system. The autopilot can be configured to handle most offsets of the centre of gravity from the geometric centre of the drone but it is suggested that the autopilot is located within a few cm of the middle of the drone and this is also true of the centre of gravity [17].

One important stability criteria is that the drone must not tip over during landing. The maximum default angle for the roll and pitch of the drone is 45°, this is set by the autopilot [18]. Figure 9.35 shows a simplified image of the forces and dimensions during an 45° roll landing, Where $L_b = 274\,\text{mm}$, $L_a = 526\,\text{mm}$ and $L_c = 70.71\,\text{mm}$. L_c is calculated from the clearance needed between the ground and the propeller, this was set at 50 mm.

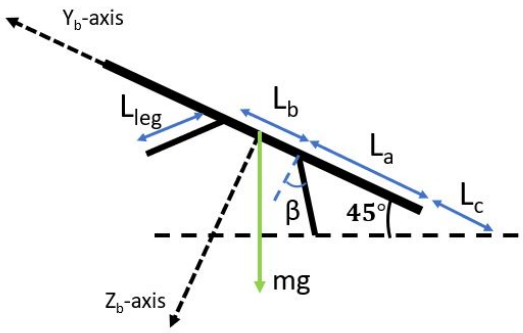

Figure 9.35: Simplified landing model at $\phi = 45°$

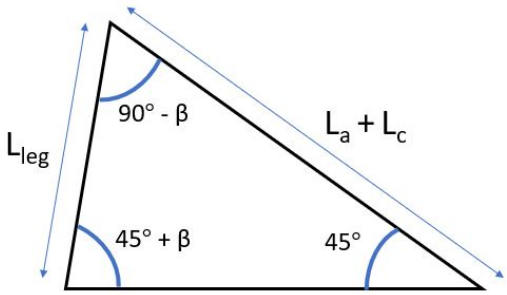

Figure 9.36: Leg length dimensions

The angle β in figure 9.35 is there to increase the spread of the legs, thereby increasing the stability of the drone during landing, this angle is set at 40° (this was chosen to be the optimal value after iterations were performed). Figure 9.36 shows how the length of the leg is determined by the previously mentioned constraints.

The length of the leg can then be calculated using equation 9.4. It is calculated that $L_{leg} = 557.7\,\text{mm}$. By taking moments around the leg that is touching the ground the centre of gravity margin (CGM) can be found, for all c.g. values within the CGM the weight of the drone should provide a restoring moment to land the drone on it's legs and not tip, at the edge of the CGM this moment will be zero, equation 9.5.

$$\frac{L_a + L_c}{\sin(45+\beta)} = \frac{L_{leg}}{\sin(45)} \tag{9.4}$$

$$0 = \frac{L_b}{2} + L_{leg}\sin(\beta) - CGM) - (L_{leg}\cos(\beta) \tag{9.5}$$

[17] `https://ardupilot.org/copter/docs/common-mounting-the-flight-controller.html` [cited June 16, 2020]
[18] `https://docs.px4.io/v1.9.0/en/flight_modes/altitude_fw.html` [cited June 15, 2020]

Upon calculation the CGM is found to be 61.26 mm, this means that the centre of gravity can be anywhere within 61.26 mm of the geometrical centre in the y_b in the positive or negative direction, this fits in the definition of a few centimetres given by the autopilot manufacturer.

As the drone is symmetrical it makes logical sense to therefore apply the same centre of gravity range in the z_b axis. Equating the distance from the geometric centre to the leg tip in the z_b direction to that in the y_b direction, the end of the leg skids can be found to be 488.48 mm from the geometrical centre of the drone. This will mean the drone will not tip over during landing, even during maximum roll and pitch making the system comply with requirement *AEMS-F-AUT-12*. These dimensions will be used to size and design the drone legs in section 10.1.2.

In-flight stability As mentioned the drone design is inherently unstable in-flight, meaning that the drone has to be stabilised by control inputs to the motors alone. Whilst flying the drone will have to make continuous adjustments in order to maintain stable flight. This is achieved by measuring the current state of the drone dynamics and comparing them to desired values, the controller then attempts to reduce this error by way of control inputs. The chosen autopilot system uses this method by changing the proportional error, the integrated error and the differential error, known as a PID controller. The basic architecture of a PID controller is shown in figure 9.37 A PID controller is used for motion in all six-degrees of freedom This way the drone can maintain stability throughout the operation. Before the drone goes into operation the controller gains K_p, K_i and K_d should be tuned during a test flight to ensure that the drone is stable and responsive to control inputs. By tuning these gains correctly risk *CS2* can be successfully prevented, in case the drone does become unstable these gains will have to be re-calibrated, as well as any control hardware, e.g, the IMU, this therefore is the risk mitigation strategy.

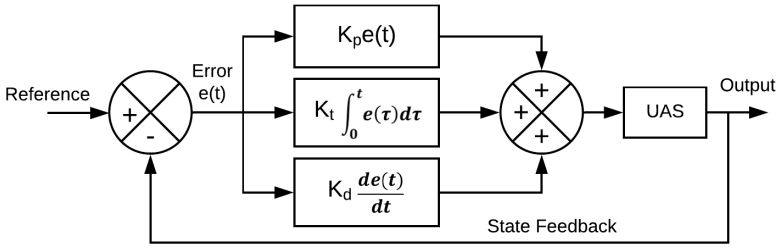

Figure 9.37: PID controller

9.4. Battery Replacement

A primary ground station is to be installed in or around the airport depending on the needs of drone, and this station is to fit under the budget requirement *AEMS-SH-FNCE-01*. It is to allow for maintenance of, communication with and storage of the vehicle of the system as stated by the operational requirements *AEMS-FCT-OPR-01*, *AEMS-FCT-OPR-02* and *AEMS-FCT-OPR-03*. The ground station is also required to check the weather and environmental conditions according to requirement *AEMS-FCT-OPR-04* to aid the decision of continuing with the scheduled operation or returning to the station. It shall be no larger than 2 m in any dimension to comply with requirement *AEMS-SH-DIMS-01*. For the drone to perform optimally and obtain as much data as possible, it should not have to dock for long periods at the ground station for charging before starting a new mission. To mitigate this, the batteries can be kept in a cycle in which a depleted battery can be exchanged for a fully charged one and then put on the charger itself, this cycle can be repeated, this approach complies with requirement *AEMS-F-AUT-06*. This will mean the ground station must be able to detach a depleted battery, replace it with a charged one and charge the depleted one. Research and prototyping by K.A.O. Suzuki, P.K. Filho and J.R. Morrison [39] has been studied as the system they designed for had to meet similar requirements. The devices and operations used for the housing, coupling, detaching and reattaching of batteries can be directly applied. The battery must be easily accessible and detachable whilst at the same time must be secure during flight, figure 9.38a shows a viable solution. As the battery is forced up against the lower angled surface it forces the sides out and allows insertion of the battery, the sides act as springs, as shown in figure 9.38b, and once the battery is placed correctly the battery terminals and drone terminals connect and the sides close into gaps into the battery housing, securing

the battery in place. Figure 9.38c shows how male connectors in the battery case and female terminals and plugs are used to connect the battery and the drone electronically. The '+' and '-' terminals in the battery case are there to power the drone when connected, these connectors are also used to recharge the battery. The numbered terminals represent magnets to secure the connection.

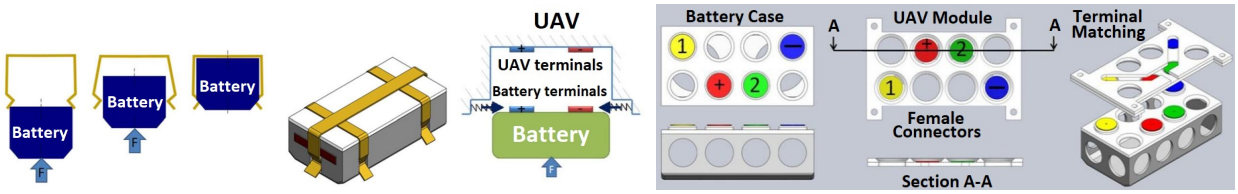

(a) Mechanical attachment for battery

(b) Battery connectors with mechanical coupler

(c) Terminal matching for connecting to the drone and charger

Figure 9.38: Mechanical attachment and electrical coupling of the battery[39]

The replacement system will be similar to that used in [39], however as only five batteries will be used in rotation the system can be made much simpler. The concept is shown graphically in figure 9.39. The system will use an electromagnet that can be turned on and off to connect to a ferromagnetic plate at the bottom of the battery housing, this can then pull the depleted battery out of the holding mechanism, by use of an actuator, to place the depleted battery on a lower platform on to tracks. The tracks then turn on and move the depleted battery into one of the two charging terminals and position a new, fully charged, battery to be placed into the drone by the actuator. The system in [39] was costed at approximately €1320, as mentioned this was a more complex system, however many of the hardware components are the same and the system proposed here is for a larger drone and bigger batteries, with this in mind €1320 is still a fair cost approximation.

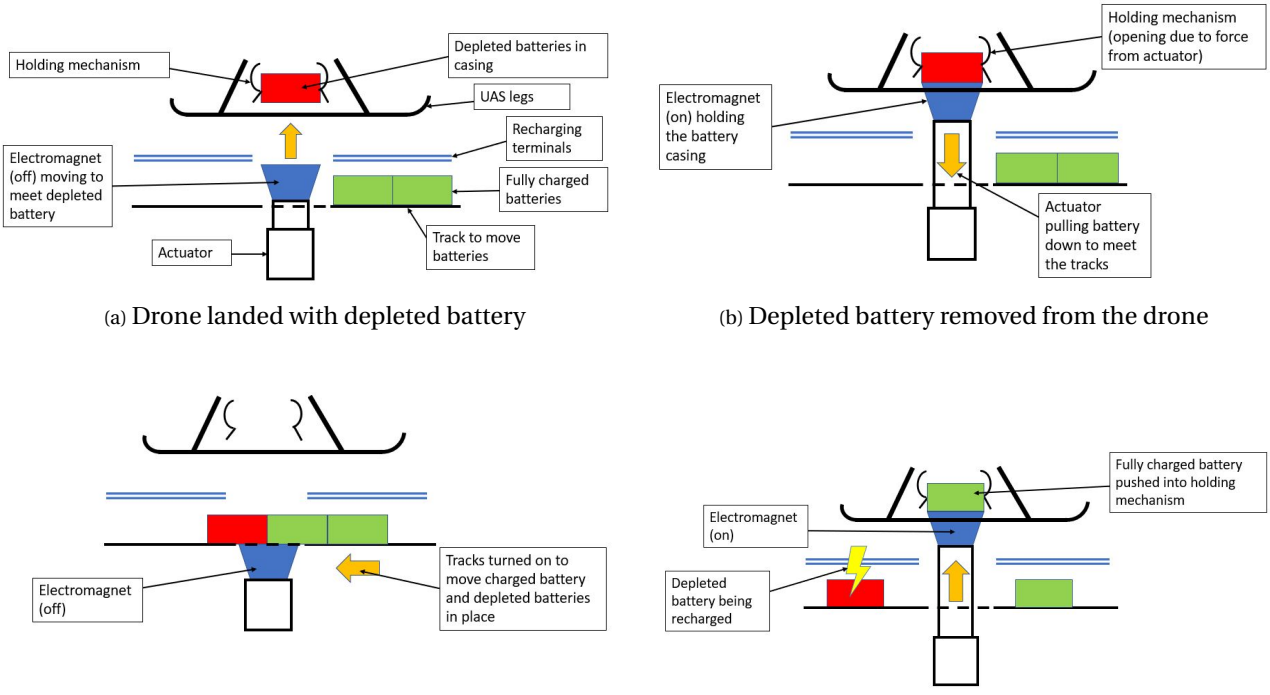

(a) Drone landed with depleted battery

(b) Depleted battery removed from the drone

(c) Track moves charged battery in place

(d) Charged battery placed in the drone

Figure 9.39: The stages of the battery replacement after landing

9.5. Verification and Validation

Path Planning The path planning program developed in section 9.2.2 was verified through hand calculations and larger mesh spacings. The program would print the furthest node and route, which could be

$$h = \frac{K_P s + K_I}{\frac{u_0}{g} s^3 + K_D s^2 + K_P s + K_I} h_{ref} \quad (9.6) \qquad h_{ref} = u + \frac{1}{2} a t^2 \quad (9.7)$$

calculated by hand. No issues were flagged. Individual functions were also tested by hand. This involved examining an intersection function and a function to make a list with unique contents. Again, with a greater mesh spacing, the results could be reproduced by hand. The function to calculate the number of points has already been verified in section 5.4. Finally the imported modules for path planning were extensively verified through the input of a problem with a known solution, the so called manufactured solution verification test. The routes could be visualised and verified by visual inspection. No issues were found here.

Navigation Controllers The autopilot system makes use of PID controllers to control and stabilise the drones velocity, altitude and attitude. An example of the control inputs were shown in figures 9.33. A general equation used for a PID controller is taken from figure 9.37, where the K parameters are gains that can be tuned in the autopilot software to produce the optimum stabilisation and control of the drone.

In order to validate that this type of controller is able to take reference values and respond by changing its trajectory, a simulation of the responses can be made. The simplest controller to simulate is the altitude controller (control input U_1) as the equations of motion are the simplest, and the control does not depend on the dimensions of the drone. Using equations found in [34] the transfer function for the altitude controller can be found used to adjust the altitude of the drone, equation 9.6, where u_0 is the signal that maintains constant acceleration and is found to be between 0.7 and 0.8, therefore it was assumed to be constant at 0.75[34]. The reference altitude used was based on manoeuvring the drone from a resting altitude, i.e. stationary on the ground or hovering, to a one metre increase in altitude at maximum vertical acceleration, this was calculated to be 12.38 m/s^2. The altitude calculation was made using the kinematic equation for constant acceleration, 9.7, where h_{ref} is the reference altitude, u is the initial velocity, a the acceleration and t is time.

This form of control always produces an overshoot between the reference height and the drone height. Figure 9.40 shows this overshoot to be 4.1%, it also shows that there is a time lag between when the reference altitude reaches one metre and the simulation reaches this point, this value is shown to be 0.15 s, this helps comply with requirement *AEMS-F-AUT-09*. Considering that the drone would be accelerating at it's maximal value and then stopping again after one metre, these values are considered very good. Therefore by using this kind of controller the drone is indeed able to navigate to locations based on reference inputs, this system will be the same for all controllers used by the autopilot. Figure 9.40 also shows that this method can achieve the desired criteria for the maximum overshoot and time lag needed to validate the system, this was achieved with the values for the gains as follows: K_p, K_I, K_d = 16, 0.8, 1.5.

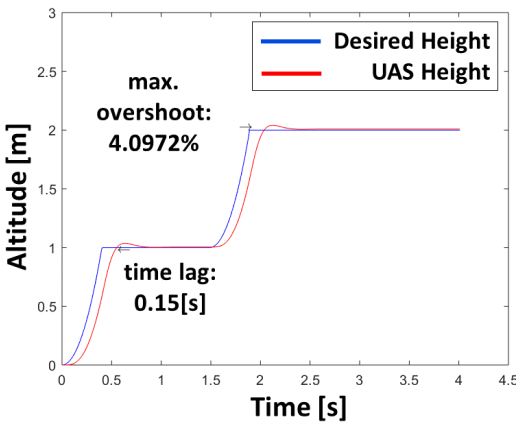

Figure 9.40: Simulated Altitude Controller

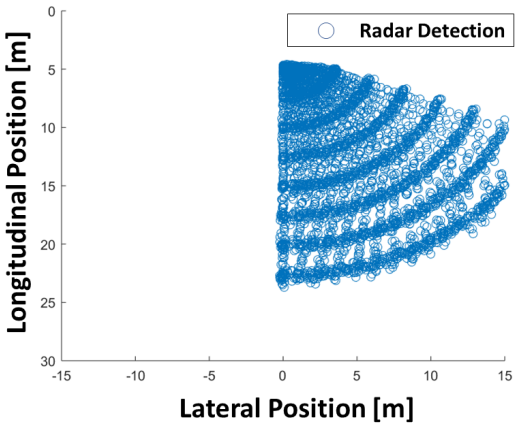

Figure 9.41: Radar detection data from an obstacle that is located to the left of the UAV

Another verification test that can be performed for the navigation system is testing whether the rotation matrix, R, does indeed transform position coordinates from the global reference frame into the body reference frame. This was done be writing a function in python that took global positions and Euler angles as inputs and returns positions in the body reference frame. The positions and angles that were used as inputs were

kept very simple and the results were compared with hand calculated coordinates for the expected body frame positions using python's *unittest* module. The results can be seen in table 9.6, all the values passed the unit test, meaning the results were the same as the expected coordinates.

Table 9.6: Unit test for coordinate transformation

Global Position (x,y,z)	**Euler Angles (ϕ,θ,ψ)**	**Expected Body Frame Position (x_b, y_b, z_b)**	**Test Result**
(0,1,0)	(45°,0,0)	$(0,\sqrt{2}/2,-\sqrt{2}/2)$	pass
(0,0,1)	(0,45°,0)	$(-\sqrt{2}/2,0,\sqrt{2}/2)$	pass
(1,0,0)	(0,0,45°)	$(\sqrt{2}/2,-\sqrt{2}/2,0)$	pass

Sense and Avoid It order to attempt to prevent risk *CS3*, the sense and avoid system with radar sensors must be verified and validated. The first step was to validate that the algorithm employed could use radar detection data to calculate the best path around an obstacles. This was achieved by simulating the drone moving in space and facing two different obstacle, the first being a wall mostly located to the left of the drone and the second to the right. It would be logical that faced with these scenarios the sense and avoid system should detect that the optimal route around the left wall would be to the right and vice versa. Figures 9.42 show that the algorithm does indeed work the drone can navigate around the obstacle in the most efficient way, from the image it can be seen that the drone has changed its trajectory to avoid the wall based on where the obstacle is, the algorithm adds new waypoints based on detections and their locations, this leads to the drone finding the most efficient path around the obstacle. The simulation was made using MATLAB® and the radar generator toolbox, the dimensions of the block were made to be similar to that of the drone and features such a the field-of-view of the radar were made to model the drone. The algorithm was written in accordance with the sense an avoid method presented in this section. The success of this test means the drone can comply with requirement *AEMS-F-AUT-04*.

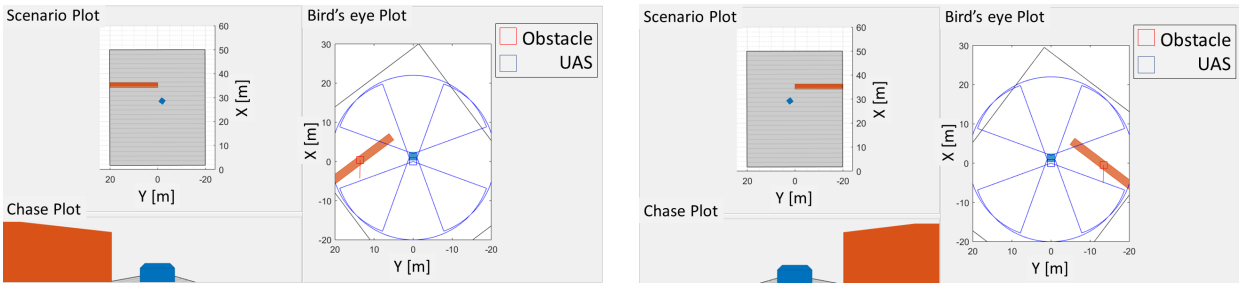

(a) Avoiding obstacle on the left

(b) Avoiding obstacle on the right

Figure 9.42: Simulation for the validation of the sense and avoid algorithm

To verify that the radar sensor data used in the above simulation is accurate to the data that would be produced by the radar sensor that is proposed a verification test is implemented. First a much simpler simulation, in which the drone block would move toward an obstacle that is offset from the drone to the left, was designed the drone will sense the obstacle and stop two metres away, the radar sensor data can then be displayed, this simulation is shown in figure 9.41. This shows the obstacle being located on the left of the drone, on the positive lateral axis, thereby verifying that radar data is suitable for use. This was made by adapting MATLAB®'s example simulation for radar detection [19].

9.6. Compliance of Requirements

There is still more work to be done, this can be in the form of tuning and calibrating software during test flights. Furthermore, algorithms presented in this chapter have only been validated using simulations. The validation conditions during the simulations are often idealised and the different algorithms should be

[19] `https://nl.mathworks.com/help/driving/examples/model-radar-sensor-detections.html` [cited June 26, 2020]

tested and implemented in a real life scenarios, where conditions are non-idealised. With this in mind, the list below shows the compliance matrix of the autonomy and navigation subsystem:

Autonomy and Control Compliance Matrix

Figure 9.43: Autonomy compliance matrix

Requirement ID.	✓ / o / x	Comment
AEMS-SYS-REG-04	✓	Section 9.2.1 ensures active runways are not breached.
AEMS-SYS-AUT-02	✓	No need for external input explained in section 9.2.2
AEMS-F-AUT-04	✓	Section 9.2.1 imposes boundaries for restricted zones. Section 9.2.3 avoids obstacles.
AEMS-F-AUT-06*	✓	Section 9.2.2 takes returning to the ground station into account during path planning and section 9.4explains the replacement of depleted batteries autonomously.
AEMS-F-AUT-07	✓	Section 9.3 state parameters are measured by the autopilot.
AEMS-F-AUT-08	✓	Section 9.2.2 ensures returning to the ground station into account for path planning
AEMS-F-AUT-09	✓	Section 9.5 shows the control response is fast enough with section 9.2.2 explaining how the path planning does not delay this response time.
AEMS-F-AUT-10	✓	Section 9.1 radar sensor that complies is chosen.
AEMS-F-AUT-11	✓	FAA approved light to enable flying and landing at night, section 9.2.4.
AEMS-F-OPR-11	✓	Section 9.2.2 presents various airport configurations
AEMS-F-AUT-12	✓	The legs are designed to prevent tipping, section 9.3.1.
AEMS-F-AUT-13	✓	An emergency landing protocol is established in section 9.2.5.

10

Structures Subsystem

This section will discuss the structural frame of the drone. The ground station mentioned in section 9.4 is not discussed, as this is beyond the scope of this project and will have to be done in future development. The structure should provide room for the sensors previously selected, as well as handle all loads the drone experiences. First of all, the requirements for the structure are presented below. Based on these requirements the frame will be designed, which is shown in section 10.1, and the tools used to create the design are validated and verified in section 10.2. Lastly, a compliance matrix is presented in section 10.3, to show that the structure does indeed adhere to all the requirements.

The structure subsystem has several requirements defined in the previous stages of the design process. All of the subsystem requirements can be found below.

Structures Subsystem Requirements	
AEMS-F-STR-01	The system shall provide structural integrity in case of a crash from a height of 110 m [Risk ST-03]
AEMS-F-STR-02	The structure of the system shall be able to sustain operational loads up to 280 N [N2 chart, Risk ST-01]
AEMS-F-STR-04	The system shall include a shield to protect the sensors during on ground operation, transportation and storage [N2 chart,Risk PL-03]
AEMS-F-STR-05	The system's shielding shall not interfere with the sensors while measuring [SH-DATA-01,-02,-03]
AEMS-NF-STR-MAT-01	The system (excluding the sensors inside the payload) shall only contain materials with a LOI higher 22.0 [D4S]
AEMS-NF-STR-MAT-02	The system shall not contain any materials that cost more than 200 €[2020] kg^{-1} [SH-FNCE-01]
AEMS-NF-STR-01	The system shall have a maximum frame length of 0.37 m [RADAR specification]
AEMS-NF-STR-02	The system shall have a maximum frame width of 0.37 m [RADAR specification]
AEMS-NF-STR-03	The camera shall be placed at the bottom of the structure [Autonomous landing]
AEMS-NF-STR-04	The GPS shall be placed at on top of the structure [GPS specifications]
AEMS-NF-STR-05	The ADS-B receiver shall be placed at on top of the structure [ADS-B specifications]
AEMS-NF-STR-06	The RADAR shall to places without other object blocking it [RADAR specifications]
AEMS-NF-STR-07	The battery shall be placed at the bottom of the structure [Autonomous battery changing]

10.1. Design and Sizing

The first step in designing the structure is to analyse which loads affect the system. There are three main components of the system; the body which carries all the payload, the arms on which the propellers will rest, and a boom. First, the sizing of the body will be discussed in section 10.1.1, then the sizing of the arms and legs in section 10.1.2.

10.1.1. Body

The body must have space for all the sensors, battery, and autonomous navigation hardware. Each of the different components had several requirements about where they have to be placed. With these requirements in mind the body was sized. There will be a protective case which contains the sensors and hardware, such that risk *PL2* is prevented. The internal layout of this case can be seen in figure 10.1. First of all, the gas sensor box, the DC/DC converter, and the PM02 are placed as depicted in figure 10.1a. The Raspberry pi and Pixhawk are placed on top of the UFP sensor, with a layer of isolation tape in between to prevent the heat from influencing the sensors. The power module is placed on top of the particle matter sensors, as shown in figure 10.1b The sound, humidity, and temperature sensors are not depicted in these diagrams, as these are small (< 0.005 m) in comparison to other components. The eight normal frequency MEMS will be distributed evenly along each side of the inside of the protective case. A small hole in the case will allow for accurate measurements. The two low-frequency MEMS will be placed opposite from one another, and will also require a small hole in the protective case, as well. This results in a final protective payload box of 0.230 m by 0.260 m by 0.09 m. The RADAR sensors are placed in the middle of each side of the case, such that they are not blocked. Lastly, the GPS and ADS-B receiver are both mounted on top of the case as well, such that signal is not blocked. The battery and camera are placed below the sensors and hardware. The size of the battery is not equal to that of the protective case, due to the geometrical shape of the modules used in the battery. In order to place 16 batteries, the battery case must have a size of of 0.249 m by 0.296 m by 0.0345 m. The camera will be placed next to the battery. The gas sensor box has fans inside to control the flow through the sensors, however, the fan can also be used to cool the batteries, which are placed below this.

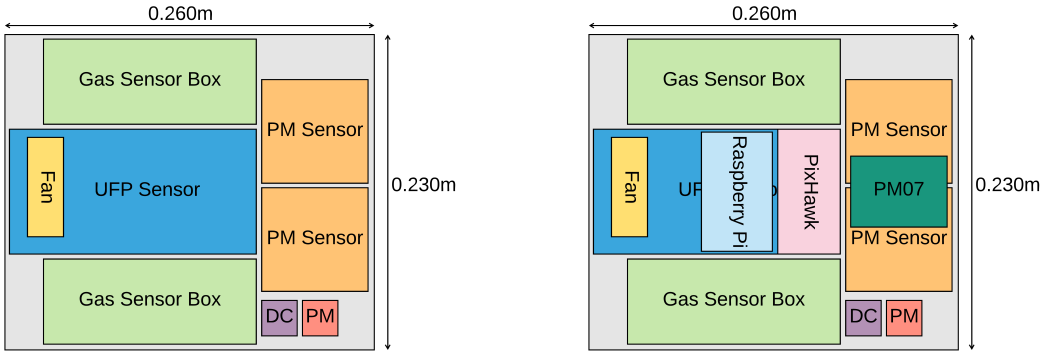

(a) Bottom layer payload

(b) Top layer payload

Figure 10.1: Top View of payload lay-out

To determine the mass of the body, there are several components that need to be taken into account. These components are the battery case, the clamps which hold the battery, and the protective case around the sensors and hardware.First of all, the battery case protects the batteries from the environment. It does not have to sustain a lot of loads, therefore it was decided to 3D print the housing with the plastic PETG. PETG is water-resistant, does not degrade because of UV radiation, and is fully recyclable [17], thus taking into account the end-of-life strategy for sustainability. A minimum manufacturing thickness of 0.001 m is required for PETG, so this shall be the thickness of the case, and therefore *MF1* is prevented. This results in a mass of 0.227 kg for the battery casing, since the density of PETG is 1.23×10^3 kg m^{-3} [17]. Besides the battery casing, it is also needed to have a magnetic plate at the bottom of the battery casing. This is necessary for the autonomous battery switching, as mentioned in section 9.4. It was decided to use stainless steel due to its magnetic properties. Stainless steel has a high density, however materials with lower density could not be used, because of their brittleness or environmental impact, following the sustainability strategy material

use. Stainless steel has a minimum manufacturing thickness of 0.001 m, therefore this will be the minimum thickness, preventing *MF1*. The plate will have the size of the battery case, 0.249 m by 0.296 m, resulting in a mass of 0.546 kg, as the density of stainless steel is 7.45×10^3 kg m^{-3} [17].There are also the clamps that hold the battery in place. The clamps have to be flexible such that they move when the battery is pushed into place, as previously mentioned in section 9.4 and visible in figure 9.38a. Besides being flexible it is necessary to carry the loads. It was decided to have eight clamps to carry the battery, distributed according to figure 10.3. The dimensions of each clamp are shown in figure 10.2. What is not shown in this diagram, is that the clamp is 0.02 m wide and 0.002 m thick. The clamps will be made of the plastic PLA, because this has a higher flexibility modulus when compared to PETG, but still has the strength to carry the battery case. The total mass of all the clamps will be 0.079 kg, based on the dimensions of the clip, the length and width of the battery case, and the density of PLA, which is 1.24×10^3 kg m^{-3} [17].

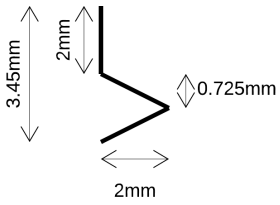

Figure 10.2: Dimensions of the clamp

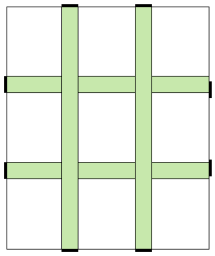

Figure 10.3: Distribution of the clamps

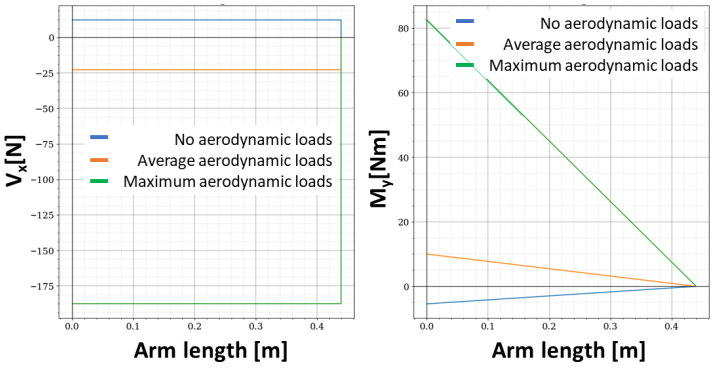

Figure 10.4: Shear and Moment plots of three different load cases

Lastly, the mass of the protective case around the sensors will be determined. This must protect the sensors and hardware from the external sources and such as water, as well as protect the sensors during a crash. It was decided to use cyanate ester with high modular carbon fibre to create the protective case. This has excellent durability against water and UV radiation, and an impact strength of 82 kJ m^{-2}, which is high compared to the typical value of 40 kJ m^{-2} for epoxy with high strength carbon fibre [17]. The protective case will be an open box, which can be clipped on the frame. The mass of the protective box will be 0.240 kg, based on a density of 1.62×10^3 kg m^{-3} [17]. This results in a total structural weight for the body of 0.240 kg + 0.079 kg + 0.546 kg + 0.227 kg = 1.09 kg

10.1.2. Structural Arms and Legs

Now that the body had been sized, the arms and legs of the drone can be done. First of the all the arms will be discussed, these will carry the motor and propellers. There will be two loads affecting the arm, the weight of the motor and propeller and the lift created by them. In order to size for this, it was decided to simplify the arm, as a cantilever beam, thus a fixed end connected to the body and a free end on which the motor and propeller are located. There are three load cases considered.

- Case 1 no aerodynamic loads: only the weight of the motors is affecting the arm (W_{mot}). The free body diagram (FBD)is presented in figure 10.5a.
- Case 2 average aerodynamic loads: the weight of the motors and thrust is effecting the arm. The thrust is average as used during hovering (T_{hov}). The FBD is depicted in figure 10.5b.
- Case 3 maximum aerodynamic loads: the weight of the motors and thrust is effecting the arm. The thrust is maximum (T_{max}). The FBD is shown in figure 10.5c.

The reaction force (F_r) and reaction moment (M_r) can be calculated by moment and force equilibrium. However, for this the length of the arm should be known. This is dependent on the propeller, since the arm should be a minimum length of the propeller radius or else it will make contact with the body. The radius of the propeller is 0.4028 m and adding clearance results in an arm of 0.440 m. The propellers will have at least 0.04 m clearance between them. Now the resultant forces and moments can be found, as well as the corresponding moment and shear diagram. The mass of the motor is 0.630 kg, the average thrust is 35.1 N, and the maximum thrust is 200 N. The shear and moment diagrams of the arm are presented in figure 10.4. These maximum values with a safety factor of 1.5 will be used to design the arm. A safety factor is used to

(a) Free body diagram with no aerodynamics loads

(b) Free body diagram with normal aerodynamics loads

(c) Free body diagram with maximum aerodynamics loads

Figure 10.5: Free body diagrams of the arm of the drone

prevent early failure, and thus risk *ST1* is prevented.

The forces that affect the arm of the system have been defined, so the arm can be designed to withstand these loads. It was decided to use a hollow circular tube for the arms. A circular cross-section does not have any stress concentrations, which are present in corners. A circular cross-section is symmetrical in all directions, thus if the thrust is angled to change in direction, the arm will still be able to withstand all loads. First of all the bending stress will be discussed. To calculate the bending stress equation 10.1 is used, in which M is the bending moment, y is the maximum distance from the neutral axis, and I is the moment of inertia. The bending stress can be found from the moment diagram and multiplying with an additional safety factor of 1.5, the stress is the yield stress of a material, and the distance from the neutral axis is the radius (r) of the arm. Equation 10.1 can be rewritten to equation 10.2 to find the minimum thickness (t_{min}) for a given radius of the arm.

$$\sigma = \frac{My}{I} \qquad (10.1) \qquad \frac{\pi}{4}r^4 - \frac{\pi}{4}(r - t_{min})^4 = \frac{Mr}{\sigma} \qquad (10.2)$$

A similar approach can be used to find the minimum thickness to withstand the deflection of the arm. To calculate the deflection of a cantilever beam with a single load equation 10.3 is used, which can be rewritten to equation 10.4 to find the minimum thickness for a given radius of the arm. The deflection presented by δ, is assumed to be 0.002 m, P is the load applied at the end of the arm, and E is Young's modulus of a material.

$$\delta = \frac{PL^3}{EI} \qquad (10.3) \qquad \frac{\pi}{4}r^4 - \frac{\pi}{4}(r - t_{min})^4 = \frac{PL^3}{\delta E} \qquad (10.4)$$

The arm should be as light as possible to optimise flight time, so the next step is to find the optimal combination of radius and thickness to minimise the weight. Both equation 10.2 and 10.4 find the minimum thickness for a given radius. A range of radius spreading from 0.01 metre to 0.05 metre is used to find their relative minimum thickness, for both bending and deflection. The higher value of the two is the most critical and this should be used to calculate the weight of the arm. Several different materials are tested to find the minimal weight. The minimum manufacturing thickness was also considered, because the parts should also be created, as a prevention strategy for risk *MF1*. If the minimum manufacturing thickness turns out to be higher than the critical thickness, the manufacturing thickness will be selected to find the weight. All materials and their mechanical properties are presented in table 10.1. Using these properties in combination with the maximum load case presented in figure 10.4, which is case 3, and equation 10.2 and 10.4 the weight of the arm is found. The radius is plotted against the weight as can be seen in figure 10.6. It can be seen that for each material there is a minimal weight. It was decided to use cyanate ester with HM carbon fibre, because it had the lowest weight at a low radius. This results in a radius of 0.024 m and a thickness of 0.002 m A low radius is desired as this is less surface area and thus less drag. HM cyanate ester also has a large impact strength, which is desired in case of a crash (assisting in prevention of *ST1*).

The arm should also able to withstand the shear caused by the loads. To calculate the shear stress (τ), equation 10.5 is used. In which V represent the shear stress, which is the absolute maximum value in figure 10.4, $\overline{A}$ is the area of the cross-section and $\overline{y}$ is the distance from the neutral axis to the c.g of the cross-sectional area. The shear will be the highest at the neutral axis of a hollow tube, thus $\overline{A}$ becomes a half circle and $\overline{y}$ will be the distance between the neutral axis and the c.g. of the semi-circle. The moment of inertia can be found with a radius of 0.024 m and a thickness of 0.002 m This results in shear stress of 2.03×10^6 Pa, thus the arm can also withstand shear. Therefore, the arm shall have an outer radius of 0.0024 m, with a

Table 10.1: Material Characteristics

Material	**Yield Strength [MPa]**	**Young's Modulus [MPa]**	**Manufacturing Thickness [m]**	**Density** [kg m^{-3}]
Cyanate Ester with HM Carbon fibre	607	101e3	0.002	1.67e3
Epoxy with HS carbon fibre	450	44.2e3	0.002	1.61e3
PA66	276	29e3	0.001	1.35e3
PARA	223	20.5e3	0.001	1.81e3
Aluminium 7074	576	71e3	0.001	2.85e3

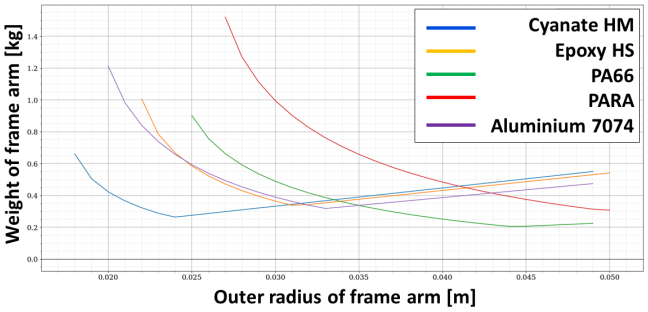

Figure 10.6: Weight of the arm plotted against the radius of the arm for different materials

thickness of 0.002 m, resulting in a weight of 0.264 kg per arm.

$$\tau = \frac{V \cdot \overline{y} \cdot \overline{A}}{I} \tag{10.5}$$

$$\sigma = \frac{F}{A} \tag{10.6}$$

Now that arms have been sized, the legs can be designed. The geometrical dimensions were given in subsection 9.2.4, however this section will discuss the materials and how the legs will be placed. It is common for the legs of drones to be placed at the corner of the body. However, due to the propellers also being mounted at the bottom of the arm, the propeller and legs would collide during flight if placed in such a way. Therefore another solution has to be found. It was decided to use the configuration depicted in figure 10.7. The endpoints are still placed in such a way that the drone will not tip over during landing. The loads will only be affected by the weight of entire system. The entire weight of the system is assumed to be 15 kg, this is used to size the legs. This assumption is based on the weight of the previously selected component, such as the sensors and weight of the body.

Using equation 10.3 and 10.6.For which σ is the compressive strength, F is the force applied, thus the weight of the entire system, and A is the area. A safety factor of 1.5 is added to weight, to make sure the legs do not fail prematurely, to prevent risk *ST1*. In case the weight turns out to be higher than 15 kg, the legs will have to reevaluated, thus mitigation risk *ST1*. The legs will be made of cyanate ester with HS carbon fibres, due to the high strength as well as impact strength. The landing is autonomous and might not always be gentle, so the structure must be able to handle the impact. Similar to the arm, the legs will also be hollow circular tubes. It will have a radius of 0.015 m and a thickness of 0.003 m, this will ensure that the compressive strength of cyanate ester of 317×10^6 Pa [17], in not reached and the reflection is less than 0.002 m. This results in a weight of 1.360 kg, using the dimension given in 10.7 and a density of 1.62×10^3 kg m^{-3} [17].

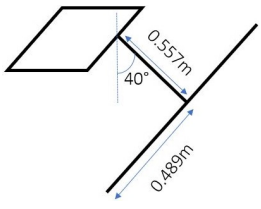

Figure 10.7: Schematic overview of the legs of the drone

Lastly, there will a plate to which the legs and arms can be mounted to. This will be made of cyanate ester with HS carbon fibre. It will have the length and width of the body, and a thickness of 0.004 m, resulting is a weight of 0.304 kg. Thus the total weight of the arm, legs, and frame becomes 2.720 kg.

10.2. Verification and Validation

In order to design and size the structure of the drone, several tools have been created in python. In this section these tools will be verified and validated.

Software Verification In order to solve equation 10.2 and 10.4, the solve function in the sympy module of python was used. To verify this function, equations with known outcomes were tested, such as $x^2-2x+1=0$. The solve function indeed gave the expected results, such as in the example given $x=1$. Equation 10.2 and 10.4, are also verified by plugging in the calculated thickness and checking if indeed the assumed deflection of 0.002 m and the yield stress of the material is the output. This is indeed the case and therefore the tool used to design the arm is verified.

Validation To perform a first validation check, the total mass of the structures it was compared to another drone of similar size, namely the ANGDA YD6-1600L Hexacopter. This has a structural mass of 2.273 kg. The total structural mass of the drone is 3.809 kg, so there is a difference. This could be explained due to the fact that the battery housing was included in the structural mass. This is not the case for the ANGDA YD6-1600L Hexacopter. Moreover, there is a 0.546 kg metal plate included for the drone, this is not present for the reference drone. Lastly, the landing gear of the reference drone is smaller when compared to the current system, thus also resulting in a lower weight. To finish the validation a test campaign needs to be performed, to assess the load and fatigue performance. They are part of the certification process as discussed in chapter 22.

10.3. Compliance of Requirements

At the beginning of this chapter all requirements for the structure were presented. In the list below it is presented if the structure adheres to all of these.

Structures Compliance Matrix

Requirement ID.	✓ / o / x	Comment
AEMS-F-STR-01	o	High impact materials are used, but extensive crash tests should be performed in future development
AEMS-F-STR-02	✓	The arm was designed to handle these loads, including a safety factor
AEMS-F-STR-04	✓	There is a protective case around the sensors
AEMS-F-STR-05	✓	All sensors are not obstructed in anyway
AEMS-NF-STR-MAT-01	✓	All materials are selected with this constraint
AEMS-NF-STR-MAT-02	✓	All materials are selected with this constraint
AEMS-NF-STR-01	✓	The frame length is 0.260 m
AEMS-NF-STR-02	✓	The frame width is 0.230 m
AEMS-NF-STR-03	✓	The camera is placed at the bottom
AEMS-NF-STR-04	✓	The GPS is placed on top of the protective case
AEMS-NF-STR-05	✓	The ADS-B receiver is placed on top of the protective case
AEMS-NF-STR-06	✓	The RADAR is placed on each side of the protective case
AEMS-NF-STR-07	✓	The battery is mounted to the bottom on structure

11
Power Subsystem

The next step in the design is to select a power system which can power the selected sensors, as well as the propulsion system. The power system is designed and sized in section 11.1. Finally, it is checked if the set requirements are met by the power system in a compliance matrix, shown in section 11.2. The requirements all stem from the functional analysis, risk assessment and the sustainability criteria.

Power Subsystem Requirements	
AEMS-SYS-EPS-01	The system shall, at all times, provide power to all subsystems, unless not under operation [FBS - 3.1.1.1].
AEMS-F-EPS-01	The system shall be able to connect to a re-chargeable power source. [FBD - 3.5.3.1]
AEMS-NF-EPS-02	The power system shall be replaceable. [PW1, PW 2, FFD - 3.5.3]
AEMS-NF-EPS-03	The power system shall not catch fire and thereby damage other subsystems. [PW2]
AEMS-NF-EPS-04	The power system shall be properly maintained [chapter 18 - PW2 and D4S, chapter 4]
AEMS-F-EPS-05	The power system shall have an operating voltage of 37 V. [section 12.6 chapter 12]
AEMS-F-EPS-06	The power management network shall supply the correct specified voltage range to each subsystem [FBD - 3.1.1.2]
AEMS-NF-EPS-07	The on board power source shall not leak during the entire lifetime of the system. [D4S, chapter 4]
AEMS-NF-EPS-08	The power system shall be designed for end-of-life requirements [Risk-PW1]

11.1. Design and Sizing

The design of the power system involves picking a battery cell and configuration, selecting a charger for the battery, a power distribution network and making sure the battery operations can be done safely. In [3], the LiPo battery technology has already been selected. At this stage of the design, a specific model of that battery technology is selected. The number of cells and cell configuration will not yet be determined, due to its dependence on the motor selection, which is done in chapter 12. Although chapter 12 follows from this, its results are used to determine other characteristics of the power system.

Battery cell selection A large dataset from EEMBS[1] was consulted to compare numerous Lithium Polymer cells. Ultimately, LP623454 cell was selected and figure 11.1 shows the gravimetric energies of 234 LiPo cells. From these cells, the three cells with the highest energy density, and a cell with high volumetric energy were selected and are shown in table 11.1. Eventually, the LP623454 was deemed the most optimal, because it is both gravimetrically and volumetrically energy-dense. The C-ratings are all acceptable, as they can support twice the nominal power output.
As further detailed in section 12.6 in chapter 12, a 10 S 16 P configuration has been chosen for the battery, based on the power requirement for the motor, which needed a nominal operating voltage of 36 V. The

[1] https://www.eemb.com/battery/rechargeable-battery/li-polymer-battery.html

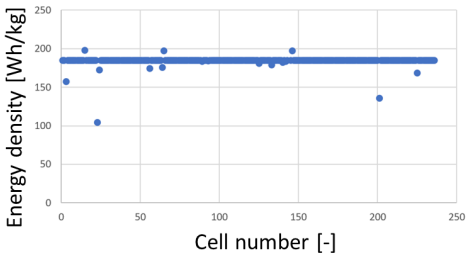

Figure 11.1: Specific Energy comparison of LiPo batteries

sizing of the battery was done in accordance with the motor needs and thus with requirement *AEMS-F-EPS-05*. The costs of the cells are all comparable, as they are from the same manufacturer. If a bigger cell with more capacity is selected, the total number of cells for a certain flight time is not as high as for a small cell with a low capacity.

Table 11.1: Batteries with highest energy density from figure 11.1

Model	Capacity [mAh]	Volume [mm^3]	Weight [g]	Specific Energy [Wh/kg]	C-rating	Charge Current [-]	Volumetric Energy Density [Wh/m^3]
LP401730	150	4.3x17.5x31	2,8	198.2	2	1	237 917
LP402535	320	4.3x25.5x36	6	197.3	2	1	299 944
LP523090	1450	5x30x90	29	185	2	1	397 407
LP623454	1200	6.2x34.5x54	22,5	197.3	2	1	384 396

Power Distribution Network The distribution of power to the other subsystems is key to perform the mission and is required by *AEMS-SYS-EPS-01*. Figure 11.2 schematically shows all subsystems that require power and how all these components are intrinsically linked. It also displays the operating voltages and connection types.

To meet requirement *AEMS-F-EPS-06*, the power modules have to supply the adequate electrical characteristics. These are represented by the pink boxes in figure 11.2. They transform the voltage of the battery, which ranges from 42 V when fully charged to 35 V when almost empty, to the required voltages of the component being powered. Note that this diagram only displays electrical properties. The data handling properties are described in figure 13.6. The PM07 is a power distribution and conversion module that is compatible with the Pixhawk 4 and can connect to the ESCs, while getting its power supply from a maximum 12 S (equivalent to 44.4 V) battery. The ESCs in turn are picked in parallel with the motor in chapter 12, so they are assumed to be fully compatible. The cooling fans have an operating voltage of 24 V. This is why a DC-DC converter[2] is placed between the battery and the cooling fans. Finally both the Arduino Micro and the Raspberry Pi require 5 V, yielding the need for a 37 V to 5 V converter, which can be done by the PM02 power module. The reason why both an Arduino and a Raspberry are present, is because neither can connect to as many sensors as required by this system.

Battery Protection and Treatment To fulfil requirement *AEMS-NF-EPS-03*, the battery shall be treated properly, protecting it against failure and catching fire. This includes protection over-charging, over-discharging, short-circuiting and over-current. An electric component that prevents these events from occurring is a battery protection circuit. It monitors the battery's voltage and switches it automatically off if it becomes too low. During charging, it also functions as a charge balancer, making sure that all batteries are evenly charged.

The Battery Management System (BMS) from SunPowerBattery has the right specifications for protecting a 10 S 37 V 19.2 AhLi-Polymer battery pack. It is 112 mmx 53 mm x 5 mm [3]. 16 of these BMS will be required. One for each 10 S module that is in parallel. They can be mounted below the battery pack. This element

[2] `https://www.meanwell.com/webapp/product/search.aspx?prod=SKMW06#1` [cited 20 June, 2020]

[3] `http://www.batterysupports.com/36v-37v-42v-10s-30a-10x-36v-lithium-ion-lipolymer-battery-bms-p-265.html` [cited 20 June, 2020]

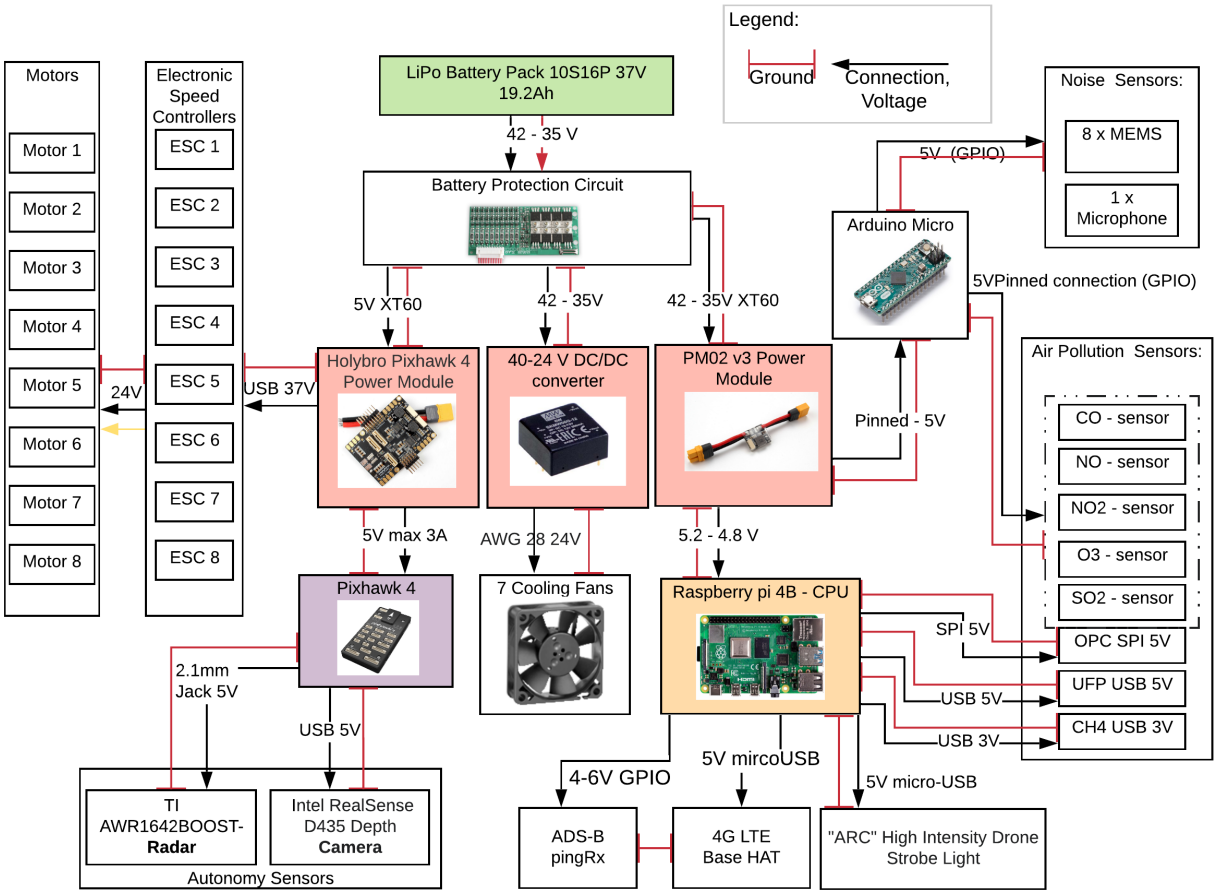

Figure 11.2: Electric Diagram

also helps in complying with requirement *AEMS-NF-EPS-07* as to prevent the battery from leaking. Other actions to be taken to fulfil this requirement are regular checking of the batteries and carefully monitoring their expiry date. When the battery is not used for an expected long time (while waiting for parts to be replaced if another major component is under maintenance), it is better to just remove it from its appliance and store them at 40-50% of their capacity [4]. This aids in the fulfilment of requirement *AEMS-NF-EPS-04* [5].

Battery Charger Selection The battery replacement routine in section 9.4 in chapter 9 presents the way the batteries will be replaced and thereby fulfils requirement *AEMS-NF-EPS-02*. *AEMS-F-EPS-01* also presents the need for rechargeable battery. LiPo batteries generally charge using a system called CC/CV (Constant Current / Constant Voltage) charging. Basically, the charger will keep the current, or charge rate, constant until the battery reaches its peak voltage (4.2 V per cell in a battery pack) and is thus fully charged [6]. A battery charger that has to charge a 10 S 16 P LiPo cell with a nominal voltage $V_{nom,1cell}$ of 3.7 V and a capacity C_{1cell} of 1200 mA h, has to be able to deliver 710.4 W as calculated in equation 11.1.

$$C_{1cell} \times 15 \times V_{nominal,1cell} \times 10 = 1.2\,\text{Ah} \times 15 \times 3.7\,\text{V} \times 10 = 666\,\text{W} \tag{11.1}$$

The safest charge rate for most LiPo batteries is at 1 C, which means one time its capacity, which equals 19.2 A h for the system's battery configuration. The charging voltage should equal the battery's nominal voltage, which is 37 V. This combination of voltage and current should be configured in the charger's configuration, to ensure a safe charging procedure, which complies to requirement *AEMS-NF-EPS-03*. The charging of the battery at 1 C should therefore take 1 h. The 10 S 37 V 20 A Lithium Battery Charger from

[4] `https://3dinsider.com/lipo-lifespan/` [cited 20 June, 2020]
[5] `https://www.panasonic-batteries.com/en/news/how-prevent-battery-leak` [cited 20 June, 2020]
[6] `https://rogershobbycenter.com/lipoguide`[cited 19 June, 2020]

SunPower Battery [7] is a charger that can provide a maximum of 1200 W and has the right specifications for charging the 10 S 16 P LiPo battery pack.

The number of required battery packs that are required to fulfil requirement *AEMS-SYS-EPS-01*, depends on the charging time of one battery and the battery depletion schedule. From chapter 12, the flight time is almost 30 min and from chapter 17 a daily routine of 18 h is obtained, meaning the battery has to be replaced 36 times per day. When the drone takes off, the ground station has 30 min to make sure a new battery is fully charged to keep the rate of battery charging as high as the rate of battery depletion from flying. It is possible to charge 2 batteries of same operating voltage simultaneously in parallel, but if their energy levels differ, parallel charging will make the more charged battery give its charge to the less charged batter due to charge diffusion [8], which makes the charging time for the first battery longer and therefore the charge rate will not keep up with the depletion rate mentioned before. It is, therefore, better to have two battery chargers, which each charge the batteries separately. Five batteries will be used in rotation, so that each battery has 1 h time to rest after being used for 30 min and then being charged for 1 h, which is in line with requirement *AEMS-NF-EPS-04*. As 36 battery replacements are required per day, the battery packs will be used at least seven times per day. Due to the limited number of charge/discharge cycles, the battery packs will have to be replaced every 41 days to meet requirement *AEMS-NF-EPS-08*. Replacing the batteries is therefore inherently part of the power subsystem. The price of these batteries is also accounted for in chapter 20.

The ground station will be powered via 20 6.1 m long 4 AWG cables with a cross-sectional area of 21 mm^2 each[9], assuming the ground station will always be within 122 m from a plug. The cable is sized such that the voltage drop across the cable is exactly 5 %, which is acceptable. [10].

11.2. Compliance of Requirements

The power subsystem has been designed using the requirements presented at the beginning of this chapter. These requirements were based on the sustainability and risk strategy and the functional analysis, meaning the power subsystem complies with the pre-defined sustainability and risk strategy as well. The list below presents whether these requirements are met or not.

Power Compliance Matrix

Requirement ID.	✓ / o / x	Comment
AEMS-SYS-EPS-01	✓	5 battery packs are used in rotation, and the rate of charge equals the rate of consumption.
AEMS-F-EPS-01	✓	The selected battery charger can re-charge the power system.
AEMS-NF-EPS-02	✓	Batteries are autonomously repleacable, explained in section 9.4.
AEMS-NF-EPS-03	✓	An adequate charge rate and a protective BMS are selected
AEMS-NF-EPS-04	✓	Regular inspection is carried out
AEMS-F-EPS-05	✓	The battery voltage matches the motor's needs. Explained in battery cell selection.
AEMS-F-EPS-06	✓	Power modules are selected such that their voltage ranges are compatible with the components they supply the power to as presented in figure 11.2
AEMS-NF-EPS-07	✓	Selected BMS protects the battery against among other leaking
AEMS-NF-EPS-08	✓	The batteries will be replaced when they completed 300 charge cycles. Described in Charger Selection paragraph.

[7] `http://www.batterysupports.com/36v-42v-20a-lithium-ion-battery-charger-10s-10x-36v-lion-lipo-p-441.html`[cited 19 June, 2020]

[8] `https://www.flitetest.com/articles/Parallel_Charging_Your_LiPo_Batteries`. [cited June 18, 2020]

[9] `https://www.amazon.com/Welding-Battery-Copper-Flexible-Inverter/dp/B01MS8ZA6M`

[10] `https://www.metroid.net.au/engineering/calculate-voltage-drop` [cited 20 June 2020]

12
Propulsion and Aerodynamics Subsystem

In this chapter the sizing of the propulsion subsystem will be explained to the reader. The propulsive system is responsible to create the necessary thrust to lift the system off the ground and move the drone around. As the propulsion system depends on the all subsystems, the design will not only depend on the subsystem specific requirements but also on the other system requirements, an iterative process will be used to set the system sizing for the multirotor. Following the explanation of the iterative scheme, the final sizing parameters will be presented and the verification and validation procedures will be explained, ultimately ending with a compliance matrix to check if the pre-set requirements are met.

Propulsion & Aerodynamics Subsystem Requirements	
AEMS-SH-PERF-01	The system shall have a maximum setup time of one hour before it is ready to take-off
AEMS-SH-PERF-02	The system shall be able to operate in wind conditions up to and including Beaufort-4
AEMS-SH-PERF-03	The system shall be able to operate in dry weather conditions
AEMS-SYS-PERF-01	The system shall include a propulsion system [FFD-3.1.5].
AEMS-SYS-PERF-03	The system shall be statically and dynamically stable at all times [Risk CS-02]
AEMS-SYS-PERF-04	The system shall be controllable up till a wind speed of $7.9\,m\,s^{-1}$ (Beaufort 4) [SH-PERF-02, Risk CS-01]
AEMS-SYS-PERF-07	The system shall be able to operate up to an altitude of 1000 m ISA above sea level. [MA, [a]]
AEMS-SYS-PERF-08	The system shall have a minimum achievable speed of $25\,m\,s^{-1}$. [14]
AEMS-SYS-PERF-09	The system shall have a minimum climb rate of $2.54\,m\,s^{-1}$ [14]
AEMS-SYS-PERF-10	The system shall have a minimum turn rate of $3\,°\,s^{-1}$ [14]
AEMS-SYS-PERF-12	The system shall be able to fly minimally up to 100 m above the local ground [MA, air pollution vertical distribution].
AEMS-SYS-PERF-13	The system shall cruise at a speed of $10\,m\,s^{-1}$.
AEMS-SYS-PERF-14	The system shall have a maximum span of 2 m in both planar directions.
AEMS-SYS-PERF-15	The system shall be able to hover in one place for at least 5 s.
AEMS-SYS-PERF-16	The propulsion system shall reduce the inherent noise disturbance to a minimum. [D4S 4]

[a] `http://www.alphasense.com/WEB1213/wp-content/uploads/2019/09/CO-A4.pdf` [cited May 20, 2020]

12.1. Assumptions

In this section, a list of assumptions that were made during the designing of the propulsion and aerodynamic system of the drone are described. Each of these assumptions has a code that is referred to in the following sections.

Propulsion & Aerodynamics Subsystem Assumptions	
PERF-AS01	Drag coefficient, C_D of both top and side of the drone is equivalent to that of a cube which is 1.05 regardless of θ
PERF-AS02	Mejzlik's propellers are compatible with motors of their recommended manufacturer, maxon
PERF-AS03	maxon's motors are compatible with maxon's ESC with right technical specifications
PERF-AS04	Drag during acceleration is kept constant at the maximum value achieved which is when velocity is at peak
PERF-AS05	Drag of due to propellers are taken into account as additional 10% of drag of non-moving structural parts
PERF-AS06	Magnitude of deceleration is equal to that of acceleration in horizontal flights
PERF-AS07	The combined efficiency of all the electromechanical components is 0.85

12.2. Design Methodology

When designing the propulsion subsystem, one must choose a combination consisting of propeller, motor and ESC together with a battery of required parameters based on different characteristics of other subsystems such as the mass of the drone from structures subsystem and voltage output of the power subsystem. To end up at the green circular blocks indicated in figure 12.1, two design considerations must be taken into account when starting this process. Based on the preliminary maximum take-off weight, one must calculate the required cruise thrust to determine the power consumption which will primarily determine the endurance of the drone. This is due to the majority of the chosen operation of mission taken up by the cruise flight. Apart from the cruise thrust, the system will require additional thrust for hovering, manoeuvring, stability and control. Thus, an upper limit for the power required is to be determined through comparing different motions and basing on motion with the greatest power required. As exact analytical solutions do not exist for these use cases, numerous iterations need to be performed and it is important to begin with a realistic number including redundancies for the various parameters. The calculated values of these parameters were religiously checked with statistical data for reality checks.

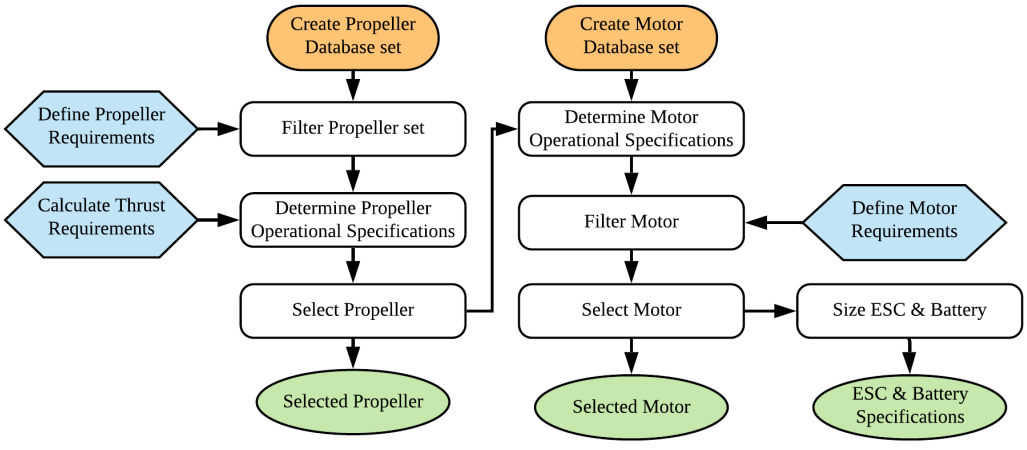

Figure 12.1: Propulsion subsystem sizing methodology approach. Simplified from [7].

12.3. Iteration Scheme

Although the figure 12.1 aided in kicking off the design of this system, multiple iterations had to be conducted in order to achieve a set of analytically optimal parameters with which the components of the drone were chosen due to the interdependent nature of subsystems of a drone. The connections between the different stages of the iteration and their inputs and outputs are described in figure 12.2 with a legend above for reference and figure 12.3 describes the procedures involved in the mentioned design phases.

It began with the system parameters such as the preliminary mass budget and performance requirements derived from the midterm phase marked by red 'start'. The iteration involves external input from the power subsystem where the battery type is to be obtained from. These rounds of calculation ultimately ends with the greatest nominal cruise flight duration able to be outputted by the final set of components put together. The focus was on the cruise flight as majority of the operation is taken up by this specific motion as aforementioned. More in-depth details about each procedure is to be described in the following sections.

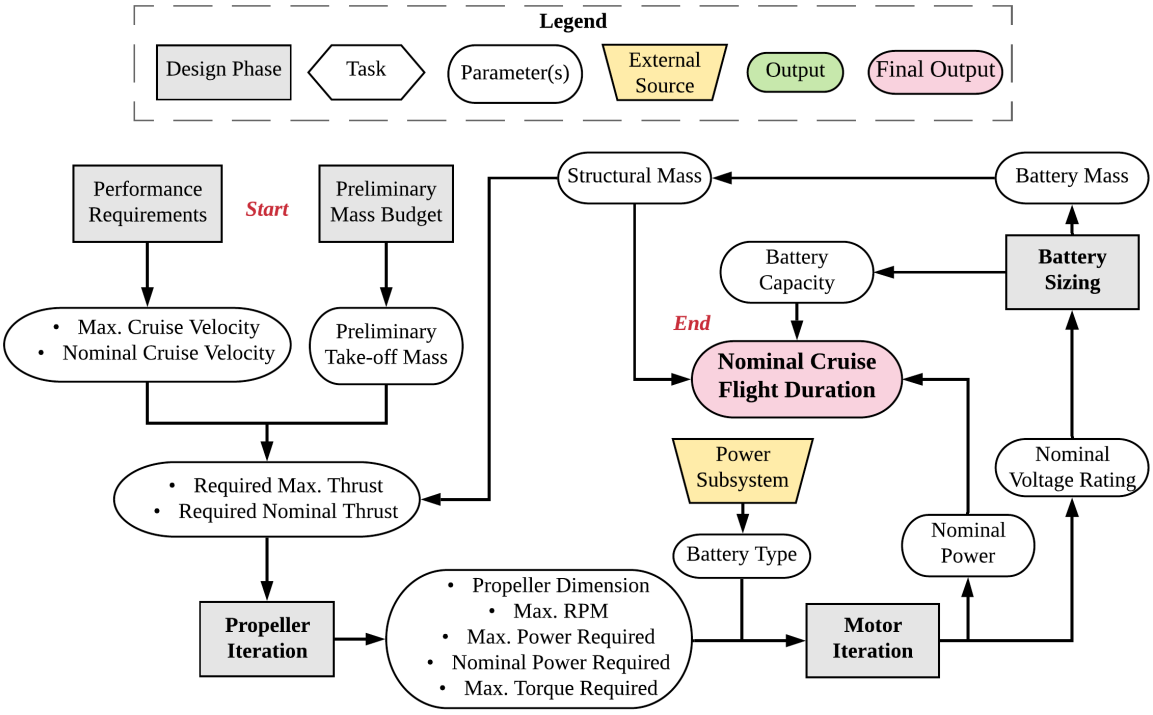

Figure 12.2: Underwent iteration procedures in selecting components

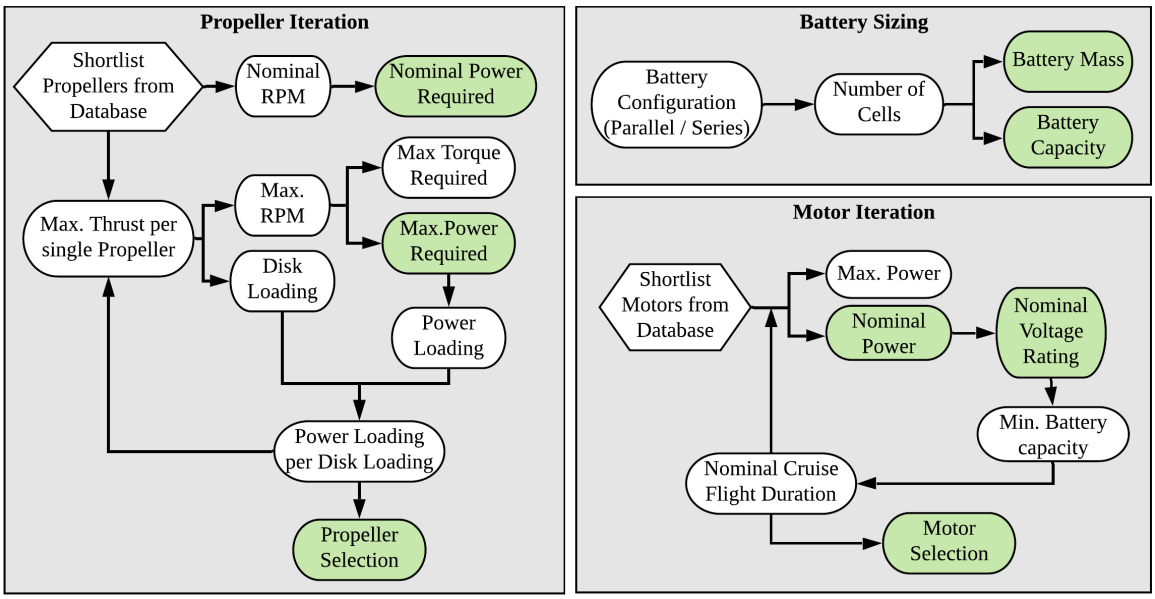

Figure 12.3: Procedures involved in each design phase of figure 12.2

12.4. Propeller Selection

In the following section, the chosen propeller choice will be explained based on the design methodology described in figure 12.1. First, the general considerations about the propeller configuration and why a coaxial

propeller design was chosen over a planar design will be explained. This is followed by the considerations taken during the creation of the database and the governing equations to the propeller performance itself. Based on this information, the reasoning behind the final propeller selection will be presented.

12.4.1. Planar vs. Coaxial Configuration

As briefly mentioned before, the system will either hover or cruise horizontally during the majority of its mission. These conditions can be translated into power requirements based on momentum theory [20], [36].

$$P_{\text{hover}} = \sqrt{\frac{T_{\text{hover}}^3}{2\rho A}} = \sqrt{\frac{(mg)^3}{2\rho A}} \tag{12.1}$$

$$P_{\text{cruise}} = T_{\text{cruise}} v_i + D_{\text{cruise}} v_{\text{cruise}} \tag{12.2}$$

$$D_{\text{cruise}} = \frac{1}{2} C_{D_{\text{front}}} \rho v_{\text{cruise}}^2 S_{\text{front}} \tag{12.3}$$

$$v_i = \frac{T_{\text{cruise}}}{2\rho A} \frac{1}{\sqrt{(v_{\text{cruise}} \cos\theta)^2 + (v_{\text{cruise}} \sin\theta + v_i)^2}} \tag{12.4}$$

$$T_{\text{cruise}} = \frac{mg}{\cos(\theta)} \tag{12.5}$$

$$\theta = \arctan\left(\frac{D}{mg}\right) \tag{12.6}$$

While analysing these equations, it was concluded that the highest power requirements are set by the cruise flight at maximum speed set by requirement AEMS-SYS-PERF-08, shown in equation 12.2. To minimise the cruise flight power, one can either maximise the disk area A or decrease the total mass m. As the system has a predefined payload mass, which is essential to perform the scientific mission, the only way to decrease the required power is to maximise the disk area. However, as the system is constrained in space by requirement *AEMS-SYS-OCT-PERF-04*, the disk area can not become unlimited.

When designing a multirotor, one aspect to overcome this limitation is by using a coaxial rather than a planar configuration. Unlike the planar configuration, coaxial rotors have a second rotor mounted above (or below) the other with the same axis of rotation, doubling the disk area while keeping the frame size and overall dimensions constant.

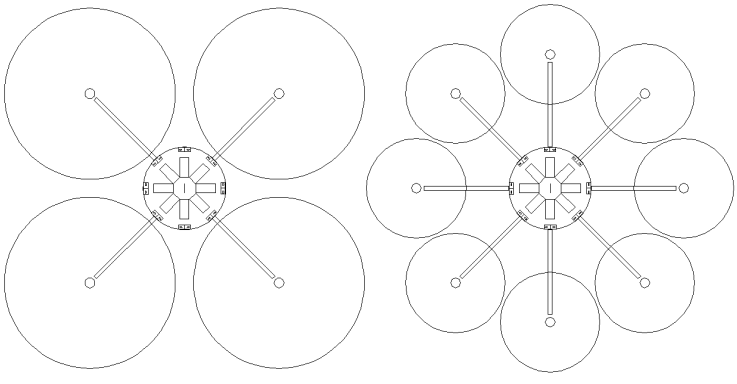

Figure 12.4: Size comparison between a coaxial (left) and planar (right) configuration for a fixed frame size. [1]

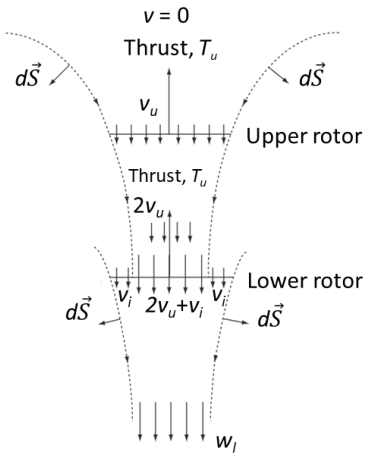

Figure 12.5: Idealised flow model for a coaxial rotor system [26]

However, as the lower propeller operates in the wake of the upstream propeller, the downstream propeller requires a smaller diameter due to the contraction of the flow, as shown in figure 12.5, and a higher pitch angle due to the operation in the accelerated flow. By decreasing the swirl loss, the coaxial configuration can have a higher efficiency compared to the single propeller when a certain disk loading T/A is exceeded as

[1] `https://www.ecalc.ch/calcinclude/help/xcoptercalchelp.htm#flat_vs_coax` [cited June 06, 2020]

shown in [40]. The increased disk loading will also provide increased stability properties which will be especially beneficial when operating in more turbulent conditions [40], allowing the drone to measure closer to the aircraft's take-off and landing. Another benefit of this configuration is the redundancy against propeller failures mitigating the *Risk PR1* whereby in case of any sudden failure of one or two motors, the vehicle will not face catastrophic failure but can instead safely return to the ground station for simple replacement. Therefore, failure of five motors is defined as a critical failure instead of one. However, the downside of this configuration is that the complexity of the system generally increases. The system can also have an increased power consumption and inherent noise generation if the aforementioned aspects are not taken into account during the design. As shown in [32], the actual power requirement can increase by around 15%.

12.4.2. 2-Blade versus 3-Blade Propellers

When selecting the appropriate propeller, one design parameter is the number of blades. By increasing the number of blades, the generated thrust will increase for a given RPM setting when directly compared to a 2-blade configuration. As a consequence, the RPM setting can be decreased with a 3-blade configuration while still maintaining the same thrust as a 2-blade configuration would provide. Even though the reduced noise will be beneficial while flying over near-airport communities, only a few OEMs offer 3-blade propellers with sufficiently large diameters out of which only one manufacturer provides technical data about the propeller performance. Therefore, as the system shall rely primarily on off-the-shelf components, only 2-blade propellers are considered, as their range of available diameters and pitch is larger.

12.4.3. Propeller Characteristics

To select an appropriate propeller that fits the given requirements, the performance of propellers must be characterised. Propellers are generally characterised by dimensionless coefficients[2] for thrust (c_T), power (c_P), advance ratio (J) and efficiency (η), shown in the equations below.

$$c_T = \frac{T}{\rho n^2 d^4} \tag{12.7}$$

$$c_P = \frac{P}{\rho n^3 d^5} \tag{12.8}$$

$$J = \frac{v}{nd} \tag{12.9}$$

$$\eta = J\frac{c_T}{c_P} \tag{12.10}$$

n is the rotational speed of the propeller, d the propeller diameter, ρ the ambient density, T is the thrust of the propeller, P the mechanical power and v is the freestream velocity. Since the efficiency will approach zero as the drone will fly slower or hovers statically, another term will be introduced which gives an indication on how the propeller is performing at any airspeed. The Figure of Merit [12] is the ratio between the ideal power required to hover and the actual power required.

$$\text{FOM} = \frac{T(V + V_i)}{P_{\text{avail}}} = \frac{c_T^{3/2}}{\sqrt{2}c_P} \tag{12.11}$$

However, as indicated in [26], the figure of merit is only a good comparison of propellers when the disk loading is equal for the chosen propeller comparison. Therefore, the efficiency comparison will be extended by comparing the disk loading versus the power loading of the propellers. By comparing these two loading factors, one can quickly compare the efficiencies of the propellers for a given operating point as one generally desires the highest power loading while having the minimum disk loading to reduce the power consumption and noise disturbance. The latter is enabled since [6] mentions that a lower disk loading would increase the efficiency and hence decrease the noise production.

12.4.4. Blade Comparison

The first step in selecting the most suitable propeller is by creating the propeller database. For this database, the most common high-performance propellers were considered. This included OEMs such as Mejzlik,

[2] `https://www.mh-aerotools.de/airfoils/propuls3.htm` [cited June 07, 2020]

Foxtech and APC. As shown in figure 12.1, the first step was to filter the propeller set based on the given subsystem requirements. Using requirement *AEMS-SYS-OCT-PERF-04*, all propellers with diameters larger than 1 m were removed. As the frame itself also takes up a certain volume which should not coincide with the propellers, the maximum dimensions further decreased to a maximum diameter of 32" (0.813 m) based on constraint *AEMS-NF-STR-01/02*. Based on the discussion in section 12.4.1, a larger disk area will directly correspond to decreased power consumption during both cruise and hovering flight, yet the required torque from the motor will increase. Therefore, the lower bound of the diameter was set to 20" (0.508 m) based on the frequency of propeller diameters in the database.

As the system shall use off-the-shelf components, according to *AEMS-SH-SYS-01*, either computer models or experimental data were required to determine the propeller performance. As not all chosen OEM's provide data for their propellers, it was chosen to only consider Mejzlik Propellers for the final selection as they published experimental propeller data for their range of commercially available propellers.

Using the estimated payload and maximum take-off weight , a nominal (corresponding to continuous conditions) and maximum (corresponding peak conditions) thrust per propeller, according to equation 12.5, were found to be equal

$$T_{\text{nom}} = 20.164\,\text{N} \tag{12.12}$$

$$T_{\text{max}} = 161.626\,\text{N} \tag{12.13}$$

To calculate T_{max}, requirement *AEMS-SYS-PERF-08* was used which corresponds to the maximum performance characteristics which are required during operations.

Based on the required thrust levels, one can determine the required rotational speed of the motor which then can be used to determine the required power and torque level for continuous and peak operating conditions. As shown in figure 12.6, increasing propeller diameters correspond to increased thrust levels for a given rotational speed but the larger propellers also require higher power and torque levels at the same rotational speed compared to smaller diameters. However, looking at the efficiency plot in the bottom right of figure 12.6, it can be seen that the three largest propellers have approximately the same efficiency for the given design points. Therefore, based on the maximum take-off weight it was chosen to use the Mejzlik 32" × 10.6" propeller as the inherent pitch level is lower than smaller propellers and the highest hover efficiency is achieved.

12.5. Motor & Electronic Speed Controller Selection

With the set of shortlisted propellers, compatible motors were shortlisted as well from the preliminarily formed database. Mejzlik, the manufacturer of the chosen propellers, specified a recommended motor manufacturer named maxon. Due to lack of compatibility data and the physical hardware, only the motors manufactured by maxon were considered as they were safe to be assumed compatible with Mejzlik's propellers producing assumption PERF-AS02. This assumption was made for ESC as well. maxon is also a manufacturer of ESC and their ESCs were considered for the chosen motor to prevent any uncertainty is incompatibility.

12.5.1. Motor Characteristics

Brushless DC motors are used in all fully electrical drones due to their efficiencies with magnitudes typically between 85% and 90% and durability which derives from the absence of parts that are physically in frictional contact with one another. The main components of a brushless motor are the stator and the rotor. As their name suggests, stator is the static outer part and rotor is an inner part which rotates, and together they convert electrical current to magnetic force then to torque. The size of the motor is one of the important parameters to consider for selection as it varies with respect to the size of the propeller. The larger the propeller, the larger the torque required, which in turn requires a larger motor. It is also to be noted that the height and width of the stator, which in turn affects the height and width of the motor, has an influence in the motor's performance as well. A taller stator has a higher top speed and poor handling at low speed. On the other hand, a wider stator has a lower top speed but it handles low speed better[3]. Apart from these

[3] `https://dronenodes.com/drone-motors-brushless-guide/` [cited June 02, 2020]

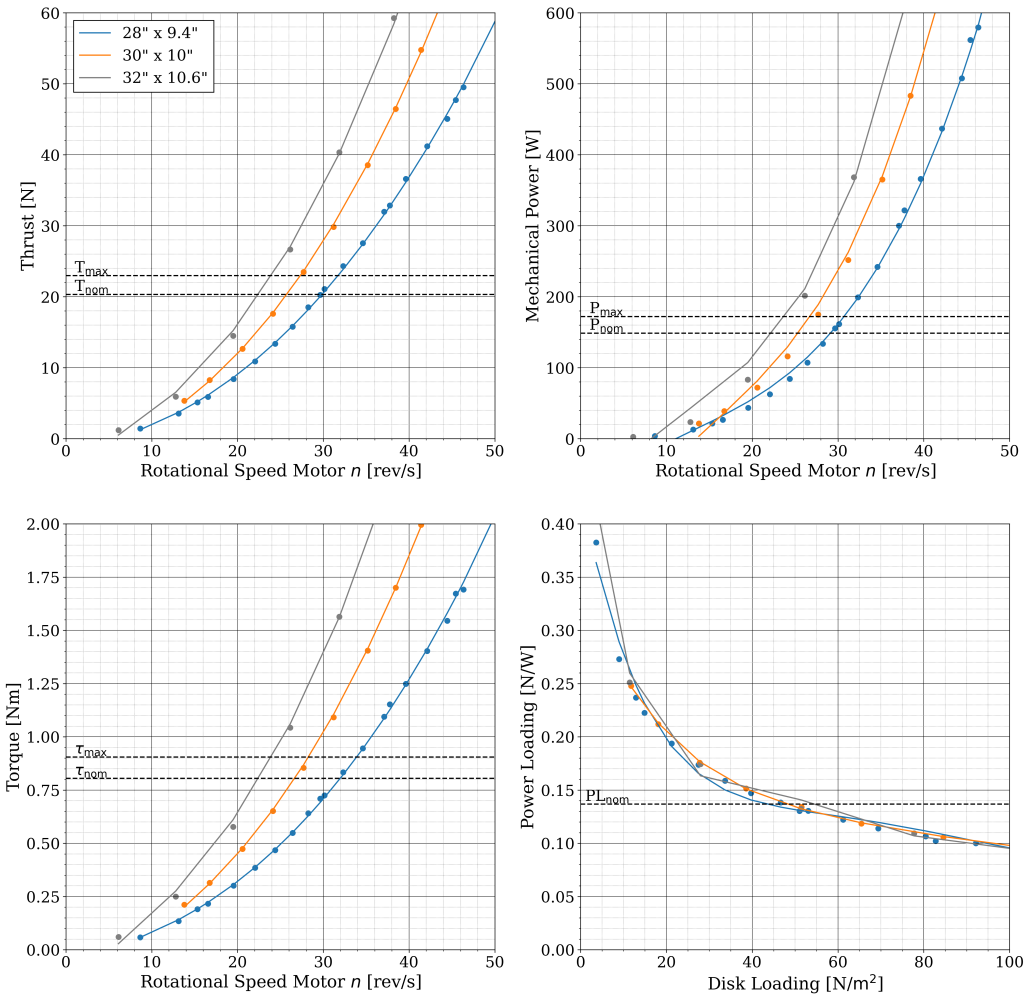

Figure 12.6: Comparison of the propeller performance for the three largest diameters which were considered. For each propeller, the thrust (top left), mechanical power (top right) and torque (bottom left) are plotted against the rotational speed together with the propeller efficiency plotted as power loading versus disk loading (bottom right).

characteristics, performance characteristics such as Kv value, efficiencies at varying thrust level and current draw are to be considered at various design phases.

12.5.2. Motor Database Selection

As mentioned in subsection 12.4.4, figure 12.6 was utilised to find the most optimal propeller model. Using the same set of plots but just looking at the chosen 32" propeller this time, a few performance requirements for the motor were defined. To begin, T_{nom} and T_{max} were taken from equations 12.12 and 12.13. They were then looked up in top left plot of figure 12.6 to determine the corresponding rotational speed levels and these numbers were looked up in the top right plot in finding the corresponding power and torque levels, P_{nom}, P_{max}, τ_{nom} and τ_{max}.

As for the size of the chosen propeller, motors above 80 mm were considered based on numerous available performance tests on propeller-motor combinations conducted by other manufacturers such as T-motor[4] and MAD components[5]. The combinations tested out by the actual manufacturers themselves are a good basis for the preliminary sizing of the components when setting up own tests were not possible and these companies are experienced and are aware of realistic combinations.

Looking up motors above 80 mm, it was found that maxon only produces motors of diameter 90 mm. Thus, technical specifications of all motors of this size were collected they are plotted in figure 12.7. The area shaded in red represents the infeasible motor models and they were based on the motor requirements as shown in table 12.1. The minimum nominal power required by each propeller to produce the required

[4] `http://store-en.tmotor.com/goods.php?id=786` [cited June 14, 2020]
[5] `http://madcomponents.co/index.php/mad8118-80kv/` [cited June 14, 2020]

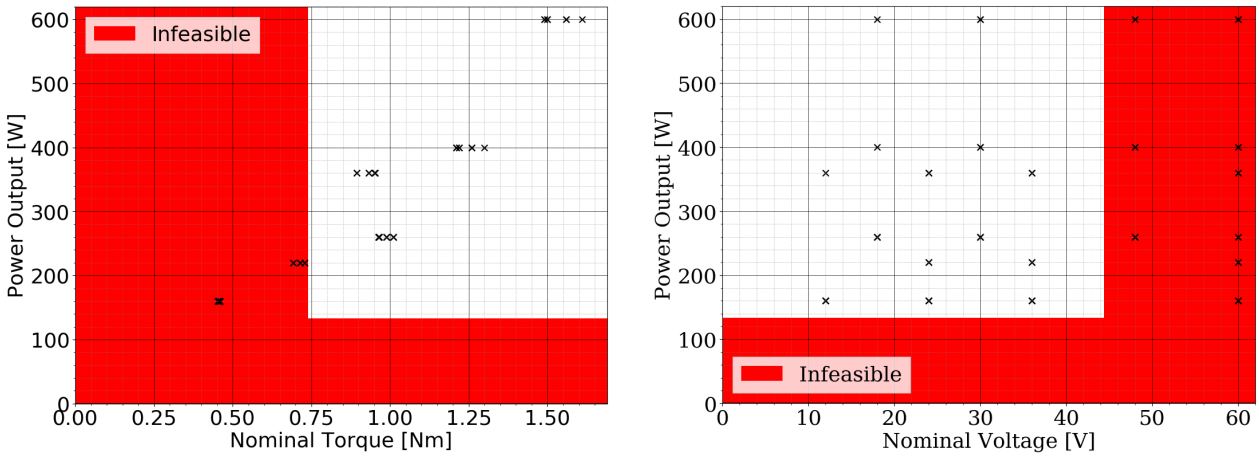

(a) Plot of motors' power output against torque output

(b) Plot of motor's power output against nominal voltage

Figure 12.7: Motor Database set

nominal thrust is 133.155 W and thus the area of the plot with power output less than this value was shaded red to present infeasibility. The corresponding torque required by the propeller, derived from figure 12.6, is 0.735 N m and thus the area of the plot with nominal torque provided by the motor less than this value was shaded red as well. The maximum Nominal voltage was calculated with requirement from 11.1 where the maximum number of 3.7 V cells in series is 12 which gives a total voltage of 44.4 V. Using this value, figure 12.7b was produced.

Table 12.1: Motor Requirements

Property	Value	Unit
Min Power output	133.155	W
Min Nominal Torque	0.735	N m
Max Nominal Voltage	44.4	V

Table 12.2: Technical specifications of maxon EC 90 flat 607955 motor

Property	Value	Unit
Nominal Voltage	36	V
Nominal Torque	0.933	N m
Nominal Current	7.61	A
Maximum Power	360	W
Diameter	90	mm
Thickness	39.9	mm
Mass	630	g

The remaining motors which survived the filtration process were compared based on their specific power, power per unit mass. Ultimately, maxon's *EC 90 flat 607955*, shown in figure 12.8, was chosen to be used in the drone and the table 12.2 describes its technical specifications [6].

12.5.3. Electronic Speed Controller Selection

Similarly, a database of ESCs was built based on maxon's available models as this creates no additional question to whether compatibility is fulfilled creating assumption PERF-AS03. The first step was to use the nominal power and maximum power used by the motor and they are 133.155 W and 186.439 W derived from figure 12.6. With these two numbers, the database was built with ESCs that could operate with motors of such power input and the database is shown in figure 12.3.

As it can be seen in the table 12.3, the nominal and maximum motor power levels handled by all of the ESCs are above the actual nominal and maximum power required. From this, a few ESCs were shortlisted based on the specifications of the motor in table 12.2 and the ESC models with at least one parameter coloured in red were filtered out as those values did not fulfil the required value. Among these, ESC of the lowest mass was chosen as this improves the overall vehicle performance and this was the maxon *ESCON Module 50/8* as shown in figure 12.9.

Electronic Speed Controller Configuration An ESC can be used for two motors as long as these two mo-

[6] `https://www.maxongroup.com/maxon/view/category/motor` [cited June 17, 2020]

Table 12.3: Technical specifications of ESCs in database

Model No.	Nominal Motor Power handled	Max Motor Power handled	Nominal Current	Max Operating Voltage	Mass
380200	250	500	5	50	9
409510	250	750	5	50	204
422969	700	2100	10	70	259
438725	250	750	5	50	12
446925	200	600	4	50	11
532872	400	750	8	50	16
586137	400	750	8	50	84

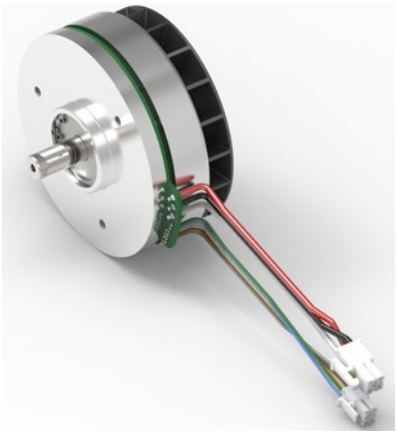

Figure 12.8: maxon EC 90 flat

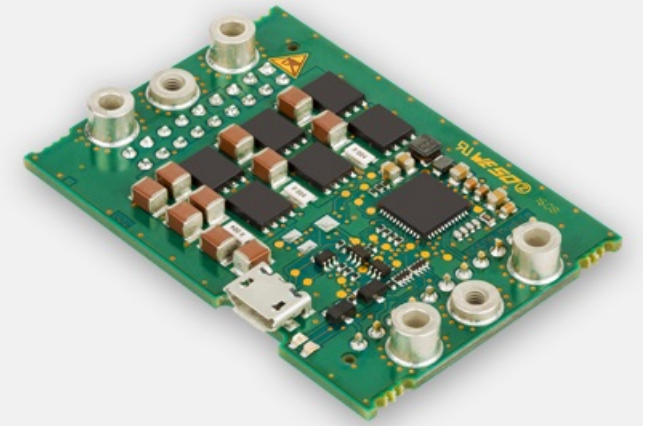

Figure 12.9: maxon ESCON Module 50/8, model number: 532872

tors share the same axis and operating parameters which is the case for the coaxial propeller configuration of the drone in this system. However, as described in section 12.4.1, one of the main reasons behind the choice of the coaxial configuration is the redundancy that it provides. When one of the two motors of an arm fails, every motor on the same plane attached to the rest of the arms need to be deactivated to provide stability. This means that all the eight motors require an ESC each for individual control thus, there will be a total of eight ESCs implemented in the drone.

12.6. Battery Configuration

The final step based on the iteration scheme shown in figure 12.2 is the battery configuration itself. As explained in chapter 11, the most efficient lithium-polymer cell has a nominal capacity of 1.2 A h, voltage of 3.7 V and cell mass of 0.0225 kg.

Based on the motor selection it was found that the best motor has a nominal operating voltage of 36 V, for which a 10S battery configuration is required. This requirement is denoted by *AEMS-F-EPS-05*from chapter 11. Using a 10S configuration, the nominal cell voltage is multiplied by 10 to obtain a nominal voltage of 37 V, which is the closest one can get to fulfil the requirement. Based on this module configuration it was then evaluated how many modules in parallel will give the system the optimum endurance during operations. The number of modules in parallel plotted against the endurance time in min is shown in figure 12.10 below. Depending on the propeller diameter, three different optimal configurations were found. With the chosen 32" x 10.6" propeller, the maximum endurance at nominal power consumption is found to be 120 modules in parallel. However, this value only indicates the theoretical optimum which does not correspond the available space within the system itself. When evaluating the maximum cross-sectional area available underneath the frame itself, a maximum of 15 modules can be placed without compromising the necessary battery cooling and the autonomous system which requires a certain field of view for the camera, specified by *AEMS-F-AUT-14*.

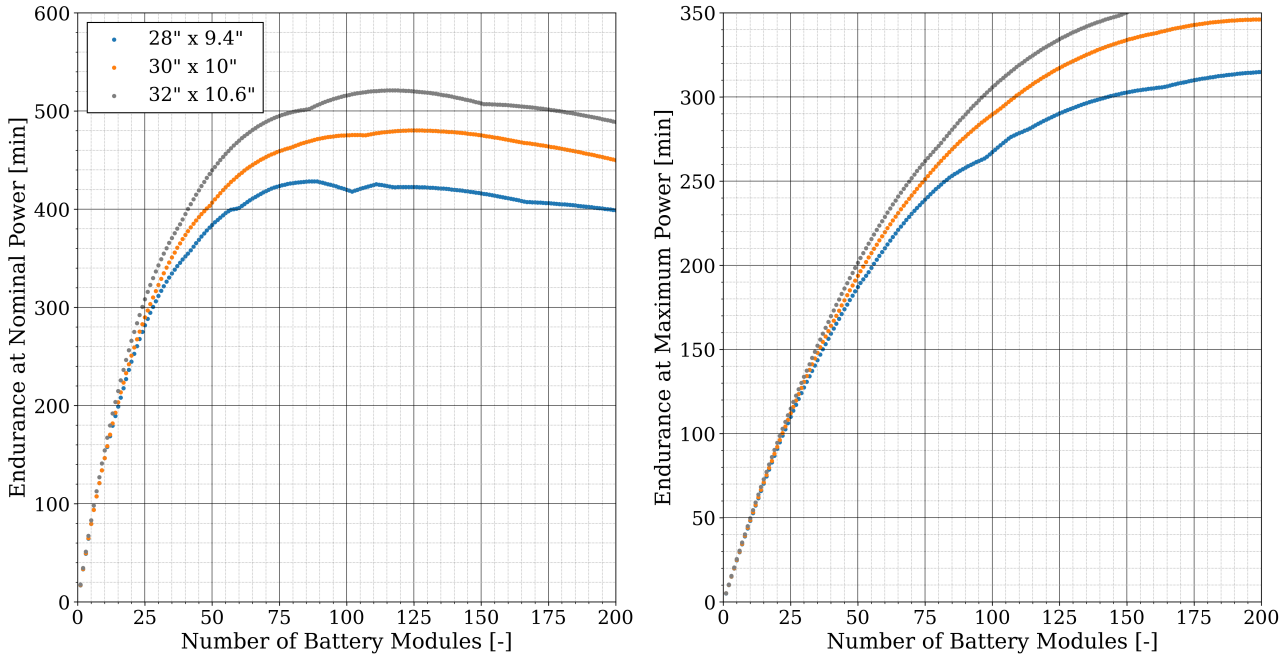

Figure 12.10: Endurance time in minutes shown for varying number of modules for a 10S battery configuration for the given nominal and maximum power requirements.

12.7. Performance Overview

The following table describes the performance parameters fulfilled by the drone with the chosen components of this chapter together with the finalised structure and payloads of other subsystems. Parameters calculated with methods that have not be aforementioned will be clarified in this section as well.

Table 12.4: Performance Overview of the Drone

Property	**Value**	**Unit**
Thrust-to-Weight Ratio	2.2655	-
Power Required for Cruise Flight	1251.768	W
Power Required for Max. vertical velocity Flight	730.156	W
Power Required for Hover Flight	728.613	W
Max Achievable Horizontal Acceleration	9.5889	$m\,s^{-2}$
Max Achievable Vertical Acceleration	12.379	$m\,s^{-2}$
Optimal Horizontal Acceleration	13.935	$m\,s^{-2}$
θ during Cruise Flight	4.1505	°
θ during Max. horizontal velocity Flight	26.083	°

12.7.1. Calculation of Surface Area

So far, many of the methods mentioned have made use of both the frontal and top areas. In the following sections, these values are utilised as well thus it is important to mention how these were calculated. For the non-moving structural components, it was trivial to calculate it both analytically and via a program. OPR3D [PRO] was made use of in order to calculate the projected frontal and top area of the drone excluding the propellers. As for propellers, it was not so simple. The translational velocity of the drone as a whole is incomparable to the tangential velocity of the propeller blades regardless of the drone's motion. The thrust generated by the propeller comes from the interaction between the blades and air in contact. Thus, some frictional drag is present and this drag could not be calculated analytically, leading to assumption PERF-AS05 where redundancy of 10% is added to both the frontal and the top area to account for the preliminarily excluded propellers.

12.7.2. Thrust-to-Weight Ratio

The thrust to weight ratio is typically calculated with thrust generated at 100% throttle and the take-off weight. As the drone makes use of eight motors with a maximum power of 360 W each, this value was looked up in the figure 12.6 and the corresponding maximum thrust was found to be around 40 N. Thus, a total of 320 N can be generated by the drone and this gave a Thrust-to-Weight ratio of 2.2655. This is only slightly above the optimal Thrust-to-Weight ratio of a racing drone which is 2 as specified by the Redbull Drone Racing[7]. Not only does this mean that the designed propulsion system is a realistic one that can actually carry the vehicle but it also mitigates Risk PR1.

12.7.3. Power Required for Cruise Flight

In calculating the power required for cruise flight at velocity of $10\,\mathrm{m\,s^{-1}}$ as specified by requirement *AEMS-SYS-PERF-13*, equations 12.3, 12.4, 12.5 12.6 and figure 12.6 for translation from thrust to power were utilised. An iterative process was involved as the calculated inclination angle, θ, of the cruising drone updates the frontal area, S_{front} (projected area in direction of velocity) which then updates the drag force of the cruise flight, D_{cruise} with equation 12.3 and this goes back to updating θ with equation 12.6. This iterative process has been shown as a pseudo code in algorithm 4 with referencing to figure 12.11. It is also to be noted that the drag coefficient was assumed constant as mentioned in assumption PERF-AS01.

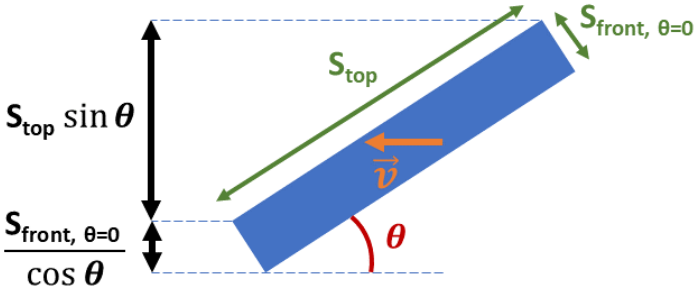

Figure 12.11: Visualisation of S_{front} with varying θ using side view of simplified model

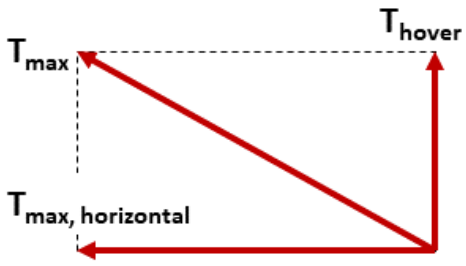

Figure 12.12: Pythagoras theorem visualisation for components of max Thrust

Algorithm 4: Iteration for Frontal Area during Cruise Flight

$S_{\text{new}} \leftarrow$ Initial Guess of S_{front} at $\theta = 0$;
while $|S_{\text{new}} - S_{\text{old}} < 10^{-5}|$ **do**
  $S_{\text{old}} \leftarrow S_{\text{new}}$;
  $D_{\text{cruise}} \leftarrow \frac{1}{2} C_{D_{\text{front}}} \rho v_{\text{cruise}}^2 S_{\text{old}}$;
  $\theta \leftarrow \arctan\left(\frac{D}{mg}\right)$;
  $S_{\text{new}} \leftarrow S_{\text{top}} \sin(\theta) + \frac{S_{\text{front}_{\theta=0}}}{\cos(\theta)}$;
end
return S_{new};

Using the returned value of S_{new}, the true value of power required for cruise flight was able to be obtained.

12.7.4. Maximum Horizontal Acceleration

Using the same maximum thrust able to be generated of 320 N as in section 12.7.2, the horizontal component of this during flight at maximum horizontal acceleration is calculated using the Pythagoras theorem as shown in figure 12.12 as thrust required for hover simply equals to the take-off weight. The drag calculated using equation 12.3 with constant drag at the maximum velocity of $25\,\mathrm{m\,s^{-1}}$ as required by the requirement *AEMS-SYS-PERF-08* using assumption PERF-AS04 was then subtracted from this horizontal thrust component.

[7] `https://www.redbull.com/us-en/racing-drone-tech-talk#:~:text=One%20rule%20of%20thumb%20is,thrust%20across%20its%20four%20motors.` [cited June 21, 2020]

12.7.5. Maximum Vertical Acceleration

The maximum vertical acceleration was found similar to the horizontal counterpart but with 100% of maximum thrust contributing to the lift. The assumption PERF-AS04 was used once again for constant drag with a maximum vertical velocity of 2.54 m s^{-1} as required by the requirement *AEMS-SYS-PERF-09*.

12.7.6. Optimum Horizontal Acceleration

The optimal value for the horizontal acceleration is dependent on the given operational characteristics where hovering time of 7 s is given by table 5.1 and the distance between two measurement points is 150 m as described in section 5.3.3. Using these two values, an optimum horizontal acceleration could be calculated with assumption PERF-AS06 and this is plotted in figure 12.13. The y-axis represents the amount of energy consumed during a single measurement including the trip to the next point. Thus, it consists of energy consumed while hovering, accelerating to v_{cruise}, cruising and decelerating to zero velocity to reach the next measurement point.

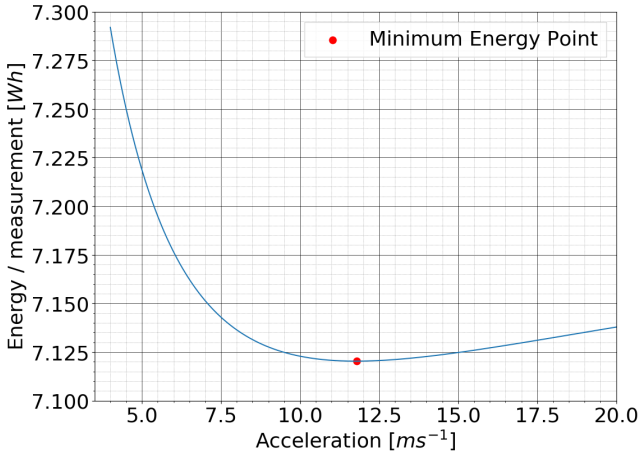

Figure 12.13: Plot for determining Optimum Acceleration

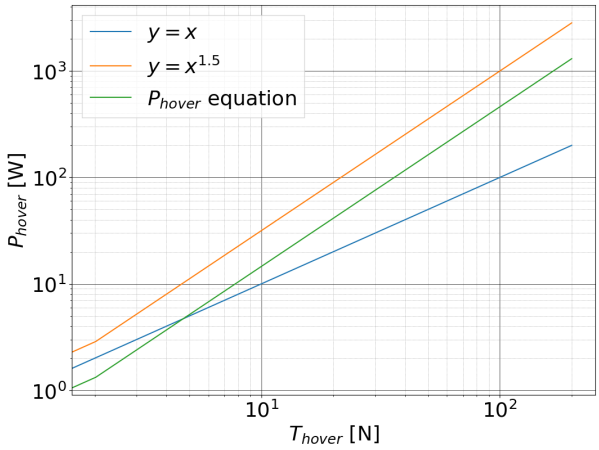

Figure 12.14: Log-log plot of equation 12.1

12.8. Verification & Validation

12.8.1. Software Verification

In this section, the programs created and used to calculate and iterate various performance parameters of the drone are verified. These programs mainly consist of Python programs making use of various packages available to speed up mathematical calculations.

PERF-U01: Power Required for Hover Flight Calculator In order to calculate the magnitude of power required for hover flight, equation 12.1 was used to set up the program. As it can be observed in the equation, P_{hover} is dependent on T_{hover} and varies at an order of 1.5 with respect to it. Thus, a graph was plotted to confirm this prediction together with two other functions, $y = x$ and $y = x^{1.5}$ for comparison. It can be seen in the figure 12.14 that the line representing the P_{hover} equation has the same slope as equation $y = x^{1.5}$ which verifies that the program is indeed calculating the equation properly.

PERF-U02: Power Required for Vertical Flight Calculator During sizing of the propeller, the flight motion which requires the highest amount of power was determined. While doing so, the power required for vertical flight was calculated at the maximum vertical velocity of 2.54 m s^{-1} as specified by the requirement *AEMS-SYS-PERF-09*. This was done using the following equation

$$P_{\text{vert}} = P_{\text{hover}} + \frac{1}{2} C_{D_{\text{top}}} \rho v_{\text{vert}}^2 S_{\text{top}} \tag{12.14}$$

Considering the simplicity of the equation, a simple verification method was applied. As the P_{vert} is dependent on $C_{D_{\text{top}}}$, ρ, v_{vert} and S_{top} apart from P_{hover}, each of these parameters were replaced with 0 once to observe the outcome of the calculations which was expected to equal to P_{hover}. The outcomes fulfilled the expectations and this program has been verified to be true to purpose.

PERF-U03: Inclination angle θ during cruise flight Calculator Just like the PERF-U02, the power required for the horizontal flight was required for determining the motion with the highest amount of power. For this program, iteration was involved as mentioned in section 12.7.3. To verify this iterative process, various initial guess of θ was tried and the same converged value was expected. As shown in figure 12.15, the non-zero initial guessed value of θ converged to the same value. Thus, the iteration calculator is verified to be working true to its purpose.

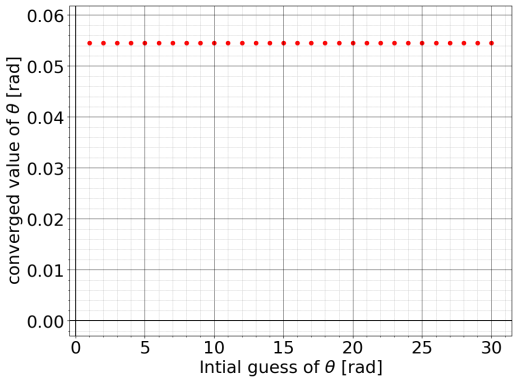

Figure 12.15: Verification of iterative theta calculating process

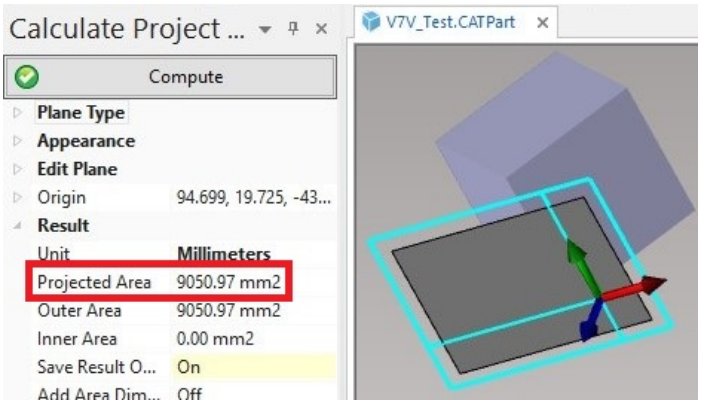

Figure 12.16: Screenshot of OPR3D [PRO] interface

PERF-U04: OPR3D [PRO] Program OPR3D [PRO] was used to calculate the projected area of the drone at various tilt angle that it makes with the ground while operating. This was required by the Propulsion and Aerodynamics subsystem to obtain the drag. To verify that the program performs the task correctly, a simple cube with each length of 80 mm was used in comparing analytically obtained result against the result given by the program. A screenshot of the program with the calculation is shown in figure 12.16. A projection plane rotated at tilt angle of 45° from one of the surfaces was used and the projected area was found to be 9050.97 mm^2. The analytical method on the other hand, is described in equation 12.15 and this gives us an exactly identical value. Thus, OPR3d [PRO] is verified to be correctly calculating the projected area.

$$\begin{aligned} \text{Projected Area} &= \text{No. of surfaces involved} \times \text{Surface Area of each surface} \times \cos(\text{Tilt Angle}) \\ &= 2 \times 80^2 \times \cos(45) \\ &= 9050.97\,\text{mm}^2 \end{aligned} \tag{12.15}$$

12.9. Compliance of Requirements

The sizing of the subsystem started from the fixed values of various involved parameters shown in the requirement list in the beginning of the chapter. Multiple iteration processes and trade-offs have been performed and it is important to check whether the finally decided design adheres to these requirements. The following compliance matrix has been provided to describe how the requirements were met.

Propulsion and Aerodynamics Subsystem Compliance Matrix

Requirement ID.	✓ / o / x	Comment
AEMS-SH-PERF-01	✓	The chosen components are not foldable thus they do not have any setup time once its manufactured and built.
AEMS-SH-PERF-02	✓	With an achievable speed of $25\,m\,s^{-1}$, such wind speed is able to be counteracted.
AEMS-SH-PERF-03	✓	The chosen components do not require any moisture to operate.
AEMS-SYS-PERF-01	✓	The propulsion system is designed in this chapter
AEMS-SYS-PERF-03	✓	A coaxial octocopter configuration is able to provide stability in all three dimensions.
AEMS-SYS-PERF-04	✓	Refer to comment for *AEMS-SH-PERF-02*.
AEMS-SYS-PERF-07	✓	With Thrust-to-Weight ratio of 2.2655 at sea-level, the propulsion system can still provide sufficient thrust for all the operation with corresponding ρ at 1000 m altitude.
AEMS-SYS-PERF-08	✓	The motor was selected based on the required maximum thrust derived from cruise velocity of $25\,m\,s^{-1}$.
AEMS-SYS-PERF-09	✓	This climb rate has much less thrust requirement than the maximum cruise velocity which was accounted for during components selections.
AEMS-SYS-PERF-10	o	The turn rate of the drone was not calculated. However, due to coaxial configuration whereby a significant amount of thrust can be generated from a single axis, it is deemed possible.
AEMS-SYS-PERF-12	o	The vertical distance the drone can travel with varying ρ was not calculated. However, with Thrust-to-Weight ratio of 2.2655, height of 100 m is definitely achievable.
AEMS-SYS-PERF-13	✓	The motor is chosen based on cruise speed of $25\,m\,s^{-1}$ thus $10\,m\,s^{-1}$ is achievable.
AEMS-SYS-PERF-14	✓	With a horizontal clearance between propellers of 0.04 m as mentioned in 10.1.2, the vehicle span 1.6656 m horizontally.
AEMS-SYS-PERF-15	✓	The system is able to hover in one place for 49.725 min at a single charge.
AEMS-SYS-PERF-16	✓	The largest possible propeller was selected as it allows for lower operating rotational velocity which is proportional to noise created.

13
Processor and Communication Subsystem

Now that the general system has been designed, it is time to take a closer look at how the different components communicate with one another. This section describes the general processor as well as the communication device. These subsystems are combined in this chapter since their actual hardware is literally and figuratively overlapping. Moreover, the overall infrastructure of these components is shown using block flow diagrams. Finally, more detail is given on the hardware and software infrastructure and how everything is connected to the processors.

Communications & Data Handling Subsystem Requirements	
AEMS-SYS-DPR-01	The system shall provide at least one back-up measure for data storing or transmission [Risk PL-01]
AEMS-F-DPR-01	The system shall process all measurements within 4 hours [FFD 4.3.5]
AEMS-F-DPR-02	The system shall distinguish between different aircraft types [SH-DATA-03]
AEMS-SH-DATA-06	The system shall be able to store or send one day's (8h) worth of measurements
AEMS-F-COMM-01	The system shall include a remote communication system to allow communication between the vehicle and the ground station(s) [FFD-2.3]

13.1. General Processor

The various subsystems described so far will each provide data to the processor/communication module. The task of this module is then to safely upload this data to the cloud database. From there, the data is downloaded and analysed by the analysis department. For the autonomy & control, this is done to further tune and optimise the system's flight controls. For the customer, this is done to infer pollution metrics and develop a model to visualise these in time and space (Data Handling). For the operational logistics, this is done to gather information on the increase of accuracy of the model, and in turn define a new path to best reach that goal.

13.1.1. Raspberry Pi 4B

At the core of this subsystem is the Raspberry Pi 4B, which is, in essence, a computing core placed on an exceptionally mendable I/O Interface. This device works well with the Pixhawk 4 autopilot module, and can easily transfer the log-files of the Pixhawk to the database.

An overview of the data streams from and to the CPU on the Raspberry Pi is shown in figure 13.6. On the left side, the measurements sensors are indicated together with their corresponding data stream to the CPU. On the right, the autonomy sensors are indicated with their data stream to the autopilot CPU. Both these CPU's are connected to the power distribution board, to request power to enable other components in the system. Finally, the data flows from the main CPU to both the cloud and an on-board storage (of 256 GB), the latter is an added safety measure to mitigate the risk of losing data when the connection is interrupted by unforeseen reasons as stated by risk *CM1*. Moreover, having a storage creates a buffer of data on the mobile system, which allows for cross-checking data points in the database for mitigation of faulty data transfer, as indicated by risk *CM2*. In an attempt to prevent these risks, a small background check should be performed on the carrier to select a stable and trustworthy 4G provider. With this, requirements *AEMS-SYS-DPR-01*

and *AEMS-SH-DATA-06* are met. The Raspberry Pi is then connected to an Arduino Micro, shown in figure 13.1. This is done to accomodate the input/output pins for the air quality and noise sensors.

13.2. Communications Device

The communication from the general CPU to the cloud is taken care of by SixFab's 3G/4G & LTE Base HAT, specifically designed for the Raspberry Pi 4B.

Raspberry Pi 3G/4G & LTE Base HAT The 4G shield will connect with the Raspberry Pi through its 40-Pin GPIO connector. An attachment is included with the device that allows passage for the GPIO pin headers. Hence, the GPIO connector can simultaneously be used to connect the measurement sensor board (accounting for conflicts). Moreover, the shield works with worldwide 4G/LTE providers, therefore meeting requirement *AEMS-F-COMM-01*. A download speed of 150 Mbps and an upload speed of 50 Mbps can be reached, which suffices for the aforementioned data streams in the up and downlink. Finally, the communication streams are indicated in figure 13.6

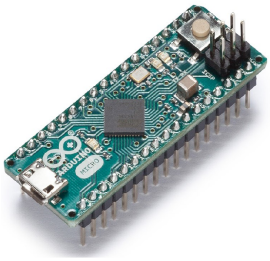

Figure 13.1: Arduino Micro[1]

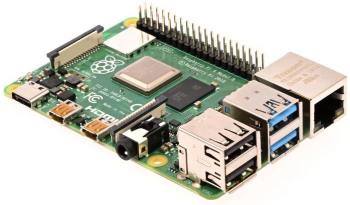

Figure 13.2: Raspberry Pi 4B[2]

Figure 13.3: SixFab 3G/4G & LTE Base HAT[3]

13.3. Hardware and Software Logistics

This section acts as a general summary of the detailed design and will show overviews of the interconnectivity between the various hardware components. The same is then done for the various software modules. The interaction diagrams serve to improve the understanding of the system. More detailed interactions are described and shown in their respective detailed design section.

Hardware Interaction Diagram The hardware interaction diagram is shown in figure 13.5. The main tangible components are the electric motors and the mass flow control for the measurement boom. These subsystems are controlled by the two control units, the Raspberry Pi for global control and the Pixhawk for (automated) flight control. These two processing subsystems base their decisions on the input signals coming from autonomy and measurement instrumentation. Lastly, the dock connector registers when the drone is on the ground station. Which in turn communicates with the ground station's processor to initialise battery replacement and weather protection measures.

Software Interaction Diagram The software interaction diagram is shown in figure 13.7. There are three main sectors of the software, guidance/navigation and control, and measuring software. and cloud software. The first one shows the blocks which depict algorithms set in place to perform autonomous transit, landing and avoidance. The measurement blocks depict blocks that mend the incoming signals to useful information. The cloud algorithms show the post-processing steps to reach the final metrics and also perform path planning for the system. These major sectors are all connected to the on-board processing unit. Moreover, the ground system has algorithms for battery replacement and weatherproofing the system.

13.4. Compliance of Requirements

At the beginning of this chapter all requirements for the communications were presented. In the list below it is presented if the subsystem adheres to all of these.

[1] `https://store.arduino.cc/arduino-micro`
[2] `https://www.raspberrypi.org/products/raspberry-pi-4-model-b/`
[3] `https://sixfab.com/product/raspberry-pi-base-hat-3g-4g-lte-minipcie-cards/1`

Noise Measuring Subsystem Compliance Matrix

Requirement ID.	✓ / o / x	Comment
AEMS-SYS-DPR-01	✓	Taken into account in section 13.1.1
AEMS-F-DPR-01	✓	The onboard processor will do its processes within seconds, the external processes depend on the external system used
AEMS-F-DPR-02	✓	Using the mentioned flight schedule data this is accounted for
AEMS-SH-DATA-06	✓	Taken into account in section 13.1.1
AEMS-F-COMM-01	✓	For this, the SixFab 4G shield is utilised as described in section 13.2

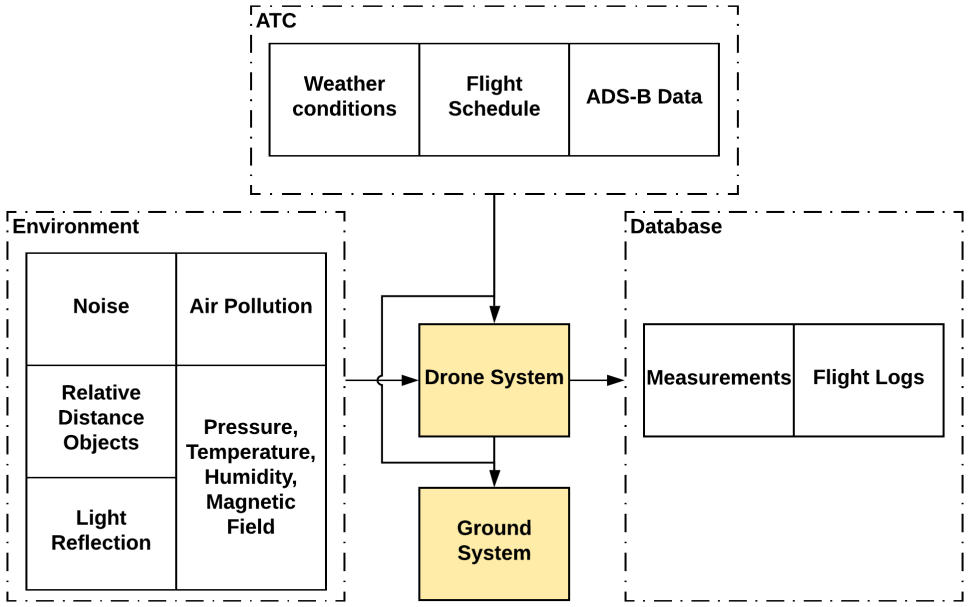

Figure 13.4: Communication Block Diagram

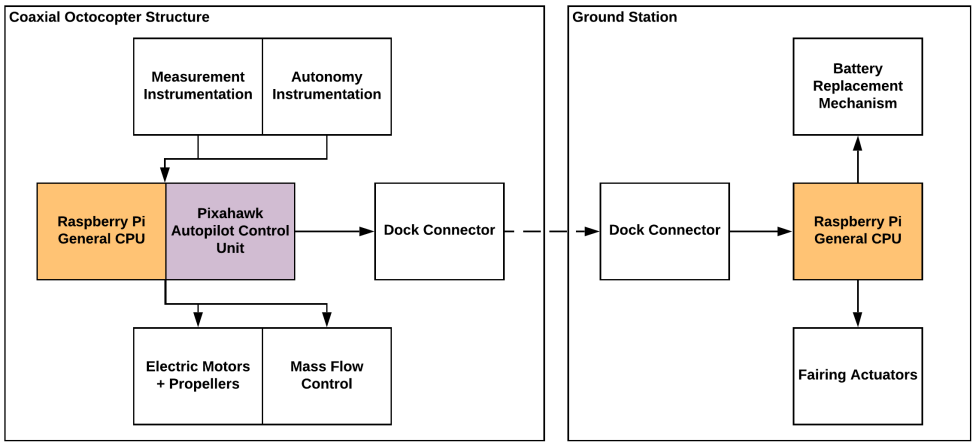

Figure 13.5: Hardware Block Diagram

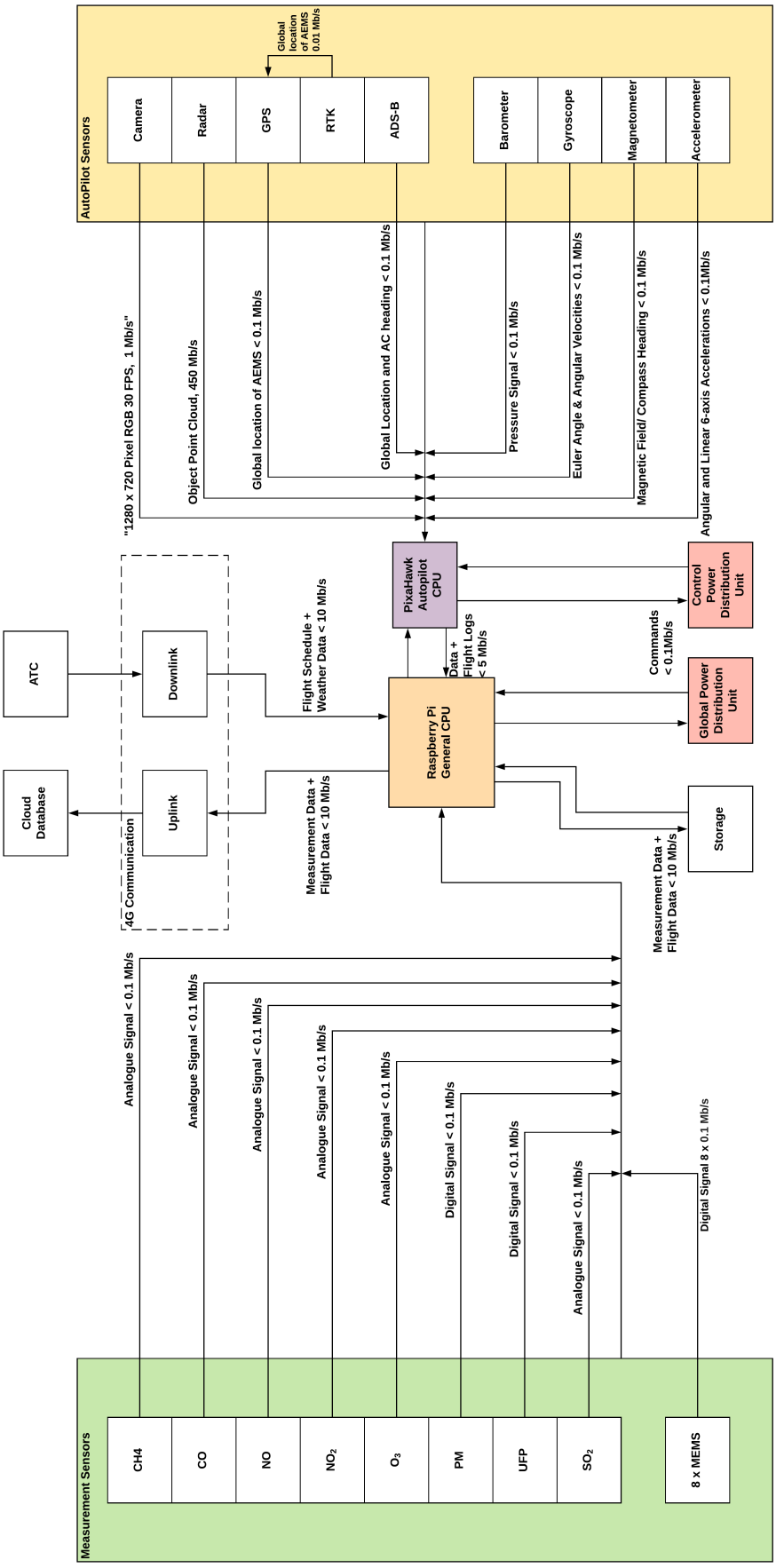

Figure 13.6: Data Handling Block Diagram

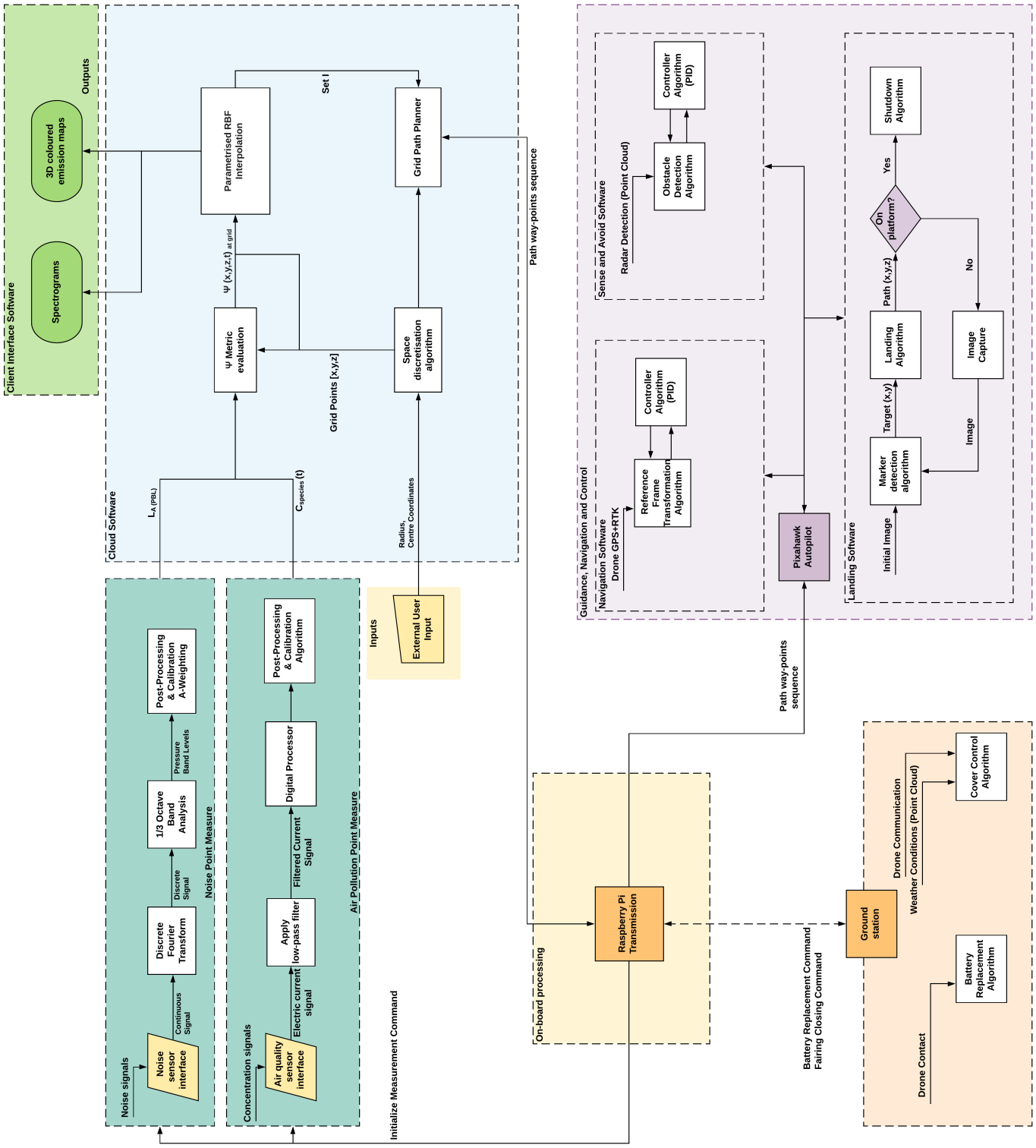

Figure 13.7: Software Block Diagram

14
Sensitivity Analysis

In finalising the software and hardware selected, it is important to conduct sensitivity analyses on certain parameters that are highly probable to be varied as some parts of the drone could be redesigned in the actual production. Thus, the extent of the effect of these parameters on the overall system can be observed. Since it is crucial for the given mission to have a long flight time, the influence on total flight duration is to be analysed. Firstly, the definition of total flight duration for this particular mission has to be stated. As it was done for section 12.7.6, the number of measurement points is the focus. Thus, to determine a realistic flight duration, it was calculated combining hovering, accelerating at optimum value, cruising at v_{cruise} and decelerating at optimum value to represent a single measurement defined in the section 12.7.6. Thus, the calculated flight duration is the total time possible for measurements with a single charge of the battery. Four different parameters are to be varied and they are as follows: structural mass, DoD of the battery, contingency added to surface areas to account for drag on propellers, and hover time.

14.1. Parameter Variation Effects

This section will investigate changes in importantly defined parameters on the overall system. This will serve as a basis of the sensitivity analysis and provide information for section 14.2.

14.1.1. Effect of Structural Mass on the Total Flight Duration

It is highly possible for the structural mass to be varied due to many neglected parts such as screws and other reinforcement parts with small, initially negligible mass adding up to a significant increase in mass which changes numerous parameters involved in the follow-up calculations, such as θ, optimum horizontal acceleration and so on. The variance of structural mass and its effect is shown in figure 14.1 and the plot is extrapolated to visualise the overall trend. It can be observed that the behaviour of the plot follows similarly to $1/x^p$ where $0 < p < 1$ with corresponding shifts in the y- and x-axis.

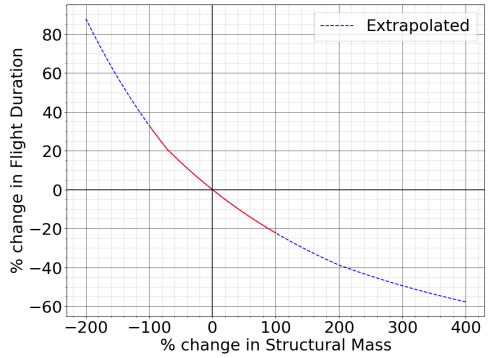

Figure 14.1: Plot representing effect of contingency on surface area on total flight time

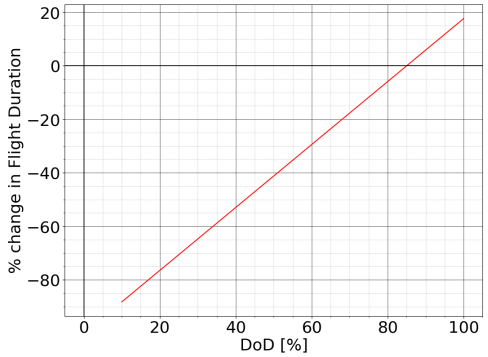

Figure 14.2: Plot representing effect of Hover time on total flight time

14.1.2. Effect of Battery's DoD on the Total Flight Duration

This battery was varied as it is possible for the customer to change the battery's DoD in order to reduce maintenance cost or the customer would disregard the maintenance cost and push the drone to conduct as many measurements as possible, using all of the battery capacity and assuming analytically, this change directly affects the total flight duration. Since the maximum DoD is 100% and 0% is not possible, a range between 10% and 100% was tried and the result is shown in figure 14.2. As expected, the plot is a linear one.

14.1.3. Effect of Drag on Propellers on the Total Flight Duration

The drag on propellers was initially taken into account by adding a 10% contingency to the frontal and top surface area of the drone excluding the propellers. Since this value of 10% is arbitrary to a large extent, sensitivity analysis must be conducted to observe a possible change in total flight time with a higher contribution to the drag from the propellers. Thus instead of 10%, a wide range of percentages were tried and the outcome is displayed in figure 14.3. The plot is a linear curve as well and it does have a significant effect on the flight duration.

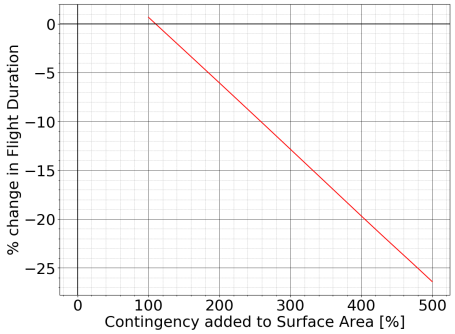

Figure 14.3: Plot representing effect of structural mass on total flight time

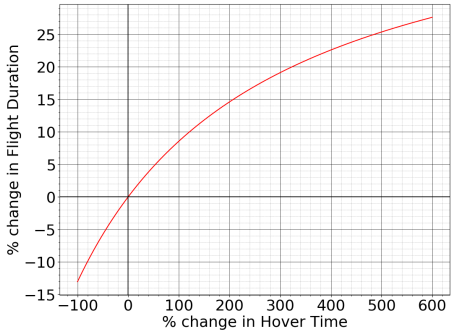

Figure 14.4: Plot representing effect of DoD on total flight time

14.1.4. Effect of Operational Characteristics on Total Flight Duration

Changes in operational characteristics could also have an effect on the total flight duration. For example, since the power required during cruise is more than that of hover, varying the hover time could alter the total flight duration. As indicated in table 6.1 the maximum response time of the selected air pollution sensors is 40 s.However, in areas of rapidly changing pollutant concentrations, the air sensors may need 40 s seconds to converge to a stable response. This means the 5 s hovering time may need to be extended to 40 s. On the other hand, it may be that even 7 s which is the hover time used in this mission is an over-estimation. Hence, a range between 1 s and 40 s was analysed which corresponds to about −86% and 470% change from the initial value which is displayed in figure 14.4. The plot behaves similarly to x^p where $0 < p < 1$.

14.2. Comparison between the effects of different parameters

In order to set up a fair comparison between the parameters and their respective effects on the total flight duration, an absolute value of change is used so that it is possible to analyse how just sensitive the total flight duration is and also since not all the parameters have the same divergence when they are increased and decreased as shown in the above plots. Furthermore, the variance of the parameters under analysis is taken as a percentage from the initially chosen values in the report.

Table 14.1: Effects of parameters under sensitivity analysis on the total flight duration as absolute values

Parameter	**% change of Total Flight Duration at Parameter change of**				
	-20%	**-10%**	**+10%**	**+20%**	**+50%**
Structural Mass	5.3480	2.6319	2.507	5.0231	7.4201
DoD of Battery	20.000	10.000	10.000	N.A.	N.A.
Contingency on Surface Areas	1.3296	0.66496	0.66530	1.3310	3.3309
Hover time	2.1569	1.0556	1.0127	1.9848	4.6819

It can be easily observed that the DoD of battery has the greatest effect on the total flight duration and the contingency on the surface area has the smallest effect. However, it is to be noted that the table was set up to show the comparison between the effects of parameters against the original values. However, in reality, different parameters have different ways of variance and analyses done in sections from 14.1 and 14.4 should be followed more closely.

15
Contingency Management & Resource Allocation

While designing, it is extremely important to keep track of parameters such as cost, mass and power consumption of parts and components that are being added to the system. These parameters have the tendency to outgrow available resources as the maturity of the design progresses. This chapter outlines the resource allocation and contingency management that are applied during the project so that budgets are not exceeded and resources do not grow in an undesired way. The preliminary budget resource allocations were defined in [2]. In [3], the coaxial quadcopter was chosen to become the winning concept, so from then on only the resource budget for this concept was valid. This chapter explains the strategy that was applied to keep the relevant resources within their allocated budget, along with a concurrent contingency plan.

15.1. Resource Allocation

Cost Breakdown In order to keep the budget for the hardware below €25000, which stems from requirement *AEMS-SH-FNCE-01*, the cost budget has been carefully monitored. The way this was monitored is detailed in section 15.2. Table 15.1 shows the result of this management, namely all the costs assigned to each subsystem. The actual goal was to keep the total allocated budget below €23750 to have a 5 %, which would be in line with the contingency management described in section 15.2, but in the end only 1% contingency was left for the production phase and this was deemed acceptable as otherwise the system would be incomplete and requirement *AEMS-SH-FNCE-01* was still met. The consequence is that during production, less components are permitted to lose their value (break) as the replacement cost would make the budget exceed €25000.

Table 15.1: Cost Budget Allocation for final design phase

Cost Category	Cost Fraction [%]	Cost [€]
Payload	48.54%	11880.88
Autonomy & Controls	8.74%	2139.57
Power	20.98%	5135.11
Propulsion	20.98%	4120.80
Structural	4.9%	1200.00
TOTAL	100%	24476.36

Mass Breakdown Table 15.2 shows the budget that was allocated to each subsystem during the preliminary design phase. The budget breakdown from [2] had a significantly different distribution and was not adhered to because it would only limit the propulsion system selection, because only 5 kg would be available for the propulsion & power subsystem. Eventually, the propellers, motors and batteries were selected with the use of an iterative process described in chapter 12, where their performance with respect to flight time was optimised. This changed the mass fractions and mass budgets allocated to them. Once this propulsion system was selected, it was important to keep track of the weight of the other subsystems, like payload and structural weight, so that they did not suddenly become heavier, which could make the propulsion system unsuitable. Eventually, the mass budgets of each subsystem remained within reasonable bounds, and the propulsion system did not have to be re-iterated.

Power Budget In the baseline report [2], it was estimated that the payload, which included autonomy, control, air pollution and noise sensors and computing hardware would use 0.65 % of the drone's power and

Table 15.2: Mass Budget Allocation for final design phase

Category	Mass Fraction [%]	Mass [kg]
Payload	9.21%	1.38
Autonomy & Controls	1.76%	0.26
Power	24.40%	3.67
Propulsion	39.27%	5.90
Structural	25.36%	3.81
TOTAL	100.00%	15.02

Table 15.3: Power Budget Allocation for final design phase

Power Category	Power Fraction [%]	Power [W]
Payload	0.81%	23.71
Autonomy & Controls	0.50%	14.66
Power	0,004%	0.12
Propulsion	98.68%	2880
Structural	0%	0
TOTAL	100%	2918.49

that the other 99.35 % would be used by power and propulsion. While designing, the battery was designed for optimal flight time and to power all subsystems. The power consumption was monitored throughout the design process, so that especially after picking the batteries, the payload would not suddenly require way more power than the power system could account for. Fortunately, no sudden increases in the allocated power budget of the payload or autonomy & controls occurred, eliminating the need for a re-iteration. If such an increase in power consumption had occurred, either flight time would have gone down, potentially jeopardising the operations of the system or more batteries would have to be taken on board. Finally, the power breakdown is illustrated by table 15.3 and is very similar to the preliminary power breakdown.

15.2. Contingency Management

The Technical Performance Parameters (TPM) refer to cost, mass and power. In figure 15.5, in each design phase a target value is set for all the TPM towards which they should converge and which they should definitely not exceed. It is key that at each stage of the design, it is checked whether the actual value of a TPM at that moment corresponds to the target value of that design phase. If the TPM exceeds the assigned target value, either the TPM has to decrease, meaning a more cost, mass or power-efficient solution has to be picked, or more resource has to be allocated to it. The choice between these two will be influenced by how the design is affected. In turn, the target value approaches the specification value for that TPM. For example, the maximum specification value for cost is €25000, and as the design progresses, this value is approached by the target value. This target value is initially valued at 80 % of the specification value, because during the preliminary phase of the design, 20 % contingency margin is applied, derived from table 15.4. This shows that the way the target value approaches the specification value in figure 15.5 is in accordance with table 15.4.

Table 15.4: Contingency Allowances per Design Phase [21]

Design phase	Contingency [%]
Conceptual Design	20
Preliminary Design	10
Detailed Design	8
Final Design	5
Production	0

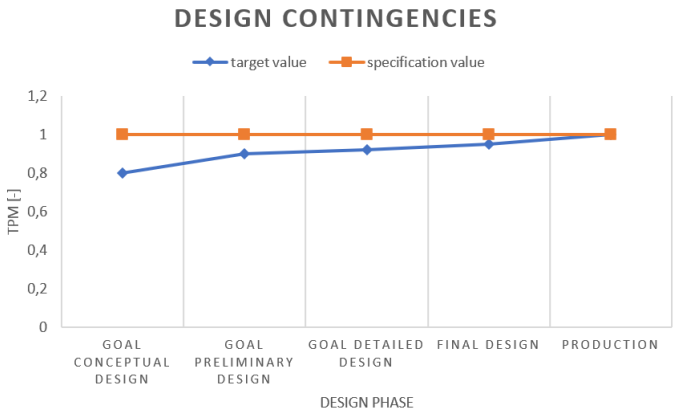

Table 15.5: TPM parameter in function of design phase

This contingency management was done for the three TPMs. However, the initial mass budget allocation from [2] was not realistic as because the contingency management limited the design too much with respect to which motors could be picked. Also, the preliminary budget breakdown in [2] was based on quadcopters in general and not on octocopters. Therefor, the mass allocation budget was updated to newer values which resulted from the sizing of the power & propulsion system. The specification value for the mass of each

subsystem was thus changed to a value that would still be suitable with the concurrent power & propulsion system's capabilities and as a result, the target value for each phase approached this specification value to ensure it would stay approximately the same and definitely not exceed it.

As during the final design the costs turned out to already exceed the 5 % contingency margin, no further action was taken to reduce them. This is justified by the fact that the major contribution to cost comes from the Naneos UFP sensor, given in chapter 6, which is not used by other comparable systems and will therefore give this system a significant market advantage. As a consequence, the contingency margin for the production was narrowed down to approximately 1 %, which altered the risk of not meeting requirement *AEMS-SH-FNCE-01*, but eventually this was deemed acceptable.

III

Further Development

16
Manufacturing and Assembly Considerations

Now that the entire system is designed and sized, the manufacturing and assembly can be considered. The UAV consists of several different components. Several of these are products are produced by external companies, such products are the hardware, the propellers, and the motor. However, several systems need to be produced by the team, such as the frame of the system. First of all, the manufacturing of individual parts will be presented in section 16.1, afterwards the assembly of the UAV is explained in section 16.2.

16.1. Part Manufacturing

The following parts need to be produced: the four arms, the case protecting all the sensors, a housing for the battery, as well as the clamps that hold the battery in place. Each of these parts will have a different production technique due to the different geometrical shapes and materials used. For each of the different parts, the production technique will be explained in the paragraphs below.

Arms and landing gear The arms carry the propeller and the motor and are these hollow tubes made of the composite *cyanate ester* with high modular strength carbon fibre. The landing gear is made of the same material and a similar shape. It was decided to use filament winding to create the arms and legs since they provide rational symmetry. This allows for a continuous fibre, thus increasing the strength of the material. Other techniques require assembly for circular parts, which will result in stress concentrations at the joining location. Lastly, there are no limitations for resin and reinforcement, so cyanate ester can be used to produce the arms and legs. The carbon fibres are spun around a mould, often referred to as a mandrel, to create the desired shape. The fibre is spun around at a certain angle to create different fibre directions. Before the fibres are placed around the mandrel, they are run through a cyanate ester bath. Once the desired shape has been created, the product should be heated to cure the resin [5]. There are a couple of items necessary for filament winding, these are the mandrel, winding machine, oven large enough for the product, and a pretensioner, required to keep the carbon fibre under tension. These are expensive equipment and since the system will not be mass-produced, the product cannot be produced in-house [5]. Thus an external company will be contacted to create the arms and legs. This is almost a fully autonomous process. There are limitations to the shape of filament winding, namely, the shape cannot be concave. This is not the case for any of them. It is also possible to create T-shape products with filament winding, however it does require a more complex machine. A T-shape junction is required for the landing gear.

Battery The battery is protected from external influences by housing and held in place by clamps. Both the housing and the clamps will be 3D-printed via the Fused Deposition Modeling (FDM) technique. This is because the parts are not primarily load-carrying structures. A thermoplastic is heated and extruded through a nozzle. The nozzle can move in all directions, thus creating the shapes of the layer, then it moves up to add the next layer in a fully autonomous process [6]. For PETG it is required to use a heated printing table, while this is not required for PLA [1]. There cannot be unsupported sections in FDM production. This is not the case for the clamps and the housing. To still to be able to replace battery modules or other maintenance inspections the battery housing will not be made of one part but two. These can be clipped together to form the box around the batteries, thus ensuring that risk *MN1* is prevented. The clamps will be made as one part. FDM technique takes into account the sustainable strategy production techniques are there is no mould required and little to no scrap parts.

Protective case and Frame There is also a protective case around all the sensors, and other hardware. This

[1] `https://www.simplify3d.com/support/materials-guide/properties-table/` [cited June 19, 2020]

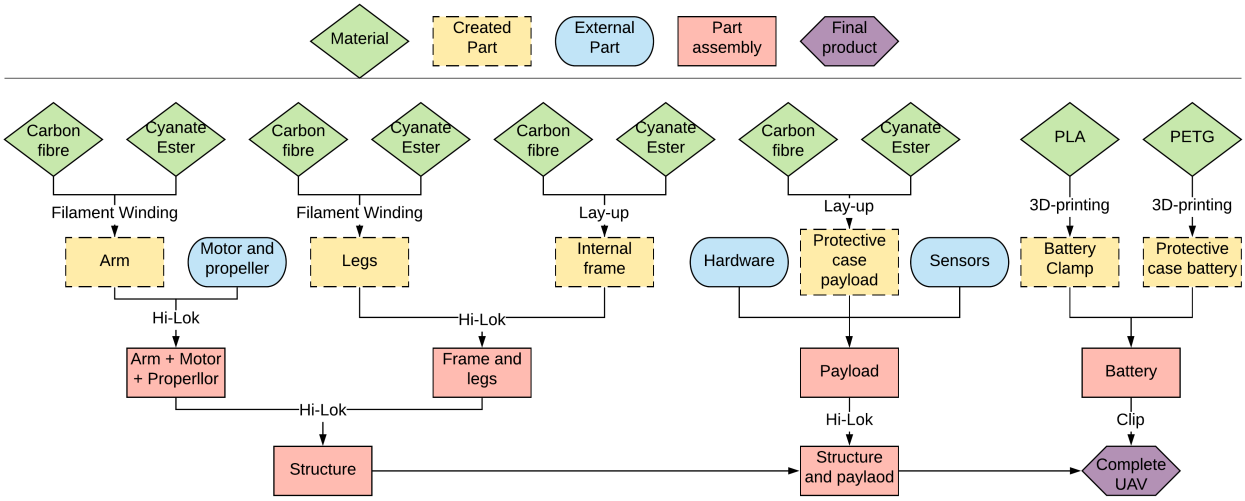

Figure 16.1: Assembly plan of the UAV

is to protect them from the external environment and prevent water from affecting them. The protective case will be located on top of the internal frame which connects all different components of the UAV . Both the frame and the protective case are made of cyanate ester with high modular carbon fibres and are flat surfaces. It was decided to create these parts by lay-up followed by vacuum bagging. For the lay-up first, a mould of the desired shape is created. In the mould, a layer of resin is spread, on which the layer of carbon fibre is added, which is coated with resin again. This process is repeated until the desired layers are reached. The carbon fibre can be orientated in any direction, to not create a unidirectional specimen. After all the layers have been added the part should be cured to set the cyanate ester. This is process is sped up with vacuum bagging. This not only decreases the time it takes to set but also decreases the void content in the material. The lay-up can be performed by hand, as well as automated. However, since the system will not be mass-produced, it is beneficial to do the lay-up by hand. By hand lay-up the sustainable strategy production technique is also taken into account because no machines are required. Similar to the battery case, the sensors and hardware also need to be inspected regularly, thus the case is not made in once piece but two. The top can be clipped off for inspection, thus resulting in the prevention of risk *MN1*.

All the components can be manufactured with the techniques described above, however if it turns out a certain shape is not exactly possible, another technique needs to chosen, or the design reevaluated, as a mitigation strategy for *MF1*.

16.2. System Assembly

The next step is to create the entire system, by assembling the different parts. There are different parts, consistent of different materials, and therefore different joining techniques should be used. Many of the parts are made of composites and conventional joining techniques cannot be used, such as riveting. The two parts will be joint together by a hi-lok, which is a combination of a rivet and a bold. The hi-lok is not deformed during the joining process and therefore a high strength can be obtained when compared to riveting. Moreover, it has a high sealing property when compared to rivet [5].

A schematic overview of the production plan is presented in figure 16.1. First of all, it depicts how the products are created out of the materials itself. These activities can be done simultaneously. The next step is to connect the legs to the frame, and at the same time connect the motor and propellers to the arm. After this, the frame with legs is mounted together with the arms. Next, the sensors and other hardware are connected onto the frame, as shown in figure 10.1, and the protective case is clipped over them. Lastly, the battery clamps are mounted to the frame and the battery is clipped in place. The assembly of the product is complete, however for the sensors to work correctly they need to measure for 12 hours in a cleanroom. This will also be done before the system is transported to the customer.

17
Operations, Regulations and Logistical Considerations

Aspects of the operation of the system have in some cases already partially been discussed due to the relevance for the appropriate subsystems. This chapter will harmonise the previously detailed sections and present a wider view on the topic.

17.1. Operational and Regulatory Requirement Analysis

Operational and Regulatory Requirements	
AEMS-NF-OPR-01	The system shall be inspected visually for structural integrity after every working day [FFD-3.5.5, D4S table 4.6]
AEMS-F-OPR-03	The system shall be equipped with ground station(s) for storage and maintenance [FFD-3.5]
AEMS-F-OPR-04	The system shall be able to check the weather and environmental conditions [SH-PERF-03]
AEMS-F-OPR-11	The system shall be operable at different European airports. [SH-DATA-01/02/03]
AEMS-F-OPR-12	The system shall judge weather the weather is safe for sensor operation [Risk PL2]
AEMS-F-OPR-13	The system shall not interfere with regular airport operations [14]
AEMS-F-REG-02	The system shall abide by the EU airports regulations [14]
AEMS-F-REG-03	The system shall abide by EU drone regulations [14]
AEMS-F-REG-05	No probable failure of the UAV or any external supporting system shall occur during the mission lifetime [14]
AEMS-F-REG-08	The system shall have permission from Airport Traffic Control (ATC) and Air Service Navigation Provider (ASNP) granted [14]
AEMS-F-REG-09	The system shall be legally certified to fly in Class B to G airspace (ARC-d) [14]
AEMS-F-REG-10	The system shall have a GRC (Ground Risk Class) of no more than 7 [14]
AEMS-F-REG-11	The system shall have a 'High' level of robustness [14]

17.2. System Procedures

This section will detail all activities relevant to preparation, transportation and operation of the system. Additionally, abnormal events will be taken into account.

17.2.1. System Preparation

The system is designed to be operable at airports with varying configurations (requirement *AEMS-F-OPR-11*). It is therefore of importance to detail the preparation steps required before operation at a new airport.

1. Contact relevant authorities on the time frame of operation around the airport
2. Determine the measuring volume and identify the location of the ground station
3. Identify active runways and obtain airport charts
4. Determine geo-caged area and upload to QGroundControl®
5. Arrange transportation of the system to the ground station

17.2.2. System Transportation

The system is transported in a van with allowable space of maximum 2x2x2 m (requirements *AEMS-SH-DIMS-01* and *AEMS-SYS-02*). The boom of the drone will be disconnected from the main body for transportation and storage as explained in section 6.4.3. This significantly reduces the height of the drone and allows its transportation within the ground station (compliant with *AEMS-F-OPR-03*). The lower section of the ground station is used for storage of the following: the disconnected boom, sensor protection gear (during flight), power cables and spare items as can be seen in figure 17.1. Additionally the drone is strapped down by use of elastic coverings at the leg skids as can be seen in figure 17.2. This set up allows for efficient transportation as all pieces are kept together. Protective foam coverings are used for the radar sensors on the body, helping decrease the probability of risk *PL2*. The van with the system inside may not be driven to the pre-defined ground station location. The set-up time is expected to take a total of no more than 40 minutes where 10 minutes are allocated to move the ground station to the appropriate location, 5 minutes to connect the power supply, 5 minutes to attach the boom and remove the elastic safety straps, 10 minutes to load in the flight path and a final 10 minutes for any further miscellaneous activities.

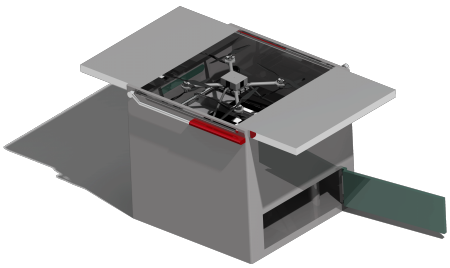

Figure 17.1: Ground Station Transportation CAD Render with Side Flap

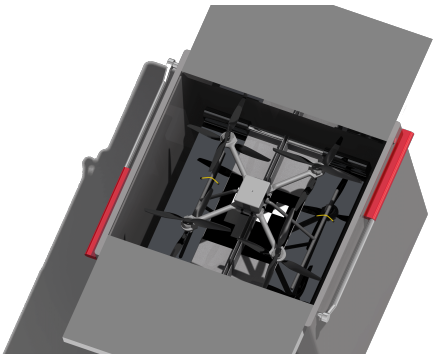

Figure 17.2: Ground Station Transportation CAD Render of Drone with Elastic Straps

17.2.3. Measuring Operation

Chapter 5 presents the specifics of the measuring operation with a detailed flowchart presented in figure 5.1. A few aspects require further operational clarification. The weather data is downloaded from the cloud as described in chapter 13, thereby enabling safety checks. This prevents risks *OP1* and *PL2* (based on table 6.1) and during flight mitigates them by spending less time in the air if higher windspeeds or adverse weather are detected. This ensures no violation of design based on requirement *AEMS-SH-PERF-02* and complies with requirement *AEMS-F-OPR-04*. Next, permission from ATC is required. ATC will be given access to the client interface software as presented in figure 17.4 (section 17.3). It will be possible to give permission for deployment, return to the ground station immediately and also enable emergency shut down in an extreme case (requirement *AEMS-F-REG-08*). ATC will be able to notify emergency services in an extreme event, thereby mitigating risk *OP3*. At the end of each day the system must be inspected in accordance with requirement *AEMS-NF-OPR-01*. One final note is to be made on the flight operations, namely, that the light as mentioned in 9.2.4 is used as a flashing strobe when not used during landing. This enables the drone to fly legally at night [14], thereby complying with requirement *AEMS-F-OPR-06*.

17.2.4. Abnormal Events

Abnormal events require special procedures. Figure 17.3 presents an overview of detectable abnormal procedures within the mission operation. Structural failure will be detected by inspection, in line with requirement *AEMS-NF-OPR-1*. A critical motor combination failure is defined as 12.4.1. This would not allow for flight and result in catastrophic failure of the system. Emergency services would need to be notified, thereby assisting with the mitigation of risk *OP3* and *PW2*. All events are assumed to occur during flight (worst scenario) apart from path planning which occurs before launch. This is implemented chapter 9.

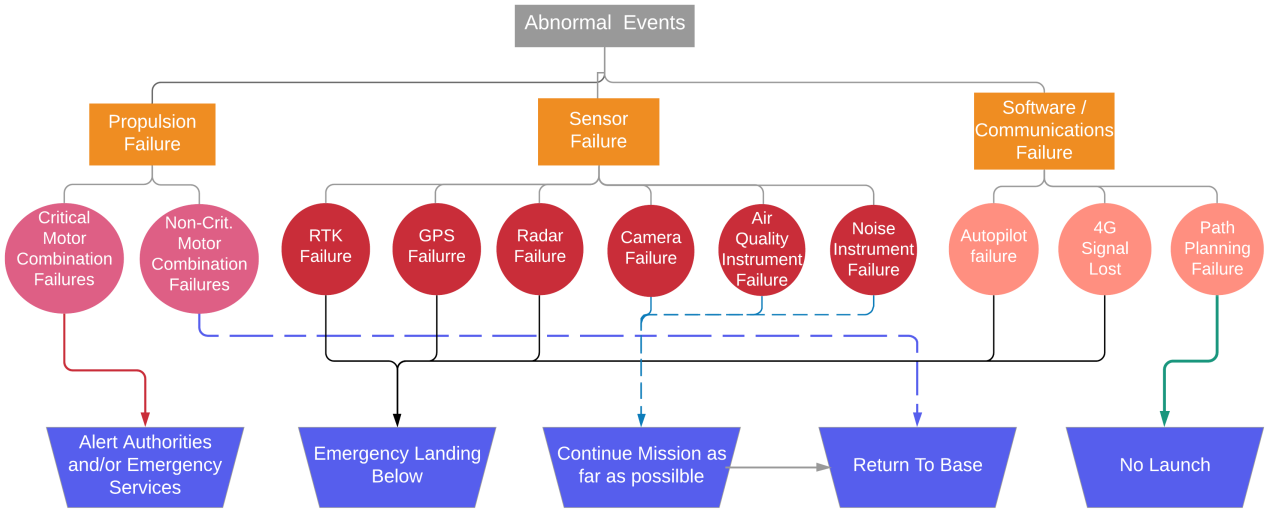

Figure 17.3: Abnormal Event Procedures

17.3. Client Interface Software

This section sketches an image of how the various involved parties would interact with the system. As shown in figure 17.4, an interface tool will be developed which offers access to the database. The data from the database is shown in for example contour plots, such as shown in figure 17.5. On this page, a species can be selected, or a selection of various pressure band levels can be made, which are then shown in the contour. Also either the raw or the interpolated values can be requested. And all this at various altitudes at each step on the timeline. Important to note is that this structure inspires an open-source kind of development of the software's functionality, where the community can add their own functions into the database to visualise other metrics from the data, e.g. the sound exposure level, which would integrate the pressure levels squared over time.

For the general public, a restricted access account can be made, through which e.g. researchers and students can access the database. Of course, customers can choose to not publish the data of their measurement system to these users. Moreover, with an account with access rights, the measurement system can be controlled. E.g. one could manually start and end the mission as well as gather information on the current location of the drone(s) or perform an emergency landing. Finally, via the same interface, service could be requested and scheduled along with emergency contact information.

17.4. Residential Awareness

It will be important to notify the communities surrounding the airport of the mission being undertaken by the system. While the drone will increase noise levels temporarily during measurement taking, locals should know the benefits of the system to overweigh this downside, thereby helping with requirement *AEMS-SYS-SUST-06*. This will likely be done by cooperation with the council of the nearby community or communities. This can involve information signs at bus stops, promotion on social media platforms as well as letters sent to residents' houses. The extent of this will depend on the budget of the customer and their willingness to inform. It would be worth stressing the importance of working with the council as they will receive complaints if any arise. These could be related to suggested nuisances caused by the system. Re-evaluation

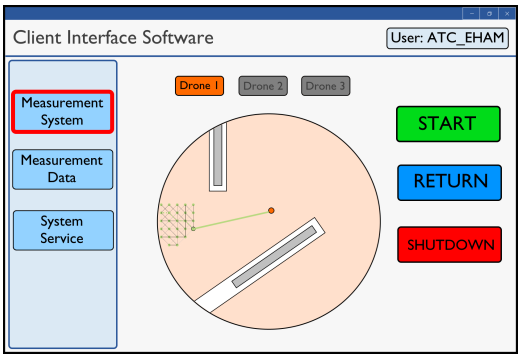

Figure 17.4: ATC CIS Screen View

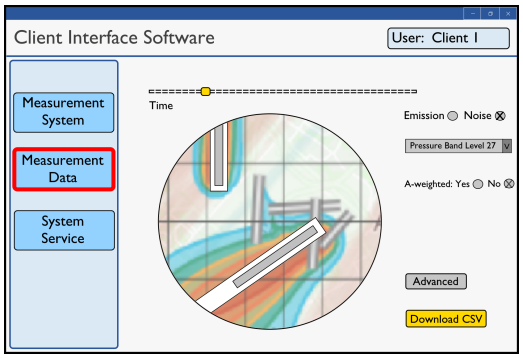

Figure 17.5: Client CIS Noise Data Screen View

would need to be undertaken within route planning and operations to mitigate any *OP2* risk occurrences.

17.5. RAMS Analysis

This section will discuss the reliability, availability, maintainability and safety (RAMS) of the system. The discussion will draw from the risks and requirements involved in the project, chapter 3 and 2, but will present a more detailed analysis into the RAMS aspects of the project.

17.5.1. Reliability

Reliability can be defined as the probability that a system, subsystem or component can no longer function in the way it was intended, as per the requirements or stakeholder intentions within operational conditions. In order to properly evaluate the reliability of the drone a metric can be employed for comparison and analysis, a commonly used metric in reliability is the Mean Time Between Failures (MTBF) , this is given in hours. It has been found that a UAV system has an MTBF of 10.000 h [1].

The MTBF of the system however does not tell the whole story, as the drone is made of many different subsystems and parts each with different probabilities of failure over a given time. The failure rate of some of those most critical subsystems will therefore be analysed, those with a higher failure rate will need more maintenance and attention than those with a lower failure rate and more redundancies may be needed. The failure rate will be given as failures per hour. The failure rates of the most critical hardware components are given in table 17.1, The failure rate per one hour can then be converted to an MTBF value and vice-versa as one is simply the reciprocal of the other. It should be noted that the values found for the air quality emission sensors were based on the length of their warranty or expected life, as stipulated by the manufacturer, as no other reliability or failure metric could be found, it was therefore assumed that the manufacturer would be confident the product would not fail before the warranty was up, making it a useful substitute for MTBF. The last point to mention is that as the ground station is unique and based around a prototype, therefore the failure rate is almost impossible to know and will be excluded.

Table 17.1: Failure rate and MTBF for subsystems

Component	**Failures/h**	**MTBF** (h)
Autopilot [2]	4.94×10^{-5}	20242.9
Motor [2]	1.0×10^{-4}	10000
Propellers [2]	8.33×10^{-4}	1200.5
ESC [2]	2.0×10^{-4}	5000
Batteries [2]	2.0×10^{-5}	50000
GPS [3]	1.66×10^{-4}	6024.1
Radar [4]	1.0×10^{-8}	1.0×10^{8}
CPU [5]	2.65×10^{-7}	3.78×10^{6}
Air quality sensors [6]	5.71×10^{-5}	17520.0
Noise sensors [7]	1.44×10^{-5}	69444.4

[1] `https://www.ncbi.nlm.nih.gov/pmc/articles/PMC6165073/` [cited 22 June 2020]

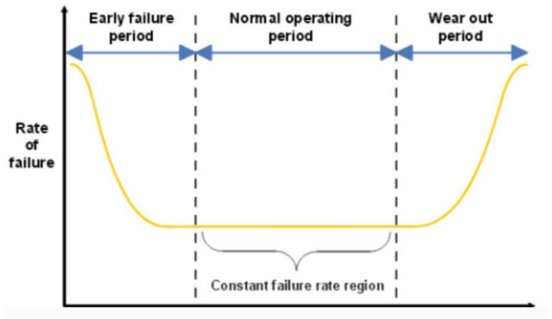

Figure 17.6: Failure rate over product life [8]

Table 17.1 shows in red the MTBF values that are the lowest and therefore will need to inspected and possibly repaired or replaced most often. The propellers are intuitively the parts that will require the most attention to maintain reliability as they are constantly moving at high speed, therefore increasing the chance of failure, the ESC's are also working throughout the operation of the drone. The GPS is a very complex system, therefore the low MTBF is also understandable. Now that all of the failure rates have been found the reliability of the system over a given operation day of 18 hours will be calculated, this is shown in equation 17.1, where λ is the failure rate of a component and t is the operation time. It should be noted that the failure rate for components were multiplied by the number of components present in the system (excluding redundancies) first and the sensors were assumed to be operating for a third of the operation time as explained in section 5. This gives a reliability that no component will fail over the day of 85.6%.

$$R(t) = R_1(t) * R_2(t) * \ldots . R_n(t) = e^{-(\lambda_1 t} * e^{\lambda_2 t} * \ldots . e^{\lambda_n) t} \tag{17.1}$$

This reliability can be greatly improved upon by adding redundancies, in the system the redundancies include four motors, propellers and ESC's (the drone can safely function with only one plane of propellers), seven air quality sensors, three noise sensors and four batteries. Equation 17.2 can be used to recalculate the reliability's including the redundancies. Using this calculation the new reliability of the system over a given day is 99.8%, again this is the probability that nothing on the system will fail that cannot be mitigated by the use of a redundant component, this high percentage therefore complies with requirement *AEMS-F-REG-05*.

$$R_{\text{component}} = \sum_{i=k}^{n} \left(\begin{array}{c} n \\ i \end{array} \right) R^{\hat{i}(1-R)^{n-i}} \tag{17.2}$$

The reliability and failure values calculated in this section were calculated assuming that the failure rate of components are constant throughout operation, this however is not true. As can be seen from figure 17.6 the failure rate at the early life of a product is high and the later stage of the product life is also high, this is due to early failures and inexperience and product wear our respectively. The normal operating lifetime can be seen to be constant, and as this period is by far the largest the failure rate can be assumed constant when calculating the reliability.

17.5.2. Availability

The availability of the system is measured by how quickly the system can be in operation when it is required. The aim is to minimise any downtime that may occur in order to make the system as functional, useful and profitable for stakeholders as possible. An important aspect in minimising downtime will be how efficiently

[2] https://apps.dtic.mil/dtic/tr/fulltext/u2/1077687.pdf [cited June 20, 2020]
[3] https://www.intechopen.com/books/accuracy-of-gnss-methods/evaluation-methods-of-satellite-navigation-system-performance [cited June 20, 2020]
[4] https://cordis.europa.eu/docs/projects/cnect/1/248231/080/deliverables/001-MOSARIMDeliverable14V161.pdf [cited June 20, 2020]
[5] https://www.r-ccs.riken.jp/en/wp-content/uploads/sites/2/2015/11/Presentation.pdf [cited June 20, 2020]
[6] https://www.sandia.gov/mesa/_assets/documents/bibliography/3_13MEMS.pdf [cited June 20, 2020]
[7] https://www.digikey.com/en/terms-and-conditions [cited June 20, 2020]
[8] https://www.meanwelldirect.co.uk/glossary/what-is-mtbf/ [cited June 20, 2020]

parts can be replaced if needed, the efficiency can be increased by having a spare parts in storage ready to be used if necessary.

It is impractical and expensive to keep spare parts for all of the components used by the system. In order to be considered in the spare parts list the component should be easy to store, critical to the mission, low-cost and the part should have a high failure rate (as it would be more likely to be needed). Table 17.2 shows the results of this analysis, the parts considered are the same as those in section 17.5.1 as they were considered critical to the mission, the metric in the table is simply High, Medium or Low where the colour green indicates if this is a good trait, yellow a medium trait and red an undesirable trait.

Table 17.2: Possible spare part comparison

Component	Failure rate	Storage needs	Cost
Autopilot	Medium	Low	Low
Motor	High	Low	Medium
Propellers	High	Low	Medium
ESC	High	Low	Medium
Batteries	Medium	Low	Medium
GPS	High	Low	Low
Radar	Low	Low	Medium
CPU	Low	Low	Low
Air quality sensors	Medium	Low	High
Noise sensors	Low	Low	Low

From table 17.2 it is clear which components are best used as spares, table 17.3 shows the spare parts that should be kept in storage along with the minimum quantity needed to replace all of those parts on the drone, if the number of spares in storage drops below this number new spares should be ordered. For the parts that are not included on this list, if they were to need replacing this would mean a new part would need to be ordered and delivered, this would increase the downtime of the system and reduce the availability. Another consideration to optimise the availability of the system is to have a duplicate system in storage for use if the current one is unavailable. Technicians and maintenance engineers should also receive adequate training in how the system works and how repairs can be made in order to improve availability. Lastly, customers should be advised that all technical aspects of the system should be dealt with by the trained staff as to reduce the possibility of damage from tampering.

Table 17.3: Spare parts

Component	Storage quantity
Autopilot	1
Motor	8
Propellers	8
ESC	8
GPS	1

17.5.3. Maintainability

The maintainability of the system will describe which components will need to be checked and the interval between them. This is an important aspect in the life-cycle of the UAV. By means of regular maintenance, mistakes can be spotted early on and prevent failure during flying time, thus increasing the safety of the entire system.

The entire system shall be inspected after each working day, according to requirement *AEMS-NF-OPR-01*. This will be a visual inspection to investigate the integrity of the UAV. The scheduled visual inspection for each component is presented in table 17.4. Based on the visual inspection there are three scenario's that can take place. First of all, there are no damages present, thus the system can perform regular operations the following day. Secondly, there is a problem spotted with the drone, however it can be resolved on the spot

Table 17.4: Daily visual inspection

Component	Inspection
Motor	Attachment to the arm, wiring, damages
Propellers	Attachment to motor, damages on blade
Batteries	Battery connections, distribution board, (water) damages,
Sensors	Membrane whole, (water, heat) damage
Electronics	Wiring, (water) damage
Frame	Cracks, with extra attention to joints of different components
Performance	Read out telemetry and sensor data

by an inspector. For example, bolts are tightened. The system can be used again the following day. Thirdly, a problem is found and further inspection is required. The system cannot be operational the following day and will have to stay on the ground. For all three cases it is important that it is documented. This could show a trend in reoccurring problems and may lead to a redesign of the system.
Besides the daily scheduled maintenance, there is other scheduled maintenance. All these are listed below.

- The software should be checked monthly for updates.
- A performance test of the propellers is required after two month of use. This is close to the expected MTBF.
- A performance test of the ESC is required after eight months of use. This is close to the expected MTBF.
- A performance test of the GPS is required after 10 months of use. This is close to the expected MTBF.
- The sensors should be changed every two years of use.

It is also possible to have unscheduled maintenance.This could be in the form a test flight to recalibrate the autonomous subsystem, the replacement of a part, or the recalibration of a sensor. The unscheduled maintenance is the result of the daily inspection. For example, the telemetry data was not as expected and therefore a ESC should be replaced. All maintenance should be performed by an inspector who has knowledge about the system, so he can easily spot if something is out of the ordinary and does not accidentally damage the system during inspection.

17.5.4. Safety

In order for the system to function properly and not cause any harm to airport or the community surrounding it, it is important that the UAV is safe. Many safety issues are presented in more detail in the detailed design, as well as risk. This section will give an overview of what has been done to take into account safety. Details on certification can be found in section 17.6.

- The UAV must not interfere with regular airport operations. In all possible scenario's the airport take-off and landing strip is avoided by the UAV, to prevent the system from colliding with an aircraft. Moreover, the system can also accelerate up to $25\,\mathrm{m\,s^{-1}}$ to avoid aircraft and other objects due to the autonomous navigation.
- The system is always able to safety perform an emergency landing.
- The drone can still fly when one of the motors fails, and thus can make it back to the ground station, or perform an emergency landing.
- All the materials that are selected are non flammable, such that the drone cannot catch fire.

17.6. Certification and Compliance

Certification is a future activity that should be taken into account in the design in order to later be able to complete the certification procedure. Its location within the timeframe can be found in chapter 22. The procedure to certify the UAV will be required to allow for commercial operation as prescribed by requirements *AEMS-F-REG-02/03*. This then allows for the compliance of requirements *AEMS-F-REG-08/09*. The following procedure is taken from EASA regulations[9]. First a ConOps description is made. This involves es-

[9]https://www.easa.europa.eu/document-library/general-publications/easy-access-rules-unmanned-aircraft-systems-regulation-eu [cited May 4, 2020]

tablishing and determining the relevant technical and operational system information for the risk analysis. Importantly it should include the interaction between the ANSP (Air Navigation Service Provider) and the UAV system or operator, thereby complying with *AEMS-F-REG-08* more specifically. Next, Important risk factors must be addressed such as the Air Risk Class and Ground Risk Class (requirements *AEMS-F-REG-09* and *AEMS-F-REG-10* respectively). An EASA-defined “High" level of robustness is needed for the former (requirement *AEMS-F-REG-11*). These aspects define further parameters required for certification. If the UAV complies with the Specific Operations Risk Assessment (SORA), then the relevant authority of operation must be approached for final approval. This would generally be the NLR for the example of operation within Dutch airspace. If, the SORA process is not satisfied, either a redesign or risk mitigation strategy must be performed, depending on the severity of non-compliance. To assure future sustainable development of the project, a full EMAS accreditation will be sought, which allows for continuous improvement in the organisation's sustainable performance.

Last but not least, before extra steps can be taken for certification, compliance with the regulations needs to be provided. It can be seen below in table 17.6. Most of the requirements are already passed while some of them (such as AEMS-F-REG-02,-03,-05) can only verified when certification tests are finalised.

Operations Compliance Matrix

Requirement ID.	✓ / o / x	Comment
AEMS-NF-OPR-01	✓	Accounted for during measuring mission (section 17.2.3)
AEMS-F-OPR-03	✓	Ground station functions as required (section 17.2.2)
AEMS-F-OPR-04	✓	Weather information can be accessed as explained in section 17.2.3
AEMS-F-OPR-11	✓	Section 17.2.1 details the procedures to operate at different airports
AEMS-F-OPR-12	✓	Weather suitability checks continuously performed as explained in section 17.2.3
AEMS-F-OPR-13	✓	Taken into account in sections 17.2 and 17.3
AEMS-F-REG-02	o	It is impossible to know before applying for certification but this has been taken into account in this project to the further possible extent
AEMS-F-REG-03	o	Same as AEMS-SYS-REG-02
AEMS-F-REG-05	o	Reliability has been calculated to be high (section 17.5.1) however not all components are considered, more research and testing is needed.
AEMS-F-REG-08	✓	Section 17.2.3 explains how the CIS (section 17.3 incorporates this
AEMS-F-REG-09/10/11	✓	Detailed in section 17.6
AEMS-SYS-SUST-06	o	Residents are informed to the fullest extent possible, however, it is incredibly difficult to fully satisfy every single resident and therefore mitigation strategies are devised for risk *OP2*
AEMS-SH-DIMS-01	✓	The system's maximum transportation dimensions are taken into account in section 17.2.2
AEMS-SH-PERF-02	✓	Section 17.2.3 ensures no violation of this requirement.
AEMS-F-AUT-11	✓	Lights as explained in section 17.2.3 are operational at night

18
Risk Assessment

Throughout the report, the risks have been incorporated systematically into the design, according to the strategy presented in chapter 3. Section 18.1 will explain the resulting prevention and mitigation strategies and section 18.2 will present the resulting risk map.

18.1. Risk Prevention and Mitigation

PW1-Power system degrades over life time and becomes unusable Probability: P, Impact: 2. This risk is aided in its prevention by ensuring the power system will be maintained properly during operation by removal of components and thorough inspection detailed in 11.1. The impact mitigation strategy is the replacement of all or some of the batteries, again explained in section 11.1.

PW2-Failure of the power system Probability: R, Impact: 3. Through the application of monitoring, maintenance and removal of the power system's batteries when not in use, this risk is further prevented (see section 11.1). The impact has been further mitigated through the abnormal events procedures as explained in section 17.2.4.

ST1-Failure due to exceeding of design loads Probability: U, Impact: 4. The maximum loads acting on the drone were calculated and a safety factor of 1.5 was used when designing the drone structure in section 10.1.2. This will be considered safe life, this will further prevent the risk. In the event the drone fails due to the loads it experiences, the structure will have to be redesigned (as seen in section 10.1.2), this to further mitigate the risk.

MF1- Unable to manufacture Probability: R, Impact: 4. The probability score has been decreased by considering the minimum manufacturing thicknesses during the design, shown in section 10.1.1. The mitigation method used to reduce the impact score for this risk is the redesign of the structure or a different choice in material used, as explained in section 16.1.

PR1-Failure to provide enough thrust to the drone Probability: R, Impact: 2. The thrust to weight ratio was calculated for the drone and compared to similar drones, it is close to the current commercially available drones, even exceeding their performance. This helps in reducing the probability score (as shown in section 12.7.2). The mitigation method used to lower the impact score was that the inherent design in the coaxial octocopter design is that multiple propellers can fail and the drone can still safely return to the ground station, this is explained in more detail in section 12.4.1.

DH1-Fails to distinguish between aircraft and background metrics Probability: U, Impact: 2. The probability is reduced by verifying and validating against the current noise and emission measurements taken around airports as well as in locations where the background levels are known. The frequency of the noise produced by the drone can also be measured and is then easily found from the measurement data (as explained in section 8.4). This risk is further mitigated by using local re-meshing and setting return points to obtain more details. This is explained in section 8.

DH2-Modelling unable to interpolate between data Probability: U, Impact: 3. Through the use of RBFs, a robust tool for interpolating multi-dimensional scattered data, the probability score is decreased (see section 8.3). The impact score is set to 3, as re-evaluation would need to be done to evaluate the issue. The service page as described in section 17.3 improves the mitigation score.

CM1-Unable to download data from the drone Probability: R, Impact: 2. The probability of this risk can

be lowered by selecting a trustworthy and stable carrier, as presented in section 13.1.1. By having sufficient storage on board for the drone to physically transfer data when it is back at ground station, this helps if the downloading of data is interrupted, the impact will be made far lower, as explained in section 13.1.1.

CM2-Data is lost before or during data transfer Probability: R, Impact: 2. A trustworthy and stable carrier is selected to lower the probability of this risk (as seen in section 13.1.1). The impact of this risk is reduced by cross-checking data points in the database and replacing lost data points. This is explained further in section 13.1.1.

PL1-Sensors fail to measure any accurate data Probability: U, Impact: 3. The design of the sensors and their location with respect to each other is such that little interference can exist with the filtered flows (section 6.4.2). Additionally, over estimations were taken into account for expected pollution species' concentrations (section 6.1.3). The backup systems, as defined by requirement *AEMS-SYS-05* help with prevention as well as mitigation.

PL2-Sensors damaged during operation, transportation or storage Probability: R, Impact: 2. The structural design takes into account the addition of a protective case as explained in section 10.1.1. In addition, weather checks are carried out before and during drone flight and foam protectors are used for the exposed radar sensors (section 17.2.3). Many sensors also come with protective housing. Again, over estimations were taken into account for pollution species' concentrations (section 6.1.3). As for mitigation, backup sensors and redundancies are in place (sections 6 and 7) which can be used until a replacement can be made during maintenance (see section 17.5.3.

CS1-The drone is uncontrollable Probability: R, Impact: 4. Use of a commonly used and widely tested autopilot system to handle the control system, described in section 9.1 lowers the probability score. The impact can be lowered by performing an emergency landing when it is uncontrollable described in section 9.1.

CS2-The drone is unstable Probability: R, Impact: 4. Tuning the controller gains and calibrating all control hardware during a test flight before product launch, section 9.3.1 lowers the probability of this risk. The drone will have to be re-calibrated and another test flight has to be performed, section 9.3.1, to lower any impact for this risk.

CS3-Insufficient reaction to necessary sensory inputs (DAA/SAA) Probability: U, Impact: 3.The probability score is lowered by the use of the radar sensors and the algorithm employed is verified and validated in section 9.5. The drone will have to be re-calibrated and another test flight performed, section 9.3.1, lowering the impact of the risk.

NV1-Global location of the drone is unknown Probability: R, Impact: 3. The GPS-RTK receiver will be mounted on top of the drone away from obstacles that may interfere with the signal, section 9.1. During brief periods of GPS-RTK signal loss the IMU, section 9.1, can be used to estimate the global position of the drone, in case the period of loss is longer the drone must perform an emergency landing 9.2, these both reduce the impact of the risk.

NV2-The drone is unable to avoid impact with the local environment or restricted area Probability: R, Impact: 3. A robust sense and avoid algorithm will be implemented, section 9.2, and an ADS-B receiver will be used to ensure that the locations of aircraft and their headings are known, section 9.1, both reduce the probability score. In case the drone is no longer able to detect and avoid obstacles and cannot keep out of restricted space it must perform an emergency landing (section 9.2), reducing the impact.

NV3-Unable to determine route pre-arranged destinations Probability: R, Impact: 2. Section 9.2.2 explains that this risk is minimised through the use of a segmented node coverage approach. The service page as described in section 17.3 improves the mitigation score, should an issue arise.

OP1-Adverse weather conditions damage/reduce the drone functionality Probability: P, Impact: 3. Through the checking of the current weather and forecast, the risk likelihood is reduced. Weather is, however, always subject to change so the probability is appropriately set to possible (P). The impact is reduced through a return to the ground station as well as the abnormal events procedures set out in section 17.2.4. More detail

on this can be found in sections 5.1 and 17.2.3.

OP2-The drone becomes a noise nuisance to people and animals Probability: U, Impact: 2. The path planning aspect aims to find an efficient route, thereby minimising the time that the noise is exposed to people or animals (section 9.2.2). Section 17.4 details the response to this risk if it occurs.

OP3-The drone causes damage to humans, animals or ground property Probability: R, Impact: 3. The abnormal events procedures as presented in section 17.2.4 further improve the prevention of this risk. The insurance, as explained in section 20.1.1, as well as the aforementioned procedures (specifically the emergency response) mitigate this risk further.

MN1-Unable to inspect parts/sections of the drone Probability: U, Impact: 2. As explained in chapter 10, many parts are assembled with suitable clips, enabling easy removal and attachment. A design re-evaluation would need to be done of the structural design.

18.2. Prevented and Mitigated Risk Map

As can be seen from figure 18.1 the risks have been successfully moved toward the bottom left of the risk map, therefore decreasing the chance of the mission failing due to the identified risks.

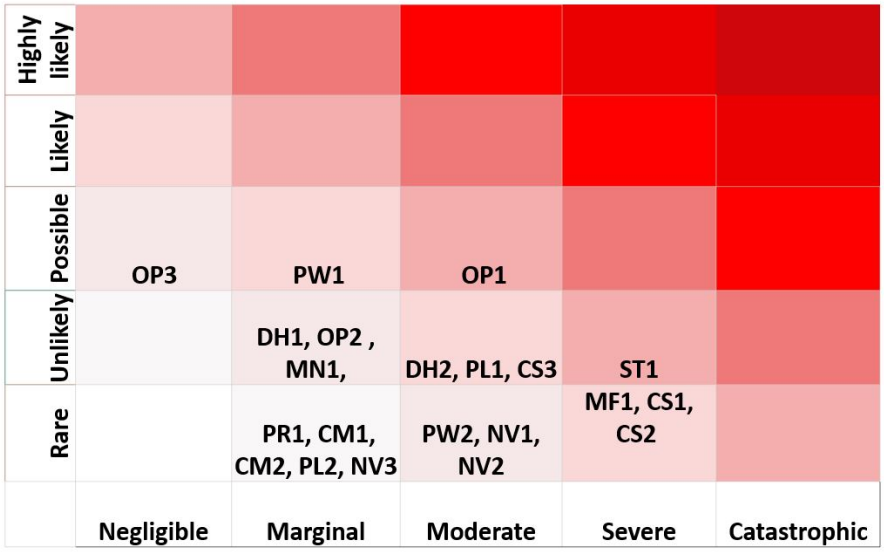

Figure 18.1: Risk map after prevention and mitigation strategies applied

19
Sustainablity Analysis

As already stated in chapter 4, a sustainable design shall adhere to the three core principal aspects: environmental, social and economical. This chapter concerns itself with analysing how the design incorporated. The process has been explained and outlined in detail in the baseline report [3].

19.1. Design Analysis

Now, based on D4S sustainability strategy wheel and impact matrix described in Part 1, the final design can be evaluated. The seven aspects of D4S were adapted to each subsystem design. The outcome of this approach will be presented here.

The performance indicators include energy efficiency, material, solid waste, toxic waste, costs and social responsibility. For each concept, the matrix is populated with possible materials and processes that are inputted and outputted at the varying life-cycle stages that may influence the sustainability performance of each different concept [10]. The populated matrices are used as an overview to determine the influences on the different design strategies for the different concepts.

Low Impact Materials In chapter 10 the material selection has as an outcome the composite Cyanate ester/HM carbon fibre. According to [17], Cyanate ester/HM carbon fibre has a specific CO2 footprint of 52.1 kg/kg during primary production while the embodied energy is 756 MJ/kg.

During production, the lithium, contained in the LiPo batteries, is highly reactive and can combust if it comes into contact with water. Since the LiPo units are off-shelf bought components that are assembled, the special attention needed was not considered as part of the manufacturing plan. Despite this, most components of the LIB (lithium-ion batteries) can be recycled and reused according to [46].

The DC motor selected by the propulsion and aerodynamics subsystem (see in chapter 12). The specific design uses an iron electromagnet and cooper for wiring. Moreover, the propeller is made of carbon fibre. Both supporting materials are at least downcyclable.

Many of the components considered for the final product contain printed circuit boards (PCB) A PCB compromises of about 70% non-metal, such as an epoxy resin, and around 30% compromises of metallic substances such as copper, solder and some precious metals [29]. The PCB's can be recycled in three possible ways: direct treatment, primitive recycling techniques and advanced recycling techniques. Advanced recycling techniques have the ability to recycle both the metallic fraction as well as the non-metallic faction. This technique, however, does use more energy.

The materials contained in the sensors arrays are, unfortunately, potentially harmful to the environment. As described in chapters 7 and 6, this aspect cannot be considered as during the design procedure since the sensors are off-the-shelf components that are selected based on their technology. Unfortunately, there is little to no control over the materials used inside by their manufacturers since, for the same sensor technology, they are bound to use the same materials. Moreover, they degrade in time so some of them have to be changed at a frequency of two years. Despite this, the manufacturers do not provide other, more sustainable, alternatives. On the other hand, as it can be seen table 19.1 the mass percentage taken by these sensors is only at 2.7% which is deemed sufficiently low.

Overall, the materials contained by the main structural components of the design have reasonable energy consumption's during production and are at least downcyclable. Despite this, the supporting materials and chemicals inside the off-shelf components are neither controlled nor chosen by the current design. Finally, the rating achieved is **"+"**.

Table 19.1: Overview of material sustainability

Components	**Material** [-]	**Percentage** [%]	**Recyclability** [-]	**CO_2 footprint** [kg/kg]	**Primary Production** [MJ/kg]
Arms	Cyanate ester + high modulus carbon fibre	7.047	Downcyclable	52.1	756
Legs	Cyanate ester + high modulus carbon fibre	9.075	Downcyclable	52.1	756
Protective Case	Cyanate ester + high modulus carbon fibre	1.601	Downcyclable	52.1	756
Battery clamps	PLA	0.079	Recyclable	2.98	58.1
Battery Housing	PETG	1.515	Recyclable	4.59	98.2
Internal frame	Cyanate ester + high modulus carbon fibre	2.029	Downcyclable	52.1	756
Magnetic metal plate	Stainless Steel	3.643	Recyclable	5.16	74.8
Rotor blades	Carbon fibre composite	4.882	Downcyclable	N/A	N/A
Motor	Iron / Copper	33.631	Recyclable	2.4 / 3.79	25.6 / 61.9
Batteries	LiPo	22.52	Recyclable	N/A	N/A
Air pollution sensors (electro-mechanical sensors)	Different toxic chemical compounds	2.7	No	N/A	N/A
Air pollution sensors (Particle counters)	Plastics & PCB	4.937	Recyclable	N/A	N/A
Cooling fans	Plastics	1.26	Recyclable	N/A	N/A
Noise sensors	PCB	0.267	Recyclable	N/A	N/A
Radars	PCB	1.068	Recyclable	N/A	N/A
GPS	Plastics & PCB	0.334	Recyclable	N/A	N/A
Stereo camera	Plastics & PCB	0.106	Recyclable	N/A	N/A
Autopilot	Plastics & PCB	0.105	Recyclable	N/A	N/A
Raspberry Pi	PCB	0.307	Recyclable	N/A	N/A

Material Use The electromechanical sensors are not considered to be very environmentally friendly, however, there is no alternative solution for these. The design team has made every effort to limit these sensors to only take up 2.7% of the final weight fraction. The weight of the final product equates to 14.99 kg. The low weight of the system makes it easy to handle for ground staff. The low weight of all the selected components ensures an efficient operation. The selected Li-Po batteries are more compact than the other possibility, lithium-ion battery[1]. The above-discussed points result in a rating of **"+"** for the material use strategy.

Production Techniques The main in-house manufacturing techniques involved are filament winding, FDM additive manufacturing and lay-up. The first two methods are automated and only concern a limited amount of steps. The lay-up is completed by hand but it does not use any complex tools. For all of the part production and assembly steps, a high degree of safety can be achieved. Last but not least, none of the methods produces material waste and renewable energy sources can be implemented to power the machines (for FDM and filament winding). To conclude, the design corresponds to many steps, low waste amounts, low non-renewable energy use, excellent safety This leads to a strategy rating of **"+"**.

Distribution System The considerations for the distribution of the system will cover the ease with which the flying system and the ground station can be transported between measuring sites, in this case, locations around the airport. As described by chapter 5, the mission was optimised for a maximum measuring time without moving the ground station. The exact locations of this station depend entirely on the airport at hand and a plan can only be build once the exact geography is known. Despite this, the system will not have to be transported over long distances within one airport but, when moving to a new airport, a van should be used to carry it there. Overall, it fits the description of "Energy-efficient transport, efficient logistical movements, overall medium distances" so **"+"** is awarded for this strategy.

Impact During use The battery power used during the mission can be recharged using renewable energy sources. Schiphol already implemented wind energy as the main source for electric power [2]. The system ground station can connect to the local airport grid and hence it can use the same electricity supplier.

As already specified during the aerodynamic design from chapter 12, the propeller size was maximised to generate the same thrust at a lower RPM. Thus, the noise generated by the design was decreased. Moreover, the motor selected also provides an acoustically isolated casing, reducing further the total noise production.

One key aspect that was treated during the design was the impact during a measuring mission. From the operational perspective, the system plans its path using a combination between an evolutionary algorithm and Dijkstra. The result becomes an improved nearing-optimal measuring time for a minimised travel time. Achieving this not only contributes to the overall reduction of energy consumption but also limits the interference between the drone and other airport systems or the local community.

Last but not least, possible environmental issues can be caused by leaking of damaged batteries. However Li-Po batteries electrolytes have a lower chance of leaking as already presented during the propulsion system design in chapter 12[3]. Overall, the score for this criterion is a **"++"** according to the description of "No toxic emissions, low energy use, reduced noise, and positive social value"

Initial Lifetime The payload contains electromechanical sensors. Manufactures of these sensors cannot guarantee accurate measurements after two years of operations, and as such, they need to be replaced bianually. A Li-Po has a shorter lifespan than a lithium-ion battery. However, Li-Po batteries still have the storage capacity for 3000 cycles of 80% discharge [33]. the charging of the battery needs to be carefully One consideration is that Li-Po batteries can be combusted if charged at high voltage or temperature [33]. In general, other components of the system have high reliability with the lowest mean time before failure of 1200.5 hours of operating time for the propellers (described in chapter 17). Other components with lower mean times before failures are the ESC and GPS. As such, the overall systems have a good initial lifetime with good reliability. Even though no alternative solution for the sensors can be found, because some of the payload sensors need to be exchanged every two years, the design strategy cannot be marked higher than a **"o"**.

[1] https://blog.ravpower.com/2017/06/lithium-ion-vs-lithium-polymer-batteries/ [cited May 15, 2020]
[2] https://www.schiphol.nl/en/schiphol-group/page/100-procent-dutch-wind-power/ [cited June 17, 2020]
[3] https://blog.ravpower.com/2017/06/lithium-ion-vs-lithium-polymer-batteries/ [cited May 15, 2020]

End-of-Life System The recyclability of the different components is tabulated in table 19.1. As is evident from the table, the majority of the materials can be either recycled or downcycled. For some off the shelf components (e.g. the GPS), it is evident that plastics are used, however, the manufacturer does not provide specific information about the type (thermoset vs. thermoplastic) of plastic is used, and as such one cannot clearly state how well it can be recycled. As mentioned above, there are multiple options for recycling PCB's. To be able to fully recycle a PCB, high energy consumption is required during the decommissioning process. The considered materials for the arm structure, landing-gear and propeller cannot be fully recycled but can be downcycled according to [17]. As previously stated, research has been conducted on LIB recycling and most parts of a LIB battery can be recycled [46]. However, the recyclability of the cathodes in LiPo batteries is not extensively researched. Not considering the off the shelf components where it is not explicitly known what type of material is used, 80.144 % of the product can be at least recycled. To fully recycle the PCB's, a high amount of energy will be required. This results in a final score of **"+"** for the end-of-life strategy. This is compliant with requirement *AEMS-SH-SUST-01*.

19.2. Sustainability Evaluation and Compliance of Requirements

Now that each strategy rating was evaluated, both the requirements compliance and the sustainability wheel can be finalised. Requirement AEMS-SYS-SUST-08 cannot be verified at this point since it requires the system to be first manufactured and then tested. Despite this, the microphones can be used to identify the propeller noise frequency and then filter it out by bandpass in the frequency domain. This is left as a future application. All the other requirements are met.
The radar diagram visualising the sustainable scores of the detailed design can be seen in 19.1. The ratings are again laid over the minimum requirements ratings.

Sustainability Compliance Matrix

Requirement ID.	✓ / o / x	Comment
AEMS-SYS-SUST-03*	✓	Achieved by using on-board batteries, rechargeable with the electrical grid
AEMS-SYS-SUST-05	✓	Achieved by using different protective cases for sensors and battery which can be replaced, see sections 9.4 and 10
AEMS-SYS-SUST-06	✓	Minimised operating time, reduced propeller noise and silent motors.
AEMS-SYS-SUST-07	✓	It is not emitting any gas while operating
AEMS-SYS-SUST-08	o	Requires validation on built system
AEMS-SYS-SUST-09	✓	It does not carry any explosive substances
AEMS-SH-SUST-01	✓	The End-of-Life system details that around 80% of the monitoring system may be recycled.

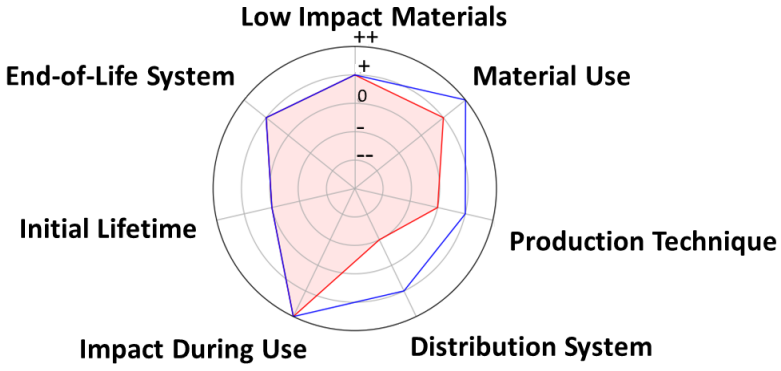

Figure 19.1: Radar diagrams visualising final sustainability ratings of the design (in blue) over the required ones (in red)

20
Financial Analysis

From the market analysis, some of the aspects of the financial feasibility of the project can already be derived. This information will be used in this chapter to formulate and present a strategy to make the project economically feasible.

20.1. Cost Breakdown Structure

Provides an overview of all the costs that are involved in the system. It contains fixed manufacturing costs as well as variable operational cost. These will be used to later calculate the return on investment in 20.2.

20.1.1. System Cost

The system cost includes the cost of all the components, hardware, software licenses etc. to create the product, assembly and production cost, testing cost and transport cost. They are shown in figures 20.1.

The assembly and production Cost includes the labour and equipment cost for manufacturing all the components and the hardware. This is thus more than solely the €25000 specified by requirement *AEMS-SHFNCE-01*, as that cost is only for the hardware. Labour and equipment cost are thus also included in that cost. The work spent on production can be approximated by 2 people who work for 2 weeks. As 1 techinicien costs €745.125 per week [1], this yields a total cost of €2980.5. The equipment needed for production includes screwdrivers and all materials needed for assembly and production [2]. This cost is estimated to equal around €569.1. Note that this is the price per drone. Adding these 3 costs, gives a total production and assembly cost of €28550.

The **Transport Cost** is estimated to lie around €945.6. This estimate is based on driving 1200 km during the production and delivery phase of the product, which gives a fuel (petrol) cost of €173.2 using €1.64 per litre and data from [9], hiring a van for a week, giving €500 and assuming 12 h of labour for an average income of €22.7 per hour [3], giving a total of €272.4. Adding these values up gives a total of €945.6 for transport cost, in figure 20.1.

The testing cost of the system is the part of the budget spent on testing and certification. During this phase, the system will undergo a certification procedure, which is monitored by the NLR in the netherlands [16]. The cost for this is found to be €2200[4]. Besides this, self-testing also has to be carried out and is estimated to lie around the same value as certification, namely €2500. This includes equipment for testing such as multimeters, calbiration of the sensors and testing their accuracy, a structural load bearing test, etc. This yields a total cost of €4700 for testing cost as can be seen in figure 20.1.

20.1.2. Operational Cost

The operational cost will not cover depreciation, because it is assumed that the system will be used until the end of its life. The values of this cost will be assessed for a yearly basis and for 1 product only.

The cost for **Maintenance** includes training the maintenance staff, paying the maintenance technicians. Spare parts also have to be accounted for in this price. Things will break and have to be replaced. As this cost can vary a lot, the estimate for this cost is based on study conducted by [24], that stated that maintenance was responsible for 44 % of production cost. The production cost equals €28550 thus resulting in €12562.

[1] ttps://www.payscale.com/research/NL/Job=Maintenance_Technician/Salary [Cited 18 June, 2020]

[2] https://www.heamar.co.uk/blog/68_what-tools-are-needed-to-build-a-drone [Cited 18 June, 2020]

[3] https://www.indeed.nl/salaries/vrachtwagenchauffeur-Salaries#:~:text=Het%20gemiddelde%20salaris%20voor%20een,%E2%82%AC%2013%2C63%20per%20uur. [Cited 18 June, 2020]

[4] https://www.nlr.nl/dronecentre/nlr-technische-keuring-van-de-drone/ [Cited 17 June, 2020]

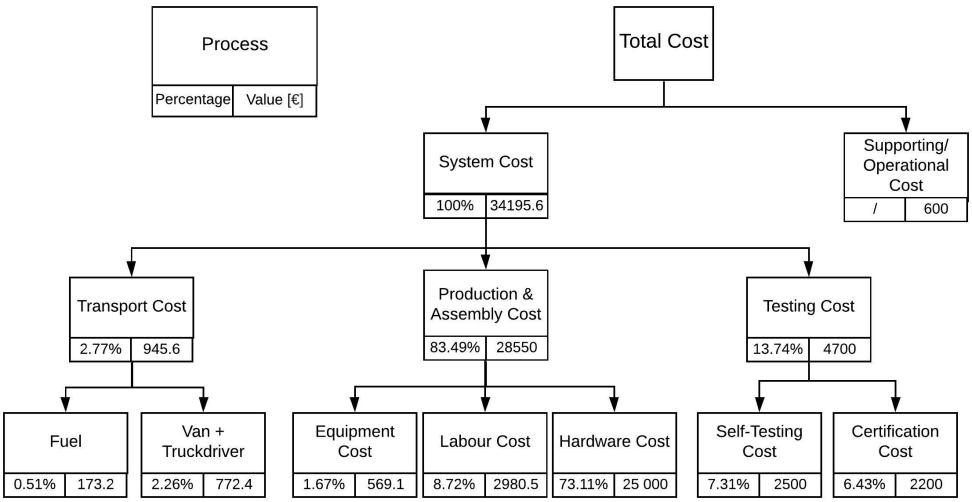

Figure 20.1: System Cost Breakdown

The Battery Operations Cost includes the cost for charging the batteries and replacing the batteries at their end-of-life. Given a flight time of roughly 30 min from chapter 12 and an 18 h daily routine from chapter, the 600 Wh battery thus has to be charged 36 times per day, giving 25.6 kWh per day and thus, given a price of €0.23 $kW^{-1}h$ [5], costs €5.88 per day. In total this gives €2147 per year. As Schiphol generates all its energy from solar panels, this is in accordance with chapter 4[6] Next to this, all 5 battery packs that are used in rotation, have to be replaced every 41 days as explained in chapter 11, meaning almost 9 times per year. As each 5 batteries cost €1712, This gives a total cost of €15408. Adding this up to the fuel cost of €17554.97

The **Insurance cost** should also definitely be accounted for. As the system is a drone, there is definitely a risk that data might be stolen, it might fall fry the sky and cause damage. This is also a big risk and covered in chapter 3. This greatly mitigates risk *OP3* as well as the general financial risks associated with the system. The yearly insurance cost for 1 product is around €650 plus 10 % of the system cost, which equals €34795, yielding roughly €4000 insurance per year [7].

What should not be forgotten, is that these are estimates, but given the number of references that were consulted to set up this pricing model, it is believed that they form a good initial estimate for the cost of the project. The operational costs are summarised in figure 20.2 in the form of an AND tree. The total annual operational cost equals €34186.5. Dividing this by 12 logically gives a monthly operational cost of €2848.9

20.2. Return on Investment

Firstly an economic model is considered where an airport is the customer and a subsidiary company of this airport provides the monitoring service for the airport in return for money. This model is picked, because it is the most realistic scenario for evaluating the financial feasibility of the system and is considered for 1 product only. From chapter 1, a competitive monthly system price was taken to be €2500, given that other comparable systems cost around €625 per month and the system in this report would add 4 times more value. On the other hand, from the cost breakdown, it is estimated that the total system cost will equal €34195 and the yearly operational cost will equal €34186.5. This results in a monthly operational cost of €2 848.9. Since the expenses and revenues are known, a cash flow can be visualised in figure 20.3. It shows the revenue, which is the sum of the monthly system cost and operational cost of €2500 and €2848.9 respectively, which gives €5348.9. This is the price the customer has to pay for the product. The red arrows show the expenses that are paid to provide the monitoring service. Firstly a total system cost of €35195.6 has to be paid up fr the product and €2848.9 is the cost for operating the system. Eventually the system will

[5] https://www.watkostenergie.nl/wat-kost-1-kwh/#:~:text=De%20gemiddelde%20prijs%20voor%20stroom,totaalprijs%20je%20uiteindelijk%20zult%20betalen [Cited 17 June, 2020]

[6] https://news.schiphol.com/solar-panels-installed-at-schiphol/

[7] https://www.thedroneu.com/blog/drone-insurance-guide-best-cheapest-coverage/#:~:text=(9)%20What%20Will%20Drone%20Insurance,cost%20will%20be%20around%20%24750. [Cited 17 June, 2020]

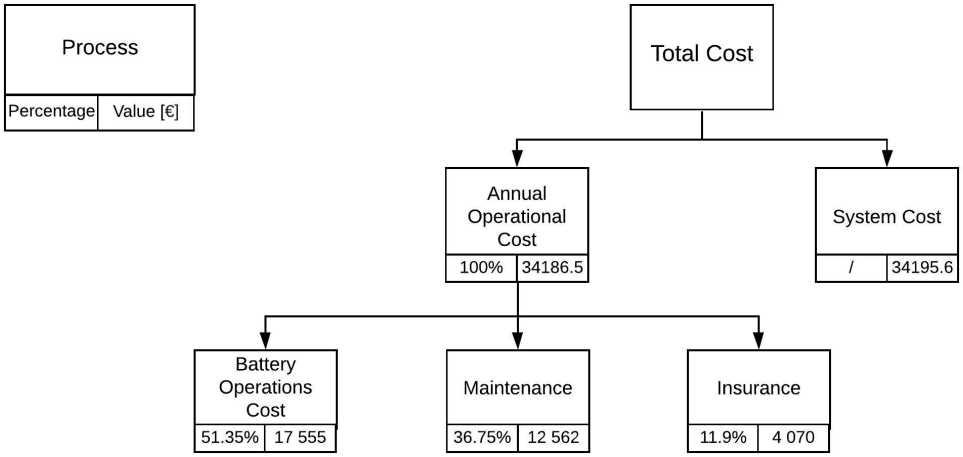

Figure 20.2: Operational Cost Breakdown

make for a net revenue of €2500 per month.

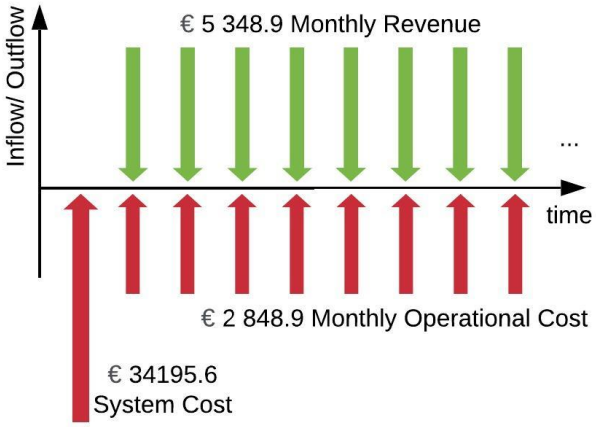

Figure 20.3: Cash Flow Visualisation

Figure 20.4: Return on Investment Graph

Based on the cash flow in figure 20.3, the return on investment can be computed. Figure 20.2 shows the balance, which is the total revenue up until that point in time minus the investments into the product, as a function of time. The break-even point, where the total invested money equals the total revenue of the money, happens after 14 months, indicated by the arrow in figure 20.4. The kinks in the line represent replacements of the payload which has to be done every 2 years, which costs €11880.9. Return of investment is calculated with the use of equation 20.1, where the current value of investment is the total revenue that can be generated from the system and the cost of investment is the money spent on the system. This can be reformulated to dividing the balance from figure 20.4 by the total cost spent on the system. As time goes by, these parameters change, which makes the return on investment time-dependent.

$$\text{Ro}I = \frac{\text{Current value of Investment} - \text{Cost of investment}}{\text{cost of investment}} = \frac{\text{Balance}}{\text{Cost}} \tag{20.1}$$

Using equation 20.1[8], the return of investment after 2,4 and 6 years are calculated to be equal to 75 %, 160 % and 211 % respectively. As the monthly revenue equals €5348.9, the yearly revenue is €64186.8. Given a market volume of 15 and a market size of €6.32 billion from chapter 1, a market share of $(15 \times 64186.8)/(6.32 \times 10^9) = 0.015$ % can be achieved.

[8] `https://www.investopedia.com/terms/r/returnoninvestment.asp` [Cited 17 June, 2020]

21

General System Requirement Compliance

Chapter 2 presented the general system requirements. These were incorporated throughout the design process and are now presented with their respected compliance in the following table.

General System Compliance Matrix

Requirement ID.	✓ / o / x	Comment
AEMS-SH-PERF-01	✓	Section 17.2.2 explains that max. 40 minutes are needed
AEMS-SH-PERF-02	✓	Up to 25 $m\,s^{-1}$ AEMS-PERF-08 design in chapter 12
AEMS-SH-PERF-03	✓	Chapter 6 presents sufficient minimum operative humidity and weather checks in place (section 17)
AEMS-SH-PERF-07	✓	Batteries are used and recharged at the ground station (sections 9.4 and 11.1)
AEMS-SH-DIMS-01	✓	The system is designed for this constraint (section 9.4)
AEMS-SH-DIMS-02	✓	Chapter 17 details transportation within a van
AEMS-SH-DATA-01*	✓	Data is acquired (chapter 6), processed (chapter 8) and visualised (section 17.3)
AEMS-SH-DATA-02	✓	Data is acquired (chapter 7), processed (chapter 8) and visualised (section 17.3)
AEMS-SH-DATA-03	✓	Section 8.2 shows the ψ list as report of both pollutants concentrations and noise, both of which can be visualised.
AEMS-SH-DATA-04	✓	Both the L_A values and the spectrograms are reported, see section 8.2
AEMS-SH-DATA-05	✓	The maximum concentration at each grid node and the Pm histograms are reported, see chapter 6 (section 8.2).
AEMS-SH-DATA-06	✓	Data is stored on a 256 GB storage card within the drone and sends the data to system's cloud database (chapter 13)
AEMS-SH-SUST-01	✓	Chapter 19 explains that around 80% of the monitoring system is recyclable
AEMS-SH-FNCE-01	✓	Chapter 15 explains that the hardware of the system costs less than €25000
AEMS-SH-SYS-01	✓	All sections make use of off-the-shelf components throughout the design
AEMS-SYS-02	✓	Section 17.2.2 presents transportation within a van
AEMS-SYS-03	✓	Maintenance procedures (section 17.5.3) as well as warranties for sensors will allow for a lifetime design of one year in the event of no major issues.
AEMS-SYS-05*	✓	The subsystems presented in chapters 6 and 7 include backup measuring instruments

22
Future Vision

This chapter will detail the project design and development logic. This examines the future development of the designed system once the DSE has ended. Section 22.1 will first present the overview this logic. A Gantt chart will also be presented. Finally, further applications are discussed in section 22.2 with a conclusion the impact of this project in section 22.3. This section is adapted from [3].

22.1. Project Design & Development Logic

After the initial design process, the team composition shall be re-evaluated to assess team member availability, address new team duties, and to maintain efficient management of resources. Thereafter, a further market analysis is performed with a focus on the commercial aspect, followed by, the technical design which performs any modifications to adhere to constraints found in the market analysis.

At this point, a prototype will be made and validation tests will be performed. Meanwhile, personnel training procedures and infrastructure are defined. Then, time is set aside for internal testing. Should there be non-compliant results, then a redesign of the subsystem (or more) may be required. If the tests are satisfied, then the project proceeds to the next step: a service branch is constructed. This includes, but is not limited to, service personnel and real estate. This training is crucial for certification and EMAS accreditation which is performed next. More on certification can be found in section 17.6.

Finally, the product is now ready to be manufactured. After this is set up, the team shall put more emphasis on operational aspects and service, as well as implementing feedback. In a larger time frame the process will iterate, leading to improved evolution of the system.

The process from final detailed design to company operation could take up to one or two years, where most time is spent on certification, authorisation and manufacturing. The next large phase is the company operation. The aforementioned feedback iteration could hatch a new version of the system about every five to ten years. This is also highly dependent on technological developments in all related sub-fields. The overall constructive plan for reaching an initial launch of the design is displayed in figure 22.2.

A Gantt chart on the future activities of the project can be found in figure 22.1. This is based on figure 22.2.

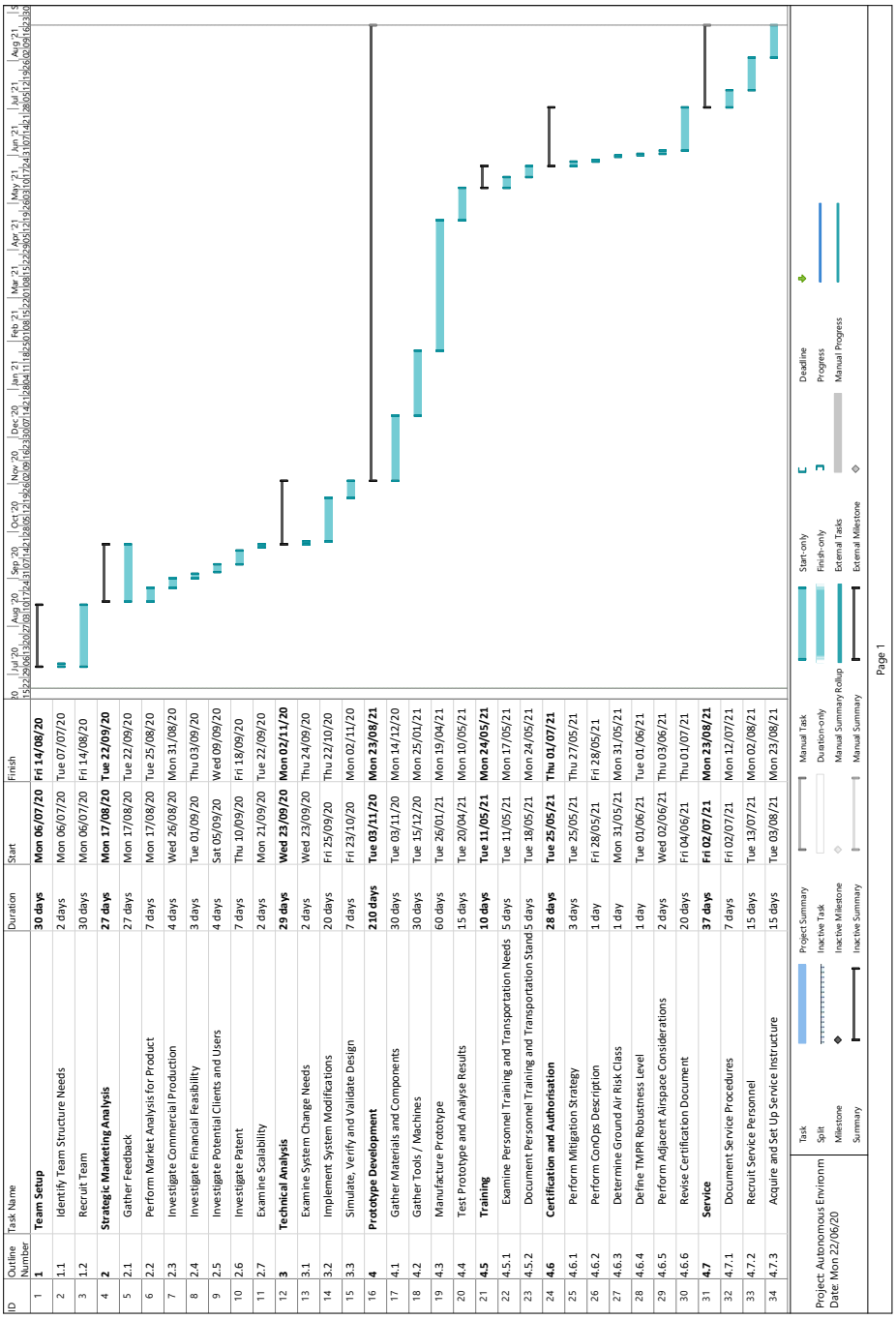

Figure 22.1: Project Gantt chart showing the future tasks which must be performed to get a working system.

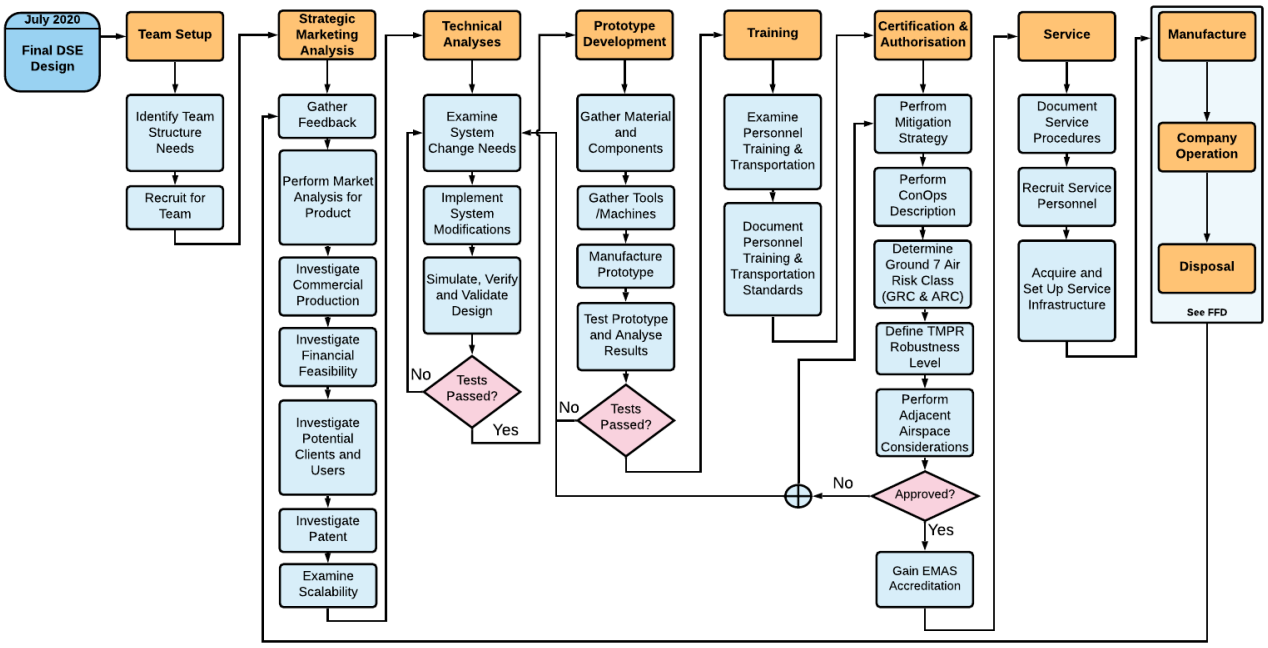

Figure 22.2: Project Design and Development Logic Diagram

22.2. Project Scalability

Scalability refers to the ability of the mission/product to grow towards a greater range of capabilities. After completion of the first operation cycle, the team can start thinking about expanding operations towards a wider range of applications. For a complete picture of when and where pollution occurs, similar pollution measurements could be done at all high pollution zones. Therefore, the system could eventually also be deployed near harbours, factories, and construction sites. With the option of interchangeable sensors, the UAV could also see an application in a field less related to aviation pollution, for example for forest fire examination, mapping purposes, mine investigation and more.

22.3. Project Impact

The primary product of the system is the metrics for noise and air pollution in the proximity of the UAV. These measurements can be used by authorities to better investigate a fitting tax for, amongst others, the airline industry. On the other hand, companies could choose to publish such measurements themselves to gain public trust. Similar efforts are increasingly being adopted by multinationals. Moreover, the data can be used to validate and improve noise and air pollution models. Finally, it can create a better understanding of what impact the aviation industry has on air and noise pollution and therefore on climate change.

23
Conclusion and Further Research

23.1. Conclusion

In the final report of the design synthesis exercise 2020, the design process for the autonomous environmental sensing drone was presented to the reader. Near-airport communities are impacted by both the emissions and noise produced by approaching and taking-off aircraft. The final design presents a mobile solution that can autonomously measure noise and pollution metrics that can assist policy makers, aircraft manufactures and airport management make informed decisions as to creating a sustainable future for that aviation industry and relationship with near-airport communities.

The system will be capable of measuring the following pollutants: methane, carbon monoxide, nitrogen monoxide, nitrogen dioxide, ozone, sulphur dioxide and particulate matter (including ultra-fine particulate matter). Alphasense was chosen as the main manufacture for air quality sensors, excluding the UFP sensor which is made by Naneos. The sensors all comply with the standards set by the European air quality directive. Expected maximum pollutant concentrations have been determined using the Gaussian plume model and aircraft engine data from the ICAO Aircraft Emissions Databank, while for the ozone and UFP measurements were taken from reference Air Quality Monitoring Stations. Toxic gas sensors were integrated into the drone using a gas sensor box. A boom structure was implemented to elevate the inlet of the sensor away from the air disturbance caused by the drone propellers. The output data was converted from analogue to digital, through a low pass filter the maximum concentration was then selected, these maxima can be compared to quantify whether the sensors are measuring accurately.

Eight MEMS microphones are used to measure sound signals in the range from 6 Hz-20 kHz. Two microphones will be placed on each side of the drone. The sensors will be calibrated, to account for temperature, humidity and pressure. The signals are processed so that the intensity for each frequency band is computed, from this the overall intensity is determined. Post-processing will remove the noise created by the system, from the total measured sound signals. These metrics are then interpolated over the x,y,z and time domain. Based on the interpolant gradient, the system flies back to asses its error. It optimises the interpolant based on the new error and creates contour plots (heat maps) and spectrograms. Moreover, other metrics like the sound exposure level (SEL) can be inferred. An ADS-B receiver outputs the flight identification number of aircraft in the area and it is used to match emissions and noise data to aircraft type.

Due to the restrictions around flying in airports and in near-airport communities requirements were documented and risks were identified. Also, the need for a sustainable system was of paramount importance. These aspects were considered heavily in the designing of the system and choices where made with these in mind. This lead to the coaxial octocopter configuration being chosen over a planar configuration, as it will both decrease the probability of failure and increase the stability inside the wake of an aircraft. The propellers used in this configuration where chosen so to minimise noise impact during operation. This was achieved by selecting an off-shelf component which can create the same pressure difference, at lower motor revolutions per minute. The system will make use of lithium-polymer cells as the energy source. These provide a large specific energy to maximise the endurance of the drone and the time spent taking measurements. Furthermore, the arms, legs, internal frame and protective casing are made up of a cyanate ester and high modulus carbon fibre composite. This light-weight, downcyclable material was selected due to its low density, high stiffness and high impact resistance, leading to a more efficient and sustainable design.

Dijkstra and a modified evolutionary algorithm are used to create efficient movement between two waypoints. The drone will make use of four radars located around the body, to safely navigate between these waypoints. Furthermore, the drone will be equipped with RTK enabled GPS for centimetre precision global

positioning and geo-caging, reducing the risk of entering restricted areas. The drone will be capable of automatic battery swapping with five batteries used in rotation, reducing the no-fly time. The autonomous landing procedure will be assisted using a pattern recognition algorithm, which can identify pattern markers located on the ground station, and guide the drone towards the final landing position. The marker will be searched for using a stereo vision camera, which is mounted on the underside of the drone body. The stereo-vision camera will also be used during emergency procedures. During the emergency procedure, a depth image is processed and scanned, to determine a large enough landing area in the drone's surroundings.

The total system will cost €34 195.6 with a monthly operational cost of €2848.9 were derived. The monthly revenue is calculated to be €5348.9, which results in a financially profitable product and a break-even point after 14 months.

The final system is compact, lightweight, sustainable and can be transported inside the 2x2x2 m ground station. Using the Design 4 Sustainability concept, a sustainable design was created where up to 80% of the final design can be either recycled or downcycled. The system can be setup within one hour and can be left to perform missions autonomously, there are however further considerations that can be made for the future of the project.

23.2. Future Research

There are topics for future work which logically follow from the entire report. Firstly, for the next iteration, it would be a suggestion to investigate whether adding a CO_2 sensor is a good investment. This is because an aircraft's thrust setting can be inferred from CO_2 measurements in the aircraft's exhaust plume. Providing noise and air pollution measurements together with the associated thrust settings could increase the potential for model development based on the system's measurements significantly, thereby increasing the value of the system. Moreover, having more state-of-the art supporting components for the sensors could greatly enhance accuracy and reduce the noise of the measurements.

Thirdly, a more detailed study on the rotors could be done to find out the impact of their rotational speed on the overall drag of the system. This would enable further optimisation of this subsystem. Likewise, the ability to tune the autopilot's PID controllers during the test flight could lead to a more versatile control experience.

In terms of the hardware, solar panels could be considered to replace or add to the current power option for the ground station. This would allow for more freedom in placing the ground station. Also, the mass production of the system is something that could show feasible, which would be required in case the demand is too high for the current production method. This also introduces the possibility to use a swarm of autonomous drones to complete the mapping.

Additionally, the path planning is optimised under heavy constraints, e.g. algorithm selection and ground station location. For future iterations, a more extensive optimisation could be performed after removing such constraints. Similarly, for the interpolation and modelling of the data, neural networks with augmented RBF kernels could be put in place that will work to shift the focus from standard partial differential equations (PDE) solutions to PDE's themselves. As an alternative, a simplex simple approach (for example B-splines) could be used to parametrically model the multi-dimensional scattered data.

Finally, machine learning tools can be build to further investigate the created data set. More intensive classification could be performed to distinguish further between a.o. aircraft configuration, thrust settings and seasonality.

Bibliography

[1] Anderson, B. E., Chen, G., and Blake, D. R. (2006). Hydrocarbon emissions from a modern commercial airliner. *Atmospheric Environment*, 40(19):3601–3612.

[2] Balsingh, V., Boerboom, L., Cook, J., Gavra, V., Lothaller, P., Park, C., Pietersma, R., Robertson, M., Schoenmaker, N., and Widmann, S. (2020a). Baseline Report (Design Synthesis Exercise 2020). Technical report, Technical University of Delft, Delft.

[3] Balsingh, V., Boerboom, L., Cook, J., Gavra, V., Lothaller, P., Park, C., Pietersma, R., Robertson, M., Schoenmaker, N., and Widmann, S. (2020b). Midterm Report (Design Synthesis Exercise 2020). Technical report, Technical University of Delft, Delft.

[4] Barrett, S. R., Britter, R. E., and Waitz, I. A. (2013). Impact of aircraft plume dynamics on airport local air quality. *Atmospheric Environment*, 74(2):247–258.

[5] Bergsma, O., Sinke, J., and Vermeeren, C. (2006). Materials and manufacturing 2. Technical report, Delft University of Technology, Faculty of Aerospace Engineering.

[6] Besnea, I. (2020). Acoustic Imaging and Spectral Analysis for Assessing UAV Noise.

[7] Biczyski, M., Sehab, R., Whidborne, J. F., Krebs, G., and Luk, P. (2020). Multirotor sizing methodology with flight time estimation. *Journal of Advanced Transportation*, 2020.

[8] CAA (2016). Uk aviation and air quality.

[9] Connekt (2017). Gebruikers en inzet van bestelauto's in Nederland. page 59.

[10] Crul, M., Diehl, J. C., and Ryan, C. (2006). Design for sustainability a practical approach for developing economies. Technical report, United Nation Environmental Programme and TU Delft.

[11] De Visscher, A. (2014). *Air Dispersion Modeling : Foundations and Applications*. John Wiley Sons, Inc.

[12] Deters, R. and Selig, M. (2008). Static testing of micro propellers. In *26th AIAA applied aerodynamics conference*, page 6246.

[13] EASA (2019). European aviation environmental report 2019.

[14] EASA (2020). Easy access rules for unmanned aircraft systems.

[15] European Parliament (2006). Directive 2006/126/EC of the European Parliament and of the Council of 20 December 2006 on driving licences (Recast). *Official Journal of the European Union*, (7):18–60.

[16] for Rulemaking of Unmanned Systems WG-3 Airworthiness, J. A. (2013). *Certification Specification for Light Unmanned Rotorcraft Systems (CS-LURS)*. NLR.

[17] Granta Design Limited, EduPack software, C. E. S. (2019). Cambridge, UK.

[18] Hu, Y., Dai, G., Fan, J., Wu, Y., and Zhang, H. (2016). Blueaer: A fine-grained urban pm2.5 3d monitoring system using mobile sensing. pages 1–9.

[19] Hu, Z., Bai, Z., Yang, Y., Zheng, Z., Bian, K., and Song, L. (2019). Uav aided aerial-ground iot for air quality sensing in smart city: Architecture, technologies, and implementation. *IEEE Network*, 33(2):14–22.

[20] Hwang, M.-h., Cha, H.-R., and Jung, S. Y. (2018). Practical endurance estimation for minimizing energy consumption of multirotor unmanned aerial vehicles. *Energies*, 11(9):2221.

[21] Jackson, G. (2003). Contingency for cost control in project management: a case study. *The Australian Journal of Construction Economics and Building I Vol 3 , No 1*, page 10.

[22] Kelly, W. and McMurry, P. H. (1992). Measurement of particle density by inertial classification of differential mobility analyzer–generated monodisperse aerosols. *Aerosol Science and Technology*, 17(3):199–212.

[23] Klees, R. and Dwight, R. P. (2016). *Applied Numerical Analysis February 2016*. Number February. TU Delft.

[24] Knights, P.F.; Oyanader, P. (2005). Best-in-class maintenance benchmarks in chilean open pit mines. *CIM Bull*, pages 98, 93.

[25] Kugele, A. and Jelinek, F. (2005). Aircraft particulate matter emission estimation through all phases of flight. *Eurocontrol Experimental Centre*.

[26] Leishman, G. J. (2006). *Principles of helicopter aerodynamics with CD extra*. Cambridge university press.

[27] Li, L., Tong, W., and Piltner, R. (2020). *Spatiotemporal interpolation methods for air pollution*. Elsevier Inc.

[28] Masiol, M. and Harrison, R. M. (2014). Aircraft engine exhaust emissions and other airport-related contributions to ambient air pollution: A review. *Atmospheric Environment*, 95:409–455.

[29] Ning, C., Lin, C. S. K., Hui, D. C. W., and McKay, G. (2017). Waste printed circuit board (pcb) recycling techniques. *Topics in Current Chemistry*, 375(2):43.

[30] Pohl, D., Dorodnicov, S., and Achtelik, M. (2019). Depth map improvements for stereo-based depth cameras on drones. *Proceedings of the 2019 Federated Conference on Computer Science and Information Systems, FedCSIS 2019*, pages 341–348.

[31] Popoola, O. A., Carruthers, D., Lad, C., et al. (2018). Use of networks of low cost air quality sensors to quantify air quality in urban settings. *Atmospheric Environment*, 194:58 – 70.

[32] Prior, S. D. (2010). Reviewing and investigating the use of co-axial rotor systems in small uavs. *International Journal of Micro Air Vehicles*, 2(1):1–16.

[33] Raza, S. S., Janajreh, I., and Ghenai, C. (2014). Sustainability index approach as a selection criteria for energy storage system of an intermittent renewable energy source. *Applied Energy*, 136:909–920.

[34] Reizenstein, A. (2017). Position and trajectory control of a quadcopter using pid and lq controllers.

[35] Romero-Ramirez, F., Muñoz-Salinas, R., and Medina-Carnicer, R. (2018). Speeded up detection of squared fiducial markers. *Image and Vision Computing*, 76.

[36] Rotaru, C. and Todorov, M. (2018). Helicopter flight physics. *Flight Physics-Models, Techniques and Technologies, DOI*, 10:19–48.

[37] Simons, D. G. (2018). Introduction to Aircraft Noise. pages 1–37.

[38] Sulfide, H., Dioxide, N., and Dioxide, S. (2014). Application Note : 109 Getting the Most from Toxic Gas Sensors. (410):1–18.

[39] Suzuki, K. A., Filho, P. K., and Morrison, J. R. (2012). Automatic battery replacement system for uavs: Analysis and design. *Journal of Intelligent and Robotic Systems: Theory and Applications*, 65:563–586.

[40] Theys, B., Dimitriadis, G., Hendrick, P., and De Schutter, J. (2016). Influence of propeller configuration on propulsion system efficiency of multi-rotor unmanned aerial vehicles. In *2016 international conference on unmanned aircraft systems (ICUAS)*, pages 195–201. IEEE.

[41] Villa, T. F., Salimi, F., Morton, K., Morawska, L., and Gonzalez, F. (2016). Development and validation of a UAV based system for air pollution measurements. *Sensors (Switzerland)*, 16(12).

[42] Welker, R. W. (2012). Size analysis and identification of particles. In *Developments in Surface Contamination and Cleaning*, pages 179–213. Elsevier.

[43] Wolfe, P. J., Yim, S. H., Lee, G., Ashok, A., Barrett, S. R., and Waitz, I. A. (2014). Near-airport distribution of the environmental costs of aviation. *Transport Policy*, 34:102–108.

[44] Wormhoudt, J., Herndon, S. C., Yelvington, P. E., Miake-Lye, R. C., and Wey, C. (2007). Nitrogen oxide (no/no2/hono) emissions measurements in aircraft exhausts. *Journal of Propulsion and Power*, 23(5):906–911.

[45] Wubben, J., Fabra, F., Calafate, C. T., Krzeszowski, T., Marquez-Barja, J. M., Cano, J. C., and Manzoni, P. (2019). Accurate landing of unmanned aerial vehicles using ground pattern recognition. *Electronics (Switzerland)*, 8(12):1–16.

[46] Xu, J., Thomas, H., Francis, R. W., et al. (2008). A review of processes and technologies for the recycling of lithium-ion secondary batteries. *Journal of Power Sources*, 177(2).

[47] Yang, L., Qi, J., Song, D., Xiao, J., Han, J., and Xia, Y. (2016). Survey of robot 3d path planning algorithms. *Journal of Control Science and Engineering*, 2016.

[48] Yang, Y., Zheng, Z., Bian, K., Song, L., and Han, Z. (2018). Real-time profiling of fine-grained air quality index distribution using uav sensing. *IEEE Internet of Things Journal*, 5(1):186–198.

A

Functional Flow Diagram

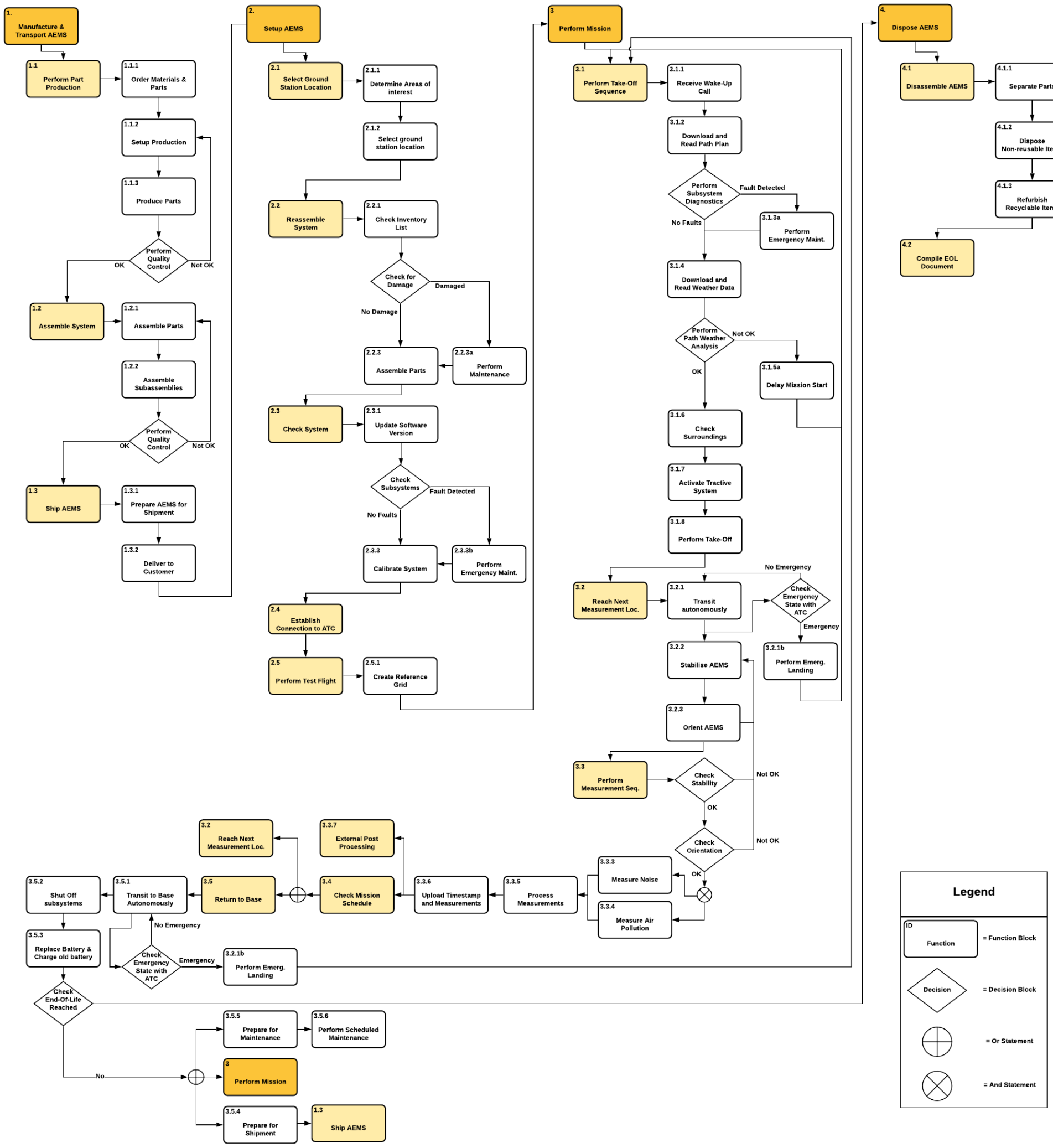

Figure A.1: Functional Flow Diagram

B

Functional Breakdown Structure

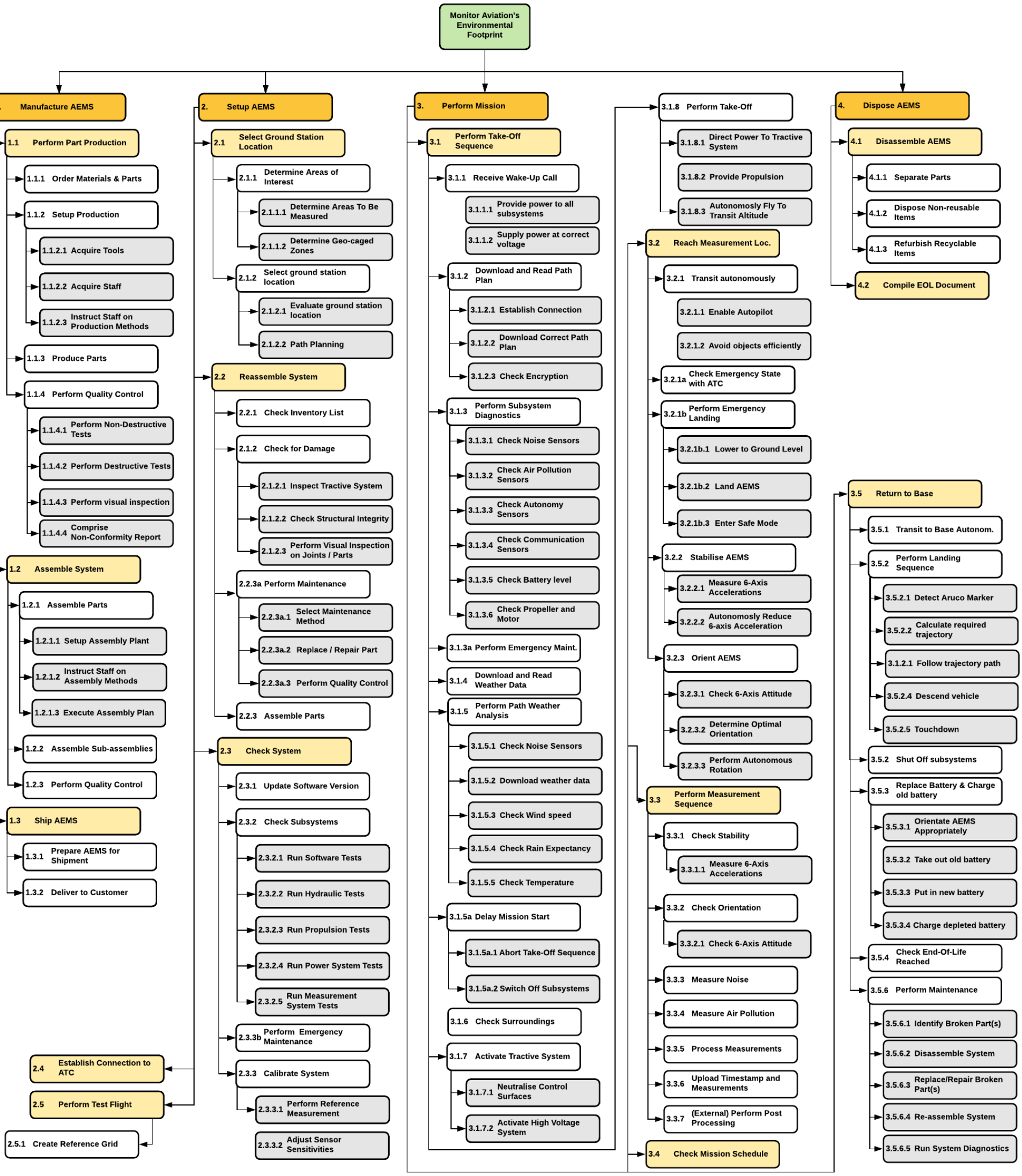

Figure B.1: Functional Breakdown Structure